

---

UNIVERSITÀ DEGLI STUDI DI PADOVA  
DIPARTIMENTO DI FISICA E ASTRONOMIA “GALILEO GALILEI”

CORSO DI DOTTORATO DI RICERCA IN ASTRONOMIA  
Ciclo XXXV

THE EVOLUTION OF COMPACT OBJECTS AND  
THEIR HOST GALAXIES ACROSS COSMIC TIME

**Coordinatore:** Ch.mo Prof. Giovanni Carraro  
**Supervisore:** Ch.ma Prof.ssa Michela Mapelli  
**Co-Supervisore:** Ch.ma Prof.ssa M. Celeste Artale

**Dottorando:** Filippo Santoliquido

---

---



*"Omai convien che tu così ti spoltre",  
disse 'l maestro; "ché, seggendo in piuma,  
in fama non si vien, né sotto coltre;*

*sanza la qual chi sua vita consuma,  
cotal vestigio in terra di sé lascia,  
qual fummo in aere e in acqua la schiuma.*

*E però leva sù; vinci l'ambascia  
con l'animo che vince ogne battaglia,  
se col suo grave corpo non s'accascia.*

*Più lunga scala convien che si saglia;  
non basta da costoro esser partito.  
Se tu mi 'ntendi, or fa sì che ti vaglia".*

– Dante, *Inferno, Canto XXIV*

*Nessuno canti più d'amore o di guerra.*

*L'ordine donde il cosmo traeva nome è sciolto;  
Le legioni celesti sono un groviglio di mostri,  
L'universo ci assedia cieco, violento e strano.  
Il sereno è cosparso d'orribili soli morti,  
Sedimenti densissimi d'atomì stritolati.  
Da loro non emana che disperata gravezza,  
Non energia, non messaggi, non particelle, non luce;  
La luce stessa ricade, rotta dal proprio peso,  
E tutti noi seme umano viviamo e moriamo per nulla,  
E i cieli si convolgono perpetuamente invano.*

– Primo Levi, *Le Stelle Nere, Ad ora incerta*



# Contents

<b>Abstract</b>	<b>VII</b>
<b>List of publications</b>	<b>IX</b>
<b>Symbols and abbreviations</b>	<b>XIV</b>
<b>Acronyms</b>	<b>XV</b>
<b>1 Introduction</b>	<b>1</b>
1.1 Demography of gravitational-wave detections . . . . .	3
1.1.1 Detection of gravitational waves . . . . .	3
1.1.2 The inferred merger rate density using gravitational-wave data . . . . .	6
1.2 Astrophysics of merging compact objects . . . . .	12
1.2.1 Single massive stellar evolution . . . . .	12
1.2.2 Isolated formation channel . . . . .	16
1.2.3 Dynamical formation channel . . . . .	18
1.3 Metallicity and Star Formation Rate evolution . . . . .	20
1.3.1 COSMORATE . . . . .	20
1.3.2 GALAXYRATE . . . . .	24
1.4 Thesis layout . . . . .	25
<b>2 The Cosmic Merger Rate Density Evolution of Compact Binaries Formed in Young Star Clusters and in Isolated Binaries</b>	<b>28</b>
2.1 Introduction . . . . .	29
2.2 Methods . . . . .	30
2.2.1 Cosmic MRD . . . . .	30
2.2.2 Population synthesis . . . . .	32
2.2.3 Dynamics . . . . .	33
2.3 Results . . . . .	34
2.3.1 Merger efficiency . . . . .	34
2.3.2 Cosmic MRD . . . . .	35
2.3.3 Mass distribution . . . . .	40
2.4 Summary . . . . .	42
2.5 Software . . . . .	43

<b>3 The cosmic merger rate density of compact objects: impact of star formation, metallicity, initial mass function and binary evolution</b>	<b>44</b>
3.1 Introduction . . . . .	45
3.2 Methods . . . . .	47
3.2.1 Population synthesis . . . . .	47
3.2.2 Cosmic merger rate density . . . . .	50
3.3 Results . . . . .	51
3.3.1 Merger efficiency . . . . .	51
3.3.2 Common envelope . . . . .	52
3.3.3 Natal kicks . . . . .	54
3.3.4 Core-collapse SN model . . . . .	54
3.3.5 Mass accretion efficiency . . . . .	54
3.3.6 Initial mass function . . . . .	58
3.3.7 Metallicity and SFR evolution . . . . .	58
3.3.8 Merger rate density as a function of metallicity . . . . .	62
3.4 Discussion . . . . .	62
3.4.1 Fitting the merger rate density at $z < 1$ . . . . .	62
3.4.2 Merger efficiency and delay time impact on merger rate density . . . . .	67
3.4.3 Comparison with previous work . . . . .	68
3.5 Summary . . . . .	68
<b>4 Modelling the host galaxies of binary compact object mergers with observational scaling relations</b>	<b>72</b>
4.1 Introduction . . . . .	73
4.2 Methods . . . . .	74
4.2.1 Binary compact objects (BCOs) . . . . .	75
4.2.2 Observational scaling relations . . . . .	75
4.2.3 Merger rate density . . . . .	83
4.2.4 Host galaxy (HG) . . . . .	84
4.3 Results . . . . .	88
4.3.1 Merger rate density . . . . .	88
4.3.2 Formation and host galaxies across cosmic time . . . . .	89
4.3.3 Merger rate per galaxy . . . . .	92
4.3.4 Role of passive galaxies . . . . .	95
4.4 Discussion . . . . .	96
4.4.1 Constant versus variable GSMF . . . . .	96
4.4.2 Main sequence of star forming and starburst galaxies . . . . .	96
4.4.3 Metallicity relationships . . . . .	99
4.5 Conclusions . . . . .	100
4.6 Appendix . . . . .	103
4.6.1 Delay time distributions and merger efficiency . . . . .	103
4.6.2 Impact of the comoving volume on the merger rate . . . . .	105
4.6.3 Impact of the minimum galaxy mass on the merger rate . . . . .	106
4.6.4 Impact of the solar metallicity on the merger rate density . . . . .	106

<b>5 Binary black hole mergers from Population III stars: uncertainties from star formation and binary star properties</b>	<b>109</b>
5.1 Introduction . . . . .	109
5.2 Methods . . . . .	111
5.2.1 Population synthesis with SEVN . . . . .	111
5.2.2 Initial conditions for Pop. III binary systems . . . . .	113
5.2.3 Formation history of Pop. III stars . . . . .	115
5.3 COSMORATE . . . . .	118
5.4 Results . . . . .	118
5.4.1 Merger rate density of BBHs born from Pop. III stars . . . . .	118
5.4.2 Evolution of BH mass with redshift . . . . .	121
5.5 Discussion . . . . .	127
5.5.1 The formation channels . . . . .	127
5.5.2 The evolution of the secondary mass . . . . .	129
5.5.3 The effect of natal kicks . . . . .	129
5.5.4 BBH mergers above the mass gap . . . . .	131
5.5.5 Merger Rate Density of BBHs born from Pop. II stars . . . . .	133
5.5.6 Comparison with previous work . . . . .	136
5.6 Summary and conclusions . . . . .	136
5.7 Appendix . . . . .	138
5.8 Comparison sample of BBHs from Pop. I-II stars . . . . .	138
<b>6 Conclusions</b>	<b>140</b>
6.1 Future developments . . . . .	144
<b>List of Figures</b>	<b>148</b>
<b>List of Tables</b>	<b>149</b>
<b>Bibliography</b>	<b>170</b>



---

## Abstract

Gravitational wave (GW) detections allow us to construct a demography of compact objects. These are exotic systems such as stellar-mass black holes (BHs) and neutron stars (NSs). The LIGO-Virgo-KAGRA (LVK) collaboration has gathered about 90 event candidates with high probability of astrophysical origin, all of them possibly associated with binary compact object mergers. In this Thesis, I explore the evolution of binary compact objects across cosmic time. This topic has become increasingly important in recent years, as the next generation of ground-based detectors will be able to detect binary black hole mergers out to  $z \sim 100$ , if there are any at such high redshift.

In this work, I evaluate the astrophysical merger rates and the properties of the host galaxies of binary black holes (BBHs), black hole-neutron star binaries (BHNSs) and binary neutron stars (BNSs). Determining their merger rate density evolution is challenging because of various sources of uncertainty. To address this issue, I have developed a code called `COSMORATE`, which combines catalogues of merging compact objects with an observation-based estimate of the metallicity-specific star formation rate density. This code is highly adaptable and allows for the exploration of different regions of the parameter space that significantly impact the merger rate density. For example, I took into account different formation channels of binary compact objects, such as dynamics or isolated binary evolution. I have found that the merger rate density of dynamically formed BBHs in young star clusters is higher than that of isolated BBHs. This is not the case for BNSs formed in young star clusters, which are less likely to merge because dynamics inhibits their formation.

Focusing on the isolated formation scenario, I examined the major sources of uncertainty that affect the merger rate density. For example, the BNS merger rate ranges from  $\sim 10^3$  to  $\sim 20$  Gpc $^{-3}$  yr $^{-1}$  at redshift  $z \sim 0$ , when the common envelope (CE) efficiency parameter is varied from  $\alpha = 7$  to 0.5 in our population synthesis code `MOBSE`. In contrast, the local merger rates of BBHs and BHNSs only change by a factor of  $\sim 2 - 3$ . The main source of uncertainty for the BBH merger rate density is the uncertainty in stellar metallicity evolution, which leads to a variation of (at least) one order of magnitude.

The host galaxies of gravitational-wave sources contain valuable insights about the formation and evolution of compact object mergers. To study this topic, I developed a code called `GALAXYRATE`, which uses observational scaling relations to estimate the astrophysical rates and host galaxy properties. I obtained the properties of the formation galaxy population from the galaxy stellar mass function (GSMF), the star-forming main sequence of galaxies, and either the mass metallicity relation or the fundamental metallicity relation (FMR). I found that the evolution of the BBH merger rate density is significantly impacted by the choice of both the galaxy main sequence and the metallicity evolution. For example, the BBH merger rate density increases more rapidly with redshift when using the mass metallicity relation. I also found that, in general, BBHs tend to form in low-mass, metal-poor galaxies and merge in high-mass, metal-rich galaxies.

The next-generation ground-based detectors will explore gravitational-wave sources at high redshift. In preparation for this, I evaluated the merger rate density and evolving mass spectrum of BBHs formed from the first generation of stars (Population III stars). I thoroughly examined a variety of initial conditions, including variations in the orbital properties and initial mass function of Population III (Pop. III) binary systems, as well as four models of the formation history of Pop. III stars. My analysis revealed that uncertainty on the orbital properties affects the BBH merger rate density by up to two orders of magnitude. Additionally, the uncertainty in the star formation history can significantly impact both the shape and the normalisation of the BBH merger rate density. Finally, the primary black holes born from Pop. III stars tend to be more massive ( $30 - 40 M_{\odot}$ ) with respect to those born from metal-rich stars ( $8 - 10 M_{\odot}$ ).

---

## List of publications

Here below you find a complete list of the papers I published during my PhD Thesis. This Thesis work is based on them (especially but not only on those papers I wrote as first author).

### Published papers

1. **Santoliquido, Filippo**, Michela Mapelli, M. Celeste Artale, and Lumen Boco. Modelling the host galaxies of binary compact object mergers with observational scaling relations. *MNRAS*, 516(3):3297–3317, November 2022.
2. S. Ronchini, M. Branchesi, G. Oganesyan, B. Banerjee, U. Dupletsas, G. Ghirlanda, J. Harms, M. Mapelli, and **F. Santoliquido**. Perspectives for multimessenger astronomy with the next generation of gravitational-wave detectors and high-energy satellites. *A&A*, 665:A97, September 2022.
3. Barbara Patricelli, Maria Grazia Bernardini, Michela Mapelli, Paolo D’Avanzo, **Santoliquido, Filippo**, Giancarlo Cella, Massimiliano Razzano, and Elena Cuoco. Erratum: Prospects for multimessenger detection of binary neutron star mergers in the fourth LIGO-Virgo-KAGRA observing run. *MNRAS*, 514(3):3395–3395, August 2022.
4. Barbara Patricelli, Maria Grazia Bernardini, Michela Mapelli, Paolo D’Avanzo, **Santoliquido, Filippo**, Giancarlo Cella, Massimiliano Razzano, and Elena Cuoco. Prospects for multimessenger detection of binary neutron star mergers in the fourth LIGO-Virgo-KAGRA observing run. *MNRAS*, 513(3):4159–4168, July 2022.
5. Carole Périgois, **Santoliquido, Filippo**, Yann Bouffanais, Ugo N. Di Carlo, Nicola Giacobbo, Sara Rastello, Michela Mapelli, and Tania Regimbau. Gravitational background from dynamical binaries and detectability with 2G detectors. *Phys. Rev. D*, 105(10):103032, May 2022.

6. Rosalba Perna, M. Celeste Artale, Yi-Han Wang, Michela Mapelli, Davide Lazzati, Cecilia Sgalletta, and **Santoliquido, Filippo**. Host galaxies and electromagnetic counterparts to binary neutron star mergers across the cosmic time: detectability of GW170817-like events. *MNRAS*, 512(2):2654–2668, May 2022.
7. Michela Mapelli, Yann Bouffanais, **Santoliquido, Filippo**, Manuel Arca Sedda, and M. Celeste Artale. The cosmic evolution of binary black holes in young, globular, and nuclear star clusters: rates, masses, spins, and mixing fractions. *MNRAS*, 511(4):5797–5816, April 2022.
8. Alessandro A. Trani, Sara Rastello, Ugo N. Di Carlo, **Santoliquido, Filippo**, Ataru Tanikawa, and Michela Mapelli. Compact object mergers in hierarchical triples from low-mass young star clusters. *MNRAS*, 511(1):1362–1372, February 2022.
9. Marco Dall’Amico, Michela Mapelli, Ugo N. Di Carlo, Yann Bouffanais, Sara Rastello, **Santoliquido, Filippo**, Alessandro Ballone, and Manuel Arca Sedda. GW190521 formation via three-body encounters in young massive star clusters. *MNRAS*, 508(2):3045–3054, December 2021.
10. Yann Bouffanais, Michela Mapelli, **Santoliquido, Filippo**, Nicola Giacobbo, Ugo N. Di Carlo, Sara Rastello, M. Celeste Artale, and Giuliano Iorio. New insights on binary black hole formation channels after GWTC-2: young star clusters versus isolated binaries. *MNRAS*, 507(4):5224–5235, November 2021.
11. Sara Rastello, Michela Mapelli, Ugo N. Di Carlo, Giuliano Iorio, Alessandro Ballone, Nicola Giacobbo, **Santoliquido, Filippo**, and Stefano Torniamenti. Dynamics of binary black holes in low-mass young star clusters. *MNRAS*, 507(3):3612–3625, November 2021.
12. Michela Mapelli, **Santoliquido, Filippo**, Yann Bouffanais, Manuel Arca Sedda, Maria Celeste Artale, and Alessandro Ballone. Mass and Rate of Hierarchical Black Hole Mergers in Young, Globular and Nuclear Star Clusters. *Symmetry*, 13(9):1678, September 2021.

13. Yann Bouffanais, Michela Mapelli, **Santoliquido, Filippo**, Nicola Giacobbo, Giuliano Iorio, and Guglielmo Costa. Constraining accretion efficiency in massive binary stars with LIGO-Virgo black holes. *MNRAS*, 505(3):3873–3882, August 2021.
14. Michela Mapelli, Marco Dall’Amico, Yann Bouffanais, Nicola Giacobbo, Manuel Arca Sedda, M. Celeste Artale, Alessandro Ballone, Ugo N. Di Carlo, Giuliano Iorio, **Santoliquido, Filippo**, and Stefano Torniamenti. Hierarchical black hole mergers in young, globular and nuclear star clusters: the effect of metallicity, spin and cluster properties. *MNRAS*, 505(1):339–358, July 2021.
15. **Santoliquido, Filippo**, Michela Mapelli, Nicola Giacobbo, Yann Bouffanais, and M. Celeste Artale. The cosmic merger rate density of compact objects: impact of star formation, metallicity, initial mass function, and binary evolution. *MNRAS*, 502(4):4877–4889, April 2021.
16. Ugo N. Di Carlo, Michela Mapelli, Nicola Giacobbo, Mario Spera, Yann Bouffanais, Sara Rastello, **Santoliquido, Filippo**, Mario Pasquato, Alessandro Ballone, Alessandro A. Trani, Stefano Torniamenti, and Francesco Haardt. Binary black holes in young star clusters: the impact of metallicity. *MNRAS*, 498(1):495–506, October 2020.
17. Sara Rastello, Michela Mapelli, Ugo N. Di Carlo, Nicola Giacobbo, **Santoliquido, Filippo**, Mario Spera, Alessandro Ballone, and Giuliano Iorio. Dynamics of black hole-neutron star binaries in young star clusters. *MNRAS*, 497(2):1563–1570, September 2020.
18. Ugo N. Di Carlo, Michela Mapelli, Yann Bouffanais, Nicola Giacobbo, **Santoliquido, Filippo**, Alessandro Bressan, Mario Spera, and Francesco Haardt. Binary black holes in the pair instability mass gap. *MNRAS*, 497(1):1043–1049, September 2020.
19. **Santoliquido, Filippo**, Michela Mapelli, Yann Bouffanais, Nicola Giacobbo, Ugo N. Di Carlo, Sara Rastello, M. Celeste Artale, and Alessandro Ballone. The Cosmic Merger Rate Density Evolution of

Compact Binaries Formed in Young Star Clusters and in Isolated Binaries. *ApJ*, 898(2):152, August 2020.

20. M. Celeste Artale, Yann Bouffanais, Michela Mapelli, Nicola Giacobbo, Nadeen B. Sabha, **Santoliquido, Filippo**, Mario Pasquato, and Mario Spera. An astrophysically motivated ranking criterion for low-latency electromagnetic follow-up of gravitational wave events. *MNRAS*, 495(2):1841–1852, June 2020.
21. M. Celeste Artale, Michela Mapelli, Nicola Giacobbo, Nadeen B. Sabha, Mario Spera, **Santoliquido, Filippo**, and Alessandro Bressan. Host galaxies of merging compact objects: mass, star formation rate, metallicity, and colours. *MNRAS*, 487(2):1675–1688, August 2019.
22. Michela Mapelli, Nicola Giacobbo, **Santoliquido, Filippo**, and Maria Celeste Artale. The properties of merging black holes and neutron stars across cosmic time. *MNRAS*, 487(1):2–13, July 2019.

## Papers under review

23. Carole Périgois, Michela Mapelli, **Santoliquido, Filippo**, Yann Bouffanais, and Roberta Rufolo. Binary black hole spins: model selection with GWTC-3. *arXiv e-prints*, page arXiv:2301.01312, January 2023.
24. Biswajit Banerjee, Gor Oganesyan, Marica Branchesi, Ulyana Dupletska, Felix Aharonian, Francesco Brighenti, Boris Goncharov, Jan Harms, Michela Mapelli, Samuele Ronchini, and **Santoliquido, Filippo**. Detecting VHE prompt emission from binary neutron-star mergers: ET and CTA synergies. *arXiv e-prints*, page arXiv:2212.14007, December 2022.
25. Giuliano Iorio, Guglielmo Costa, Michela Mapelli, Mario Spera, Gastón J. Escobar, Cecilia Sgalletta, Alessandro A. Trani, Erika Korb, **Santoliquido, Filippo**, Marco Dall’Amico, Nicola Gaspari, and Alessandro Bressan. Compact object mergers: exploring uncertainties from stellar and binary evolution with SEVN. *arXiv e-prints*, page arXiv:2211.11774, November 2022.

## Others

26. **Santoliquido, Filippo.** The evolution of compact object mergers and their host galaxies across cosmic time. In APS April Meeting Abstracts, volume 2022 of APS Meeting Abstracts, page D15.008, April 2022.

---

## Symbols

$M_\odot$	solar mass = $1.98892 \times 10^{30}$ kg
$R_\odot$	solar radius = $6.957 \times 10^8$ m
au	astronomical unit = $1.495978707 \times 10^{11}$ m
$G$	gravitational constant = $6.6743 \times 10^{-11}$ m $^3$ kg $^{-1}$ s $^{-2}$
$\alpha$	ejection efficiency parameter of the common envelope
$z$	cosmological redshift
$Z$	metallicity fraction
$Z_\odot$	solar metallicity $Z \sim 0.02$
$\eta$	merger efficiency
$\psi(z)$	star formation rate density as function of redshift
$\mathcal{R}(z)$	merger rate density as function of redshift
$\mathcal{R}_0$	merger rate density in the local Universe

---

## Acronyms

BBH	binary black hole
BH	black hole
BHNS	black hole-neutron star binary
BNS	binary neutron star
CE	common envelope
EM	electromagnetic
ET	Einstein telescope
FMR	fundamental metallicity relation
GSMF	galaxy stellar mass function
GW	gravitational wave
GWTC	gravitational-wave transient catalogue
KAGRA	Kamioka Gravitational Wave Detector
LIGO	Laser Interferometer Gravitational-Wave Observatory
LVK	LIGO–Virgo–KAGRA
MRD	merger rate density
MZR	mass-metallicity relation
NS	neutron star
Pop. III	population III
SFR	star formation rate
SFRD	star formation rate density
SN	supernova



# 1

## Introduction

In less than ten years, the field of gravitational wave astrophysics has made significant strides in our understanding of the Universe, managing to become a powerful tool to explore complex and unanswered questions. The first gravitational-wave direct detection (GW150914, Abbott et al., 2016a) was pivotal in this sense, confirming that binary black holes exist and can merge within an Hubble time.

A historical turning point occurred on August 2017, when the Laser Interferometer Gravitational-Wave Observatory (LIGO) and Virgo observed the merger of two neutron stars (Abbott et al., 2017c), followed by the detection,  $\sim 1.7$  s later, of a gamma-ray burst from the same source by the Fermi gamma-ray space telescope (Goldstein et al., 2017) and INTEGRAL (Savchenko et al., 2017). These observations could together spot the event well enough that its host galaxy was also readily found by optical telescopes (Levan et al., 2017; Im et al., 2017; Ebrová et al., 2020; Kilpatrick et al., 2022). The merger produced electromagnetic (EM) emission that were captured by telescopes across the entire spectrum from radio (Alexander et al., 2017) to infrared (Chornock et al., 2017); and optical (Soares-Santos et al., 2017; Coulter et al., 2017; Cowperthwaite et al., 2017) to X-rays (Margutti et al., 2017; Nicholl et al., 2017).

These observational results gave us insights to decades of old unanswered questions in astronomy. For instance, they verified that gravitational waves travel essentially at the speed of light, they confirmed that binary neutron star mergers are both progenitors of short gamma ray bursts (Abbott et al., 2017f) and prolific sites for the formation of heavy elements (Kasen et al., 2017), they measured the Hubble constant in a completely new way using GWs for the source's luminosity distance (Fishbach et al., 2019) and EM observations for its redshift.

During this decade, the LIGO-Virgo-KAGRA (LVK) collaboration performed three observing runs, O1, O2 and O3. At the end of 2018, the LVK collaboration, based on the data collected from O1 and O2, published the first gravitational-wave transient catalogue of compact binary mergers (GWTC-1, Abbott et al., 2019a), reporting a total of 10 BBHs and 1 BNS detections. Most remarkably, this catalogue contains the first direct detection of two coalescing black holes (BHs) GW150914 (Abbott et al., 2016c), the first joint detection of the three gravitational-wave detectors (GW170814, Abbott et al., 2017b) and the already-cited GW170817 (Abbott et al., 2017c) which was both the first detection of two colliding neutron

stars and the first (and only, at the time of writing this Thesis) multi-messenger event.

The second catalogue GWTC-2 (Abbott et al., 2020b) was released at the end of 2020, and reports the first detection with a clear evidence for unequal-mass components (GW190412 Abbott et al., 2020a), and GW190521 (Abbott et al., 2020d) which happened to be the binary black hole merger with the largest total binary mass, equal to  $m_1 = 163.9^{+39.2}_{-23.5} M_\odot$  at 90% credibility. Both these detections challenged the astrophysical models of that time to interpret such exotic systems, leading to new and interesting ideas for their formation scenarios (e.g. Abbott et al., 2020f; Fragione et al., 2020; Fishbach & Holz, 2020; Costa et al., 2021; Dall’Amico et al., 2021; Arca-Sedda et al., 2021).

At the time of writing this thesis the most updated catalogue is GWTC-3, counting 90 event candidates (Abbott et al., 2021a). This catalogue reports the first two candidate detections of black hole-neutron star binaries: GW200105 and GW200115 (Abbott et al., 2021c). It is thus possible since GWTC-3 to perform population inference by considering the three classes of merging compact objects: BNSs, BHNSs and BBHs. Overall, the LVK detections have sparked excitement among astrophysicists and have laid the groundwork for further groundbreaking discoveries in the field.

One of the several open questions that stem by looking at these detections is the interpretation of the astrophysical merger rates of compact objects. The merger rate density is a quantity extracted through a Bayesian hierarchical analysis from the population of detected objects. The LVK provides it both in the local Universe, since most of the detections are found within  $z < 1$ , and as function of redshift.

With the purpose of extending the redshift horizon of the current gravitational-wave detector network, several improvements are planned: from updating the current network at design sensitivity to developing the future generation of detectors: the Einstein Telescope (ET, Punturo et al., 2010) and the Cosmic Explorer (Reitze et al., 2019). The latter instruments feature unprecedented characteristics, by being able to detect merging stellar-mass BHs at  $z \gtrsim 100$  (Maggiore et al., 2020; Ng et al., 2021, 2022b).

In this thesis, I studied the evolution of compact objects and their host galaxies across cosmic time. To do so, I took in account the evolution and formation of compact objects: from birth as massive stars to binary mergers detectable with LVK interferometers. I put together a wide set of interdisciplinary knowledge, ranging from population-synthesis to galaxy evolution across cosmic time. I thus developed two codes that reconstruct the evolving properties with redshift of compact object mergers: COSMO $\mathcal{R}$ ATE and GALAXY $\mathcal{R}$ ATE.

This introductory chapter is structured as follows: Section 1.1 outlines the basic physical principles of gravitational-wave detections and summarises the properties of the detected population with a focus on the inferred merger rate density; Section 1.2 explores the physical principles of the formation and evolution of compact objects; and Section 1.3 explores the evolution across cosmic time of metallicity and star formation rate (SFR), and introduces the architecture of COSMO $\mathcal{R}$ ATE and GALAXY $\mathcal{R}$ ATE.

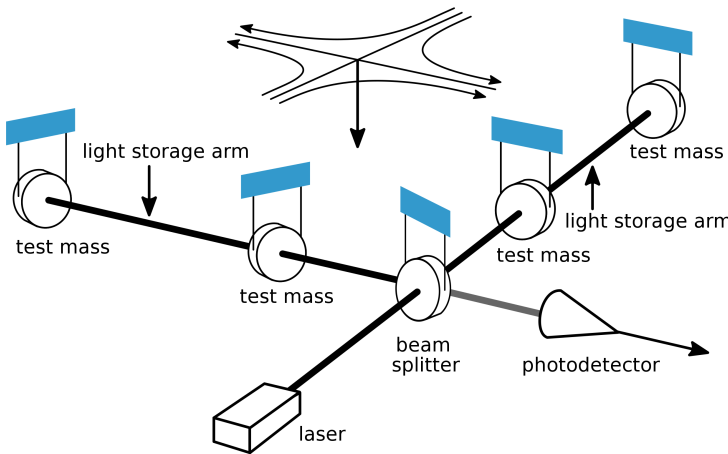


Figure 1.1: Diagram of a basic interferometer design. [Credits: LIGO]

## 1.1 Demography of gravitational-wave detections

Gravitational waves are distortions of space-time propagating at the speed of light ([Einstein, 1915, 1916](#)) and they result from the acceleration of masses that are asymmetrically distributed. One of the loudest sources of gravitational waves are binaries of compact objects, namely neutron stars and black holes. As the two compact objects orbit around each other in a circular orbit, they emit gravitational waves with frequency equal to twice the orbital frequency ([Carroll, 2003](#)). During this process, the binary system loses energy through the emission of gravitational waves and the two compact objects inspiral towards each other ([Peters, 1964](#)). When their orbital separation is small, they start to rapidly approach each other and merge in a single compact object.

### 1.1.1 Detection of gravitational waves

Gravitational waves are currently detected with the second-generation gravitational-wave detectors: Advanced LIGO ([Aasi et al., 2015b](#)) and Advanced Virgo ([Acernese et al., 2015b](#)). The Kamioka Gravitational Wave Detector (KAGRA) also joined the network beginning data collection in February 2020 ([Abbott et al., 2018](#)).

These are large-scale enhanced Michelson interferometers. Figure 1.1 is a schematic diagram of the laser interferometer technique used in GW detectors. When a GW passes through a detector, it causes differences in the relative arm length, generating power variations in the laser output captured by the photodetector. The detectors are operational between the GW frequencies of 10 Hz and 5 kHz. This frequency range corresponds to the GW chirp frequency of merging stellar mass compact objects like BHs and NSs ([Aasi et al., 2015b](#)). The Advanced LIGO detectors consist of two twin detectors located in Livingston (Louisiana) and Hanford (Washington) and are identical in design, with 4 km-long arms. Advanced Virgo has a similar design, with 3 km-long arms.

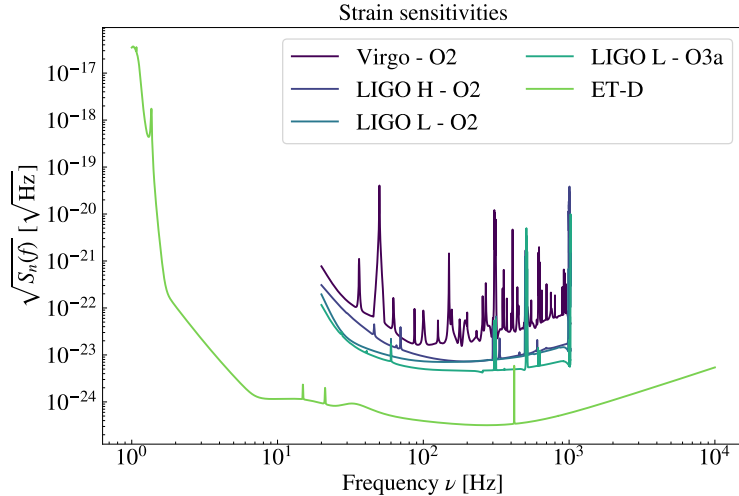


Figure 1.2: One-sided noise power spectral density  $S_n(f)$  of past, current and future detectors. In violet, dark blue and blue I show the strain sensitivity of Virgo, LIGO Hanford (H) and LIGO Livingston (L) during O2, respectively (Abbott et al., 2019a). Advanced LIGO L during O3a is shown in light blue (Abbott et al., 2020b), while in green I show the strain sensitivity expected for the Einstein Telescope in D configuration (for more details see Maggiore et al., 2020).

There are several noise sources that parasite the signal measured by the detector. These sources of noises have distinct effects and occur in various parts of the frequency band. For high frequencies ( $\sim 10^3$  Hz), the main source of noise comes from quantum fluctuations in the number of emitted laser photons and is referred as photon shot noise (Aasi et al., 2013). In the intermediate band, thermal fluctuations in the mirror and their suspensions result in thermal noise that dominates in this frequency band of frequency (Harry et al., 2002). For low frequencies, the main source of noise are seismic vibrations of the Earth that couple with the test masses (Matichard et al., 2015). Finally for the very low frequency regime ( $\sim 10$  Hz), local variations of gravitational potential originating from moving objects close to the detector, pressure waves or thermal fluctuations in the atmosphere introduce an unwanted gravitational attraction on the test masses. These noise sources are referred to as Newtonian noise and will become important especially for the next generation of detectors (Driggers et al., 2012). If we put everything together, we can define an operating band of frequencies in which the detector is sensitive, and characterise the noise level in this band with the one-sided noise power spectral density  $S_n(f)$ , also referred as strain sensitivity. In Figure 1.2, I present the sensitivity of past, current and future detectors.

The upcoming observing run (O4), scheduled to begin in June 2023, is expected to feature a sensitivity improvement for KAGRA, which is expected<sup>1</sup> to operate with a sensitivity above 1 Mpc. This will enable the detection of even more gravitational waves (Abbott et al., 2018). In addition, during the fifth observing run (O5), LIGO-India<sup>2</sup> is also expected to join the

<sup>1</sup><https://observing.docs.ligo.org/plan/>

<sup>2</sup><https://www.ligo-india.in/>

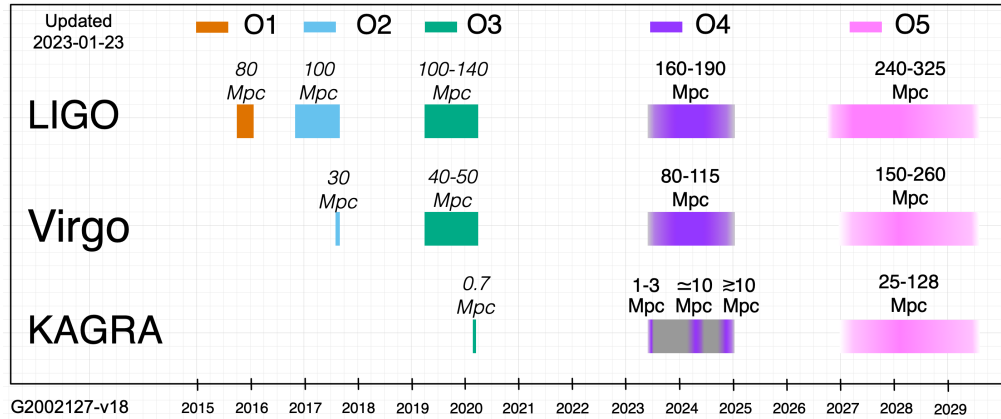


Figure 1.3: The planned sensitivity evolution and observing runs of the Advanced LIGO, Advanced Virgo and KAGRA detectors over the coming years. The colored bars show the observing runs, with achieved sensitivities in O1, O2 and O3, and the expected sensitivities for future runs (see <https://observing.docs.ligo.org/plan/> for further updates).

global network of gravitational-wave detectors. To provide an overview of future plans for GW detection, I have included Figure 1.3, which illustrates the planned sensitivity evolution and observing runs for the GW detector network in the coming years.

### Third-generation detectors

Unlike current detectors, the third generation of ground-based detectors will use brand new technological concepts to significantly improve the sensitivity of current detectors. Two detectors are currently being proposed: the Einstein Telescope (Punturo et al., 2010) and Cosmic Explorer (Reitze et al., 2019). The Einstein Telescope is an European proposal for a gravitational wave detector with arm lengths of  $L = 10$  km. The detector will be located deep underground to shield it from gravitational perturbations and will have a triangular configuration with three laser links. As a consequence, the lower frequency cutoff will be decreased to  $\sim 1$  Hz and the sensitivity will be lower on the entire frequency band (see Figure 1.2). The Cosmic Explorer is an US proposal for a gravitational wave detector that would have a L-design with arm lengths of  $L = 40$  km.

The science potential of the third-generation network is immediately apparent from the dramatic improvement in strain sensitivity (see Figure 1.2). Third-generation detectors will be able of detecting most of the sources that are currently overlooked with the current network. For instance, the large increase in the sensitivity and detection range make an advancement of 1–2 orders of magnitude in the redshift reach for binary coalescences compared to Advanced LIGO and Virgo (see Figure 1.4). The third-generation network will thus survey a large redshift range for merging BBHs and will provide a massive catalogue of detections. As a consequence, it will be possible to better constrain the details of the evolution and the properties of the BBH population. Since the low frequency cutoff of the detector is also lowered, the detectors will also be far more sensitive to the coalescence of intermediate mass black hole binaries (Fragione & Loeb, 2022).

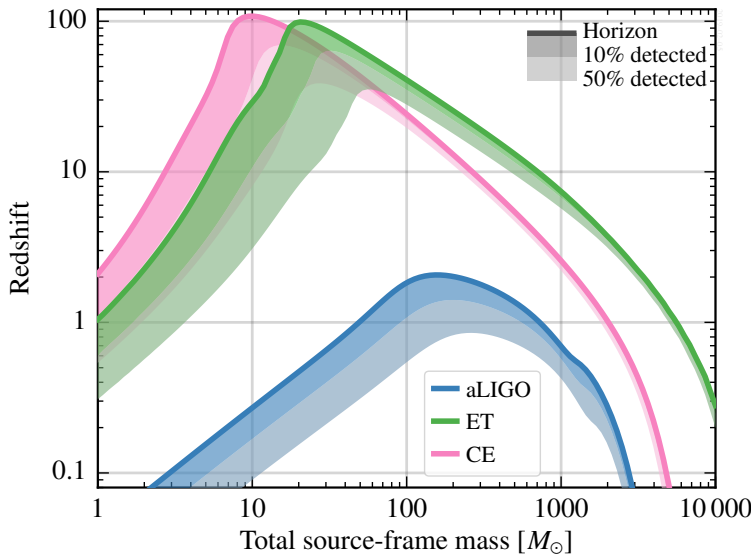


Figure 1.4: Astrophysical reach for equal-mass, non-spinning binaries distributed isotropically in sky and inclination (Kalogera et al., 2021).

The European Strategy Forum on Research Infrastructures (ESFRI)<sup>3</sup> included the Einstein Telescope in 2021 Roadmap. This means that the Einstein Telescope has been identified as one of the most promising European scientific infrastructures. Previous updates of the ESFRI Roadmap have proved to be very influential, providing strategic guidance for investment by member states and associated countries.

### 1.1.2 The inferred merger rate density using gravitational-wave data

The last available release of confirmed gravitational-wave transients counts 90 candidates (GWTC-3, Abbott et al., 2021a). In this section, I present the analyses the LIGO-Virgo-KAGRA (LVK) collaboration carried out on GWTC-3 (Abbott et al., 2021b) to infer the population properties of black holes and neutron stars.

GWTC-3 combines observations from the first three observing runs (O1 and O2, Abbott et al. 2016a, 2019a) and O3 (Abbott et al., 2020b) of the Advanced LIGO and Advanced Virgo gravitational-wave observatories. By taking into account only events with false alarm rate (FAR)<sup>4</sup> of  $< 0.25 \text{ yr}^{-1}$ , they count two binary neutron stars, two neutron star–black hole binaries and 63 confident binary black holes. Considering the BBH population only and a FAR of  $< 1 \text{ yr}^{-1}$ , they can increase the number of BBHs to be equal to 69 confident events. The observed population of events is used to infer the properties of the underlying astrophysical populations of BNSs, BHNSs and BBHs. In particular, in this Section I will focus on the merger rate density, investigating also its cosmological evolution.

<sup>3</sup><https://www.esfri.eu/about>

<sup>4</sup>The FAR is used as a measure of significance, and defines how regularly we would expect to see a noise (non-astrophysical background) event with the same, or higher, ranking statistic as the candidate (Abbott et al., 2021a)

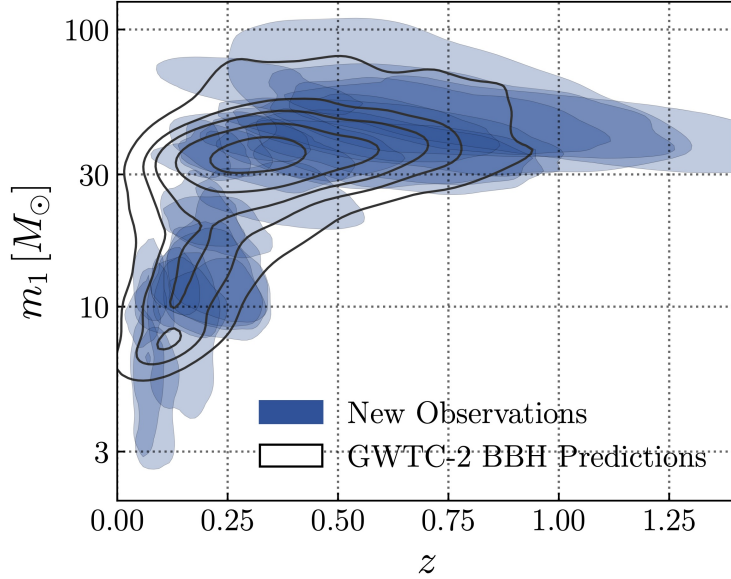


Figure 1.5: The measured redshift  $z$  and primary mass  $m_1$  of compact object mergers released in GWTC-3 (blue shaded regions, Abbott et al., 2021b), compared to the expected population of detected BBHs (black contours) as inferred from the past analysis GWTC-2 (Abbott et al., 2019b).

Figure 1.5 shows the primary mass distribution as a function of redshift of the observations included in GWTC-3. The shaded regions show the two-dimensional marginal distributions for individual events. The redshift of the events is denoted with  $z$ , inferred from the measured luminosity distance using  $H_0 = 67.9 \text{ km s}^{-1} \text{ Mpc}^{-1}$  and  $\Omega_m = 0.3065$  (Ade et al., 2016). The clear evolution of the observed mass distribution with redshift is a consequence of a selection effect: the detectors are more sensitive to higher mass systems. Consequently, from Figure 1.5 alone, the LVK collaboration is not able to directly draw inferences on the merger rate density. It is thus necessary to run an analysis that takes in account both the uncertainties on the parameter estimations and the selection effects.

### Population analysis framework

To infer the parameters describing the population of compact objects, the LVK collaboration adopts a hierarchical Bayesian approach (Mandel et al., 2019; Thrane & Talbot, 2020). Given a set of data  $d_i$  from  $N_{\text{det}}$  gravitational-wave detections, the total number of events is modelled as an inhomogeneous Poisson process. The likelihood of the data given population parameters  $\Lambda$  is (Loredo, 2004; Mandel et al., 2019):

$$\mathcal{L}(d, N_{\text{det}} | \Lambda, N) \propto N^{N_{\text{det}}} e^{-N \xi(\Lambda)} \prod_{i=1}^{N_{\text{det}}} \int \mathcal{L}(d_i | \theta) \pi(\theta | \Lambda) d\theta \quad (1.1)$$

Here,  $N$  is the expected number of mergers over the full duration of an observation period

for the population model  $\Lambda$  (including both detectable and undetectable signals), and  $\xi(\Lambda)$  is the fraction of mergers that are detectable for a population with parameters  $\Lambda$ . The term  $\mathcal{L}(d_i|\theta)$  is the individual event likelihood for the  $i$ -th event in our data set that is described by a set of parameters  $\theta$ . The conditional prior  $\pi(\theta|\Lambda)$  governs the population distribution on event parameters  $\theta$ , e.g., the masses ( $\mathcal{M}, q$ ), spins ( $\chi_{\text{eff}}$ ), and redshifts  $z$ , given a specific population model and set of hyper-parameters  $\Lambda$  to describe the model.

A notable simplification results if a log-uniform prior is imposed on  $N$ , the total number of events (detectable or not): one can then marginalize Equation 1.1 over  $N$  to obtain (Mandel et al., 2019; Fishbach et al., 2018):

$$\mathcal{L}(d|\Lambda) \propto \prod_{i=1}^{N_{\text{det}}} \frac{\int \mathcal{L}(d_i|\theta) \pi(\theta|\Lambda) d\theta}{\xi(\Lambda)} \quad (1.2)$$

The detection fraction  $\xi(\Lambda)$  estimates the fraction of systems that are expected to be successfully detected. Thus, the detection fraction quantifies selection biases, and so it is critical. For a population described by parameters  $\Lambda$ , the detection fraction is

$$\xi(\Lambda) = \int p_{\text{det}}(\theta) \pi(\theta|\Lambda) d\theta \quad (1.3)$$

Here,  $p_{\text{det}}(\theta)$  is the detection probability: the probability that an event with parameters  $\theta$  would be detected by a particular search. The detection probability depends on the angular/sky position and orientation of the source binary, and crucially for my purposes, on the masses and redshift of a system. In simple cases the integral in Equation 1.3 can be evaluated analytically. But for most realistic applications, like those presented here, the detection efficiency  $\xi(\Lambda)$  must be estimated via a Monte Carlo method (e.g. Tiwari, 2018; Farmer et al., 2019).

## Population models

The hyper-parameters  $\Lambda$  can be either astrophysical parameters, such as the common-envelope ejection efficiency  $\alpha$  (see e.g. Bouffanais et al., 2019), or they can be the parameters of phenomenological distributions, as in LVK analysis. In the case of a non-evolving merger rate with redshift, the LVK collaboration assumes a mass spectrum that fits the three classes of compact object mergers at the same time. This procedure has been introduced for the first time with GWTC-3 and it has many advantages. For instance, a joint analysis eliminates the ambiguities in source classification, especially close to the lower mass gap between neutron stars and black holes. Here, I report and briefly describe three different parameter distributions: POWER LAW + DIP + BREAK (PDB), MULTI SOURCE (MS) and BINNED GAUSSIAN PROCESS (BGP). I want to show the impact of different model choices, since they can lead to systemic differences, on the merger rate density (see Table 2.1).

The POWER LAW + DIP + BREAK model (PDB, Fishbach et al., 2020; Farah et al., 2022) consists in a broken power law with a notch filter. The variable depth of this notch filter  $A$  allows for a dearth of events between two potential sub-populations at low and high mass. No gap corresponds to  $A = 0$ , whereas  $A = 1$  corresponds to precisely zero merger

rate over some interval. This notch filter has been inserted to take into account the putative mass gap between neutron stars and black holes (See more in Appendix 1.f in Abbott et al. (2021b)). In the MULTI SOURCE (MS) model, all source categories are modelled in a mixture model, with one sub-population for BNS, BHNS and BBH (See more details in Section C.3 of Abbott et al. (2021b)). The BINNED GAUSSIAN PROCESS (BGP) is a non-parametric model and it is based on Gaussian Processes (Mandel et al., 2017).

For high-mass binary black holes, the network sensitivity allows for a cosmologically significant reach, over which the merger rate density may evolve. Therefore, the case of a merger rate density evolving with redshift is done only for the BBH class. LVK collaboration adopted the fiducial POWER LAW + PEAK (PP) model (Fishbach et al., 2019; Talbot & Thrane, 2018). In PP, the mass-redshift distribution (per unit comoving volume and observer time) was assumed to be of the form

$$p(m_1, q, z) \propto q^\beta p(m_1)(1+z)^{\kappa-1}, \quad (1.4)$$

with  $p(m_1)$  a mixture model containing two components: a power law with some slope and limits; and a Gaussian with some mean and variance (see more in Appendix 1 in Abbott et al. 2021b). The merger rate normalization is chosen such that the source-frame merger rate per comoving volume at redshift  $z$  is given by

$$\mathcal{R}(z) = \frac{dN}{dV_c dt}(z) = \mathcal{R}_0(1+z)^\kappa, \quad (1.5)$$

where  $\mathcal{R}_0$  is the local merger rate density at  $z=0$  and  $\kappa$  is a free parameter governing the evolution of  $\mathcal{R}(z)$  with higher redshift. The corresponding redshift distribution of BBHs (per unit redshift interval) is (Fishbach et al., 2019)

$$p(z|\kappa) \propto \frac{1}{1+z} \frac{dV_c}{dz} (1+z)^\kappa, \quad (1.6)$$

where the leading factor of  $(1+z)^{-1}$  converts time increments from the source frame to the detector frame.

## Merger Rates

Models spanning all source classifications allow the LVK collaboration to self-consistently measure the merger rates for all detected compact objects. Moreover, because events can be classified into each category using mass limits with relatively high confidence, this approach also provides the fiducial BNS, BHNS, and BBH merger rates.

In particular, taking NS masses to lie between 1 and  $2.5 M_\odot$  and BH masses to be between  $2.5$  and  $100 M_\odot$  and taking the lowest 5% and highest 95% credible interval out of all three models, LVK collaboration infers merger rates between  $10 \text{ Gpc}^{-3} \text{ yr}^{-1} - 1700 \text{ Gpc}^{-3} \text{ yr}^{-1}$  for BNS,  $7.8 \text{ Gpc}^{-3} \text{ yr}^{-1} - 140 \text{ Gpc}^{-3} \text{ yr}^{-1}$  for BHNS, and  $16 \text{ Gpc}^{-3} \text{ yr}^{-1} - 61 \text{ Gpc}^{-3} \text{ yr}^{-1}$  for BBH. Table 1.1 provides the rate estimate obtained by taking the union of the intervals resulting from the three models used in this section.

Model	BNS	BHNS	BBH
	$m_1 \in [1, 2.5] M_\odot$	$m_1 \in [2.5, 50] M_\odot$	$m_1 \in [2.5, 100] M_\odot$
	$m_2 \in [1, 2.5] M_\odot$	$m_2 \in [1, 2.5] M_\odot$	$m_2 \in [2.5, 100] M_\odot$
PDB	$44^{+96}_{-34}$	$73^{+67}_{-37}$	$22^{+8.0}_{-6.0}$
MS	$660^{+1040}_{-530}$	$49^{+91}_{-38}$	$37^{+24}_{-13}$
BGP	$98.0^{+260.0}_{-85.0}$	$32.0^{+62.0}_{-24.0}$	$33.0^{+16.0}_{-10.0}$
MERGED	10 – 1700	7.8 – 140	16 – 61

Table 1.1: Merger rates in [ $\text{Gpc}^{-3} \text{ yr}^{-1}$ ] for the various mass bins, assuming merger rates per unit comoving volume are redshift-independent (Abbott et al., 2021b). BNS, BHNS and BBH regions are based solely upon component masses, with the split between NS and BH taken to be  $2.5 M_\odot$ . For all but the last row, merger rates are quoted at the 90% credible interval. For the last row, I provide the union of 90% credible intervals for the preceding three rows, as a conservative realistic estimate of the merger rate for each class accounting for model systematics.

For most categories, the merger rate estimates are consistent with previously published values. LVK inferred from GWTC-2 a BBH merger rate to be  $23.9^{+14.9}_{-8.6} \text{ Gpc}^{-3} \text{ yr}^{-1}$ , while for BNS the merger rate was equal to  $320^{+490}_{-240} \text{ Gpc}^{-3} \text{ yr}^{-1}$  (Abbott et al., 2020e).

To further highlight the impact of model systematics on inferred merger rates, in Table 1.1, I present the derived merger rates across the mass space using all three models presented in the previous Section.

The models used in this Section do not take into account the redshift evolution of the merger rate density, and instead report a constant-in-comoving-volume merger rate density, i.e.  $\kappa = 0$  in Equation 1.5. For most of the mass intervals considered, LVK surveys to date extend to only modest redshift, so the rate evolution versus redshift can be safely neglected.

## Evolution of rate with redshift

The observation of BBH mergers offers the opportunity of not only measuring the local merger rate per comoving volume but also the evolution of this merger rate as we look back towards larger redshifts. Given the limited range of redshift to which LVK searches are sensitive, the merger rate per comoving volume is parametrised as a simple power law (see Equation 1.5)

In a previous study (Abbott et al., 2020c), the redshift distribution was weakly constrained, exhibiting a preference for a rate that increased with redshift but still consistent with a non-evolving merger rate. The LVK collaboration now confidently claims to see the evolution of the BBH merger rate with redshift, inferring that  $\kappa > 0$  at 99.6% credibility. While the exact distribution of  $\kappa$  does depend on the chosen mass model, the LVK collaboration rules out a redshift-independent merger rate at similar credible levels when adopting

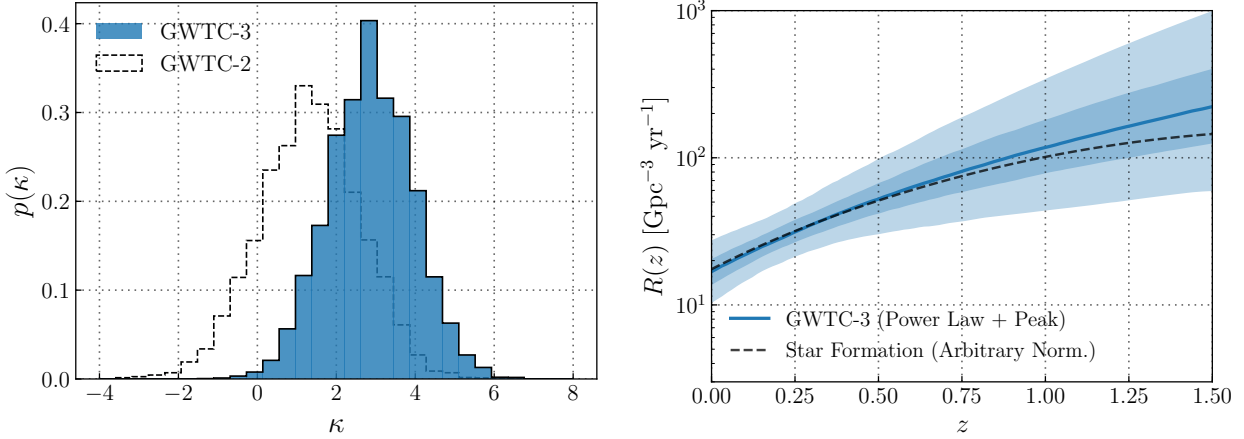


Figure 1.6: *Left:* Posterior on the power-law index  $\kappa$  governing the BBH rate evolution, which is assumed to take the form  $\mathcal{R}(z) \propto (1 + z)^\kappa$  (Abbott et al., 2021b). The blue histogram shows LVK latest constraints using GWTC-3 ( $\kappa = 2.9^{+1.7}_{-1.8}$ ), while the dashed distribution shows previous constraints under GWTC-2 (Abbott et al., 2020c). *Right:* Central 50% (dark blue) and 90% (light blue) credible bounds on the BBH merger rate  $\mathcal{R}(z)$  (Abbott et al., 2021b). The dashed line, for reference, is proportional to the rate of cosmic star formation (Madau & Dickinson, 2014); LVK collaboration infers that  $\mathcal{R}(z)$  remains consistent with evolution tracing star formation.

any of the parameterized mass distribution models used in Abbott et al. (2020c).

The left-hand panel of Figure 1.6 shows the marginal posterior on  $\kappa$  given GWTC-3 in blue, obtained with the PP model. The dashed distribution, meanwhile, shows the previously published measurement of  $\kappa$  obtained with GWTC-2. In the right-hand panel of the same Figure 1.6, I also show the corresponding constraints on  $\mathcal{R}(z)$  itself as a function of redshift. The dark blue line traces the median estimate on  $\mathcal{R}(z)$  at each redshift, while the dark and light shaded regions show central 90% and 50% credible bounds. The best measurement of the BBH merger rate occurs at  $z \sim 0.2$ , at which  $\mathcal{R}(z = 0.2) = 19 - 42$  Gpc $^{-3}$  yr $^{-1}$ . For comparison, the dashed black line in the right-hand panel of Figure 1.6 is proportional to the Madau–Dickinson star formation rate model (Madau & Dickinson, 2014), whose evolution at low redshift corresponds to  $\kappa_{\text{SFR}} = 2.7$ . While the rate evolution remains consistent with the Madau & Dickinson (2014) star formation rate density (SFRD) model, it is not expected for these two rates to agree completely due to the time delays from star formation to merger (O’Shaughnessy et al., 2010; Mapelli & Giacobbo, 2018; Rodriguez & Loeb, 2018; Yang et al., 2019; Antonini & Gieles, 2020; Martinez et al., 2020; Santoliquido et al., 2020; Fishbach et al., 2021; van Son et al., 2022b).

## 1.2 Astrophysics of merging compact objects

The LVK interferometers have marked a milestone in the field of astrophysics by capturing gravitational-wave signals from merging compact objects. According to our current understanding of stellar evolution, neutron stars and black holes are believed to form from massive stars. However, the formation channels of merging compact objects remain a subject of ongoing investigation, with many uncertainties and questions still to be addressed (e.g., [Mapelli, 2018, 2020](#)). These uncertainties stem from the complex processes involved in the evolution of massive stellar binaries, including the the process of common envelope and dynamics of binary systems.

This section provides a brief description of the main astrophysical processes that lead a binary system to be a gravitational-wave source. In other words, I will show how two compact objects form in a binary systems and what makes them merge within an Hubble time. I will start describing some salient features of single stellar evolution, such as stellar winds, supernova (SN) engines and natal kicks. Then, I will outline the physical processes taking place within a binary system, such as mass transfer and common envelope phase. Finally, I will also have a quick look on the formation of merging compact objects within star clusters, i.e. through the dynamical formation scenario.

### 1.2.1 Single massive stellar evolution

#### Stellar winds

Hot massive stars ( $T \gtrsim 10^4$  K,  $M_{\text{ZAMS}} \gtrsim 30 M_{\odot}$ ) lose stellar mass through stellar winds. According to the most recent models, the mass-loss rate by stellar winds scales as a power law with metallicity  $\dot{M} \propto Z^{\beta}$  (see e.g. [Vink et al. 2001](#) and references therein). The power-law index  $\beta$  is likely not a constant, but it is expected to depend on the luminosity of the star  $L_{\star}$ . For example, according to a model by [Chen et al. \(2015\)](#), and based on [Gräfener & Hamann \(2008\)](#):

$$\beta = \begin{cases} 0.85, & \text{if } \Gamma_e \leq 2/3 \\ 2.45 - 2.4\Gamma_e, & \text{if } 2/3 < \Gamma_e \leq 1 \\ 0.05, & \text{if } \Gamma_e > 1, \end{cases} \quad (1.7)$$

where  $\Gamma_e$  is the Eddington ratio, defined as the ratio between the luminosity of the star and its Eddington value  $L_{\text{Edd}}$ <sup>5</sup>. The closer the luminosity is to the Eddington value, the higher the mass loss, cancelling the dependence on metallicity when  $L_{\star} > L_{\text{Edd}}$ .

Figure 1.7 shows how in single stellar evolution, stellar winds determine the final mass of the star at the onset of core-collapse. For instance, if we consider a star with  $M_{\text{ZAMS}} = 90 M_{\odot}$  and metallicity  $Z = 0.02$  (i.e. approximately solar), its final mass will be only  $M_{\text{fin}} \sim 30 M_{\odot}$ ; while the same star with  $Z = 0.005$  retains most of its initial mass ( $M_{\text{fin}} \sim M_{\text{ZAMS}}$ ).

---

<sup>5</sup>The Eddington value is the maximum luminosity a star can achieve when there is balance between the force of radiation acting outward and the gravitational force acting inward.

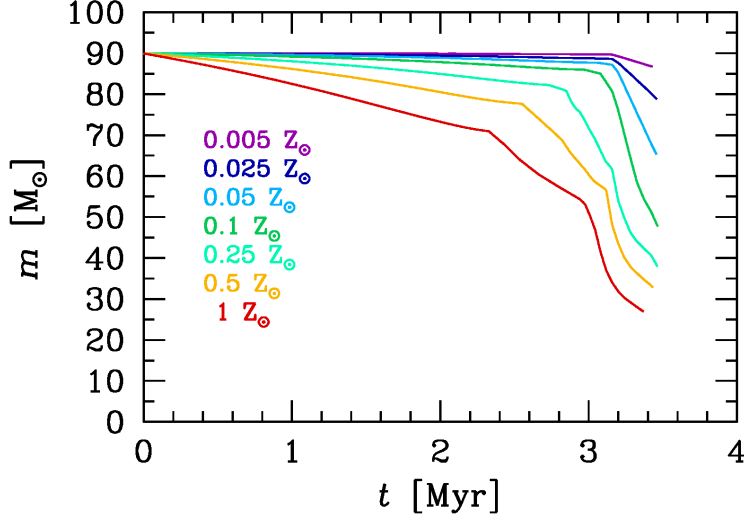


Figure 1.7: Mass evolution of a star with  $M_{\text{ZAMS}} = 90 \text{ M}_{\odot}$  at metallicity of  $Z = 1, 0.5, 0.25, 0.1, 0.05, 0.025, 0.005 Z_{\odot}$  computed with MOBSE (Giacobbo et al., 2018).

Therefore, stellar winds have a vital importance in shaping the mass spectrum of binary black holes, since the final mass of a star  $M_{\text{fin}}$  is the strongest upper limit to the mass of the remnant.

### Core-collapse supernovae and Pair instability

The final outcome of a core-collapse SN is highly debated in the literature. For example, Fryer (1999) and Fryer & Kalogera (2001) suggest the direct collapse mechanism: if the final mass of the star is  $M_{\text{fin}} \gtrsim 40 \text{ M}_{\odot}$ , it collapses directly into a black hole, without supernova explosion. This is due to the binding energy of the outer stellar layers that is too large to be overcome by the explosion.

Alternatively, O'Connor & Ott (2011) developed the idea of the compactness parameter, defined as

$$\xi_M = \frac{M/M_{\odot}}{R(\leq M)/1000 \text{ km}}, \quad (1.8)$$

where  $R(\leq M)$  is the radius which encloses a given mass  $M$ . Usually, the compactness is defined for  $M = 2.5 \text{ M}_{\odot}$  ( $\xi_{2.5}$ ). If the compactness is small (e.g.  $\xi_{2.5} \leq 0.2 - 0.4$ ), the SN explosion is successful, otherwise we expect the star to collapse directly (O'Connor & Ott, 2011). All of these simplified models as well as more sophisticated ones (e.g. Ertl et al. 2016) point toward a similar direction: if the star ends its life with a large final mass, its carbon-oxygen core is larger and thus its compactness is generally higher. As a consequence, metal-poor stars, which retain a large fraction of their mass due to their inefficient stellar-wind mass loss (see Figure 1.7), are expected to develop large cores, i.e. they are more likely to collapse directly to more massive black holes (e.g. Mapelli et al., 2009, 2010; Belczynski et al., 2010).

Core-collapse SNe are not the single mechanism that can end the life of a massive star. When the helium core of a star grows to  $\gtrsim 60 M_{\odot}$  and the central temperature reaches  $\sim 10^9$  K, electron and positron pairs are produced at a higher efficient rate, leading to a decrease in the internal pressure of the star. Thus, the star undergoes the so-called pair instability (Heger et al., 2003; Woosley, 2017): oxygen, neon and silicon are burned explosively and the entire star is disrupted leaving no remnant, unless its helium core is  $\gtrsim 130 M_{\odot}$ . In the latter case, the gravity of the outer layers is large enough for the star to collapse directly to a massive BH (Heger et al., 2003).

Smaller helium cores ( $\sim 30 - 60 M_{\odot}$ ) are linked with a less dramatic manifestation of pair instability: the decrease in internal pressure produces oscillations of the core (pulsational pair instability, Woosley, 2017; Yoshida et al., 2016); during each oscillation the star loses mass until it finds a new equilibrium to a lower core mass, thus leaving a BH smaller than expected without pulsational pair instability (Woosley, 2017; Belczynski et al., 2016; Spera & Mapelli, 2017).

From the combination of pair instability, core-collapse SNe and stellar-wind mass loss prescriptions, we expect the mass spectrum of massive-star remnants to be roughly as shown in Figure 1.8. In particular, pair instability is expected to create a mass gap in the mass spectrum of BHs between  $\sim 50^{+20}_{-10} M_{\odot}$  and  $\sim 120 - 130 M_{\odot}$ . The uncertainty of the boundaries of this mass gap is mainly connected with uncertainties on nuclear reaction rates (Farmer et al., 2019; Costa et al., 2021), on the collapse of the residual hydrogen envelope and on the role of stellar rotation (Mapelli et al., 2020b). We predict a mass range for stellar-origin BHs to be within  $\sim 3$  and  $65 M_{\odot}$ , assuming the most conservative value for the lower edge of pair-instability mass gap. Metal-poor stars, such as population III stars, with mass  $m_{\text{ZAMS}} > 250 M_{\odot}$  might directly collapse to intermediate-mass BHs with mass  $> 100 M_{\odot}$  (Costa & et al., 2023).

## Natal kicks

Compact objects are expected to receive a kick once they form, a so-called natal kick. This can be generated because of asymmetric supernova explosions (e.g. Janka & Mueller, 1994; Burrows & Hayes, 1996) or a non-isotropic emission of neutrinos (e.g. Woosley et al., 1987; Bisnovatyi-Kogan, 1993; Fryer & Kusenko, 2006; Kusenko et al., 2008; Sagert & Schaffner-Bielich, 2008; Nagakura et al., 2019). In addition, if the SN occurs in a binary star, we expect the natal kick affects also the orbital properties of the binary system (Blaauw, 1961), such as by increasing the orbital separation.

Most observational estimates of natal kicks are derived from pulsar proper motions (Lyne & Lorimer, 1994; Hansen & Phinney, 1997; Arzoumanian et al., 2002; Hobbs et al., 2005; Faucher-Giguère & Kaspi, 2006). However, the inferred kick distribution is still a matter of debate. For instance, Hobbs et al. (2005) observed the proper motions of 73 Galactic pulsars younger than  $\sim 3$  Myr. In this way their proper motions were less likely to be affected with dynamical interaction from the environment. They fit a Maxwellian distribution to the natal kick velocities, with one dimensional root-mean square  $\sigma \sim 265 \text{ km s}^{-1}$ .

Other works suggested a bimodal velocity distribution of pulsars, with a first peak at low velocities (e.g.  $\sim 0 \text{ km s}^{-1}$ , (Fryer et al., 1998) or  $\sim 90 \text{ km s}^{-1}$ , (Arzoumanian et al., 2002))

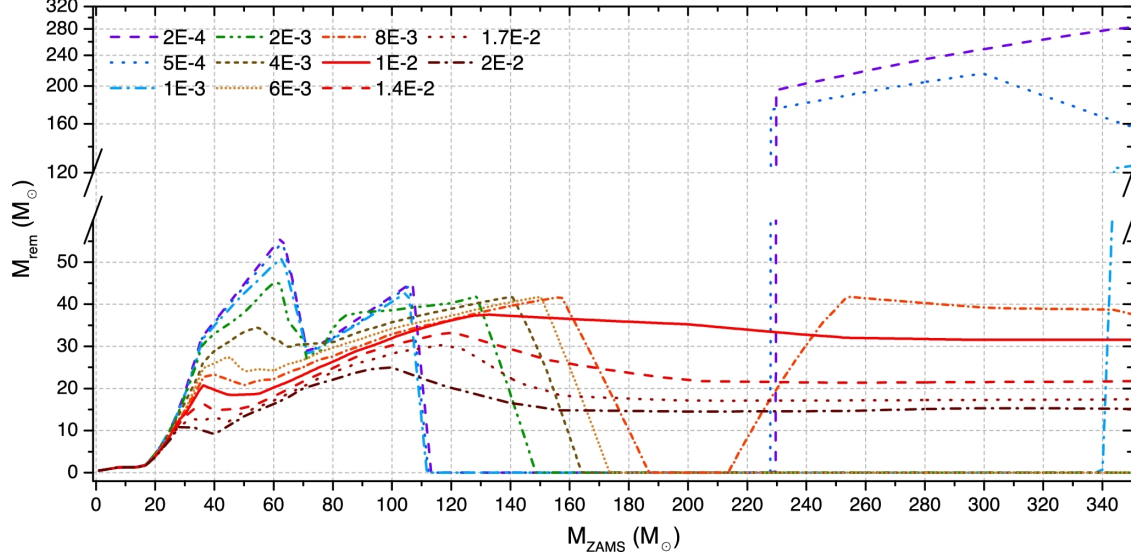


Figure 1.8: Predicted compact object mass ( $M_{\text{rem}}$ ) as a function of the zero-age main-sequence (ZAMS) mass of the progenitor star ( $M_{\text{ZAMS}}$ ) for 11 different metallicities, ranging from  $Z = 2 \times 10^{-4}$  to  $Z = 2 \times 10^{-2}$ , as shown in the legend. These models are obtained with the SEVN population synthesis code (Spera et al., 2019), using PARSEC evolutionary tracks (Bressan et al., 2012) and the delayed model from Fryer et al. (2012). See Spera & Mapelli (2017) for details.

and a second peak at high velocities ( $\sim 500 \text{ km s}^{-1}$ , (Arzoumanian et al., 2002), or  $> 600 \text{ km s}^{-1}$ , (Fryer et al., 1998)). Similarly, Verbunt et al. (2017) indicate that a double Maxwellian distribution provides a significantly better fit to the observed velocity distribution than a single Maxwellian distribution. The low-velocity peak has been attributed to electron-capture SNe, which are less energetic than core-collapse SN (Dessart et al., 2006; Schwab et al., 2015; Gessner & Janka, 2018; Giacobbo & Mapelli, 2019)

The situation for black hole natal kicks is even more uncertain, because data are scanty and difficult to interpret (Nelemans et al., 1999; Mirabel et al., 2001; Mirabel & Rodrigues, 2003; Gualandris et al., 2005; Fragos et al., 2009; Repetto et al., 2012, 2017; Wong et al., 2014). While recent studies (Repetto et al., 2017; Atri et al., 2019) suggest that several Galactic black holes received a relatively high natal kick ( $\sim 100 \text{ km s}^{-1}$ ), we are still far from inferring a distribution of BH kicks from observations.

Giacobbo & Mapelli (2020) proposed a formalism that matches the proper motions of young Galactic pulsars and can naturally account for the differences between different SN engines. As a starting point, they assumed that the Maxwellian distribution derived by Hobbs et al. (2005) is a good description of neutron-star kicks from single stellar evolution. After that, they include in their prescriptions the mass of the ejecta  $m_{\text{ej}}$ , since it is reasonable to assume that the magnitude of the kick depends on the total mass ejected during the SN explosion. Finally, to satisfy linear momentum conservation, they also include a term depending on the mass of the compact object  $m_{\text{rem}}$ . Hence, the new prescription they adopt

for SN kicks can be expressed as

$$v_{\text{kick}} = f_{\text{H05}} \frac{m_{\text{ej}}}{\langle m_{\text{ej}} \rangle} \frac{\langle m_{\text{NS}} \rangle}{m_{\text{rem}}} \quad (1.9)$$

where  $f_{\text{H05}}$  is a random number extracted from a Maxwellian distribution with one-dimensional root-mean-square  $\sigma = 265 \text{ km s}^{-1}$  (Hobbs et al., 2005),  $\langle m_{\text{NS}} \rangle$  is the average NS mass (in Giacobbo & Mapelli (2020),  $\langle m_{\text{NS}} \rangle = 1.2 \text{ M}_\odot$ ) and  $\langle m_{\text{ej}} \rangle$  is the average mass of the ejecta associated with the formation of a NS of mass  $\langle m_{\text{NS}} \rangle$  from single stellar evolution.

### 1.2.2 Isolated formation channel

The scenario highlighted in the previous section assumes that the progenitor star is single. But gravitational waves have shown the existence of binary black holes with a very short orbital separation: the initial separation of a BBH must be of the order of few ten solar radii for the BBH to merge within a Hubble time by gravitational-wave emission. This challenges the understanding of binary star evolution. A close binary star undergoes several physical processes during its life, which can completely change its final fate (see e.g. Eggleton, 2006). The most important processes include mass transfer and common envelope (Hurley et al., 2002).

If two stars exchange matter to each other, it means they undergo a mass transfer episode. This might be driven either by stellar winds or by an episode of Roche-lobe filling. When a massive star loses mass by stellar winds, its companion might be able to capture some of this mass. However, this kind of mass transfer is usually rather inefficient (Bondi & Hoyle, 1944), while the mass transfer by Roche lobe overflow is usually more efficient.

#### Stable mass transfer

The Roche lobe of a star in a binary system is the maximum equipotential surface around the star within which matter is bound to the star. While the exact shape of the Roche lobe should be calculated numerically, a widely used approximate formula (Eggleton, 1983) is

$$r_{\text{L},1} = a \frac{0.49q^{2/3}}{0.6q^{2/3} + \ln(1 + q^{1/3})} \quad (1.10)$$

where  $a$  is the semi-major axis of the binary and  $q = m_1/m_2$  ( $m_1$  and  $m_2$  are the masses of the two stars in the binary). This formula describes the Roche lobe of star with mass  $m_1$ , while the corresponding Roche lobe of star with mass  $m_2$  ( $r_{\text{L},2}$ ) is obtained by swapping the indexes. The Roche lobes of the two stars in a binary are thus connected by the L1 Lagrangian point. Since the Roche lobes are equipotential surfaces, matter orbiting at or beyond the Roche lobe can flow freely from one star to the other. We say that a star overfills (underfills) its Roche lobe when its radius is larger (smaller) than the Roche lobe. If a star overfills its Roche lobe, a part of its mass flows toward the companion star which can accrete (a part of) it. The former and the latter are thus called donor and accretor star, respectively. Mass transfer obviously changes the mass of the two stars in a binary, and thus the final

mass of the compact remnants of such stars, but also the orbital properties of the binary. If mass transfer is non conservative (which is the most realistic case in both mass transfer by stellar winds and Roche lobe overflow), it leads to an angular momentum loss, which in turn affects the semi-major axis.

If mass transfer is unstable<sup>6</sup> or both stars overfill their Roche lobe, then the binary is expected to merge – if the donor lacks a steep density gradient between the core and the envelope – or to enter common envelope – if the donor has a clear distinction between core and envelope.

### Common envelope phase

If two stars enter in the CE phase, the envelope of both stars engulf the entire binary system. The CE might also happen when a star has already left its compact remnant. However, hereafter I describe the CE phase as if there are two cores.

In CE phase, the envelopes stop corotating with their cores. The two stellar cores are embedded in the same non-corotating envelope and start spiralling in as an effect of gas drag exerted by the envelope. Part of the orbital energy lost by the cores as an effect of this drag is likely converted into heating of the envelope, making it more loosely bound with the binary system. This energy transfer process might lead to the complete ejection of the envelope. In this case, the orbital separation of the two cores is considerably smaller than the initial orbital separation of the binary, as an effect of the spiral in.

This circumstance is crucial for the fate of a compact object binary. In fact, if the binary which survives a CE phase evolves into a binary compact object, this will have a very short semi-major axis, much shorter than the sum of the maximum radii of the progenitor stars, and may be able to merge by GW emission ([Peters, 1964](#)) within a Hubble time. In contrast, if the envelope is not ejected, the two cores spiral in until they eventually merge. This premature merger of a binary during a CE phase prevents the binary from evolving into merging compact objects.

The CE phase presents significant challenges in physical modelling and observations. Hydrodynamical simulations of this process are still incomplete, and direct observations of massive stars during their CE phase are still scarce. This results in a large degree of uncertainty that hinders our understanding of the process. On the other hand, the  $\alpha\lambda$  formalism ([Webbink, 1984](#)) is the most common formalism adopted to describe a common envelope in population-synthesis simulations. The basic idea of this formalism is that the energy needed to unbind the envelope comes uniquely from the loss of orbital energy of the two cores during the spiral in. The fraction of the orbital energy of the two cores which goes into unbinding the envelope can be expressed as

$$\Delta E = \alpha(E_{b,f} - E_{b,i}) = \alpha \frac{Gm_{c1}m_{c2}}{2} \left( \frac{1}{a_f} - \frac{1}{a_i} \right), \quad (1.11)$$

where  $E_{b,i}$  ( $E_{b,f}$ ) is the orbital binding energy of the two cores before (after) the CE phase,  $a_i$  ( $a_f$ ) is the semi-major axis before (after) the CE phase,  $m_{c1}$  and  $m_{c2}$  are the masses of the

---

<sup>6</sup>The stability of the mass transfer is preserved when the change in radius of the donor is always leading to a new hydrostatic and thermal equilibrium (see more in Section 3.1 of [Mapelli \(2018\)](#))

two cores, and  $\alpha$  is a dimensionless parameter that measures which fraction of the removed orbital energy is transferred to the envelope. If the primary is already a compact object,  $m_{c2}$  is the mass of the compact object. The binding energy of the envelope is

$$E_{\text{env}} = \frac{G}{\lambda} \left[ \frac{m_{\text{env},1}m_1}{R_1} + \frac{m_{\text{env},2}m_2}{R_2} \right], \quad (1.12)$$

where  $m_1$  and  $m_2$  are the masses of the primary and the secondary member of the binary,  $m_{\text{env},1}$  and  $m_{\text{env},2}$  are the masses of the envelope of the primary and the secondary member of the binary,  $R_1$  and  $R_2$  are the radii of the primary and the secondary member of the binary, and  $\lambda$  is the parameter which measures the concentration of the envelope (the smaller  $\lambda$  is, the more concentrated is the envelope). By imposing  $\Delta E = E_{\text{env}}$  we can derive what is the value of the final semi-major axis  $a_f$  for which the envelope is ejected:

$$\frac{1}{a_f} = \frac{1}{\alpha\lambda} \frac{2}{m_{c1}m_{c2}} \left[ \frac{m_{\text{env},1}m_1}{R_1} + \frac{m_{\text{env},2}m_2}{R_2} \right] + \frac{1}{a_i} \quad (1.13)$$

If  $a_f$  is lower than the sum of the radii of the two cores (or than the sum of the Roche lobe radii of the cores), then the binary will merge during CE, otherwise the binary survives and equation 1.13 tells us the final orbital separation. This means that the larger (smaller)  $\alpha\lambda$  is, the larger (smaller) the final orbital separation.

This simple formalism is a poor description of the complex physics of CE (see [Ivanova et al. \(2013\)](#) for a review). For example, there is a number of observed systems for which an  $\alpha > 1$  is required to be explained, which is obviously not physical. In this case, other sources of energy that are not directly modelled by the  $\alpha\lambda$  formalism can contribute to dissociate more efficiently the envelope (e.g. radiative losses, [Ivanova et al., 2013](#)). Moreover,  $\lambda$  cannot be the same for all stars. It is expected to vary not only from star to star but also during different evolutionary stages of the same star. Several authors ([Xu & Li, 2010](#); [Claeys et al., 2014](#)) have estimated  $E_{\text{env}}$  directly from their stellar models, which removes the  $\lambda$  parameter from Equation 1.13 and significantly improves this formalism. However, even in this case, we cannot get rid of the  $\alpha$  parameter.

The isolated binary evolution scenario has several characteristic signatures. In the common envelope isolated binary evolution scenario, the masses of the two BHs span from  $\sim 3 M_\odot$  up to  $\sim 45 M_\odot$  (see e.g. [Giacobbo et al. \(2018\)](#)) and the mass ratios are preferentially close to 1 (although mass ratios  $q = m_2/m_1 \gtrsim 0.1$  are possible, see e.g. [Giacobbo et al. 2018](#)).

### 1.2.3 Dynamical formation channel

Star clusters are among the densest places in the Universe and there is a number of different star clusters, with their distinguishing characteristics:

- *globular clusters* are old ( $\sim 12$  Gyr) and massive systems ( $\sim 10^4 - 10^6 M_\odot$ , [Gratton et al., 2019](#)),

- *nuclear star clusters* can be even more massive ( $\sim 10^7 M_\odot$ ) and lie at the centre of many galaxies, in some cases coexisting with the supermassive BH (Neumayer et al., 2020),
- *open clusters* and *young star clusters* are generally less massive (up to  $\sim 10^5 M_\odot$ ) and short lived (less than a few Gyr). However, they are the main birthplace of massive stars in the local Universe (Portegies Zwart et al., 2010; Lada & Lada, 2003).

The central density of star clusters is sufficiently high ( $\gtrsim 10^3$  stars pc $^{-3}$ ) that the orbits of stars and binary stars in a star cluster are constantly perturbed by dynamical encounters with other cluster members. This process affects the formation and the evolution of compact objects in multiple ways (Portegies Zwart & McMillan, 2000).

Dynamical exchanges occur when a binary system interacts with a single stellar object and the latter replaces one of the members of the binary. Massive objects are more likely to acquire companions by dynamical exchanges (Hills & Fullerton, 1980). Since BHs are among the most massive objects in a star cluster, they are very efficient in forming new binaries through exchanges (Ziosi et al., 2014).

During a three-body encounter, a binary star exchanges a fraction of its internal energy with the third body. If the binary is particularly tight, a so-called hard binary, such encounters tend to further harden the binary star. In this process called dynamical hardening, the binary binding energy increases by reducing the semi-major axis. In the case of a BBH, this hardening might speed up the merger, because it drives the semi-major axis of the BBH in the regime where orbital decay by gravitational waves becomes efficient (Mapelli et al., 2010). However, the least massive BBHs can even be ionised. In other words, the binary system can be split by strong dynamical encounters with massive intruders.

Mergers of massive stars, before leaving any remnant, are common in dense young star clusters (Portegies Zwart et al., 2010). These mergers can lead to the formation of massive BHs ( $m_{\text{BH}} > 60 M_\odot$ ), with mass in the pair-instability gap (Di Carlo et al., 2019b). In star clusters, such massive BHs can acquire a companion by dynamical exchanges, leading to the formation of BBHs in the mass gap. A fast sequence of stellar mergers in the dense core of a young star cluster (also known as runaway collision, Portegies Zwart et al. 2004; Giersz et al. 2015) might even lead to the formation of intermediate-mass BHs with mass  $m_{\text{BH}} > 100 M_\odot$ , especially at low metallicity (Mapelli, 2016; Di Carlo et al., 2021).

The dynamical processes I briefly summarised above leave a clear imprint on the population of BBHs. For example, the mass spectrum of dynamically formed BBHs extend to higher masses than that of isolated ones. In other words, they might even be found in the pair-instability mass gap or in the intermediate-mass BHs regime (Di Carlo et al., 2021; Rodriguez et al., 2019). These signatures provide an unique opportunity to constrain the fraction of black holes formed in the isolated and the dynamical formation channel. However, this will be possible when the number of gravitational-wave detections will be of the order of a few hundreds (Zevin et al., 2017; Bouffanais et al., 2019).

## 1.3 Metallicity and Star Formation Rate evolution

The average metallicity at which newly stars form is expected to increase across cosmic time (e.g. [Madau & Dickinson, 2014](#)), as the next generations of stars evolve and pollute the surrounding medium with elements heavier than hydrogen and helium. Metals are produced in fusion reactions taking place in stellar interiors. After that, several phenomena can cause a fraction of this enriched material to be released in the surrounding: during supernova explosions, during the merger of white dwarfs or neutron stars (e.g. [Kasen et al., 2017](#)), through stellar winds, and during thermal pulsations of asymptotic giant branch stars (e.g. [Wheeler et al., 1989](#); [Nomoto et al., 2013](#)).

The quantity that describes the distribution of birth metallicities of stars forming at different cosmic times is called metallicity-dependent (or metallicity-specific) cosmic star formation history  $\text{SFRD}(z, Z)$  (e.g. [Dominik et al., 2015](#); [Neijssel et al., 2019](#); [Vitale et al., 2019](#); [Chruścińska, 2022](#)). Various methods were used in the literature to evaluate the metallicity distribution used in studies that estimate the properties of gravitational-wave sources, leading to a wide range of  $\text{SFRD}(z, Z)$ . In this Thesis, I adopt two methods. In Section [1.3.1](#), I present the  $\text{COSMO}\mathcal{R}\text{ATE}$  software, where I adopted averaged properties of the stars in the Universe to retrieve the star formation rate per metallicity bin. Section [1.3.2](#) instead describes  $\text{GALAXY}\mathcal{R}\text{ATE}$ , where galaxy properties are used to reconstruct  $\text{SFRD}(z, Z)$ .

### 1.3.1 $\text{COSMO}\mathcal{R}\text{ATE}$

The simplest way of expressing  $\text{SFRD}(z, Z)$  is by considering the product of a metallicity distribution at a given redshift  $p(Z|z)$  with the redshift-dependent star formation rate  $\psi(z)$  (e.g. [Neijssel et al., 2019](#); [Santoliquido et al., 2020, 2021](#); [van Son et al., 2022a](#)):

$$\text{SFRD}(z, Z) = \psi(z) p(Z|z) \quad (1.14)$$

Measuring the star formation rate at a given time  $\psi(z)$  means inferring mass content from integrated light from galaxies. In order to achieve this, a conversion factor  $\mathcal{K}_\nu$  relates the specific luminosity  $L_\nu$  to the star formation rate ([Madau & Dickinson, 2014](#)). This conversion factor  $\mathcal{K}_\nu$  varies for instance with the metal content, the star formation history of the galaxy, as well as with the initial mass function (IMF). The most common tracers of star formation rate are UV emissions from massive and young stars. IR radiation is also an indirect tracer of star forming regions, since infrared photons are absorbed as UV photons and remitted by dust. Some specific spectral lines are also star-forming indicators. For instance, H-alpha and Lyman-alpha lines come from recombination of ionised gas after ionization by UV photons emitted by young stars.

General consensus in the literature accepts that the comoving SFR density evolves according to the following equation:

$$\psi(z) = a \frac{(1+z)^b}{1 + [(1+z)/c]^d} \quad [\text{M}_\odot \text{ yr}^{-1} \text{ Mpc}^{-3}] \quad (1.15)$$

The best-fitting values in [Madau & Dickinson \(2014\)](#) are  $a = 0.015$ ,  $b = 2.7$ ,  $c = 2.9$  and  $d = 5.6$  (see panel 1 of Figure [1.10](#)). Later on, [Madau & Fragos \(2017\)](#) updated Equation

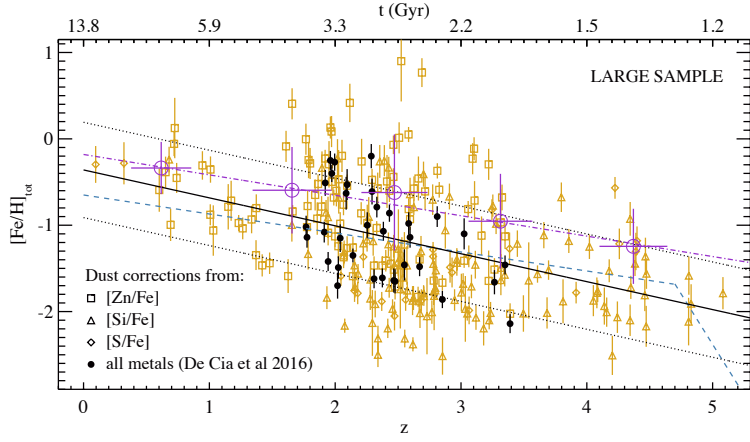


Figure 1.9: Dust-corrected metallicities as a function of redshift. The shape of the symbols indicates which reference was used for dust correction, as labelled in the legend (see also De Cia et al. 2018). The black solid and dotted line display the linear fit to the data and the intrinsic scatter of the relation, respectively. The large open purple circles show the mean DLA metallicities weighted for the neutral gas content, in bins of redshift and the linear fit to those points is shown by the dotted-dashed purple line (expressed in equation 1.17). The uncertainties are the standard deviations of the metallicities and redshifts of the damped Lyman- $\alpha$  system in each redshift bin. The dashed blue curve shows the average damped Lyman- $\alpha$  metallicity derived by Rafelski et al. (2012) and the drop at high  $z$  is suggested by Rafelski et al. (2014), although it is not considered in this Thesis.

1.15 by considering a number of recent results at higher redshift ( $4 \leq z \leq 10$ , Bowler et al., 2015; Finkelstein et al., 2015; Ishigaki et al., 2015; MacLeod et al., 2015; McLeod et al., 2016; Oesch et al., 2015). They provide the best-fit parameters to be equal to  $b = 2.6$ ,  $c = 3.2$  and  $d = 6.2$  (see also Equation 2.2). The normalization factor  $a$  has been multiplied by 0.66 to convert SFRs estimates from a Salpeter IMF (Salpeter, 1955) to a Kroupa IMF (Kroupa, 2001).

The metallicity distribution at a given redshift  $p(Z|z)$  can be a symmetric (e.g. Santoliquito et al., 2020) or an asymmetric distribution (e.g. van Son et al., 2022a). In the case a normal distribution is adopted,  $p(Z|z)$  becomes:

$$p(Z|z) = \frac{1}{\sqrt{2\pi \sigma_Z^2}} \exp \left\{ -\frac{[\log(Z/Z_\odot) - \mu(z)]^2}{2\sigma_Z^2} \right\}. \quad (1.16)$$

where the standard deviation  $\sigma_Z$  is usually redshift independent. In Chapter 3, I discuss the impact of different values of this parameter, ranging from 0 to 0.7 dex. The evolution of the mean value with redshift  $\mu(z)$  can be a linear relation (De Cia et al., 2018) or a power law as in Madau & Fragos (2017).

In the former case, the metal abundances are inferred from absorption line spectroscopy of damped Lyman- $\alpha$  (DLA) systems (Rafelski et al., 2012; De Cia et al., 2018). The main

novelty of De Cia et al. (2018) is the adoption of state-of-the-art simulations to evaluate the dust depletion. In fact, dust can affect the metal abundance measurement up to 0.5 dex. They applied these updated dust corrections on a large sample that contains 236 damped Lyman- $\alpha$  systems. To provide the average metallicity of neutral gas, the dust-corrected metallicities (see Figure 1.9) must be weighted for neutral hydrogen content, to avoid giving too much importance to low-metallicity systems which happen to carry less gas. To this purpose, they divided the sample in bins of redshift ( $z < 1$ ,  $1 \leq z \leq 2$ ,  $2 \leq z \leq 3$ , and  $z \geq 4$ ), and the corresponding weighted metallicity values are shown in Figure 1.9. They derived the linear fit to weighted metallicities and the result is

$$\mu(z) = (-0.24 \pm 0.14)z + (-0.18 \pm 0.21) \quad (1.17)$$

Dust correction provides an intercept that approaches solar metallicity ( $Z_{\odot} = 0.02$ ) at redshift zero. This result is rather important, since Gallazzi et al. (2008) estimated from the Sloan Digital Sky Survey (SDSS) that the average metal content in the local Universe  $Z_*$  is consistent with solar metallicity, i.e.  $Z_* = 1.04 \pm 0.14 Z_{\odot}$ .

This relation of metallicity with redshift also shows a large scatter ( $\sim 0.5$  dex) at fixed redshift. At any given redshift, I expect that damped Lyman- $\alpha$  systems may select galaxies with a range of different masses and metallicities. The scatter of metallicity versus redshift is therefore physical and it reflects a spread in metallicity. For example, following the mass metallicity relation (e.g. Tremonti et al., 2004), a galaxy with low mass will contribute less to the average metallicity evolution. Therefore, the spread in metallicity  $\sigma_Z$  in Equation 1.16 is meant to reproduce indeed this physical scatter.

The method outlined here to evaluate  $\text{SFRD}(z, Z)$  is thus based on average properties, i.e. without considering individual galaxies (Santoliquido et al., 2020, 2021). This evaluation of  $\text{SFRD}(z, Z)$  is implemented in COSMORATE, which estimates the merger rate density as

$$\mathcal{R}(z) = \int_{z_{\min}}^z \left[ \int_{Z_{\min}}^{Z_{\max}} \text{SFRD}(z', Z) \mathcal{F}(z', z, Z) dZ \right] \frac{dt(z')}{dz'} dz' \quad (1.18)$$

where

$$\frac{dt(z')}{dz'} = [H_0(1+z')]^{-1} [(1+z')^3 \Omega_M + \Omega_{\Lambda}]^{-1/2} \quad (1.19)$$

In the above equation,  $H_0$  is the Hubble constant,  $\Omega_M$  and  $\Omega_{\Lambda}$  are the matter and energy density, respectively. I adopt the values in Ade et al. (2016). The term  $\mathcal{F}(z', z, Z)$  is given by

$$\mathcal{F}(z', z, Z) = \frac{1}{\mathcal{M}_{\text{TOT}}(Z)} \frac{d\mathcal{N}(z', z, Z)}{dt(z)} \quad (1.20)$$

where  $\mathcal{M}_{\text{TOT}}(Z)$  is the total simulated initial stellar mass, and  $d\mathcal{N}(z', z, Z)/dt(z)$  is the rate of binary compact objects forming from stars with initial metallicity  $Z$  at redshift  $z'$  and merging at  $z$ , extracted from our catalogues. Figure 1.10 is a chart where a schematic representation of all the quantities entering in COSMORATE are shown.

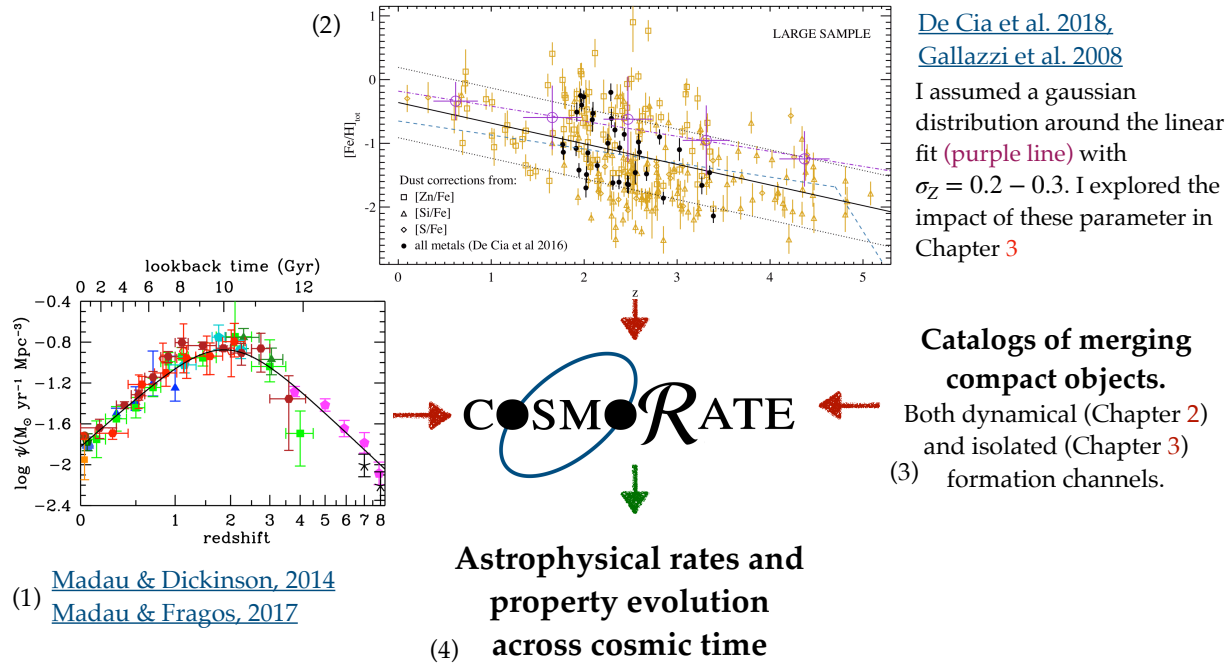


Figure 1.10: Schematic representation of the input and output required for COSMORATE. As input, (1) is the cosmic star formation rate density  $\psi(z)$  in Equation 1.15, (2) is the evolution of the average metallicity with redshift  $\mu(z)$  in Equation 1.17 (see also Figure 1.9 for more details), and (3) are the catalogues of merging compact objects, obtained either through  $N$ -body simulations (Chapter 2) or population-synthesis (Chapter 3). From the catalogues of merging compact objects, I evaluate  $\mathcal{F}(z', z, Z)$  as shown in Equation 1.20. As output, COSMORATE provides the merger rate density of compact objects and the distribution of the properties (e.g. masses, spins) as a function of redshift (4).

### 1.3.2 GALAXYRATE

An alternative way of estimating  $\text{SFRD}(z, Z)$  is based on the chemical evolution of galaxies (Chruścińska et al., 2020; Boco et al., 2021; Chruścińska et al., 2021; Santoliquido et al., 2022). Galaxies show a great variety of chemical and star formation histories, depending, for instance, on their mass, environment and merger history. However, when a volume that contains a representative population of galaxies is considered, the average properties of galaxies (masses, star formation rates and metallicities) appear to be linked through relatively tight and simple relations (e.g. Tremonti et al., 2004; Brinchmann et al., 2004; Ellison et al., 2008).

For instance the star formation rate of star-forming galaxies follows a tight relation with the stellar mass of the galaxy. This relation is known as the galaxy main sequence (Speagle et al., 2014; Lapi et al., 2020; Popesso et al., 2022). Another example concerns the metallicity of galaxies, where two main relations have been proposed: the mass-metallicity relation (MZR, Tremonti et al., 2004; Maiolino et al., 2008; Sanders et al., 2020) and the fundamental metallicity relation (Mannucci et al., 2010; Curti et al., 2020).

These empirical relations can be used to obtain an observation-based estimate of  $\text{SFRD}(z, Z)$  (see Chapter 4 for all the details) without the need for a detailed description of the evolution of individual galaxies. However, differences in the methods used to estimate the galaxy properties from observations lead to a great variety of empirically derived relations (e.g. Kewley & Ellison, 2008; Maiolino & Mannucci, 2019; Telford et al., 2016; Cresci et al., 2019). For instance, in Figure 4.17, I show the impact of two different definitions of the fundamental metallicity relation on the merger rate density. In this case the difference stemmed from the choice of different metallicity calibrations.

Furthermore, observational results are increasingly uncertain or incomplete with increasing redshift and decreasing galaxy luminosity, in which regimes one has to rely on extrapolations. These factors introduce considerable uncertainty in the galaxy-based  $\text{SFRD}(z, Z)$  derivation. Given the sensitivity of compact objects to metallicity (especially BBH, see Section 3.3.1 for all the details), it is thus essential to consider the uncertainties associated with  $\text{SFRD}(z, Z)$  in the calculations of astrophysical rates and properties of the population of gravitational-wave sources.

Furthermore, the host galaxies of compact object mergers are believed to carry crucial information to understand the source of gravitational waves. For instance, the properties of host galaxies (e.g. the stellar mass and the star-formation rate) are expected to be linked with the properties and evolution pathways of compact objects (Toffano et al., 2019; Santoliquido et al., 2022). For these reasons, I developed GALAXYRATE: a new tool that is built on observational scaling relations and their uncertainties, to both recreate the environment in which compact objects form and retrieve the properties of their host galaxies. In Chapter 4, I present the main results I found with GALAXYRATE (Santoliquido et al., 2022).

One of the main novelties of GALAXYRATE is the algorithm I adopted to retrieve the properties of the galaxies that host the mergers. I adapted in a convenient and computationally efficient way the merger trees of cosmological simulations. A merger tree is a data structure that encodes the entire assembly history and property evolution of each single galaxy across cosmic time (e.g. McAlpine et al., 2016). In the end, I condensed the information contained

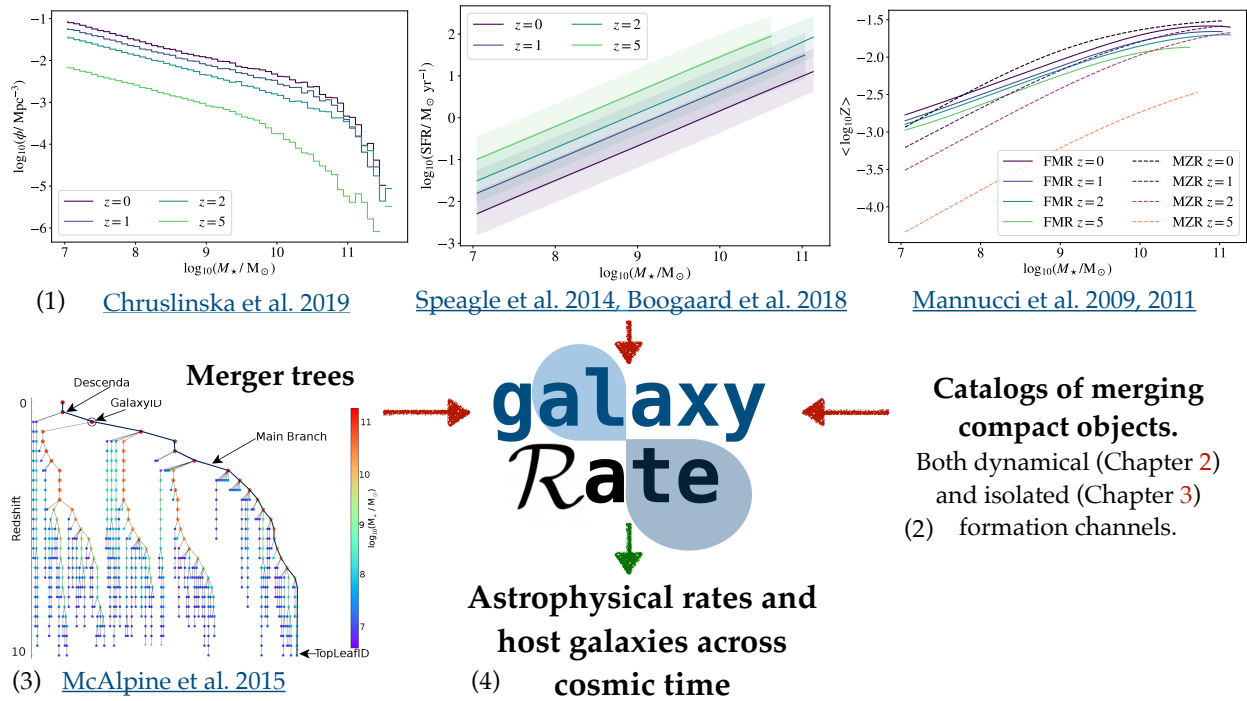


Figure 1.11: Schematic representation of the input and output required for GALAXY RATE. As input, (1) are the observational scaling relation required to evaluate  $SFRD(z, Z)$ , namely starting from left: the galaxy stellar mass function ([Chruslinska et al., 2019](#)), the main sequence of star-forming galaxies ([Speagle et al., 2014; Boogaard et al., 2018](#)), the metallicity relation ([Mannucci et al., 2009, 2011](#)). (2) are the catalogues of merging compact objects, as in Figure 1.10. (3) are the merger trees (e.g. [McAlpine et al., 2016](#)) adapted in a conditional probability (for more details see Section 4.2) to retrieve the properties of the host galaxies. As output, GALAXY RATE provides the merger rate density of compact objects and the properties (e.g. mass, SFR and metallicity) of the host galaxies as a function of redshift (4).

in the merger trees into a conditional probability (see Section 4.2.4 for all the details). This conditional probability links the properties of the formation galaxy, such as stellar mass and star-formation rate at the moment the compact object form, with the same properties of the host galaxy, where the compact object merge. Figure 1.11 shows a chart that schematically represents the building blocks of GALAXY RATE.

## 1.4 Thesis layout

The next four chapters of this Thesis contain original research works, that aim to improve our understanding of compact objects evolution across cosmic time.

In **Chapter 2**, I use COSMORATE to estimate the merger rate density evolution of compact objects with redshift. Catalogues of compact object mergers are coupled with observational constraints on the cosmic star formation rate density and on the average metallicity

evolution with redshift. I adopt catalogues of compact object mergers derived both from recent  $N$ -body and population-synthesis simulations. In this way, I describe the merger rate density of compact object formed in young star clusters (dynamical formation channel) and in the field (isolated formation channel). The local merger rate density of dynamical BBHs is consistent with the 90% credible interval inferred from the third observing run of the LVK collaboration (O3, Abbott et al., 2021b), and with the local merger rate density of isolated BBHs. The local merger rate density of dynamical binary neutron stars is a factor of two lower than that of isolated BNSs. The interplay between cosmic star formation rate, metallicity evolution and delay time of binary compact objects makes the merger rate density for all compact object classes grow with redshift, reaching its maximum at  $z \in [1.5, 2.5]$ , and then decreases.

In **Chapter 3**, I further explore the redshift distribution of BBHs, BHNS and BNS mergers with COSMORATE. In this case, I look at the main sources of uncertainty: star formation rate density, metallicity evolution, common envelope, mass transfer via Roche lobe overflow, natal kicks, core-collapse supernova model and initial mass function. Among binary evolution processes, uncertainties on common envelope ejection have a major impact: the local merger rate density of BNSs varies from  $\sim 10^3$  to  $20 \text{ Gpc}^{-3} \text{ yr}^{-1}$  if I change the common envelope efficiency parameter  $\alpha$  from 0.5 to 7, while the local merger rates of BBHs and BHNSs vary by a factor of  $\sim 2 - 3$ . The BBH merger rate changes by one order of magnitude, when  $1\sigma$  uncertainties on metallicity evolution are taken into account. In contrast, the BNS merger rate is almost insensitive to metallicity.

In **Chapter 4**, I present GALAXYRATE, a new code that estimates the merger rate density of binary compact objects and the properties of their host galaxies, based on observational scaling relations. I generate a population of synthetic galaxies according to the galaxy stellar mass function. I estimate the metallicity according to both the mass-metallicity relation and the fundamental metallicity relation. The slope of the merger rate density of BBHs and BHNSs is steeper if I assume the MZR with respect to the FMR, because the latter predicts a shallower decrease of metallicity with redshift. In contrast, BNSs are only mildly affected by the metallicity relations. Overall, BBHs and BHNSs tend to form in low-mass metal-poor galaxies and merge in high-mass metal-rich galaxies, while BNSs form and merge in massive galaxies. I predict that passive galaxies host at least  $\sim 5 - 10\%$ ,  $\sim 15 - 25\%$ , and  $\sim 15 - 35\%$  of all BNS, BHNS and BBH mergers in the local Universe

In **Chapter 5**, I introduce new models for the binary evolution of Population III stars, which are believed to have produced the first stellar-born BBH mergers in the Universe. To assess the uncertainty in the merger rate density evolution and mass spectrum of Pop. III BBHs, I consider four different star formation histories of Pop. III stars and 11 different configurations of the initial orbital properties of binary systems. My analysis shows that the uncertainty on the orbital properties affects the BBH merger rate density by up to two orders of magnitude, with models having shorter initial orbital periods leading to higher BBH merger rates. This is because such models favour the merger through stable mass transfer episodes. Moreover, the uncertainty on the star formation history has a substantial impact

on both the shape and the normalisation of the BBH merger rate density: the peak of the merger rate density shifts from  $z \sim 8$  up to  $z \sim 16$  depending on the assumed star formation rate, while the maximum rate for our fiducial binary population model spans from  $\sim 2$  to  $\sim 30 \text{ Gpc}^{-3} \text{ yr}^{-1}$ . However, the typical BBH masses are not affected by the star formation rate model and only mildly affected by the binary population parameters. Furthermore, I find that the primary black holes born from Pop. III stars tend to be more massive ( $30 - 40 \text{ M}_\odot$ ) with respect to those born from metal-rich stars ( $8 - 10 \text{ M}_\odot$ ). On the other hand, we expect that Pop. III BBH mergers with primary mass  $m_1 > 60 \text{ M}_\odot$  are extremely rare ( $< 10^{-2} \text{ Gpc}^{-3} \text{ yr}^{-1}$ ).

Chapter 6 outlines the conclusions of this Thesis.

## 2

# The Cosmic Merger Rate Density Evolution of Compact Binaries Formed in Young Star Clusters and in Isolated Binaries

Next generation ground-based gravitational-wave detectors will observe binary black hole (BBH) mergers up to redshift  $z \gtrsim 10$ , probing the evolution of compact binary (CB) mergers across cosmic time. Here, we present a new data-driven model to estimate the cosmic merger rate density (MRD) evolution of CBs, by coupling catalogs of CB mergers with observational constraints on the cosmic star formation rate density and on the metallicity evolution of the Universe. We adopt catalogs of CB mergers derived from recent  $N$ -body and population-synthesis simulations, to describe the MRD of CBs formed in young star clusters (hereafter, dynamical CBs) and in the field (hereafter, isolated CBs). The local MRD of dynamical BBHs is  $\mathcal{R}_{\text{BBH}} = 64_{-20}^{+34} \text{ Gpc}^{-3} \text{ yr}^{-1}$ , consistent with the 90% credible interval from the first and second observing run ( $O1$  and  $O2$ ) of the LIGO–Virgo collaboration, and with the local MRD of isolated BBHs ( $\mathcal{R}_{\text{BBH}} = 50_{-37}^{+71} \text{ Gpc}^{-3} \text{ yr}^{-1}$ ). The local MRD of dynamical and isolated black hole – neutron star binaries is  $\mathcal{R}_{\text{BHNS}} = 41_{-23}^{+33}$  and  $49_{-34}^{+48} \text{ Gpc}^{-3} \text{ yr}^{-1}$ , respectively. Both values are consistent with the upper limit inferred from  $O1$  and  $O2$ . Finally, the local MRD of dynamical binary neutron stars (BNSs,  $\mathcal{R}_{\text{BNS}} = 151_{-38}^{+59} \text{ Gpc}^{-3} \text{ yr}^{-1}$ ) is a factor of two lower than the local MRD of isolated BNSs ( $\mathcal{R}_{\text{BNS}} = 283_{-75}^{+97} \text{ Gpc}^{-3} \text{ yr}^{-1}$ ). The MRD for all CB classes grows with redshift, reaching its maximum at  $z \in [1.5, 2.5]$ , and then decreases. This trend springs from the interplay between cosmic star formation rate, metallicity evolution and delay time of binary compact objects.

Based on:

**Santoliquido F.**, Mapelli M., Bouffanais Y., Giacobbo N., Di Carlo U. N., Rastello S., Artale M. C., Ballone A., 2020, ApJ, 898, 152

## 2.1 Introduction

Thirteen gravitational-wave (GW) events have been published by the LIGO–Virgo collaboration (LVC, Aasi et al. 2015a; Acernese et al. 2015a) since 2016, eleven of them associated with binary black hole (BBH) mergers (Abbott et al., 2016b; Abbott et al., 2016d,a, 2017b,a,g, 2019a,b, 2020a) and two events with binary neutron stars (BNSs) (Abbott et al., 2017c, 2020e). Several additional BBHs were claimed by other studies, based on different pipelines (Venumadhav et al., 2019, 2020; Zackay et al., 2019a,b). This data sample marks the dawn of GW astrophysics, and makes it possible to estimate the local merger rate density (MRD) of binary compact objects. The LVC has inferred a local MRD (within 90 % credible intervals)  $\mathcal{R}_{\text{BBH}} \sim 24 - 140 \text{ Gpc}^{-3} \text{ yr}^{-1}$  (Abbott et al., 2019b),  $\mathcal{R}_{\text{BHNS}} < 610 \text{ Gpc}^{-3} \text{ yr}^{-1}$  (Abbott et al., 2019a) and  $\mathcal{R}_{\text{BNS}} = 250 - 2810 \text{ Gpc}^{-3} \text{ yr}^{-1}$  (Abbott et al., 2020e) for BBHs, black hole–neutron star binaries (BHNSs) and BNSs, respectively.

At design sensitivity, LIGO and Virgo will be sensitive to BBHs up to  $z \gtrsim 1$  and to BNSs up to  $z \sim 0.1$ . Moreover, third-generation ground-based GW interferometers, Einstein Telescope in Europe (Punturo et al., 2010; Maggiore et al., 2020) and Cosmic Explorer in the US (Reitze et al., 2019), are being planned, with a target sensitivity that will allow us to observe BBH mergers up to  $z \gtrsim 10$  and BNS mergers up to  $z \sim 2$  (Kalogera et al., 2019). This will open new perspectives on the study of binary compact objects: we might even reconstruct their formation channels through their redshift evolution. Moreover, we will be able to infer their delay time (i.e. the time elapsed from their formation to their merger, Safarzadeh & Berger 2019) and we might constrain the cosmic star formation rate (SFR) and metallicity evolution based on GWs (Kalogera et al., 2019). Hence, it is crucial to model the cosmic evolution of binary compact objects.

Current theoretical predictions about the cosmic MRD follow two approaches. The first one consists in seeding compact-object binaries (CBs) in cosmological simulations, based on the properties of simulated galaxies (Lamberts et al., 2016, 2018; O’Shaughnessy et al., 2017; Schneider et al., 2017; Mapelli et al., 2017; Mapelli & Giacobbo, 2018; Mapelli et al., 2018, 2019; Toffano et al., 2019; Artale et al., 2019, 2020b,a). This approach is effective if we are interested in the properties of the host galaxies, but is computationally challenging. The alternative approach consists in interfacing catalogs from population-synthesis models, or simpler phenomenological models, with data-driven prescriptions for the evolution of the star-formation rate and the metallicity in the Universe (O’Shaughnessy et al., 2010; Dominik et al., 2013, 2015; Belczynski et al., 2016; Giacobbo & Mapelli, 2018, 2020; Baibhav et al., 2019; Neijssel et al., 2019; Boco et al., 2019; Tang et al., 2020). The latter approach is more effective to sample the parameter space and can be used to probe different formation pathways (such as the isolated binary formation and the dynamical formation scenarios).

While the aforementioned studies focus only on the formation of CBs from isolated binary evolution, several additional works have tried to quantify the MRD evolution of BBHs from globular clusters (Portegies Zwart & McMillan, 2000; Tanikawa, 2013; Rodriguez et al., 2016; Askar et al., 2017; Fragione & Kocsis, 2018; Choksi et al., 2018, 2019; Hong et al., 2018; Rodriguez & Loeb, 2018), nuclear star clusters (Antonini & Rasio, 2016; Petrovich & Antonini, 2017; Sedda, 2020), AGN disks (Bartos et al., 2017; Stone et al., 2017; McKernan et al., 2018; Yang et al., 2019; Tagawa et al., 2019) and open clusters (Ziosi et al., 2014; Kumamoto

et al., 2020). Among these studies, Rodriguez & Loeb (2018) compared the MRD estimated for isolated binaries with the one inferred for globular clusters.

No previous study focused on the cosmic MRD of BBHs born in young star clusters. Since the majority of massive stars are thought to be born in young star clusters, these are a crucial environment for binary compact objects, at least in the local Universe (Lada & Lada, 2003; Portegies Zwart et al., 2010). Young star clusters are short-lived (few Myr to few Gyr) and generally less massive than globular clusters, but are much more common. They continuously form across cosmic time (both at high and at low redshift), while globular cluster formation is strongly suppressed at low redshift. As in globular clusters, dynamical encounters affect the formation of CBs in young star clusters, but with two crucial differences: i) the two-body relaxation timescale is at least a factor of ten shorter in young star clusters with respect to globular clusters, ii) the escape velocity from a typical young star cluster is a factor of 5 – 10 lower than that from a globular cluster (Portegies Zwart et al., 2010). Hence, most dynamical encounters in young star clusters happen in the first  $\sim 10$  Myr and involve the stellar progenitors of a binary compact object, rather than the binary compact object itself (Mapelli, 2016; Kumamoto et al., 2019; Di Carlo et al., 2019b,a). After this early dynamical interaction phase, binary compact objects are generally ejected from their parent young star cluster.

Here, we derive the MRD of CBs (BBHs, BHNSs and BNSs) from young star clusters and compare it with the prediction from isolated binary evolution, using a new data-driven approach. We combine catalogs of simulated CB mergers with the cosmic SFR density evolution inferred by Madau & Fragos (2017) and with a description of the metallicity evolution based on measurements of damped Lyman- $\alpha$  systems up to redshift  $z \sim 5$  (De Cia et al., 2018). The catalogs of simulated mergers of CBs formed in young star clusters (hereafter, dynamical CBs) come from the  $N$ -body simulations presented in Rastello et al. (2020) and Di Carlo et al. (2020), while the isolated CBs are taken from Giacobbo & Mapelli (2018).

## 2.2 Methods

### 2.2.1 Cosmic MRD

We derive the cosmic MRD of CBs as

$$\mathcal{R}(z) = \int_{z_{\min}}^z \psi(z') \frac{dt_{lb}(z')}{dz'} dz' \int_{Z_{\min}(z')}^{Z_{\max}(z')} \eta(Z) \mathcal{F}(z', z, Z) dZ \quad (2.1)$$

where  $t_{lb}(z)$  is the look-back time at redshift  $z$ ,  $\psi(z')$  is the cosmic SFR density at redshift  $z'$ ,  $Z_{\min}(z')$  and  $Z_{\max}(z')$  are the minimum and maximum metallicity of stars formed at redshift  $z'$ ,  $\eta(Z)$  is the merger efficiency at metallicity  $Z$ , and  $\mathcal{F}(z', z, Z)$  is the fraction of CBs that form at redshift  $z'$  from stars with metallicity  $Z$  and merge at redshift  $z$ , normalized to all CBs that form from stars with metallicity  $Z$ . To calculate the lookback time we take the cosmological parameters ( $H_0$ ,  $\Omega_M$  and  $\Omega_\Lambda$ ) from Ade et al. (2016). The maximum considered redshift in equation 2.1 is  $z_{\max} = 15$ , which we assume to be the epoch of formation of the first stars.

The cosmic SFR density  $\psi(z)$  is given by the following fitting formula (Madau & Fragos, 2017)

$$\psi(z) = 0.01 \frac{(1+z)^{2.6}}{1 + [(1+z)/3.2]^{6.2}} \text{ M}_\odot \text{ Mpc}^{-3} \text{ yr}^{-1}. \quad (2.2)$$

To estimate the uncertainty on  $\psi(0)$ , we assume that the errors follow a log-normal distribution with mean  $\log \psi(0) = -2$  and standard deviation  $\sigma_{\log \psi} = 0.2$  (taking into account the typical  $1\sigma$  error bars on single data points, see Figure 9 of Madau & Dickinson 2014).

We define the merger efficiency  $\eta(Z)$  as

$$\eta(Z) = \frac{\mathcal{N}_{\text{TOT}}(Z)}{M_*(Z)}, \quad (2.3)$$

where  $\mathcal{N}_{\text{TOT}}(Z)$  is the total number of CBs (BBHs, BHNSs or BNSs) that have delay time (i.e. the time elapsed from the formation of the binary star to the merger of the two compact objects)  $t_{\text{del}} \leq 14$  Gyr born from stars with metallicity  $Z$  in our population-synthesis simulations, and  $M_*(Z)$  is the total initial stellar mass (corresponding to the zero-age main sequence mass) simulated with metallicity  $Z$ . Thus, the merger efficiency is the number of mergers occurring in a population of initial stellar mass  $M_*$  and metallicity  $Z$ , integrated over a Hubble time (see e.g. Giacobbo & Mapelli 2018; Klencki et al. 2018).

In equation 2.1, the values of  $\eta(Z)$  and  $\mathcal{F}(z', z, Z)$  are estimated from catalogs of CB mergers obtained with population synthesis and with dynamical simulations, as detailed in the next sections. The catalogs contain information on the masses of the two compact objects, the delay time and the metallicity of the progenitor stars. In practice, since we have 6 (3) catalogs corresponding to 6 (3) different metallicities for isolated (dynamical) binary compact objects, the values of  $\eta(Z)$  are linearly interpolated between the available metallicities (Figure 2.1).

The value of  $\mathcal{F}(z', z, Z)$  depends on the metallicity  $Z$  of stars that form at redshift  $z'$ . To derive the average metallicity evolution as a function of redshift we use the following fitting formula:

$$\mu(z) = \log \left( \frac{Z(z)}{Z_\odot} \right) = \log a + b z, \quad (2.4)$$

where  $a = 1.04 \pm 0.14$  and  $b = -0.24 \pm 0.14$ . In the above equation, the slope  $b$  comes from De Cia et al. (2018), who provide a fit to the metallicity evolution of a large sample of damped Lyman- $\alpha$  systems with redshift between 0 and 5. The original fit by De Cia et al. (2018) yields a metallicity  $Z(z=0) = 0.66 Z_\odot$ , which is low compared to the average stellar metallicity measured at redshift zero (see, e.g., the discussion in Madau & Dickinson 2014). Hence, in equation 2.4, we have re-scaled the fitting formula provided by De Cia et al. (2018) to yield  $Z(z=0) = (1.04 \pm 0.14) Z_\odot$ , where  $Z_\odot = 0.019$ , consistent with the average metallicity of galaxies at  $z \sim 0$  from the Sloan Digital Sky Survey (Gallazzi et al., 2008). The value of  $a = 1.04 \pm 0.14$  adopted in equation 2.4 is the result of this rescaling. The quoted uncertainties on both  $a$  and  $b$  are at  $1\sigma$ , assuming (as done in the original papers by Gallazzi et al. 2008 and De Cia et al. 2018) that the observational values follow a Gaussian distribution.

We model the distribution of stellar metallicities  $\log(Z/Z_\odot)$  at a given redshift as a normal distribution with mean value  $\mu(z)$  from eq. 2.4 and standard deviation<sup>1</sup>  $\sigma_Z = 0.20$

$$p(z', Z) = \frac{1}{\sqrt{2\pi\sigma_Z^2}} \exp\left\{-\frac{[\log(Z/Z_\odot) - \mu(z')]^2}{2\sigma_Z^2}\right\}. \quad (2.5)$$

Based on our definition,  $\mathcal{F}(z', z, Z)$  and  $p(z', Z)$  are connected by the following relation:

$$\mathcal{F}(z', z, Z) = \frac{\mathcal{N}(z, Z)}{\mathcal{N}_{\text{TOT}}(Z)} p(z', Z), \quad (2.6)$$

where  $\mathcal{N}(z, Z)$  is the number of CBs that form from stars with metallicity  $Z$  and merge at redshift  $z$ , while  $\mathcal{N}_{\text{TOT}}(Z)$  is the total number of CBs that merge within a Hubble time and form from stars with metallicity  $Z$  (as already detailed above).

We performed  $10^3$  realizations of equation 2.1 per each considered model, in order to estimate the impact of observational uncertainties on the MRD. At each realization, we randomly draw the normalization value of the SFR density (equation 2.2), the intercept and the slope of the average metallicity (equation 2.4) from three Gaussian distributions with mean (standard deviation) equal to  $\log\psi(0) = -2$  ( $\sigma_{\log\psi} = 0.2$ ),  $a = 1.04$  ( $\sigma_a = 0.14$ ) and  $b = -0.24$  ( $\sigma_b = 0.14$ ), respectively. The value of the intercept and that of the slope are drawn separately, assuming no correlation. This procedure is implemented in the new python script COSMORATE, which allows us to calculate up to  $10^3$  models per day on a single core.

## 2.2.2 Population synthesis

The catalogs of isolated binaries have been generated with our population-synthesis code MOBSE (Mapelli et al., 2017; Giacobbo et al., 2018; Giacobbo & Mapelli, 2018; Mapelli & Giacobbo, 2018). In MOBSE, the mass loss of massive hot stars is described as  $\dot{M} \propto Z^\beta$ , where  $\beta$  is defined as in Giacobbo et al. (2018):

$$\beta = \begin{cases} 0.85, & \text{if } \Gamma_e \leq 2/3 \\ 2.45 - 2.4\Gamma_e, & \text{if } 2/3 < \Gamma_e \leq 1 \\ 0.05, & \text{if } \Gamma_e > 1 \end{cases} \quad (2.7)$$

In eq. 2.7,  $\Gamma_e$  is the Eddington ratio, i.e. the ratio between the luminosity of the star and its Eddington value.

MOBSE includes two different prescriptions for core-collapse supernovae (SNe) from Fryer et al. (2012): the *rapid* and the *delayed* SN models. The former model assumes that the SN explosion is launched  $\lesssim 250$  ms after the bounce, while the latter has a longer timescale ( $\gtrsim 500$  ms). In both models, a star is assumed to directly collapse into a black hole (BH) if its final carbon-oxygen mass is  $\gtrsim 11 M_\odot$ . For the simulations described in this work we adopt

---

<sup>1</sup>We assume  $\sigma_Z = 0.20$ , based on the metallicity spread found in cosmological simulations (e.g., EAGLE, Artale et al. 2019). In Santoliquido et al. (2021), we discuss the impact of a different choice of  $\sigma_Z$  (Santoliquido et al. (2021); see also Chruslinska et al. 2019; Chruślińska et al. 2020).

the rapid model, which enforces a gap in the mass function of compact objects between 2 and  $5 M_{\odot}$ . Recipes for electron-capture SNe are included in MOBSE as described in Giacobbo & Mapelli (2019).

Prescriptions for pair instability and pulsational pair instability are implemented using the fitting formulas derived by Spera & Mapelli (2017). In particular, stars which grow a helium core mass  $64 \leq m_{He}/M_{\odot} \leq 135$  are completely disrupted by pair instability and leave no compact objects, while stars with  $32 \leq m_{He}/M_{\odot} < 64$  undergo a set of pulsations, which enhance mass loss and cause the final compact object mass to be significantly smaller than it would be if we had accounted only for core-collapse SNe.

Natal kicks are randomly drawn from a Maxwellian velocity distribution. In the run presented here, we adopt a one-dimensional root mean square velocity  $\sigma = 15 \text{ km s}^{-1}$  for neutron stars. BH natal kicks are drawn from the same distribution as neutron-star kicks, but reduced by the amount of fallback as  $v_{\text{KICK}} = (1 - f_{\text{fb}}) v$ , where  $f_{\text{fb}}$  is the fallback parameter described in Fryer et al. (2012) and  $v$  is the velocity drawn from the Maxwellian distribution.

Binary evolution processes such as tidal evolution, Roche lobe overflow, common envelope and GW energy loss are taken into account as described in Hurley et al. (2002). In particular, the treatment of common envelope is described by the efficiency parameter  $\alpha$ . In this work, we assume  $\alpha = 5$ , as suggested by recent studies (Fragos et al., 2019; Giacobbo & Mapelli, 2020). Orbital decay and circularization by GW emission are calculated according to Peters (1964).

We have simulated  $6 \times 10^7$  isolated binaries with MOBSE,  $10^7$  per each metallicity we considered ( $Z = 0.0002, 0.0008, 0.002, 0.008, 0.016$  and  $0.02$ ). The mass of the primary star is randomly drawn from a Kroupa (2001) initial mass function, with minimum mass  $5 M_{\odot}$  and maximum mass  $150 M_{\odot}$ . The orbital periods, eccentricities and mass ratios of binaries are drawn from Sana et al. (2012). In particular, we derive the mass ratio  $q = m_2/m_1$  as  $\mathcal{D}(q) \propto q^{-0.1}$  with  $q \in [0.1 - 1]$ , the orbital period  $P$  from  $\mathcal{D}(P) \propto P^{-0.55}$  with  $P = \log_{10}(P/\text{day}) \in [0.15 - 5.5]$  and the eccentricity  $e$  from  $\mathcal{D}(e) \propto e^{-0.42}$  with  $0 \leq e \leq 1$ . These simulations are part of run CC15a5 in Giacobbo & Mapelli (2018).

### 2.2.3 Dynamics

We derive the catalogs of CB mergers from a set of direct N-body simulations already described in Di Carlo et al. (2020) and Rastello et al. (2020). These dynamical simulations were ran with the direct N-body code NBODY6++GPU (Wang et al., 2015, 2016), coupled with the population-synthesis code MOBSE, as already described in Di Carlo et al. (2019b). In this way, the dynamical simulations include binary population synthesis, performed with the same code as the isolated-binary simulations.

The masses of the simulated young star clusters range from  $300 M_{\odot}$  to  $30000 M_{\odot}$ . In particular, we consider  $7.5 \times 10^4$  star clusters with mass  $M_{\text{SC}} \in [300, 1000] M_{\odot}$  ( $2.5 \times 10^4$  runs per each considered metallicity:  $Z = 0.0002, 0.002$  and  $0.02$ , from Rastello et al. 2020) and 3000 star clusters with mass  $M_{\text{SC}} \in [1000, 30000] M_{\odot}$  (1000 runs per each considered metallicity:  $Z = 0.0002, 0.002$  and  $0.02$ , presented as set A in Di Carlo et al. 2020). The total mass  $M_{\text{SC}}$  of a star cluster is drawn from a distribution  $dN/dM_{\text{SC}} \propto M_{\text{SC}}^{-2}$ , consistent with the mass function of young star clusters in the Milky Way (Lada & Lada, 2003).

The initial half-mass radius  $r_h$  of star clusters is distributed according to the Marks & Kroupa relation (Marks et al., 2012), which relates the total mass of the star cluster  $M_{\text{SC}}$  with its initial half mass radius  $r_h$  as

$$r_h = 0.10_{-0.04}^{+0.07} \text{ pc} \left( \frac{M_{\text{SC}}}{M_{\odot}} \right)^{0.13 \pm 0.04}. \quad (2.8)$$

The star clusters are initialized in virial equilibrium.

The initial distribution of stellar positions and velocities in the star clusters have been generated through the MCLUSTER code (Küpper et al., 2011), according to a fractal distribution with fractal dimension  $D = 1.6$  (Goodwin & Whitworth, 2004). This ensures that the initial conditions of the simulated star clusters are clumpy and asymmetric as observed embedded star clusters. The mass of the stars is drawn from a Kroupa (2001) initial mass function between 0.1 and 150  $M_{\odot}$ . The total initial binary fraction is  $f_{\text{bin}} = 0.4$ . The mass ratios between secondary and primary star and the orbital properties of the binary systems (period and eccentricity) are drawn according to Sana et al. (2012), to ensure a fair comparison with the isolated binary simulations. The force integration includes a solar neighborhood-like static external tidal field. In particular, the simulated star clusters are assumed to be on a circular orbit around the center of the Milky Way with a semi-major axis of 8 kpc (Wang et al., 2016). Each star cluster is evolved until its dissolution or for a maximum time  $t = 100$  Myr.

Only three metallicities ( $Z = 0.0002, 0.002$  and  $0.02$ ) were available from young star cluster simulations (Rastello et al., 2020; Di Carlo et al., 2020). Running a larger metallicity set is computationally prohibitive. Thus, we linearly interpolated the merger efficiency  $\eta(Z)$  (Figure 2.1) in our dynamical simulations to infer the values of  $\eta(Z)$  for three additional metallicities ( $Z = 0.0008, 0.008, 0.016$ ). We assigned to these three interpolated metallicities the available catalogs of dynamical CB mergers with the closest metallicity to the interpolated values.

## 2.3 Results

### 2.3.1 Merger efficiency

Figure 2.1 shows the merger efficiency  $\eta(Z)$  from young star clusters and isolated binaries. This quantity gives us an idea of the impact of progenitor's metallicity on the merger rate in the different scenarios (isolated and dynamical) we considered. The trend of BNS merger efficiency with metallicity is similar in young star clusters and in isolated binaries, but isolated binaries are more efficient in producing BNS mergers. The main reason is that dynamical encounters may perturb the evolution of relatively low mass binaries (such as BNSs and their progenitors), widening their orbit or even leading to their disruption (e.g. Hills & Fullerton 1980; Ye et al. 2020).

As already noted in several other works (e.g. Dominik et al. 2013; Giacobbo & Mapelli 2018; Klencki et al. 2018; Mapelli et al. 2019), the merger efficiency of BNSs is not significantly affected by progenitor's metallicity.

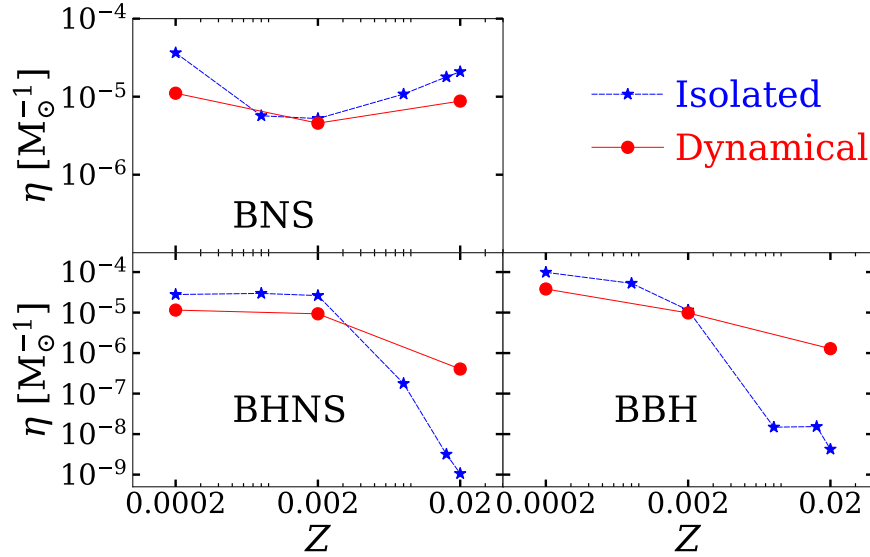


Figure 2.1: Merger efficiency ( $\eta$ ) as a function of progenitor’s metallicity for binaries formed in isolation (blue dashed line and stars) and in young star clusters (red solid line and filled circles).

The most interesting difference between isolated binaries and young star clusters is the behavior of BHNSs and BBHs at solar metallicity. The merger efficiency at solar metallicity is about a factor of 100 higher for BBHs/BHNSs formed in young star clusters than for BBHs/BHNSs formed in isolated binaries. The vast majority of dynamical BBH/BHNS mergers at solar metallicity originate from dynamical exchanges<sup>2</sup> (see Di Carlo et al. 2020 for further details). This means that dynamical encounters tend to boost the merger rate of BBHs and BHNSs in the solar metallicity environment.

### 2.3.2 Cosmic MRD

Figure 2.2 shows the MRD of BBHs as a function of time when considering young star clusters (i.e. dynamical binaries) and isolated binaries. In either case, we assume that the entire population of mergers forms from a single channel (i.e. either from young star clusters or from isolated binaries). It is more likely that a percentage of all mergers comes from young star clusters and another percentage from isolated binaries. In Bouffanais et al. (2019), we constrained these percentages based on LVC results. Here, we just want to compare the differences between the two scenarios.

The MRD of BBHs (in both young star clusters and isolated binaries) grows with redshift (a MRD uniform in comoving volume would be an horizontal line in the plot), peaks at  $z \sim 1.5 - 2.5$ , and finally drops at  $z > 2.5$ . This trend is mostly determined by the cosmic SFR density, which peaks at  $z \sim 2$ , convolved with the delay time and the metallicity dependence.

<sup>2</sup>Exchanges favor the formation of the most massive binaries in a star cluster (Hills & Fullerton, 1980). BHs are particularly efficient in acquiring companions through dynamical exchanges, because they are among the most massive objects in a star cluster.

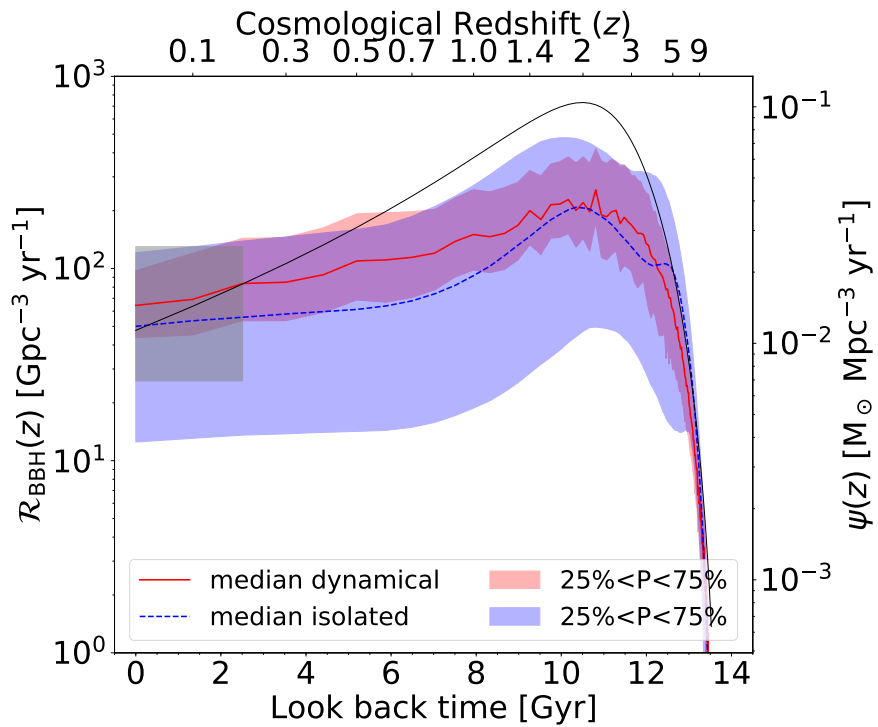


Figure 2.2: The thick lines show the evolution of the MRD of BBHs  $\mathcal{R}_{\text{BBH}}(z)$  in the comoving frame, calculated as explained in section 2.2.1, for BBHs that form in young star clusters (red solid line) and isolated binaries (blue dashed line). The shaded areas represent 50% of all realizations (between the 75% percentile and the 25% percentile). The black solid thin line is the SFR density (from equation 2.2). The gray shaded area shows the 90% credible interval for the local BBH MRD, as inferred from the LVC (Abbott et al., 2019a,b). The width of the gray shaded area on the  $x$ -axis corresponds to the instrumental horizon obtained by assuming BBHs of mass  $(10 + 10) M_{\odot}$  and O2 sensitivity (Abbott et al., 2018).

These results are fairly consistent with previous papers, which consider different population-synthesis models, metallicity evolution and SFR evolution with redshift (e.g. Dominik et al. 2013; Belczynski et al. 2016; Mapelli et al. 2017; Mapelli & Giacobbo 2018; Artale et al. 2019; Neijssel et al. 2019; Tang et al. 2020).

At  $z = 0$ , the median values of the MRD of BBHs formed dynamically in young star clusters (hereafter, dynamical BBHs) and the one of isolated BBHs are  $R_{\text{BBH}} \sim 64$  and  $50 \text{ Gpc}^{-3} \text{ yr}^{-1}$ , respectively. Both values are consistent with the ones inferred from O1 and O2 (Abbott et al., 2019b). The median merger rate of dynamical BBHs is higher than the one of isolated BBHs up to  $z \sim 4$  (see Table 2.1 for more details). This trend can be interpreted by looking at the merger efficiency (Figure 2.1): around solar metallicity, the dynamical channel is more efficient than the isolated channel. Hence, we expect a higher number of dynamical BBH mergers with short delay time in the local Universe, where metallicity is higher. In contrast, the merger efficiency of dynamical BBHs formed from metal-poor stars ( $Z = 0.002$ ) is a factor of  $\sim 2$  lower than the one of isolated BBHs with the same metallicity. Hence, isolated binaries are associated with a higher merger rate from very metal-poor systems.

The MRD of isolated BBHs increases by a factor of  $\sim 1.8$  from local Universe up to  $z = 1$ , and then it grows up faster from redshift  $z = 1$  to redshift  $z = 2$  (Table 2.1). On the other hand, the MRD of dynamical BBHs increases almost with the same trend from  $z = 0$  to  $z \sim 2$  (i.e. without a change of slope at redshift  $z \sim 1$ ). The main reason for the change of slope in the MRD of isolated BBHs is again the stronger dependence of the merger efficiency on metallicity. In the isolated model, most mergers at redshift  $z < 1$  are due to BBHs that formed at higher redshift in lower metallicity environments ( $Z \sim 0.0002$ ) and have a long delay time (Mapelli et al., 2017, 2018).

The uncertainty on MRD resulting from cosmic SFR and metallicity evolution is large, especially for the isolated scenario. For isolated BBHs, the 50% credible interval spreads over more than one order of magnitude between redshift 0 and 4. The 50% credible interval for the MRD of dynamical BBHs is contained within the credible interval of isolated BBHs. The 50% credible interval is smaller for dynamical BBHs, because the merger efficiency is less sensitive to metallicity in the dynamical scenario than in the isolated one (Figure 2.1).

Figure 2.3 shows the MRD evolution of BHNSs. At  $z = 0$ ,  $\mathcal{R}_{\text{BHNS}} = 41^{+33}_{-23}$  and  $49^{+48}_{-34} \text{ Gpc}^{-3} \text{ yr}^{-1}$  for dynamical and isolated BHNSs, respectively. At redshift  $z = 2$ ,  $\mathcal{R}_{\text{BHNS}} = 168^{+138}_{-76}$  and  $406^{+516}_{-331} \text{ Gpc}^{-3} \text{ yr}^{-1}$  for dynamical and isolated BHNSs, respectively. For most of the cosmic time, the boundaries of the 50% credible intervals of our two models have similar values. The higher boundary of the 50% credible interval for both dynamical and isolated BHNSs is below the upper limit from the LVC ( $\mathcal{R}_{\text{BHNS}} < 610 \text{ Gpc}^{-3} \text{ yr}^{-1}$ , Abbott et al. 2019a), indicating that our model is consistent with O1 and O2 results. In the case of both BBHs and BHNSs, most of the uncertainty comes from metallicity evolution, because BBHs and BHNSs are extremely sensitive to metallicity variations (as shown in Figure 2.1).

Finally, Figure 2.4 shows the MRD evolution of dynamical and isolated BNSs. At redshift  $z \leq 0.1$ , the MRD of dynamical BNSs ( $\mathcal{R}_{\text{BNS}} = 151^{+59}_{-38} \text{ Gpc}^{-3} \text{ yr}^{-1}$ ) is a factor of  $\sim 2$  lower than the one of isolated BNSs ( $283^{+97}_{-75} \text{ Gpc}^{-3} \text{ yr}^{-1}$ ). A similar difference is found at  $z = 2$ , where the MRD is  $\mathcal{R}_{\text{BNS}} = 460^{+177}_{-130}$  and  $777^{+354}_{-228} \text{ Gpc}^{-3} \text{ yr}^{-1}$ , for dynamical and isolated BNSs respectively. Overall, the MRD of dynamical BNSs is significantly lower than the one of isolated BNSs, even if the MRD evolution with redshift is similar. This trend is

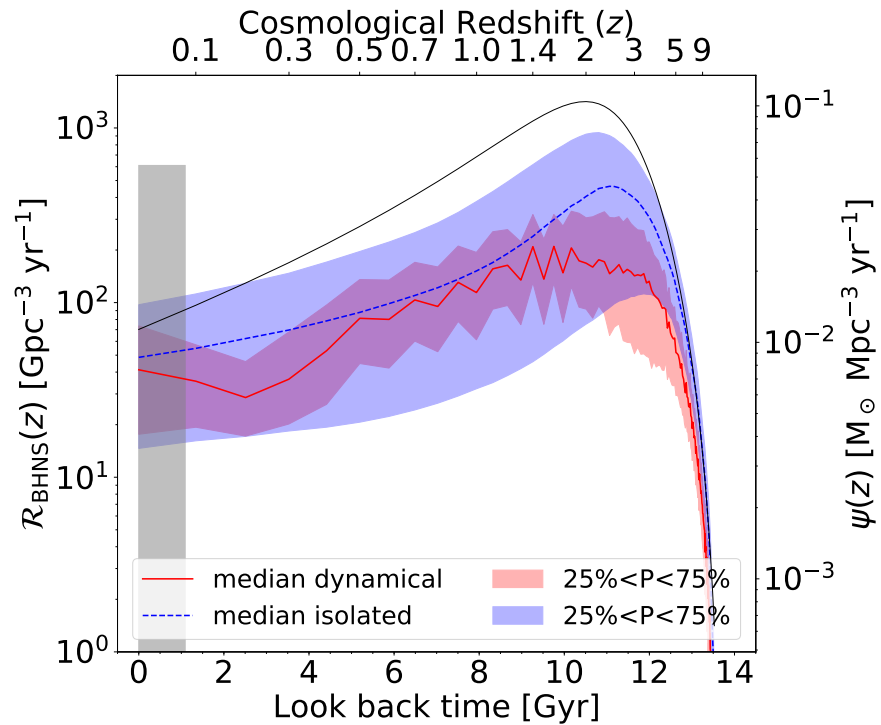


Figure 2.3: Same as Figure 2.2 for BHNSs. The gray box is the upper limit inferred from LVC data (Abbott et al., 2019a). The width of the gray shaded area on the  $x$ -axis corresponds to the instrumental horizon obtained by assuming BHNSs of mass  $(1.4 + 5) M_\odot$  and O2 sensitivity (Abbott et al., 2018).

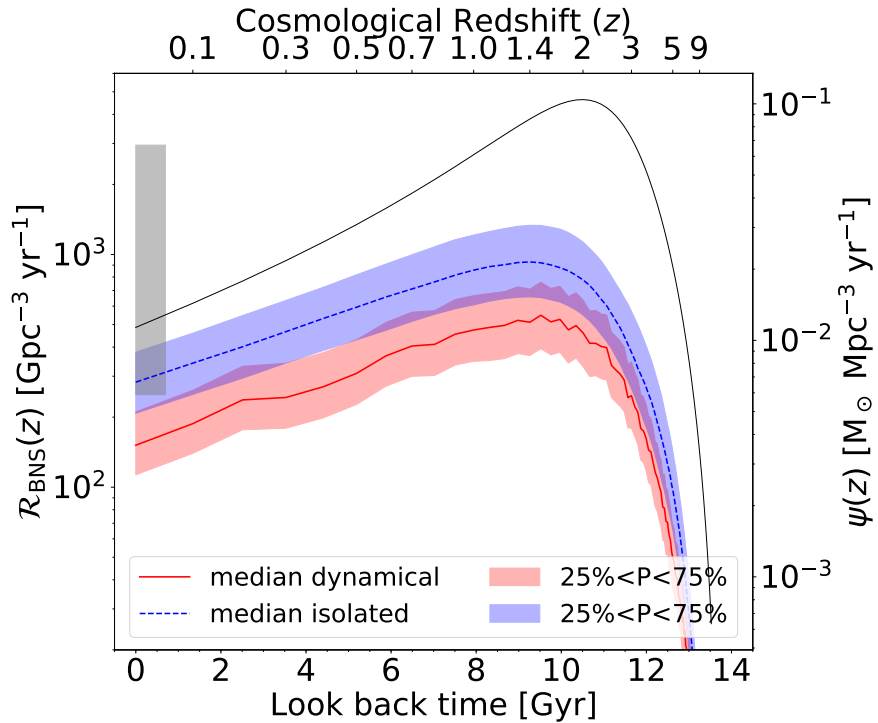


Figure 2.4: Same as Figure 2.2 for BNSs. The gray box is the 90% credible interval inferred by considering both GW170817 and GW190425 (Abbott et al., 2020e). The width of the gray shaded area on the  $x$ -axis corresponds to the instrumental horizon obtained by assuming BNSs of mass  $(1.4 + 1.4) \text{ M}_\odot$  and O2 sensitivity (Abbott et al., 2018).

Table 2.1: MRD in [ $\text{Gpc}^{-3} \text{ yr}^{-1}$ ] for five redshift intervals. We show a comparison between dynamical CBs formed in young star clusters and isolated CBs.

CB	Redshift intervals									
	$z \in [0, 0.1]$		$z \in [0.9, 1.0]$		$z \in [1.9, 2.0]$		$z \in [2.9, 3.0]$		$z \in [3.9, 4.0]$	
	Dynamical	Isolated	Dynamical	Isolated	Dynamical	Isolated	Dynamical	Isolated	Dynamical	Isolated
BBH	$64^{+34}_{-20}$	$50^{+71}_{-37}$	$150^{+107}_{-52}$	$92^{+178}_{-73}$	$220^{+161}_{-77}$	$207^{+256}_{-160}$	$168^{+136}_{-71}$	$130^{+192}_{-91}$	$101^{+75}_{-51}$	$105^{+191}_{-83}$
BHNS	$41^{+33}_{-23}$	$49^{+48}_{-34}$	$114^{+80}_{-53}$	$152^{+227}_{-120}$	$168^{+138}_{-76}$	$406^{+516}_{-331}$	$142^{+129}_{-91}$	$395^{+286}_{-286}$	$99^{+62}_{-55}$	$225^{+131}_{-124}$
BNS	$151^{+59}_{-38}$	$283^{+97}_{-75}$	$473^{+192}_{-126}$	$856^{+355}_{-249}$	$460^{+177}_{-130}$	$777^{+354}_{-228}$	$247^{+98}_{-68}$	$379^{+191}_{-113}$	$110^{+44}_{-31}$	$190^{+98}_{-63}$

expected by looking at Figure 2.1, because the merger efficiency of dynamical BNSs is lower at all metallicities. In young star clusters, the formation of BNSs is slightly suppressed with respect to isolated binaries, because such relatively low-mass binaries tend to be broken or softened (i.e. their orbital separation is increased) by dynamical encounters.

The local MRD of isolated BNSs is consistent with the one inferred from the LVC, while the local MRD of dynamical BNSs is below the 90% credible interval from the LVC. This suggests that (young) star clusters *alone* might not be able to explain all the BNS mergers detected by the LVC.

The models presented in this work assume small natal kicks for neutron stars, which are in tension with the proper motions of Galactic young pulsars (Giacobbo & Mapelli, 2018). We recently proposed a new model for natal kicks that can reproduce the proper motions of Galactic pulsars and gives a value for the MRD close to the one presented in this study (Giacobbo & Mapelli, 2020). As a result, we do not expect significant differences in the MRD between the model adopted in this work and the one proposed by Giacobbo & Mapelli (2020).

The 50% credible interval of simulated BNSs is significantly smaller than that of both BHNSs and BBHs, because BNSs are less sensitive to stellar metallicity (Fig. 2.1). Hence, the uncertainty on BNS merger rate comes mostly from the SFR, for a fixed binary evolution model.

Our local MRDs for dynamical BNSs and BHNSs are higher than the values estimated by Ye et al. (2020) for globular clusters ( $\mathcal{R}_{\text{BNS}} \sim \mathcal{R}_{\text{BHNS}} \sim 0.02 \text{ Gpc}^{-3} \text{ yr}^{-1}$ ). This is not surprising because globular clusters form mostly at  $z \gtrsim 2$ , while smaller star clusters, like the ones we simulated, form all the time from high to low redshift and are an important channel of star formation in the local Universe.

### 2.3.3 Mass distribution

Figure 2.5 shows the mass distribution of BBHs, BHNSs and BNSs merging across cosmic time. We plot together binaries merging at different redshift because we find no significant dependence of the mass distribution on the merger redshift, consistent with Mapelli et al. (2019). The main difference between the mass distribution of dynamical BBHs and the one of isolated BBHs is that low-mass BBHs are less numerous in the former than in the latter scenario. Moreover, the maximum mass of merging BHs from isolated binaries is  $m_{\text{BH}, \text{max}} \sim 45 \text{ M}_\odot$ , whereas dynamics in young star clusters leads to a significantly larger

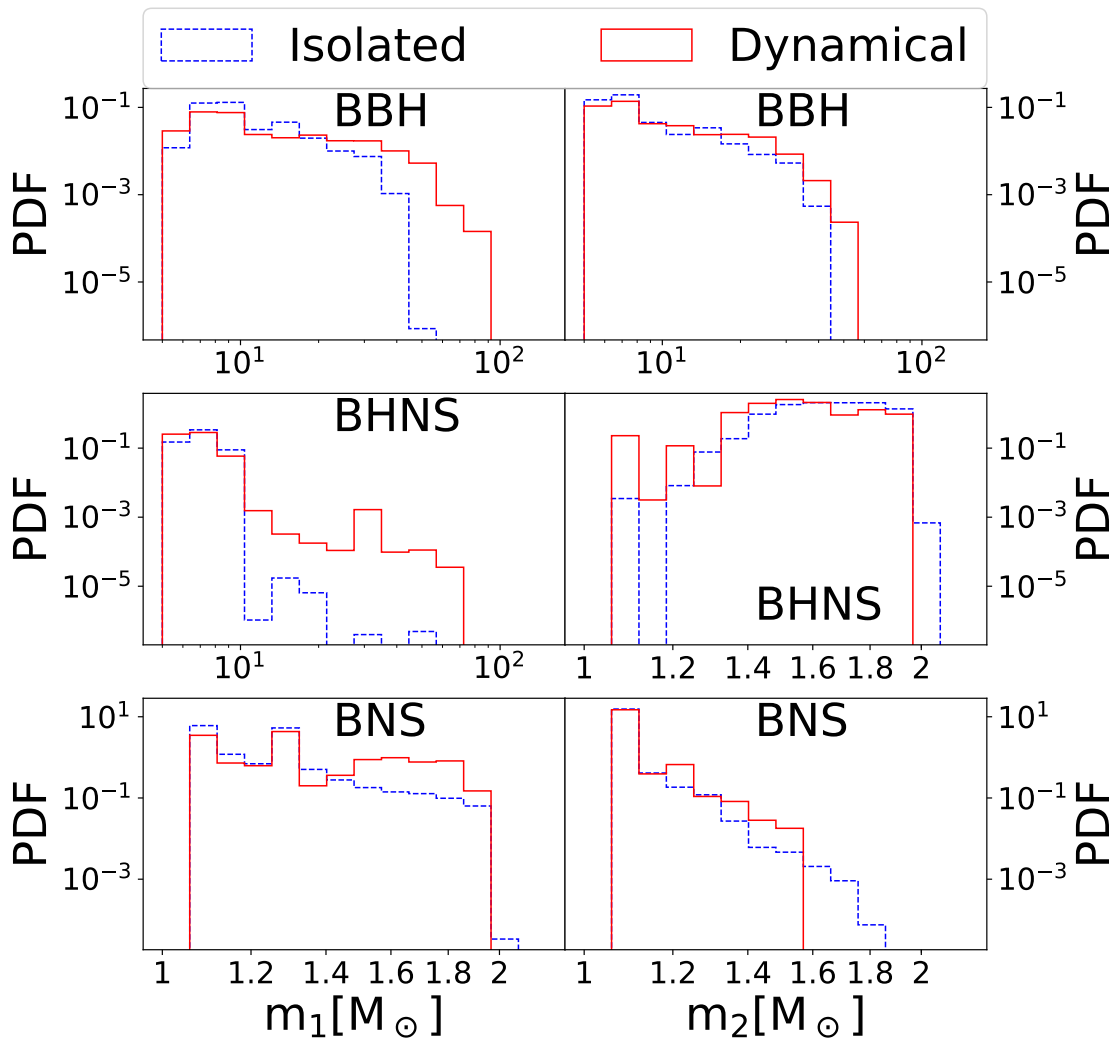


Figure 2.5: Distribution of primary (left) and secondary mass (right) of BBHs (top), BHNSs (middle) and BNSs (bottom panel). Blue dashed and red solid histograms refers to isolated and dynamical CBs, respectively

maximum mass  $m_{\text{BH}, \text{max}} \sim 90 M_{\odot}$ . Quantitatively, the percentage of isolated BBHs that have a primary mass  $> 40 M_{\odot}$  is equal to 0.07%, while it is 10.6% for dynamical BBHs. This marked difference in the maximum mass of merging BHs between isolated and dynamical BBHs can be understood as follows (see also Di Carlo et al. 2019b,a). The stellar wind and core collapse SN prescriptions adopted in MOBSE allow the formation of BHs with mass up to  $\sim 65 M_{\odot}$  (Giacobbo et al., 2018), but only BHs with masses up to  $\sim 45 M_{\odot}$  are able to merge within a Hubble time in isolated BBHs, because of a subtle interplay between mass transfer and stellar radii. In fact, BHs with masses  $> 45 M_{\odot}$  form only from stars with zero-age main sequence mass  $\sim 60 - 80 M_{\odot}$  which retain a large fraction of hydrogen envelope and collapse to a BH directly (Figure 4 of Giacobbo et al. 2018). When such stars are members of a tight binary system, most of the hydrogen envelope is removed by mass transfer (or by common envelope) before the collapse; hence, even if they might end up into a BBH merger, the mass of the final BHs will be smaller than the one we expect from single star evolution. In contrast, if such stars are members of loose binaries (initial orbital separation  $a \gtrsim 10^4 R_{\odot}$ ), which do not undergo mass transfer, they produce BBHs with individual BH masses  $> 45 M_{\odot}$ , but the orbital separation is too large to lead to coalescence.

In young star clusters, instead, BHs with masses  $> 45 M_{\odot}$  are able to merge within a Hubble time, because i) if they form from the collapse of single stars, they can acquire companions through dynamical exchanges, and ii) if they are members of loose binaries, these massive binaries are efficiently hardened by three body encounters (Di Carlo et al., 2019b). Moreover, (multiple) stellar mergers can even lead to the formation of BHs with masses  $> 65 M_{\odot}$ , as discussed in Di Carlo et al. (2019a). Such massive BHs are single at birth but can acquire a companion by dynamical exchanges.

Figure 2.5 shows that dynamical BHNSs can host significantly more massive BHs than isolated BHNSs. Only  $9 \times 10^{-4}\%$  of BHs in isolated BHNSs have masses  $m_{\text{BH}} > 20 M_{\odot}$ , while 1.6% of BHs in dynamical BHNSs have masses above this value. This is another effect of dynamics, which boosts the formation of massive binaries by dynamical exchanges and facilitates the coalescence of binaries with extreme mass ratio by dynamical hardening (see the discussion in Rastello et al. 2020 for additional details). Finally, we do not find any significant difference between the mass distribution of dynamical BNSs and that of isolated BNSs<sup>3</sup>.

## 2.4 Summary

The next generation of ground-based GW interferometers (Einstein Telescope and Cosmic Explorer) will observe BBH (BNS) mergers up to  $z \gtrsim 10$  ( $z \sim 2$ ), allowing us to probe the evolution of CBs across cosmic time. Here, we have investigated the cosmic evolution of CBs formed in young star clusters by evaluating their MRD. Young star clusters are the most common birthplace of massive stars across cosmic history. Hence, a large fraction of BBHs, BHNSs and BNSs might have formed in young star clusters and might retain the signature of dynamical processes (such as exchanges or stellar collisions) occurring in star clusters.

---

<sup>3</sup>The cut-off of secondary NS masses above  $\sim 1.6 M_{\odot}$  in the dynamical model is a consequence of the lower statistics of dynamical BNSs with respect to isolated BNSs in the original catalogs we used.

The dynamical BBH merger rate is higher than the isolated BBH merger rate between  $z = 0$  and  $z \sim 4$ . The main reason for this difference is that the merger efficiency of dynamical BBHs at solar metallicity is two orders of magnitude higher than the merger efficiency of isolated BBHs, because dynamical exchanges enhance the merger of BBHs formed from metal-rich stars.

The MRD of dynamical BHNSs is always consistent with that of isolated BHNSs, within the estimated uncertainty. In contrast, the MRD of dynamical BNSs is a factor of  $\sim 2$  lower than that of isolated BNSs, because dynamics suppresses the formation of relatively low-mass binaries.

We find a local MRD of  $\mathcal{R}_{\text{BBH}} = 64^{+34}_{-20} \text{ Gpc}^{-3} \text{ yr}^{-1}$ ,  $\mathcal{R}_{\text{BHNS}} = 41^{+33}_{-23} \text{ Gpc}^{-3} \text{ yr}^{-1}$  and  $\mathcal{R}_{\text{BNS}} = 151^{+59}_{-38} \text{ Gpc}^{-3} \text{ yr}^{-1}$  for dynamical BBHs, BHNSs and BNSs, respectively. The rates of dynamical BBHs and BHNSs are consistent with the values inferred from O1 and O2 (Abbott et al., 2019a,b) within the uncertainties, while the rate of dynamical BNSs is below the lower edge of the 90% credible interval inferred by the LVC ( $250 - 2810 \text{ Gpc}^{-3} \text{ yr}^{-1}$ , Abbott et al. 2020e). The local MRDs of isolated BBHs, BHNSs and BNSs ( $\mathcal{R}_{\text{BBH}} = 50^{+71}_{-37} \text{ Gpc}^{-3} \text{ yr}^{-1}$ ,  $\mathcal{R}_{\text{BHNS}} = 49^{+48}_{-34} \text{ Gpc}^{-3} \text{ yr}^{-1}$  and  $\mathcal{R}_{\text{BNS}} = 283^{+97}_{-75} \text{ Gpc}^{-3} \text{ yr}^{-1}$ ) are all consistent with the values inferred from O1 and O2.

The main difference between isolated BBHs/BHNSs and dynamical BBHs/BHNSs is the mass of the BH component: dynamical systems harbor BHs with mass up to  $m_{\text{BH,max}} \sim 90 M_\odot$ , significantly higher than isolated binaries ( $m_{\text{BH,max}} \sim 45 M_\odot$ ). The mass distribution of both isolated and dynamical CBs do not significantly change with redshift. These results provide a clue to differentiate the dynamical and isolated formation scenario of binary compact objects across cosmic time, in preparation for next-generation ground-based detectors.

## 2.5 Software

MOBSE (Giacobbo et al., 2018); NBODY6++GPU (Wang et al., 2015); COSMORATE ([GitLab](#)).

# 3

## The cosmic merger rate density of compact objects: impact of star formation, metallicity, initial mass function and binary evolution

We evaluate the redshift distribution of binary black hole (BBH), black hole – neutron star binary (BHNS) and binary neutron star (BNS) mergers, exploring the main sources of uncertainty: star formation rate (SFR) density, metallicity evolution, common envelope, mass transfer via Roche lobe overflow, natal kicks, core-collapse supernova model and initial mass function. Among binary evolution processes, uncertainties on common envelope ejection have a major impact: the local merger rate density of BNSs varies from  $\sim 10^3$  to  $\sim 20 \text{ Gpc}^{-3} \text{ yr}^{-1}$  if we change the common envelope efficiency parameter from  $\alpha = 7$  to 0.5, while the local merger rates of BBHs and BHNSs vary by a factor of  $\sim 2 - 3$ . The BBH merger rate changes by one order of magnitude, when  $1\sigma$  uncertainties on metallicity evolution are taken into account. In contrast, the BNS merger rate is almost insensitive to metallicity. Hence, BNSs are the ideal test bed to put constraints on uncertain binary evolution processes, such as common envelope and natal kicks. Only models assuming values of  $\alpha \gtrsim 2$  and moderately low natal kicks (depending on the ejected mass and the SN mechanism), result in a local BNS merger rate density within the 90% credible interval inferred from the second gravitational-wave transient catalogue.

Based on:

**Santoliquido F., Mapelli M., Giacobbo N., Bouffanais Y., Artale M. C., 2021, MNRAS, 502, 4877**

### 3.1 Introduction

Gravitational-wave (GW) observations give us an insight into the merger rate density of binary compact objects in the local Universe (Abadie et al., 2010; Abbott et al., 2016b; Abbott et al., 2016e,a, 2019a,b). Based on the results of the first (O1) and the second observing runs (O2), the LIGO-Virgo collaboration (LVC) has inferred a local merger rate density  $\mathcal{R}_{\text{BBH}} \sim 24 - 140 \text{ Gpc}^{-3} \text{ yr}^{-1}$  and  $\mathcal{R}_{\text{BHNS}} < 610 \text{ Gpc}^{-3} \text{ yr}^{-1}$  for binary black holes (BBHs) and black hole – neutron star binaries (BHNSs), respectively (Abbott et al., 2019a,b).

While this paper was in the review stage, the LVC published 39 events observed during the first half of the third observing run (O3a, Abbott et al. 2020b). This leads to a sample of 50 binary compact object mergers from O1, O2 and O3a, known as the second GW transient catalogue (GWTC-2). From these new data and assuming the POWER LAW + PEAK mass distribution model (which is shown to be preferred by the data), the BBH merger rate density inside the 90% credible interval is estimated to be  $\mathcal{R}_{\text{BBH}} = 23.9_{-8.6}^{+14.9} \text{ Gpc}^{-3} \text{ yr}^{-1}$  ( $\mathcal{R}_{\text{BBH}} = 58_{-29}^{+54} \text{ Gpc}^{-3} \text{ yr}^{-1}$ ) if we exclude (include) the event GW190814 (Abbott et al., 2020c). Abbott et al. (2020e) inferred a BNS local merger rate density  $\mathcal{R}_{\text{BNS}} = 250 - 2810 \text{ Gpc}^{-3} \text{ yr}^{-1}$  from the two published binary neutron star (BNS) mergers, GW170817 (Abbott et al., 2017c,e) and GW190425 (Abbott et al., 2020e). This number has recently been revised to account for the entire O3a data, leading to a new estimate  $\mathcal{R}_{\text{BNS}} = 320_{-240}^{+490} \text{ Gpc}^{-3} \text{ yr}^{-1}$  (Abbott et al., 2020c).

Moreover, the target sensitivity of third-generation ground-based GW interferometers, namely the Einstein Telescope in Europe and Cosmic Explorer in the US, will allow us to observe BBH mergers up to  $z \gtrsim 10$  and BNS mergers up to  $z \gtrsim 2$  (Punturo et al., 2010; Reitze et al., 2019; Kalogera et al., 2019; Maggiore et al., 2020). This will make possible to fully reconstruct the evolution of the merger rate with redshift, opening new perspectives on the study of binary compact objects.

From a theoretical perspective, several studies attempt to predict the cosmic merger rate evolution, based on either cosmological simulations (Lamberts et al., 2016, 2018; O’Shaughnessy et al., 2017; Schneider et al., 2017; Mapelli et al., 2017; Mapelli & Giacobbo, 2018; Mapelli et al., 2018, 2019; Toffano et al., 2019; Artale et al., 2019, 2020a; Graziani et al., 2020) or semi-analytical models (O’Shaughnessy et al., 2010; Dominik et al., 2013, 2015; Belczynski et al., 2016; Eldridge & Stanway, 2016; Giacobbo & Mapelli, 2018, 2020; Boco et al., 2019; Eldridge et al., 2019; Baibhav et al., 2019; Neijssel et al., 2019; Vitale et al., 2019; Tang et al., 2020).

Overall, our current understanding of the merger rate evolution is hampered by large uncertainties. On the one hand, our knowledge of the cosmic star formation rate (SFR) (e.g., Madau & Dickinson, 2014; Madau & Fragos, 2017), and the metallicity evolution of stars (e.g. Maiolino et al., 2008; Rafelski et al., 2012; Madau & Dickinson, 2014; Maiolino & Mannucci, 2018; De Cia et al., 2018; Chruslinska et al., 2019; Chruślińska et al., 2020) are affected by a number of observational uncertainties. On the other hand, the very process of binary compact object formation is still matter of debate (see, e.g. Mandel & Farmer 2018 and Mapelli 2018 for two recent reviews).

Several formation channels have been proposed for binary compact objects: binary evolution via common envelope (e.g., Tutukov & Yungelson, 1973; Bethe & Brown, 1998; Portegies

Zwart & Yungelson, 1998; Belczynski et al., 2002, 2008; Voss & Tauris, 2003; Podsiadlowski et al., 2004; Belczynski et al., 2016; Eldridge & Stanway, 2016; Stevenson et al., 2017; Giacobbo & Mapelli, 2018; Kruckow et al., 2018; Vigna-Gómez et al., 2018; Spera et al., 2019; Tanikawa et al., 2020) or via chemical mixing (e.g., Marchant et al., 2016; de Mink & Mandel, 2016; Mandel & de Mink, 2016), dynamical evolution in triples (e.g., Antonini & Rasio, 2016; Antonini et al., 2017; Arca-Sedda et al., 2018; Fragione & Loeb, 2019), in young star clusters (e.g., Banerjee et al., 2010; Ziosi et al., 2014; Mapelli, 2016; Banerjee, 2017, 2020; Kumamoto et al., 2019; Di Carlo et al., 2019b, 2020; Rastello et al., 2020), in globular clusters (e.g., Portegies Zwart & McMillan, 2000; Downing et al., 2010; Rodriguez et al., 2015, 2016; Rodriguez & Loeb, 2018; Samsing et al., 2014; Askar et al., 2017; Samsing, 2018; Fragione & Kocsis, 2018; Zevin et al., 2019; Fragione & Silk, 2020; Antonini & Gieles, 2020) and in galactic nuclei (e.g., O’Leary et al., 2009; Miller & Lauburg, 2009; McKernan et al., 2012, 2018; Antonini & Rasio, 2016; Bartos et al., 2017; Stone et al., 2017; Rasskazov & Kocsis, 2019; Arca Sedda et al., 2020; Arca Sedda, 2020; Yang et al., 2019; Tagawa et al., 2019). Each of these formation channels will likely leave an imprint on the evolution of the merger rate density with redshift (e.g. Dominik et al. 2013, 2015; Mapelli et al. 2017; Mapelli & Giacobbo 2018; Rodriguez & Loeb 2018; Choksi et al. 2018, 2019; Eldridge et al. 2019; Yang et al. 2019; Kumamoto et al. 2020; du Buisson et al. 2020; Mapelli et al. 2020a; Santoliquido et al. 2020). In particular, the merger rate of BBHs can be dramatically affected by dynamics, because of BH masses favouring dynamical exchanges (Hills & Fullerton, 1980).

Even if we restrict our attention to just one possible formation channel, we are faced with major uncertainties. For example, we do not have a satisfactory picture of the process of common envelope. Most population-synthesis models describe it through a free parameter,  $\alpha$ , which was originally meant to indicate the fraction of orbital energy that is transferred to the envelope (Webbink, 1984). According to its original definition,  $\alpha$  should assume only values  $\leq 1$  and still theoretical models suggest that values of  $\alpha > 1$  better describe the formation of BNSs (e.g., Mapelli & Giacobbo, 2018; Fragos et al., 2019; Giacobbo & Mapelli, 2020).

Here, we focus on the formation of binary compact objects in isolation, through common envelope evolution, and we investigate all the main sources of uncertainty that affect the merger rate density evolution. In particular, we account for uncertainties on the cosmic SFR, metallicity evolution, common envelope (by varying the  $\alpha$  parameter over more than one order of magnitude), natal kicks, core-collapse supernova (SN) models, mass transfer efficiency and on the slope of the initial mass function. We use COSMORATE (Santoliquido et al., 2020), a semi-analytic code that combines information on cosmic SFR and metallicity evolution with catalogues of binary compact objects obtained via binary population-synthesis. COSMORATE is computationally optimised to extensively probe the parameter space.

## 3.2 Methods

### 3.2.1 Population synthesis

We use catalogues of isolated compact binaries from our population-synthesis code MOBSE<sup>1</sup> (Mapelli et al., 2017; Giacobbo et al., 2018; Giacobbo & Mapelli, 2018). MOBSE includes an up-to-date model for the mass loss rate of massive hot stars, scaling as  $\dot{M} \propto Z^\beta$ , where  $Z$  is the metallicity and  $\beta$  depends on the Eddington ratio, as defined in Giacobbo et al. (2018).

The prescriptions for core-collapse SNe adopted in MOBSE come from Fryer et al. (2012) and have been slightly modified to enforce a minimum neutron star (NS) mass of  $\approx 1.23 M_\odot$  (Giacobbo & Mapelli, 2020). Here, we consider both the rapid and the delayed SN model described by Fryer et al. (2012). The two models differ only by the time when the explosion is launched, which is  $\lesssim 250$  ms ( $\gtrsim 500$  ms) after the bounce in the rapid (delayed) model. According to these models, stars with final carbon-oxygen mass  $m_{\text{CO}} \gtrsim 11 M_\odot$  collapse to a BH directly. In terms of compact remnant masses, the main difference between the rapid and the delayed model is that the former enforces a mass gap between 2 and  $5 M_\odot$ , while the latter does not.

Following Timmes et al. (1996) and Zevin et al. (2020), we compute neutrino mass loss for both NSs and BHs as

$$m_\nu = \min \left[ \frac{(\sqrt{1 + 0.3 m_{\text{bar}}} - 1)}{0.15}, 0.5 M_\odot \right], \quad (3.1)$$

where  $m_{\text{bar}}$  is the baryonic mass of the compact object. The resulting gravitational mass of the compact object is  $m_{\text{rem}} = m_{\text{bar}} - m_\nu$ . Prescriptions for pair instability SNe and pulsational pair instability SNe are also implemented, as described in Mapelli et al. (2020b). Our treatment for electron-capture SNe is described in Giacobbo & Mapelli (2019).

We consider different SN kick prescriptions, in order to assess their impact on the cosmic merger rate density. As our fiducial model, we adopt the natal kick prescription proposed by Giacobbo & Mapelli (2020):

$$v_{\text{kick}} = f_{\text{H05}} \frac{m_{\text{ej}}}{\langle m_{\text{ej}} \rangle} \frac{\langle m_{\text{NS}} \rangle}{m_{\text{rem}}}, \quad (3.2)$$

where  $f_{\text{H05}}$  is a random value extracted from a Maxwellian distribution with one-dimensional root mean square  $\sigma_{1D} = 265 \text{ km s}^{-1}$  (Hobbs et al., 2005),  $m_{\text{ej}}$  is the mass of the ejecta,  $m_{\text{rem}}$  is the mass of the compact remnant,  $\langle m_{\text{NS}} \rangle$  is the average NS mass and  $\langle m_{\text{ej}} \rangle$  is the average mass of the ejecta associated with the formation of a NS of mass  $\langle m_{\text{NS}} \rangle$  from single stellar evolution. Equation 3.2 provides the natal kick for both NSs and BHs, and for both electron-capture and core-collapse SNe. Since BHs that form from direct collapse have  $m_{\text{ej}} = 0$ , they receive no kick. This kick prescription matches the proper motions of young Galactic pulsars (Hobbs et al., 2005; Bray & Eldridge, 2016, 2018) and at the same time the merger rate density inferred from LVC (Tang et al., 2020; Giacobbo & Mapelli, 2020).

We also consider a simplified model in which the natal kick velocity is randomly drawn from a Maxwellian distribution with fixed one-dimensional root mean square  $\sigma_{1D}$ . We consider three different values of  $\sigma_{1D} = 265, 150$  and  $50 \text{ km s}^{-1}$ . In this simple model, the natal

---

<sup>1</sup><https://mobse-webpage.netlify.app/>

kicks of BHs and NSs are drawn from the same Maxwellian distribution, without accounting for direct collapse or fallback. Furthermore, we consider two alternative kick models. The model F12 (from Fryer et al. 2012) draws the natal kicks from a Maxwellian distribution with  $\sigma_{1D} = 265 \text{ km s}^{-1}$  and then modulates the kick magnitude as

$$v_{\text{kick}} = (1 - f_{\text{fb}}) f_{\text{H05}}, \quad (3.3)$$

where  $f_{\text{fb}}$  is the fraction of fallback defined as in Fryer et al. (2012). Finally, the model VG18 (from Vigna-Gómez et al. 2018) draws the kicks from two different Maxwellian distributions with  $\sigma_{1D} = 265$  and  $30 \text{ km s}^{-1}$  for NSs born via core-collapse and electron-capture SNe, respectively. Also in this model, the kick is then modulated by the amount of fallback using equation 3.3.

In the default version of MOBSE, mass transfer via Roche lobe overflow is described as in Hurley et al. (2002). This yields a nearly conservative mass transfer if the accretor is a non-degenerate star. Here, we introduce also an alternative model in which the mass accretion rate ( $\dot{m}_a$ ) is described as

$$\dot{m}_a = \begin{cases} f_{\text{MT}} |\dot{m}_d| & \text{if the accretor is non-degenerate} \\ \min(f_{\text{MT}} |\dot{m}_d|, \dot{m}_{\text{Edd}}) & \text{otherwise,} \end{cases} \quad (3.4)$$

where  $\dot{m}_d$  is the mass loss rate by the donor star,  $\dot{m}_{\text{Edd}}$  is the Eddington accretion rate and  $f_{\text{MT}} \in [0, 1]$  is the accretion efficiency. Here, we explore  $f_{\text{MT}} = 0.1, 0.5$  and  $1$ .

Other binary evolution processes are implemented as described in Hurley et al. (2002) and Santoliquido et al. (2020). In this work, we assume that the common envelope (CE) ejection efficiency parameter,  $\alpha$ , can assume values from  $0.5$  and  $10$ , while  $\lambda_{\text{CE}}$  is derived as described in Claeys et al. (2014).

In the fiducial model, the mass of the primary star in each binary system is randomly drawn from a Kroupa (2001) initial mass function (IMF), with minimum mass  $5 M_{\odot}$  and maximum mass  $150 M_{\odot}$ . For stars with mass  $> 0.5 M_{\odot}$ , the Kroupa IMF behaves as a power law  $dN/dm \propto m^{-\alpha_{\text{IMF}}}$  with  $\alpha_{\text{IMF}} = 2.3$ . We also explored different IMF slopes for stars with mass  $> 0.5 M_{\odot}$ . In particular, we consider two cases in which  $\alpha_{\text{IMF}} = 2.0$  and  $2.7$ .

Table 3.1 provides a summary of the different runs performed in this work. We have considered 12 different stellar metallicities for each run:  $Z = 0.0002, 0.0004, 0.0008, 0.0012, 0.0016, 0.002, 0.004, 0.006, 0.008, 0.012, 0.016, 0.02$ . For each run, we have simulated  $10^7$  binaries per each metallicity comprised between  $Z = 0.0002$  and  $0.002$ , and  $2 \times 10^7$  binaries per each metallicity  $Z \geq 0.004$ , since higher metallicities are associated with lower BBH and BHNS merger efficiency (e.g. Giacobbo & Mapelli 2018; Klencki et al. 2018). Thus, we have simulated  $1.8 \times 10^8$  binaries per each run shown in Table 3.1.

In all runs, the orbital periods, eccentricities and mass ratios of binaries are drawn from Sana et al. (2012). In particular, we derive the mass ratio  $q = m_2/m_1$  as  $\mathcal{F}(q) \propto q^{-0.1}$  with  $q \in [0.1 - 1]$ , the orbital period  $P$  from  $\mathcal{F}(P) \propto P^{-0.55}$  with  $P = \log(P/\text{day}) \in [0.15 - 5.5]$  and the eccentricity  $e$  from  $\mathcal{F}(e) \propto e^{-0.42}$  with  $0 \leq e \leq 0.9$ .

Table 3.1: Summary of the models.

Model Name	$\alpha$	Kick Model	SN Model	$f_{\text{MT}}$	$\alpha_{\text{IMF}}$
$\alpha 0.5$	0.5	Eq. 3.2	Delayed	H02	2.3
$\alpha 1$	1	Eq. 3.2	Delayed	H02	2.3
$\alpha 2$	2	Eq. 3.2	Delayed	H02	2.3
$\alpha 3$	3	Eq. 3.2	Delayed	H02	2.3
$\alpha 5$	5	Eq. 3.2	Delayed	H02	2.3
$\alpha 7$	7	Eq. 3.2	Delayed	H02	2.3
$\alpha 10$	10	Eq. 3.2	Delayed	H02	2.3
$\alpha 1s265$	1	$\sigma_{1D} = 265 \text{ km/s}$	Delayed	H02	2.3
$\alpha 5s265$	5	$\sigma_{1D} = 265 \text{ km/s}$	Delayed	H02	2.3
$\alpha 1s150$	1	$\sigma_{1D} = 150 \text{ km/s}$	Delayed	H02	2.3
$\alpha 5s150$	5	$\sigma_{1D} = 150 \text{ km/s}$	Delayed	H02	2.3
$\alpha 1s50$	1	$\sigma_{1D} = 50 \text{ km/s}$	Delayed	H02	2.3
$\alpha 5s50$	5	$\sigma_{1D} = 50 \text{ km/s}$	Delayed	H02	2.3
$\alpha 1F12$	1	Eq. 3.3	Delayed	H02	2.3
$\alpha 5F12$	5	Eq. 3.3	Delayed	H02	2.3
$\alpha 1VG18$	1	$\sigma_{\text{high}} = 265 \text{ km/s } \sigma_{\text{low}} = 30 \text{ km/s}$	Delayed	H02	2.3
$\alpha 5VG18$	5	$\sigma_{\text{high}} = 265 \text{ km/s } \sigma_{\text{low}} = 30 \text{ km/s}$	Delayed	H02	2.3
$\alpha 1R$	1	Eq. 3.2	Rapid	H02	2.3
$\alpha 5R$	5	Eq. 3.2	Rapid	H02	2.3
$\alpha 1MT0.1$	1	Eq. 3.2	Delayed	0.1	2.3
$\alpha 1MT0.5$	1	Eq. 3.2	Delayed	0.5	2.3
$\alpha 1MT1.0$	1	Eq. 3.2	Delayed	1.0	2.3
$\alpha 5MT0.1$	5	Eq. 3.2	Delayed	0.1	2.3
$\alpha 5MT0.5$	5	Eq. 3.2	Delayed	0.5	2.3
$\alpha 5MT1.0$	5	Eq. 3.2	Delayed	1.0	2.3
$\alpha 10MT0.1$	10	Eq. 3.2	Delayed	0.1	2.3
$\alpha 10MT0.5$	10	Eq. 3.2	Delayed	0.5	2.3
$\alpha 10MT1.0$	10	Eq. 3.2	Delayed	1.0	2.3
$\alpha 1IMF2.0$	1	Eq. 3.2	Delayed	H02	2.0
$\alpha 1IMF2.7$	1	Eq. 3.2	Delayed	H02	2.7
$\alpha 5IMF2.0$	5	Eq. 3.2	Delayed	H02	2.0
$\alpha 5IMF2.7$	5	Eq. 3.2	Delayed	H02	2.7

Column 1: model name. Column 2: parameter  $\alpha$  of the CE. Column 3: kick model; runs  $\alpha 1s265/\alpha 5s265$ ,  $\alpha 1s150/\alpha 5s150$  and  $\alpha 1s50/\alpha 5s50$  have natal kicks drawn from a Maxwellian distribution with root mean square  $\sigma_{1D} = 265$ , 150 and 50 km s<sup>-1</sup>, respectively; runs  $\alpha 1F12$  and  $\alpha 5F12$  adopt the natal kick model in eq. 3.3; runs  $\alpha 1VG18$  and  $\alpha 5VG18$  assume the same model as Vigna-Gómez et al. (2018); in all the other models, the kicks are calculated as in eq. 3.2. Column 4: core collapse SN model; models  $\alpha 1R$  and  $\alpha 5R$  adopt the rapid model from Fryer et al. (2012), while all the other models adopt the delayed model from the same authors. Column 5: accretion efficiency  $f_{\text{MT}}$  onto a non-degenerate accretor; H02 means that we follow the same formalism as in Hurley et al. (2002). For the other models, see eq. 3.4. Column 6: slope of the IMF; models  $\alpha_{\text{IMF}}$  of the IMF for  $m > 0.5 \text{ M}_\odot$ ;  $\alpha 1K2.0$ ,  $\alpha 5K2.0$  ( $\alpha 1K2.7$ ,  $\alpha 5K2.7$ ) have  $\alpha_{\text{IMF}} = 2.0$  ( $\alpha_{\text{IMF}} = 2.7$ ). All the other models assume the "standard" slope  $\alpha_{\text{IMF}} = 2.3$  (Kroupa, 2001).

### 3.2.2 Cosmic merger rate density

We model the cosmic merger rate density  $\mathcal{R}(z)$  following [Santoliquido et al. \(2020\)](#):

$$\mathcal{R}(z) = \frac{d}{dt_{lb}(z)} \left[ \int_{z_{\min}}^z \psi(z') \frac{dt_{lb}(z')}{dz'} dz' \int_{Z_{\min}}^{Z_{\max}} \eta(Z) \mathcal{F}(z', z, Z) dZ \right], \quad (3.5)$$

where  $t_{lb}(z)$  is the look-back time at redshift  $z$ ,  $Z_{\min}$  and  $Z_{\max}$  are the minimum and maximum metallicity,  $\psi(z')$  is the cosmic SFR density at redshift  $z'$ ,  $\mathcal{F}(z', z, Z)$  is the fraction of compact binaries that form at redshift  $z'$  from stars with metallicity  $Z$  and merge at redshift  $z$ , and  $\eta(Z)$  is the merger efficiency, namely the ratio between the total number  $\mathcal{N}_{\text{TOT}}(Z)$  of compact binaries (formed from a coeval population) that merge within an Hubble time ( $t_{H_0} \lesssim 14$  Gyr) and the total initial mass  $M_*(Z)$  of the simulation with metallicity  $Z$ :

$$\eta(Z) = f_{\text{bin}} f_{\text{IMF}} \frac{\mathcal{N}_{\text{TOT}}(Z)}{M_*(Z)}, \quad (3.6)$$

where  $f_{\text{bin}} = 0.5$  is the binary fraction, and  $f_{\text{IMF}}$  is a correction factor that takes into account that only stars with mass  $m > 5 M_\odot$  are simulated. This parameter depends on the adopted IMF, in particular  $f_{\text{IMF}} = 0.483, 0.285$  and  $0.123$  when  $\alpha_{\text{IMF}} = 2.0, 2.3$  and  $2.7$  respectively. The cosmological parameters used in equation 3.5 are taken from [Ade et al. \(2016\)](#). The maximum considered redshift in equation 3.5 is  $z_{\max} = 15$ .

The SFR density  $\psi(z)$  is described as ([Madau & Fragos, 2017](#)):

$$\psi(z) = 0.01 \frac{(1+z)^{2.6}}{1 + [(1+z)/3.2]^{6.2}} M_\odot \text{Mpc}^{-3} \text{yr}^{-1}. \quad (3.7)$$

As detailed in [Santoliquido et al. \(2020\)](#), we assume that the errors follow a log-normal distribution with mean  $\log \psi(0) = -2$  and standard deviation  $\sigma_{\log \psi} = 0.2$ .

The normalisation of equation 3.7 is obtained for a Kroupa IMF with  $\alpha_{\text{IMF}} = 2.3$ . When we vary the slope of the IMF, we have to change the normalisation of eq. 3.7 ([Madau & Dickinson, 2014](#)). Thus, we re-scale the normalisation by multiplying equation 3.7 by a factor 0.58 and 2.40 for  $\alpha_{\text{IMF}} = 2.0$  and  $2.7$ , respectively (see, e.g., [Klencki et al., 2018](#)).

The average stellar metallicity  $\mu(z)$  evolves with redshift as

$$\mu(z) = \log \left( \frac{Z(z)}{Z_\odot} \right) = \log(a) + b z, \quad (3.8)$$

where  $a = 1.04 \pm 0.14$  and  $b = -0.24 \pm 0.14$ , based on observational results ([Gallazzi et al., 2008](#); [De Cia et al., 2018](#)). We refer to [Santoliquido et al. \(2020\)](#) for a discussion on the choice of  $a$  and  $b$ .

We model the distribution of stellar metallicities  $\log(Z/Z_\odot)$  at a given redshift as a normal distribution with mean value  $\mu(z)$  from equation 3.8 and standard deviation  $\sigma_Z = 0.20$  dex as our fiducial value:

$$p(z', Z) = \frac{1}{\sqrt{2\pi \sigma_Z^2}} \exp \left\{ - \frac{[\log(Z/Z_\odot) - \mu(z')]^2}{2 \sigma_Z^2} \right\}. \quad (3.9)$$

In Section 3.3.7, we discuss the impact of a different choice of  $\sigma_Z$  on the merger rate density. Previous works have calculated the metallicity evolution based on a number of different assumptions and have shown its importance for the estimate of the merger rate (e.g., Dominik et al. 2013, 2015; Belczynski et al. 2016; Lamberts et al. 2016; Mapelli et al. 2017; Mapelli & Giacobbo 2018; Neijssel et al. 2019; Baibhav et al. 2019; Chruslinska et al. 2019; Chruślińska et al. 2020).

The fraction of compact binaries that form at redshift  $z'$  from stars with metallicity  $Z$  and merge at redshift  $z$  is thus given by

$$\mathcal{F}(z', z, Z) = \frac{\mathcal{N}(z', z, Z)}{\mathcal{N}_{\text{TOT}}(Z)} p(z', Z), \quad (3.10)$$

where  $\mathcal{N}(z', z, Z)$  is the total number of compact binaries that merge at redshift  $z$  and form from stars with metallicity  $Z$  at redshift  $z'$ .

We performed  $2 \times 10^3$  realisations of equation 3.5 per each model in Table 3.1. In each realisation, we randomly draw the normalisation value of the SFR density (equation 3.7), and the intercept and the slope of the average metallicity (equation 3.8) from three Gaussian distributions with mean (standard deviation) equal to  $\log \psi(0) = -2$  ( $\sigma_{\log \psi} = 0.2$ ),  $a = 1.04$  ( $\sigma_a = 0.14$ ) and  $b = -0.24$  ( $\sigma_b = 0.14$ ), respectively. For simplicity, the value of the intercept and that of the slope are drawn separately, assuming no correlation.

## 3.3 Results

### 3.3.1 Merger efficiency

Figure 3.1 shows the merger efficiency  $\eta(Z)$  as defined in equation 3.6, as a function of progenitor's metallicity and for different values of the  $\alpha$  parameter. The BNS merger efficiency (hereafter,  $\eta_{\text{BNS}}$ ) mildly depends on the metallicity of the progenitor star, as already found by previous works (e.g., Mapelli et al., 2010; Chakrabarti et al., 2017; Giacobbo et al., 2018; Klencki et al., 2018; Chruslinska et al., 2018; Neijssel et al., 2019). The behaviour of  $\eta_{\text{BNS}}$  as a function of metallicity is different for different values of  $\alpha$ . For example, for  $\alpha = 1$ ,  $\eta_{\text{BNS}}$  has a U-shaped trend with metallicity and has a minimum at  $Z = 0.002$ , while, for  $\alpha = 2$ ,  $\eta_{\text{BNS}}$  decreases almost monotonically from  $Z = 0.0002$  to  $Z = 0.02$ . The BNS merger efficiency changes by less than one order of magnitude with  $Z$ , while it increases by two orders of magnitude with increasing  $\alpha$ . Thus, the BNS merger efficiency is strongly affected by the CE parameter  $\alpha$  and only mildly affected by metallicity.

The behaviour of the BHNS merger efficiency (hereafter,  $\eta_{\text{BHNS}}$ ) as a function of metallicity dramatically depends on the value of  $\alpha$ . By decreasing the value of  $\alpha$ ,  $\eta_{\text{BHNS}}$  progressively decreases at low  $Z$  and increases at high  $Z$ . For large values of  $\alpha$  ( $\geq 5$ ),  $\eta_{\text{BHNS}}$  decreases by three orders of magnitude going from  $Z = 0.0002$  up to  $Z = 0.02$ , while for  $\alpha = 0.5$   $\eta_{\text{BHNS}}$  is almost independent of  $Z$ .

This can be physically explained by an interplay between stellar winds and CE. A small value of  $\alpha$  ( $\alpha \lesssim 1$ ) means inefficient CE ejection: the binary has to shrink a lot before the envelope is ejected. At low  $Z$ , inefficient CE ejection suppresses the merger of small BHs

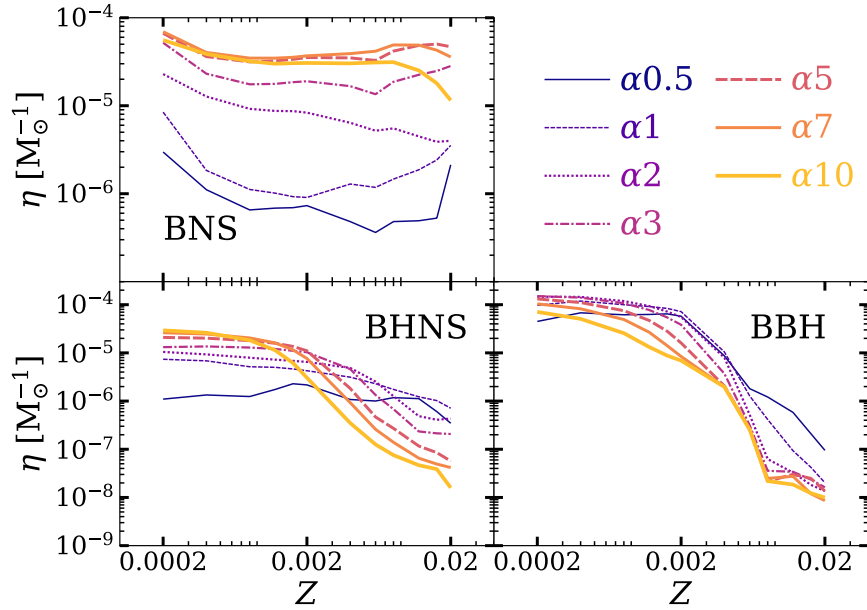


Figure 3.1: Merger efficiency  $\eta$  as a function of progenitor’s metallicity for models  $\alpha_{0.5}$  to  $\alpha_{10}$ . See Table 3.1 for further details.

(with mass  $< 10 M_\odot$ ), because their progenitor stars retain large envelopes and merge during CE, before giving birth to BHNSs. In contrast, at solar metallicity, stellar winds peel off stars and their envelopes are relatively small, making it difficult for CE to harden the system enough to merge by GW emission. Hence, an inefficient CE ejection tends to boost mergers of low-mass BHs at solar metallicity, by efficiently shrinking their progenitor binaries.

The BBH merger efficiency (hereafter,  $\eta_{\text{BBH}}$ ) strongly depends on progenitor’s metallicity and is only mildly affected by  $\alpha$ .  $\eta_{\text{BBH}}$  decreases by three–four orders of magnitude from the lowest to the highest considered metallicity. Lower values of  $\alpha$  result in higher values of  $\eta_{\text{BBH}}$ , with the exception of the case with  $\alpha = 0.5$  and  $Z = 0.0002$ .

### 3.3.2 Common envelope

Figure 3.2 shows the cosmic merger rate density  $\mathcal{R}(z)$  as a function of redshift for the same values of the CE parameter as shown in Figure 3.1. The BNS merger rate density is up to two orders of magnitude higher for large values of  $\alpha$  than for low values. This trend can be easily explained by looking at the merger efficiency (Figure 3.1): for BNSs, larger values of  $\alpha$  translate into higher merger efficiency.

The top panel of Figure 3.2 shows the merger rate density of BBHs. In the local Universe,  $\mathcal{R}_{\text{BBH}}(z)$  changes by a factor of  $2 - 3$  if we change  $\alpha$ . Thus, the impact of  $\alpha$  on the local BBH merger rate is smaller than in the case of BNSs. Moreover, models with large  $\alpha$  result in lower BBH merger rates, with an opposite trend with respect to BNSs. These differences are also explained by the behaviour of the merger efficiency at different  $\alpha$  (Figure 3.1).

The merger rate density of BHNSs follows an evolution similar to that of BBHs: lower values of  $\alpha$  give higher merger rates (with the exception of  $\alpha = 0.5$ ) and the difference

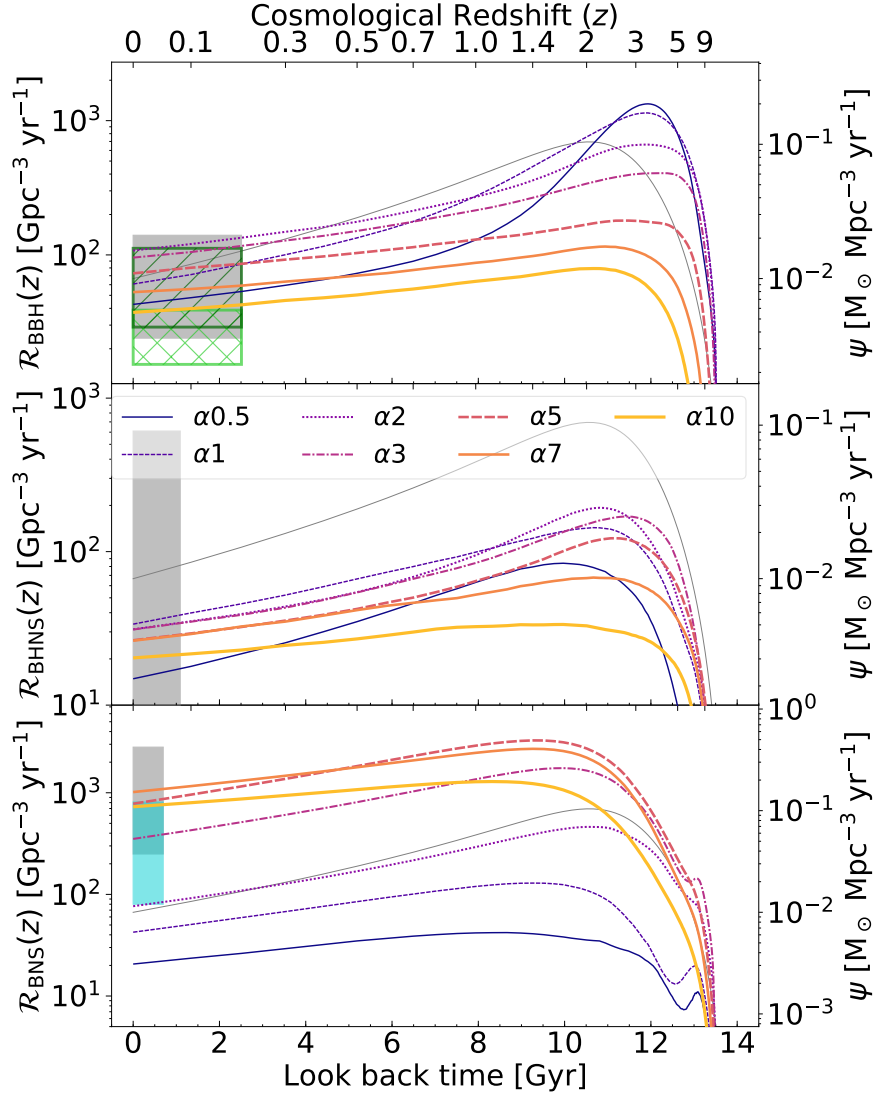


Figure 3.2: Left  $y$ -axis: Evolution of the merger rate density  $\mathcal{R}(z)$  for BBHs (top), BHNSs (centre) and BNSs (bottom) in the comoving frame, as a function of the look-back time (lower  $x$ -axis) and of the redshift (upper  $x$ -axis). We vary  $\alpha$  from 0.5 (model  $\alpha 0.5$ ) to 10 (model  $\alpha 10$ ). For both BBHs and BHNSs, the grey shaded area shows the 90% credible interval of the local merger rate density, as inferred from the first two observing runs of the LVC (Abbott et al., 2019a,b). For BBHs, we consider the union of the rates obtained with model A, B and C in Abbott et al. (2019b). For BNSs, the grey shaded area shows the merger rate density estimated in Abbott et al. (2020e). The hatched green areas in the upper panel show the local BBH merger rate density inferred including O3a events (Abbott et al., 2020c). In particular, the dark-green and light-green hatched areas show the 90% credible interval calculated including and excluding GW190814-like events, respectively (Abbott et al., 2020c). Finally, the cyan shaded area in the lower panel shows the 90% credible interval of the local BNS merger rate density, as estimated by Abbott et al. (2020c). The width of the shaded and hatched areas on the  $x$ -axis corresponds to the instrumental horizon obtained by assuming BBHs, BHNS, BNSs of mass  $(10 + 10)$ ,  $(1.4 - 5)$  and  $(1.4 - 1.4)$   $M_\odot$  respectively and O2 sensitivity (Abbott et al., 2018). Right  $y$ -axis and grey solid thin line: SFR density evolution (equation 3.7).

between models with different  $\alpha$  is only a factor of  $\sim 2$  in the local Universe. As for BNSs and BBHs, this trend can be explained by looking at the merger efficiency. From now on, we consider  $\alpha = 1$  and 5 as our fiducial cases.

In Figure 3.2 and following, we show the 90% credible intervals inferred by the LVC. The grey boxes represent the values inferred from the first and second observing runs (GWTC-1, Abbott et al. 2019a) for BBHs ( $\mathcal{R}_{\text{BBH}} = 24 - 140 \text{ Gpc}^{-3} \text{ yr}^{-1}$ ), BHNSs ( $\mathcal{R}_{\text{BHNS}} \leq 610 \text{ Gpc}^{-3} \text{ yr}^{-1}$ ) and BNSs ( $\mathcal{R}_{\text{BNS}} = 250 - 2810 \text{ Gpc}^{-3} \text{ yr}^{-1}$ ). From GWTC-2 (Abbott et al., 2020b), we considered the 90% credible intervals inferred for BBHs, with and without taking into account GW190814, which are  $\mathcal{R}_{\text{BBH}} = 23.9^{+14.9}_{-8.6} \text{ Gpc}^{-3} \text{ yr}^{-1}$  (hatched light-green box) and  $\mathcal{R}_{\text{BBH}} = 58^{+54}_{-29} \text{ Gpc}^{-3} \text{ yr}^{-1}$  (hatched dark-green box), respectively. The cyan box is the updated 90% credible interval inferred for BNSs, which is equal to  $\mathcal{R}_{\text{BNS}} = 320^{+490}_{-240} \text{ Gpc}^{-3} \text{ yr}^{-1}$ .

### 3.3.3 Natal kicks

Figure 3.3 shows that the higher the natal kick is, the lower is the merger rate density at each given redshift, for BBHs, BHNSs and BNSs. In fact, high natal kicks tend to disrupt the binary system. SN kicks drawn from a Maxwellian distribution with  $\sigma_{1D} = 50 \text{ km s}^{-1}$  yield a merger rate density similar to that given by equation 3.2.

As expected from the binary binding energy, the effect of different SN natal kick prescriptions is higher for BNSs, where there is a difference up to an order of magnitude if we consider natal kicks drawn from a Maxwellian with  $\sigma_{1D} = 265 \text{ km s}^{-1}$  with respect to  $\sigma_{1D} = 50 \text{ km s}^{-1}$ .

Only models with relative low natal kicks and large values of  $\alpha$  (like  $\alpha 5$ ,  $\alpha 5s50$ ,  $\alpha 5s150$ , and  $\alpha 5VG18$ ) are inside the 90% credible interval of GWTC-2 (Abbott et al., 2020b,c). On the other hand, a single Maxwellian curve with  $\sigma_{1D} = 50 \text{ km s}^{-1}$  (e.g., models  $\alpha 1s50$  and  $\alpha 5s50$ ) is in tension with the observed proper motions of young pulsars in our Galaxy (Hobbs et al., 2005; Verbunt et al., 2017; Pol et al., 2019). Hence, only models  $\alpha 5$ ,  $\alpha 5s150$  and  $\alpha 5VG18$  are still consistent with both pulsars' proper motions and GW data.

### 3.3.4 Core-collapse SN model

Choosing the delayed or the rapid core-collapse SN model has a minor impact on the cosmic merger rate density (Figure 3.4). The delayed model slightly enhances  $\mathcal{R}_{\text{BNS}}(z)$ , because it produces more massive NSs which can merge on a shorter timescale. For the same reason, the delayed model slightly suppresses  $\mathcal{R}_{\text{BBH}}(z)$ , because it produces a number of low-mass BHs ( $3 - 5 M_\odot$ ), which merge on a longer timescale than more massive BHs. For BHNSs, the effect of the core-collapse SN model depends on the choice of the  $\alpha$  parameter.

### 3.3.5 Mass accretion efficiency

Figure 3.5 shows the impact of different values of the mass accretion efficiency on the cosmic merger rate density. Lower values of  $f_{\text{MT}}$  result in a lower  $\mathcal{R}_{\text{BBH}}(z)$ , especially for large values

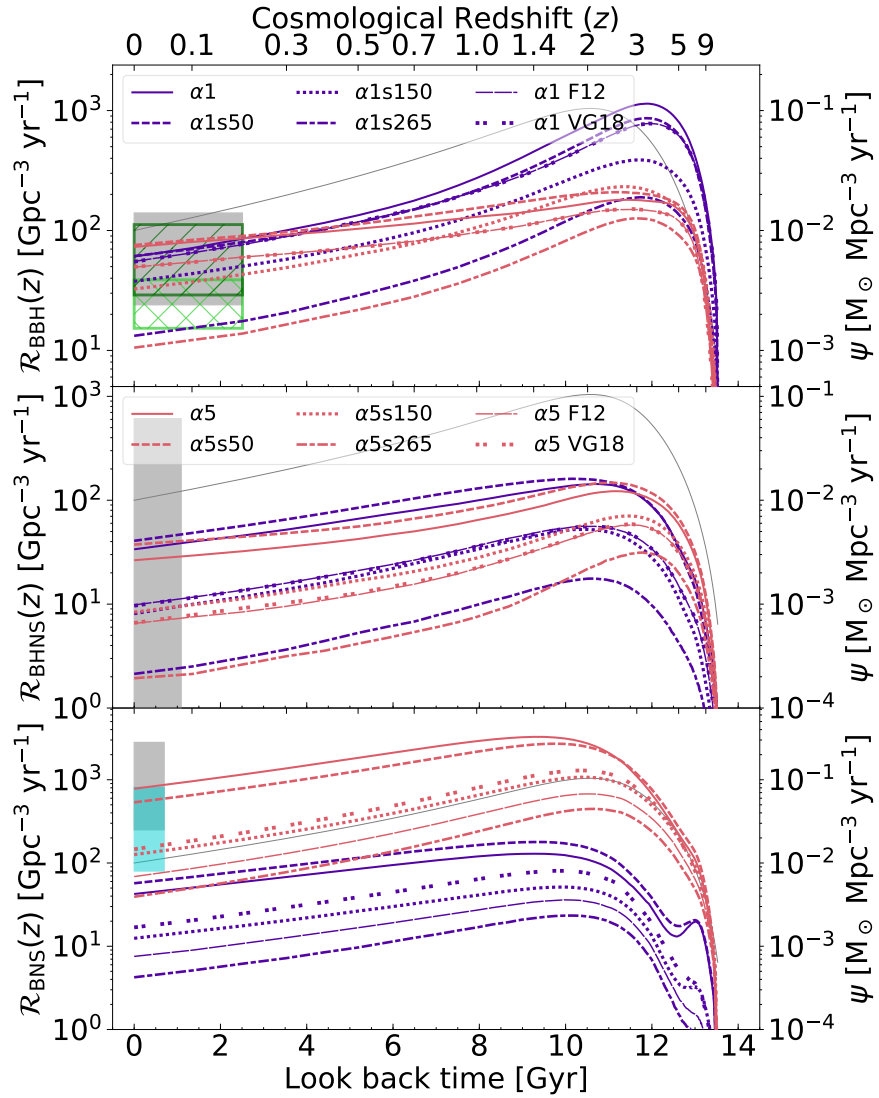


Figure 3.3: Merger rate density of BBHs (top), BHNSs (centre) and BNSs (bottom). Same as Figure 3.2, but we compare different natal kicks.

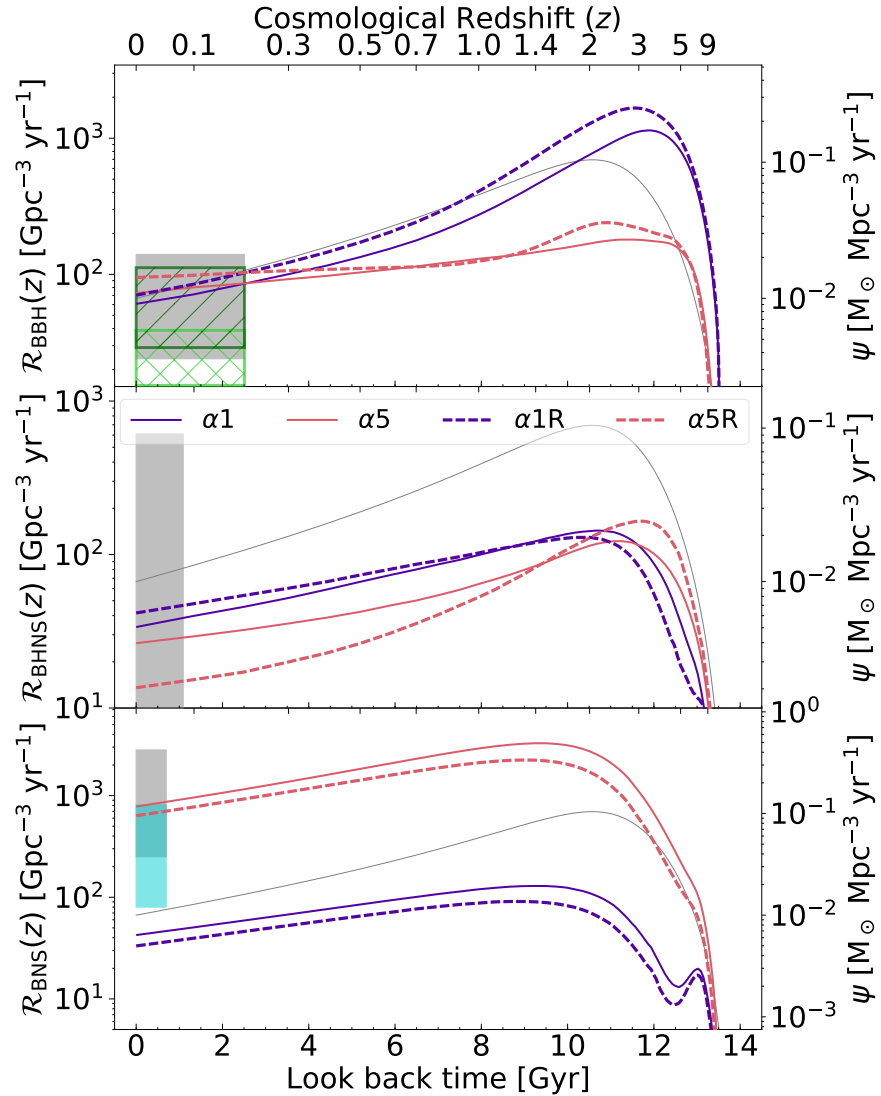


Figure 3.4: Merger rate density of BBHs (top), BHNSs (centre) and BNSs (bottom). Same as Figure 3.2, but we compare the rapid and delayed core-collapse SN models.

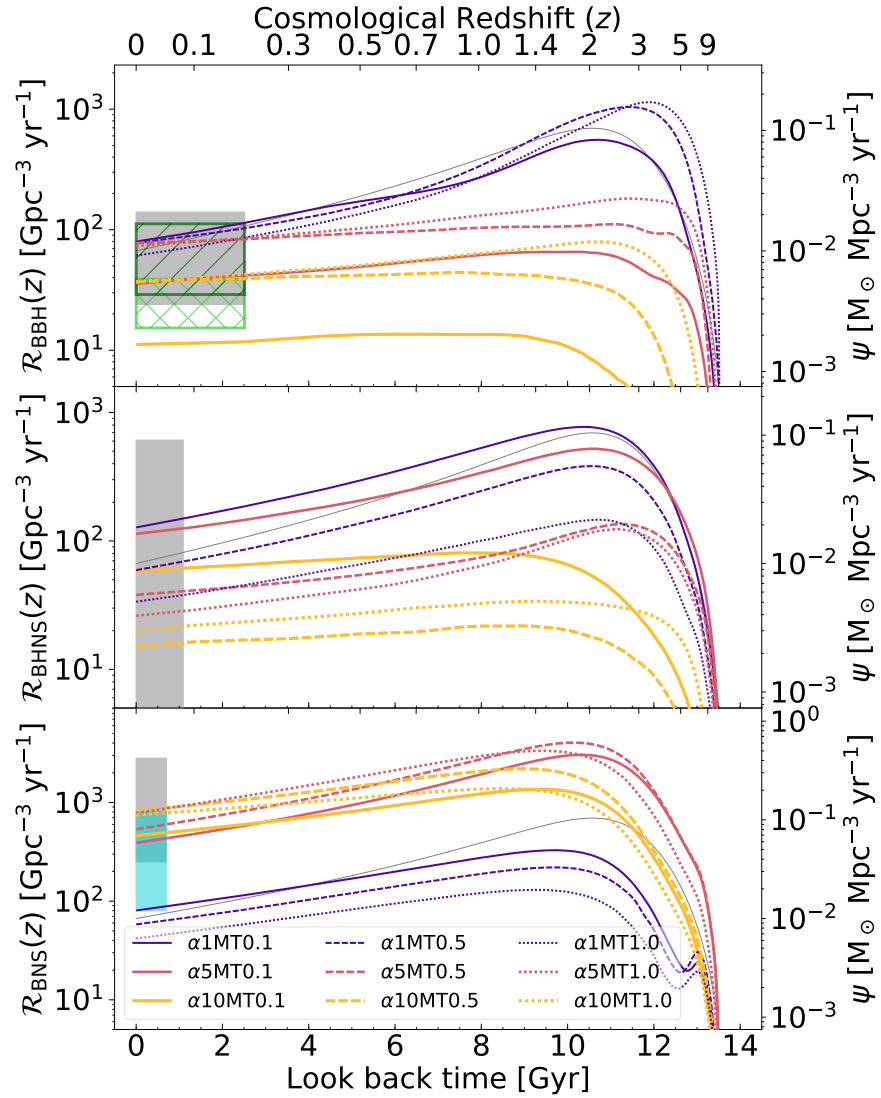


Figure 3.5: Merger rate density of BBHs (top), BHNSs (centre) and BNSs (bottom). Same as Figure 3.2, but we compare different values of the accretion efficiency parameter  $f_{\text{MT}}$ .

of  $\alpha$ . In contrast, lower values of  $f_{\text{MT}}$  lead to a higher  $\mathcal{R}_{\text{BHNS}}(z)$ . Finally, the impact on BNS merger rate density is very mild and depends on  $\alpha$ .

The physical reason is that highly non-conservative mass accretion significantly reduces the total mass of the binary star. In particular, the secondary star accretes just a small fraction of the mass lost by the primary star during Roche lobe overflow. This implies that non-conservative mass transfer enhances the formation of unequal mass binary compact objects, such as BHNSs.

### 3.3.6 Initial mass function

Figure 3.6 shows that the impact of varying the IMF’s slope on the cosmic merger rate is very mild, as already found by Klencki et al. (2018).  $\mathcal{R}_{\text{BBH}}(z)$  and  $\mathcal{R}_{\text{BNS}}(z)$  show an opposite trend: the former is higher when a shallower IMF slope is considered. This result has a trivial explanation: if  $\alpha_{\text{IMF}} = 2.0$ , the fraction of massive stars that end up collapsing into BHs is higher with respect to  $\alpha_{\text{IMF}} = 2.7$ .

### 3.3.7 Metallicity and SFR evolution

As we detailed in Section 3.2.2, the cosmic merger rate density is evaluated by assuming the fit from Madau & Fragos (2017) for the SFR density (equation 3.7) and a metallicity evolution model (equation 3.8). These two functions are affected by observational uncertainties; in this Section, we show their impact on the merger rate density. We take in account the uncertainty on four quantities, namely the normalisation factor of the SFR density  $\psi(0)$  in equation 3.7, the intercept  $a$  and slope  $b$  of equation 3.8, and the metallicity spread  $\sigma_Z$  in equation 3.9. We assume the metallicity spread  $\sigma_Z$  to follow a log-normal distribution with standard deviation 0.1 dex.

We evaluate the cosmic merger rate density by varying the value of the aforementioned parameters in a  $[-2\sigma, +2\sigma]$  interval, where  $\sigma$  is the standard deviation associated with each parameter. We assume here, for simplicity, that the considered quantities follow a Gaussian distribution and that they are not correlated with each other.

Figure 3.7 shows the dependence of the merger rate density on these observational parameters. For sake of clarity, we just plotted the merger rate density in the local Universe ( $z_{\text{loc}} < 0.1$ ) and at  $z = 2$  for two different values of  $\alpha$ .  $\mathcal{R}_{\text{BNS}}(z)$  is only mildly affected by the parameters that concern metallicity ( $a$ ,  $b$  and,  $\sigma_Z$ ), especially at low redshift. The most important parameter for BNSs is the normalisation of the SFR  $\psi(0)$ . In order for the local merger rate density to be within the 90% credible interval inferred from the O1, O2 and O3a GW data collection, we have to assume a value of  $\psi(0) \leq 0.01 \text{ M}_\odot \text{ Mpc}^{-3} \text{ yr}^{-1}$  ( $\psi(0) \geq 0.02 \text{ M}_\odot \text{ Mpc}^{-3} \text{ yr}^{-1}$ ) for the model  $\alpha 5$  ( $\alpha 1$ ). Thus, the cosmic merger rate density of BNSs is mainly affected by population-synthesis uncertainties and by the uncertainty on the SFR.

In contrast,  $\mathcal{R}_{\text{BBH}}(z)$  changes by orders of magnitude when varying the parameters that describe metallicity evolution. For instance, if we assume  $\sigma_Z > 0.35$  (0.29) dex for model  $\alpha 1$  ( $\alpha 5$ ), while keeping the other parameters at their fiducial values, the local merger rate density of BBHs is outside the 90% credible interval inferred by the LVC from the GWTC-2,

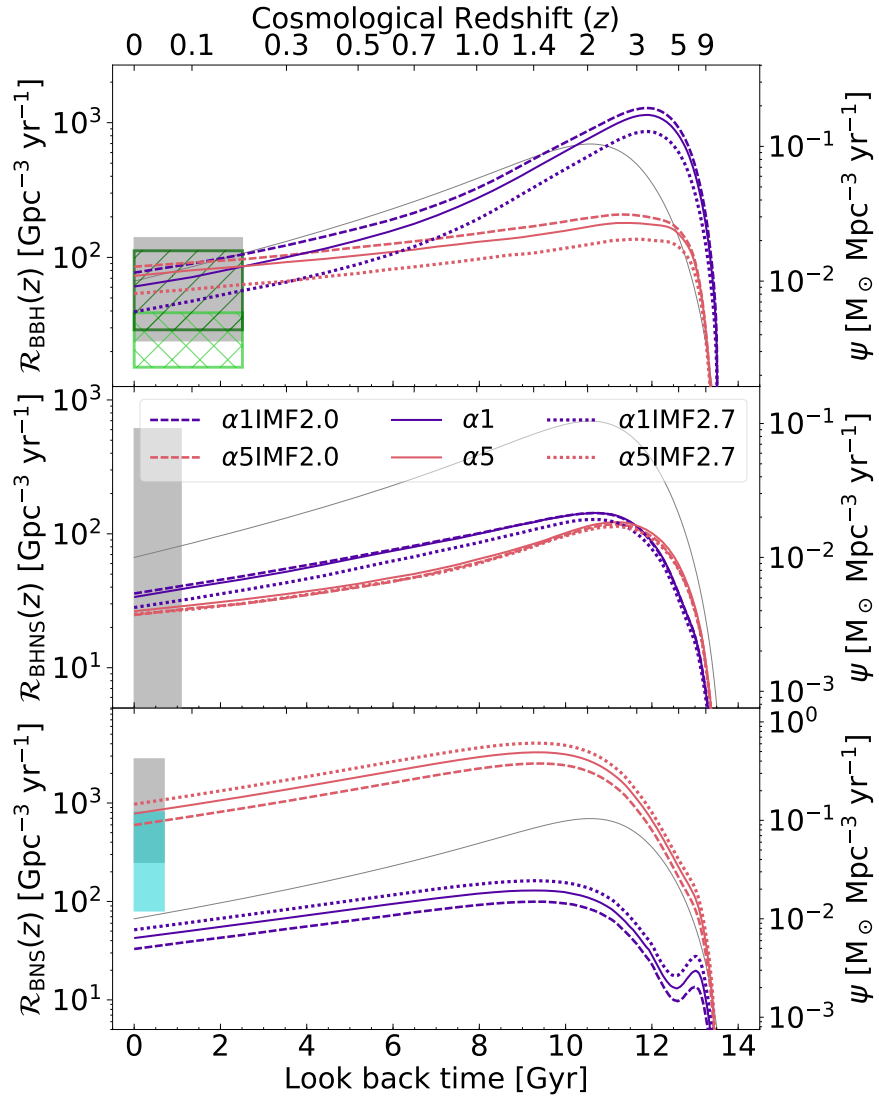


Figure 3.6: Merger rate density of BBHs (top), BHNSs (centre) and BNSs (bottom). Same as Figure 3.2, but we compare different values of the IMF slope  $\alpha_{\text{IMF}}$ .

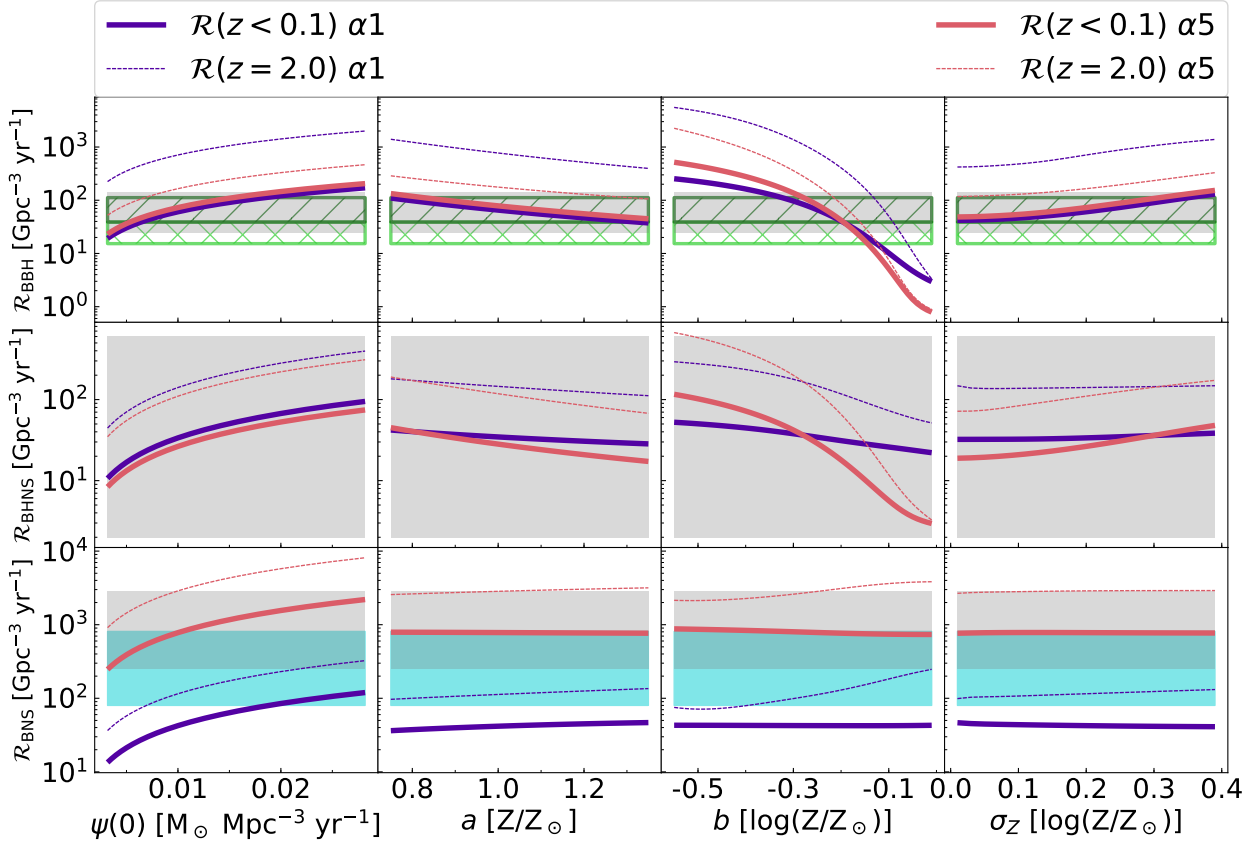


Figure 3.7: Merger rate density in the local Universe  $\mathcal{R}(z < 0.1)$  (thick line) and at  $z = 2$  (thin dashed line) as a function of the SFR density normalisation  $\psi(0)$  (equation 3.7, leftmost column), the intercept  $a$  and slope  $b$  of the metallicity evolution model (equation 3.8, two central columns), and the metallicity spread  $\sigma_Z$  (equation 3.9, rightmost column) for two different population-synthesis models:  $\alpha 1$  and  $\alpha 5$ , as displayed in Table 3.1. For BBHs and BHNSs, the grey shaded area shows the 90% credible interval of the merger rate density in the local Universe, as inferred from the first two observing runs of the LVC. For BBHs, we consider the union of the rates obtained with model A, B and C in Abbott et al. (2019a,b). For BHNSs, the grey shaded area shows the merger rate density estimated in Abbott et al. (2020e). The hatched green areas show the local BBH merger rate density inferred including O3a events (Abbott et al., 2020c). In particular, the dark-green and light-green hatched areas show the 90% credible interval calculated including and excluding GW190814-like events, respectively (Abbott et al., 2020c). Finally, the cyan shaded area shows the 90% credible interval of the local BNS merger rate density, as estimated by Abbott et al. (2020c).

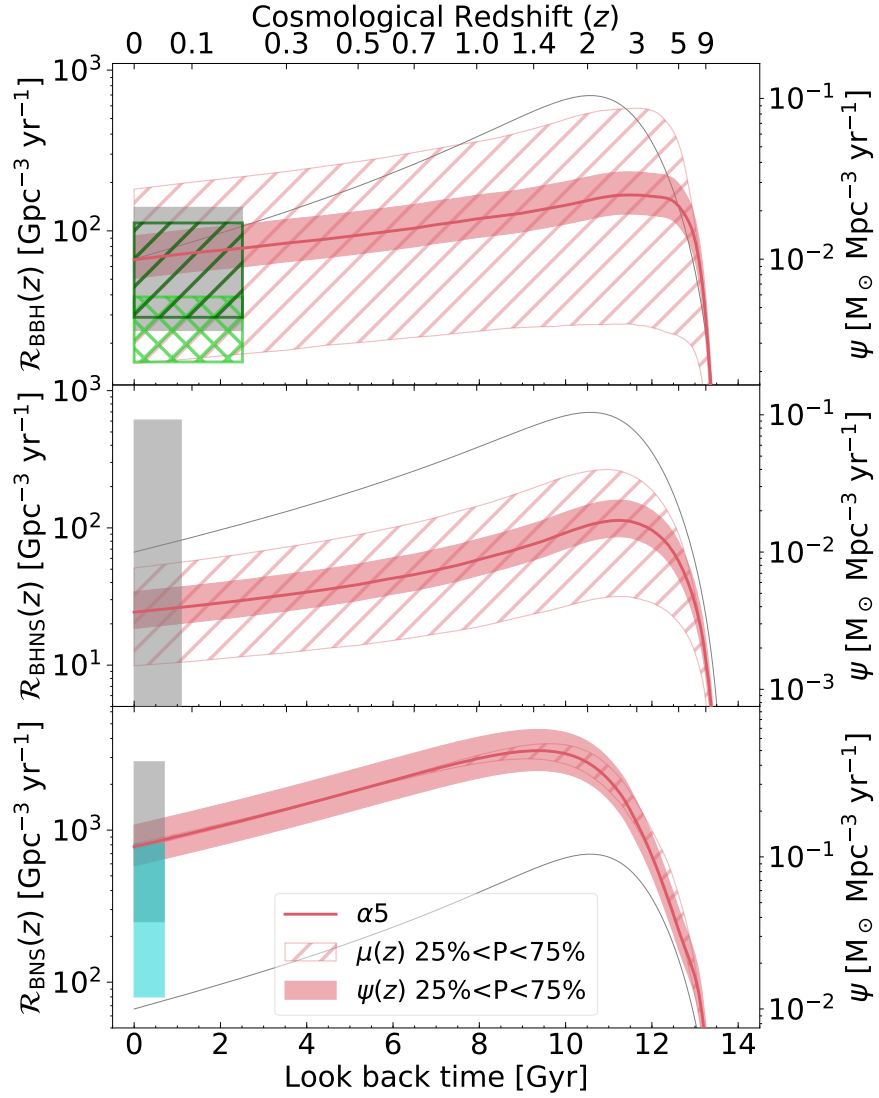


Figure 3.8: Merger rate density of BBHs (top), BHNSs (centre) and BNSs (bottom). Same as Figure 3.2, but we show the uncertainties on SFR and metallicity evolution. The contour areas represent 50% of different realisations (between the 25% and 75% percentile), while the thick solid line is the median. See Section 3.2.2 for details. To obtain the hatched area (with vertical lines), we varied only the slope and intercept of the metallicity fit (equation 3.8). To derive the shaded area we varied only the SFR density normalisation  $\psi(0)$  (equation 3.7). Hence, the hatched area and the shaded area quantify the uncertainty on metallicity and SFR, respectively.

evaluated including GW190814-like events. We expect  $\mathcal{R}_{\text{BBH}}$  to grow with  $\sigma_Z$  because a larger value of  $\sigma_Z$  means that the percentage of metal-poor stars at low redshift is higher. As we have seen from Figure 3.1, the BBH merger efficiency is orders of magnitude higher for metal-poor stars. For the same reason, the cosmic merger rate density of BBHs decreases for increasing values of the intercept in equation 3.8.

The value of the slope  $b$  in equation 3.8 represents the largest source of uncertainty for  $\mathcal{R}_{\text{BBH}}$ , compared to the other observational parameters. The local BBH merger rate density changes by two to four orders of magnitude by varying  $b$  within  $2\sigma$ . The local merger rate density is inside the 90% credible interval inferred from GWTC-2 only for  $b \in [-0.19, -0.12]$  ( $[-0.19, -0.15]$ ) for the model  $\alpha 1$  ( $\alpha 5$ ).

BHNSs behave in a similar way to BBHs, but all the considered realisations are still within the upper limit from the LVC.

Figure 3.8 shows the overall uncertainty affecting the cosmic merger rate density due to SFR and metallicity. We evaluate this uncertainty through the Monte Carlo method presented in Section 3.2.2.  $\mathcal{R}_{\text{BBH}}(z)$  and  $\mathcal{R}_{\text{BHNS}}(z)$  are heavily affected by uncertainties on metallicity evolution. In contrast, the uncertainty on  $\mathcal{R}_{\text{BNS}}(z)$  is much smaller and is dominated by the SFR.

### 3.3.8 Merger rate density as a function of metallicity

Figure 3.9 shows the contribution of different progenitor's metallicities to the cosmic merger rate density, for three different values of  $\alpha = 1, 5$  and  $10$ . For  $\alpha = 1$ , progenitor stars with  $Z \sim 0.004$  produce most of the BBHs merging at  $z \lesssim 4$ .

In contrast,  $\mathcal{R}_{\text{BNS}}(z)$  is dominated by solar metallicity progenitors for  $z \lesssim 1$ . Again, this springs from the different dependence of BBH and BNS merger efficiency on metallicity.

Different values of  $\alpha$  change the relative contribution of different metallicities to the merger rate. For all kind of compact object binaries considered here (BBHs, BHNSs and BNSs), larger values of  $\alpha$  correspond to a larger contribution of metal-poor stellar populations to the local merger rate with respect to metal-rich stellar populations. This happens because the delay times are generally longer for large values of  $\alpha$  than for small values of  $\alpha$ . In fact, larger values of  $\alpha$  imply that the CE is ejected without much shrinking of the binary system. Hence, the final binary that emerges from CE has a larger orbital separation, and needs more time to merge by GW emission.

## 3.4 Discussion

### 3.4.1 Fitting the merger rate density at $z < 1$

Our models show that the merger rate density of binary compact objects is broadly reminiscent of the cosmic SFR density. Here, we want to quantify how close is the slope of the merger rate density to that of the cosmic SFR in our different models. Since LIGO and Virgo at design sensitivity will observe BBH mergers up to  $z \sim 1$ , we restrict our attention to the slope of the merger rate density up to such redshift (Fishbach et al., 2018). We assume that

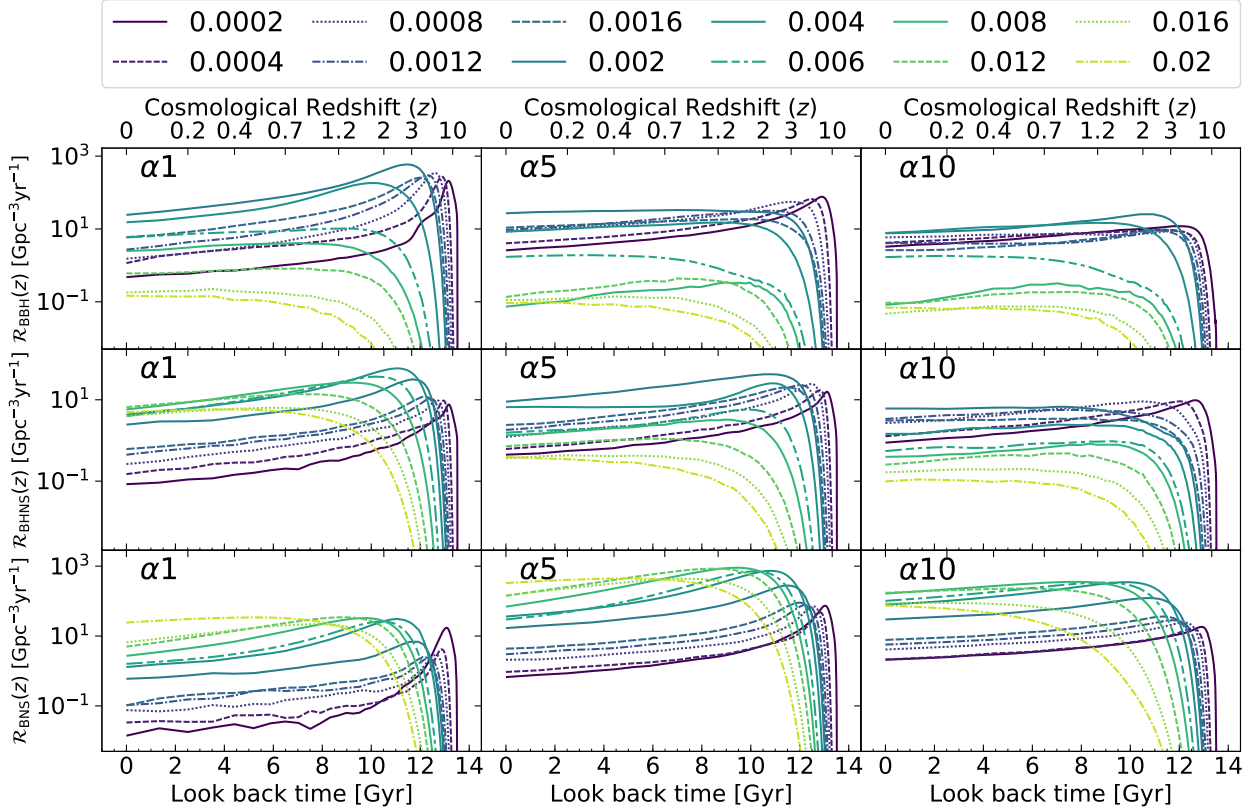


Figure 3.9: Contribution of progenitor's metallicity to the cosmic merger rate density for three different population-synthesis model:  $\alpha 1$ ,  $\alpha 5$ , and  $\alpha 10$ , as reported in Table 3.1. The considered metallicities are shown in the legend in the upper panel ( $Z = 0.0002 - 0.02$ ).

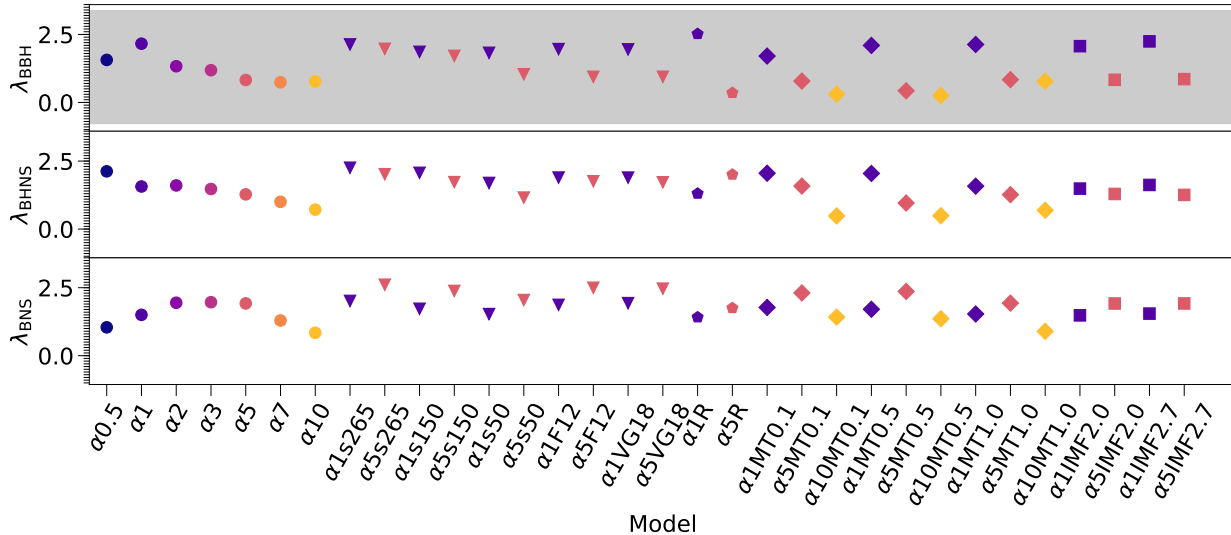


Figure 3.10: Values of  $\lambda$  (defined in equation 3.11) for each considered model. From top to bottom: BBHs, BHNSs and BNSs. The grey shaded area represents the 90% credible interval of  $\lambda_{\text{BBH}} = 1.3^{+2.1}_{-2.1}$ , inferred by the LVC from GWTC-2, adopting the POWER LAW + PEAK MODEL (Abbott et al., 2020c).

$\mathcal{R}_{\text{BBH}}(z) \propto (1+z)^\lambda$  if  $z < 1$ . Under such assumption, we can fit the following quantities

$$\log [\mathcal{R}(1+z)] = \log \mathcal{R}_0 + \lambda \log (1+z). \quad (3.11)$$

We expect to find  $\lambda \approx 2.6$  if the merger rate density scales approximately with the cosmic SFR density, given equation 3.7.

We show the results of the fit for  $z \in [0, 1]$  in Table 3.2 and Figure 3.10. Most of our models have  $\lambda < 2.6$  for BBHs, BHNSs and BNSs. This suggests that the actual slope of the merger rate density is shallower than the one of the cosmic SFR, because of the delay time distribution, which encodes information on binary evolution processes, and because of the impact of metallicity on the merger efficiency.

The model closest to  $\lambda = 2.6$  is  $\alpha_{5s265}$  for BNSs, i.e. the model with large natal kicks. With this kick choice, only the tightest and most massive systems can survive the SN explosion, and these systems are also those that merge with the shortest delay times by GW radiation. In contrast, the model with the shallowest slope is  $\alpha_{10MT0.5}$  for BBHs, which yields  $\lambda = 0.25$ . As we have already seen in Figure 3.9, models with  $\alpha = 10$  have longer delay times than the other models.

The slope  $\lambda$  of each of considered model in this work is within the 90% credible interval inferred by the LVC (Abbott et al., 2020c) for BBHs, as also shown in Figure 3.10.

Table 3.2: Coefficients of the fit in equation 3.11 with  $0 \leq z < 1$  for each considered model.

Model name	BBH		BHNS		BNS	
	$\mathcal{R}_0$	$\lambda$	$\mathcal{R}_0$	$\lambda$	$\mathcal{R}_0$	$\lambda$
$\alpha 0.5$	40.39	1.56	14.74	2.12	21.75	1.04
$\alpha 1$	57.74	2.16	34.45	1.57	44.59	1.50
$\alpha 2$	105.42	1.33	29.58	1.60	76.54	1.95
$\alpha 3$	94.08	1.19	30.10	1.47	358.44	1.97
$\alpha 5$	73.76	0.83	25.74	1.28	812.20	1.92
$\alpha 7$	52.08	0.74	26.88	1.00	1036.82	1.29
$\alpha 10$	37.09	0.77	20.23	0.72	746.12	0.84
$\alpha 1s265$	12.36	2.13	2.07	2.26	4.26	2.01
$\alpha 5s265$	10.00	1.97	1.84	2.02	39.17	2.61
$\alpha 1s150$	36.16	1.86	8.10	2.07	12.83	1.72
$\alpha 5s150$	31.69	1.71	8.32	1.73	124.97	2.38
$\alpha 1s50$	57.78	1.82	41.62	1.70	59.85	1.53
$\alpha 5s50$	74.93	1.03	36.20	1.16	544.78	2.05
$\alpha 1F12$	53.82	1.96	9.73	1.89	7.67	1.87
$\alpha 5F12$	49.85	0.94	6.22	1.76	67.94	2.50
$\alpha 1VG18$	54.07	1.95	9.61	1.89	17.31	1.93
$\alpha 5VG18$	49.69	0.94	6.57	1.72	147.00	2.46
$\alpha 1R$	65.28	2.52	42.54	1.31	35.31	1.41
$\alpha 5R$	95.73	0.35	12.34	2.01	669.05	1.75
$\alpha 1MT0.1$	83.03	1.71	128.04	2.05	82.99	1.77
$\alpha 5MT0.1$	35.95	0.78	110.34	1.58	384.90	2.31
$\alpha 10MT0.1$	11.39	0.31	59.69	0.48	464.31	1.42
$\alpha 1MT0.5$	71.20	2.10	59.29	2.05	60.13	1.71
$\alpha 5MT0.5$	77.70	0.43	37.36	0.96	535.59	2.36
$\alpha 10MT0.5$	37.50	0.25	15.35	0.49	836.07	1.36
$\alpha 1MT1.0$	58.47	2.13	34.06	1.58	43.88	1.53
$\alpha 5MT1.0$	73.18	0.84	25.67	1.27	813.39	1.93
$\alpha 10MT1.0$	36.99	0.78	20.55	0.69	761.75	0.90
$\alpha 1IMF2.0$	72.98	2.07	36.70	1.49	34.60	1.48
$\alpha 5IMF2.0$	84.34	0.83	24.07	1.29	620.73	1.92
$\alpha 1IMF2.7$	37.45	2.25	28.28	1.62	53.97	1.55
$\alpha 5IMF2.7$	53.71	0.86	24.36	1.26	1013.70	1.92

$\mathcal{R}_0$  is given in  $[\text{Gpc}^{-3} \text{ yr}^{-1}]$ . In order to check the goodness of the fits, we calculated the *coefficient of determination*  $R^2$  which is  $> 0.95$  for all the linear fits, except for the model  $\alpha 5MT0.1$ , which yields  $R^2 = 0.84$ .

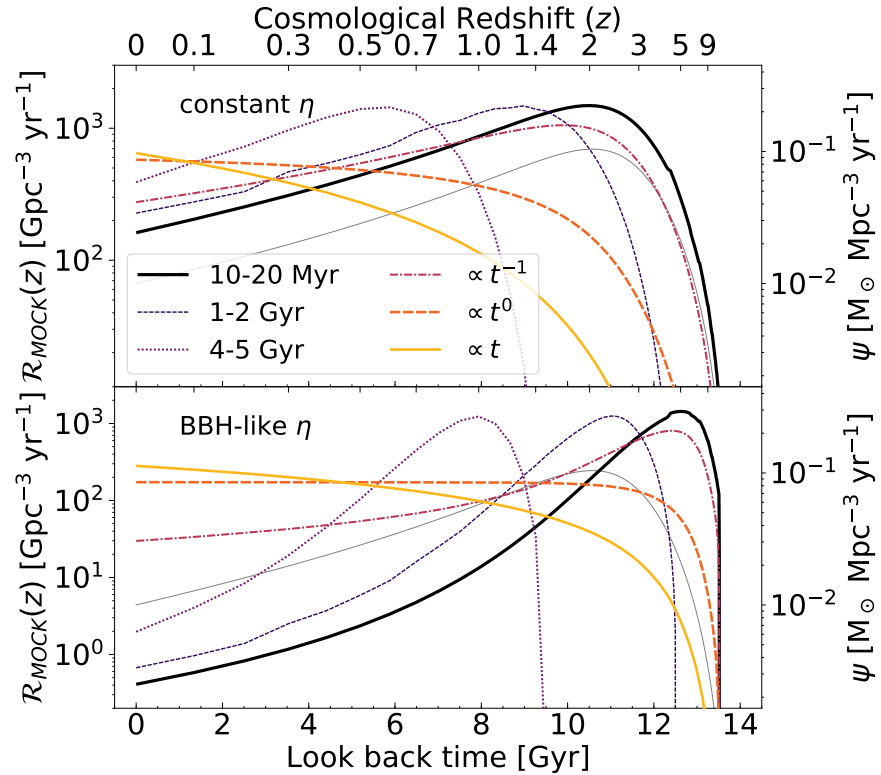


Figure 3.11: Evolution of the cosmic merger rate density evaluated with mock catalogues of merging compact binaries with constant (top) and BBH-like (bottom) merger efficiency  $\eta$ ; and with six different delay time distributions. The thin grey line is the SFR from [Madau & Fragos \(2017\)](#).

### 3.4.2 Merger efficiency and delay time impact on merger rate density

In this Section, we want to use a simple toy model to interpret the results we found in the previous Section. In order to understand what are the effects on the cosmic merger rate density of the convolution of the SFR density with different delay time distributions and with metallicity, we performed some mock simulations<sup>2</sup>.

The first ingredient of our mock simulations is the merger efficiency, which encodes a possible dependence on metallicity. We consider two different cases. In the first case, we assume a constant merger efficiency  $\eta$ , independent of metallicity; in the second case, we adopt a BBH-like  $\eta$ , higher at low metallicity. Specifically, for the latter case we use the merger efficiency of the  $\alpha 5$  case, as displayed in Figure 3.1.

The second ingredient is the delay time  $t_{\text{del}}$  distribution. For simplicity, we assume that the delay time distribution does not depend on metallicity. We consider four cases in which we assume a uniform delay time distribution: three narrow distributions with  $t_{\text{del}}$  uniform from 10 to 20 Myr, from 1 to 2 Gyr and from 4 to 5 Gyr; and a broader distribution with  $t_{\text{del}}$  uniform from 10 Myr to 14 Gyr. Then, we consider two power law distributions:  $\propto t^{-1}$  and  $\propto t$ , defined from 10 Myr to 14 Gyr.

Figure 3.11 shows the merger rate density evaluated with the aforementioned mock simulations. Let us start considering the cases with constant  $\eta$ . If the delay time is uniformly distributed between 10 and 20 Myr, the merger rate density has exactly the same slope and peak redshift as the cosmic SFR. The other two narrow delay time distributions have the effect to shift the merger rate density peak towards lower redshifts than the peak of the cosmic SFR. The case with  $dN/dt \propto t^{-1}$  has a very similar slope to the cosmic SFR density ( $\lambda \sim 2.6$ ), while the cases with  $dN/dt \propto t^0$  and  $t$  have significantly flatter and even upturning slopes ( $\lambda < 0$ ). The case with constant  $\eta$  and  $\propto t^{-1}$  delay time distribution is reminiscent of our BNS simulations. However, the fact that our BNS models generally have a slope flatter than  $\lambda = 2.6$  (Table 3.2) tells us that, for a constant  $\eta$ , the delay time distribution in our models is flatter than  $t^{-1}$ .

Let us now look at the cases with a BBH-like  $\eta$ . The delay time distribution uniform between 10 and 20 Myr peaks at a higher redshift ( $z_{\text{peak}} \gtrsim 5$ ) with respect to the cosmic SFR density. This happens because the BBH-like merger efficiency is maximum for metallicity  $Z \sim 0.0002$ , which is common in the early Universe. This result is similar to our BBH models with  $\alpha \leq 1$  and is indicative of a strong dependence on metallicity combined with short delay times. For a uniform delay time distribution between 10 Myr and 14 Gyr, the merger rate density is almost constant with time, similar to the trend of  $\mathcal{R}_{\text{BBH}}(z)$  in the  $\alpha 10$  model. Indeed, the delay time distribution of  $\alpha 10$  is nearly flat, because  $\alpha > 5$  implies less effective shrinking of the binaries during CE, hence longer delay times.

---

<sup>2</sup>Mock models have been extensively applied in the early years of binary evolution studies, where they were adopted to interpret short gamma-ray burst redshift distributions (see for instance Nakar et al. 2006; Zheng & Ramirez-Ruiz 2007; Berger et al. 2007).

### 3.4.3 Comparison with previous work

One of the main results of our analysis is that the BBH merger rate varies by more than one order of magnitude because of uncertainties on metallicity evolution, while the merger rate of BNSs is substantially unaffected by metallicity. This result is in agreement with previous studies (e.g. Giacobbo & Mapelli 2018; Chruslinska et al. 2019; Neijssel et al. 2019; Tang et al. 2020; Belczynski et al. 2020).

On top of that, the merger rates of BBHs, BHNSs and BNSs strongly depend on CE efficiency ( $\alpha$ ), mass transfer efficiency ( $f_{\text{MT}}$ ) and natal kicks. For the merger rate of BBHs, the uncertainty connected with such binary evolution parameters is of the same order of magnitude as the uncertainty on metallicity evolution, consistent with Neijssel et al. (2019) and Belczynski et al. (2020). In these previous studies, the authors pointed out the importance of inter-parameter degeneracy while deriving astrophysical conclusions from GW observations.

For a suitable choice of these binary evolution parameters (namely  $\alpha \geq 2$  and moderately low natal kicks), we find reasonable agreement between our models and the LVC rates after O1, O2 and O3a (Abbott et al., 2019a,b, 2020e,c). In particular, only models with moderately low kicks (depending on the ejected mass and the SN model), such as those described by Giacobbo & Mapelli (2020), Tang et al. (2020), Zevin et al. (2020) and Vigna-Gómez et al. (2018), can match the BNS merger rate in the local Universe.

When we compare our results with models adopting the cosmic SFR and metallicity evolution from cosmological simulations (e.g., Lamberts et al., 2016; Mapelli et al., 2017; Mapelli & Giacobbo, 2018; Artale et al., 2020a), we find more conspicuous differences. For example, Figure 3.12 shows the comparison between the merger rates estimated with COSMORATE and those estimated by Mapelli & Giacobbo (2018) and Artale et al. (2020a), using the ILLUSTRIS (Vogelsberger et al., 2014b,a; Nelson et al., 2015) and the EAGLE cosmological simulation (Schaye et al., 2015), respectively. To make a one-to-one comparison, we have re-run COSMORATE with the binary compact object catalogues from model CC15 $\alpha$ 5, obtained with an old version of MOBSE (see Giacobbo & Mapelli, 2018) and adopted in both Mapelli & Giacobbo (2018) and Artale et al. (2020a). The merger rate density of BBHs, BHNSs and BNSs in the local Universe is a factor of  $\sim 3 - 5$  higher in Mapelli & Giacobbo (2018) than in this work. This difference is due to the cosmic SFR of the ILLUSTRIS cosmological simulation, which is a factor of  $\sim 2 - 2.5$  higher in the local Universe than the one described by Madau & Fragos (2017), and to the metallicity evolution of the ILLUSTRIS, which has a larger contribution from metal-poor stars (see the bottom panel of Figure 3.12). The results of COSMORATE are more similar to those reported in Artale et al. (2020a). However, the cosmic SFR of the EAGLE is significantly lower than the one measured by Madau & Fragos (2017), as reported previously by Katsianis et al. (2017). This is compensated by the fact that the EAGLE average metallicity in the local Universe is lower with respect to equation 3.8.

## 3.5 Summary

We investigated the cosmic merger rate density evolution of compact binaries, by exploring the main sources of uncertainty. We have made use of the COSMORATE code (Santoliquido et al., 2020), which evaluates the cosmic merger rate density by combining catalogues of

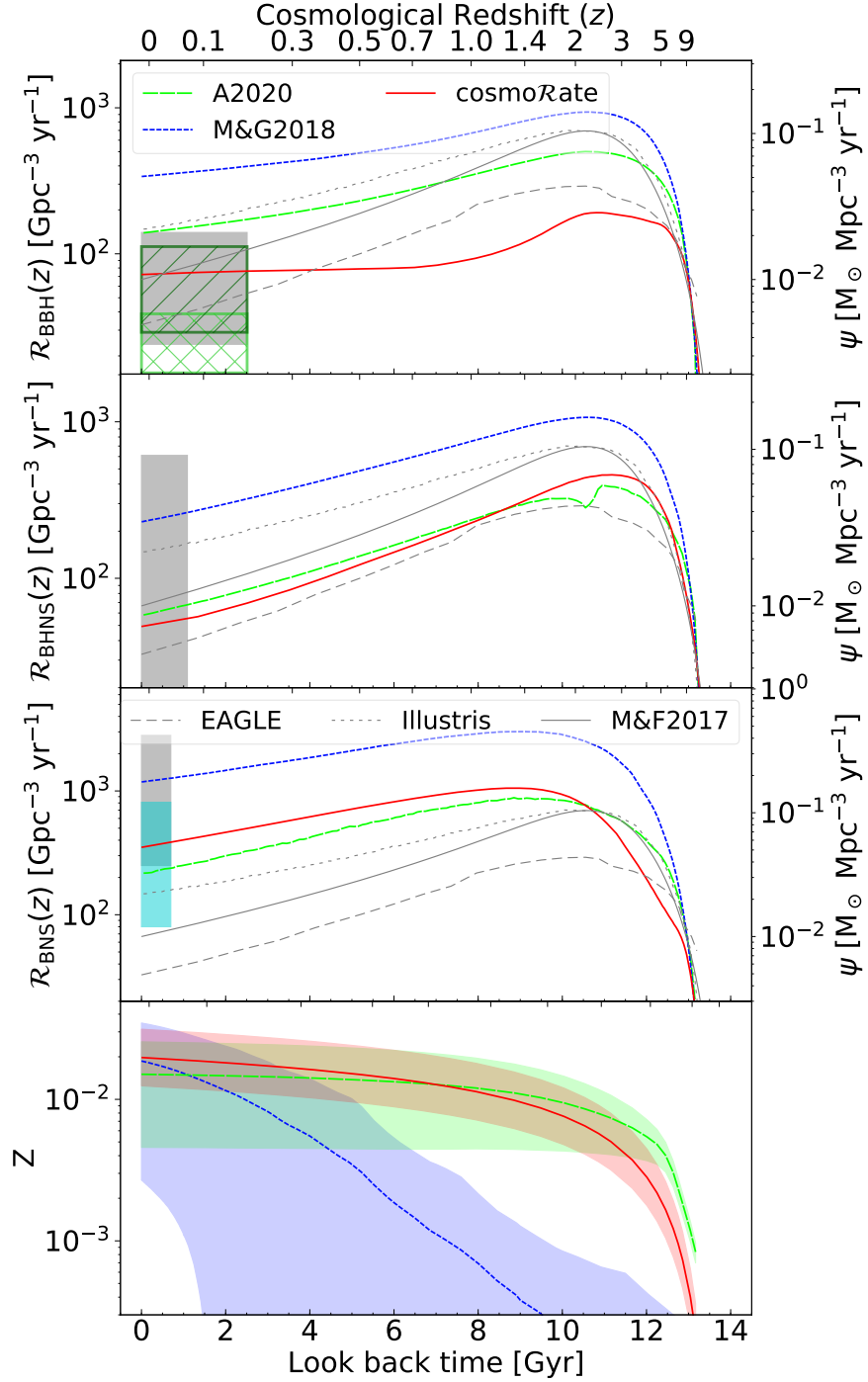


Figure 3.12: Comparison between the merger rate density of BBHs, BHNSs and BNSs obtained with **COSMORATE** (red solid lines) and the ones derived by [Artale et al. \(2020a\)](#), green long-dashed lines with label A2020), based on the EAGLE cosmological simulation ([Schaye et al., 2015](#)), and by [Mapelli & Giacobbo \(2018\)](#), blue short dashed lines with label M&G2018), based on the ILLUSTRIS cosmological simulation ([Vogelsberger et al., 2014b](#)). Solid grey line: SFR density from [Madau & Fragos \(2017\)](#), with label M&F2017); long-dashed grey line: SFR density from the EAGLE simulation; short-dashed grey line: SFR density from the ILLUSTRIS simulation. The lower panel shows the average metallicity evolution in each model. Short-dashed blue line: ILLUSTRIS; long-dashed green line: EAGLE; solid red line: this work. The shaded area shows one standard deviation from the average metallicity.

merging compact binaries, obtained from population-synthesis simulations, with the [Madau & Fragos \(2017\)](#) fit to the SFR density and with a metallicity evolution model based on [De Cia et al. \(2018\)](#) and [Gallazzi et al. \(2008\)](#).

We took into account uncertainties on the most relevant binary evolution processes: CE, SN kicks, core-collapse SN models and mass accretion by Roche lobe overflow. These represent the main bulk of uncertainty on the merger rate density due to binary evolution prescriptions. In addition, we varied the slope of the IMF. Our results confirm that the core-collapse SN model and the IMF produce negligible variations of the merger rate density.

The parameter  $\alpha$ , quantifying the efficiency of CE ejection, is one of the main sources of uncertainty. The merger rate density of BNSs spans up to 2 orders of magnitude if  $\alpha$  varies from 0.5 to 10. For the same range of  $\alpha$ ,  $\mathcal{R}_{\text{BHNS}}(z)$  and  $\mathcal{R}_{\text{BBH}}(z)$  vary up to a factor of 2 and 3, respectively. Only values of  $\alpha \geq 2$  give local BNS merger rate densities within the 90% credible interval inferred from GWTC-2 ([Abbott et al., 2019a,b, 2020e](#)) when we adopt our fiducial kick model.

Large natal kicks ( $\sigma = 265 \text{ km s}^{-1}$ ) yield BNSs merger rate densities below the 90% credible interval from GWTC-2. Only models with moderately low kicks and large values of  $\alpha$  ([Bray & Eldridge, 2016, 2018; Vigna-Gómez et al., 2018; Giacobbo & Mapelli, 2020; Tang et al., 2020](#)) predict values of the BNS merger rate within the 90% LVC credible interval inferred from GWTC-2.

Different values of the mass transfer efficiency parameter do not result in appreciable differences in the BNS merger rate density. The difference between  $f_{\text{MT}} = 0.1$  and  $f_{\text{MT}} = 1$  (conservative mass transfer) is up to a factor of 5–10 for BHNSs and BBHs. The BBH local merger rate density with  $f_{\text{MT}} = 0.1$  can be as low as  $\mathcal{R}_{\text{BBH}}(z_{\text{loc}} < 0.1) \sim 11 \text{ Gpc}^{-3} \text{ yr}^{-1}$  with  $\alpha = 10$ , within the 90% credible interval inferred from GWTC-2 ([Abbott et al., 2020b,c](#)).

[Callister et al. \(2020\)](#) show that models with local merger rates  $\mathcal{R}_{\text{BBH}}(z) \propto (1+z)^\lambda$  with  $\lambda \geq 7$  are rejected, based on the O1 and O2 LVC data and on the analysis of the stochastic background. Recently, the LVC has reported  $\lambda = 1.3^{+2.1}_{-2.1}$  within the 90% credible interval, based on GWTC-2 ([Abbott et al., 2020c](#)). All of our models yield a slope  $\lambda \leq 2.6$  for  $z < 1$ ; hence, none of them can be rejected by current data. Most of our models are fitted by  $\lambda \leq 2$ , a shallower slope with respect to the cosmic SFR. We show that this is indicative of a delay time distribution flatter than  $t^{-1}$ .

We have also investigated the effect of observational uncertainties on the cosmic SFR and on metallicity evolution.  $\mathcal{R}_{\text{BNS}}(z)$  is not significantly affected by metallicity evolution (Figure 3.8). In contrast, the metallicity evolution has a tremendous impact on the merger rate density of BBHs (Figure 3.8).  $\mathcal{R}_{\text{BBH}}(z)$  is inside the 90% credible interval inferred from GWTC-2 (considering GW190814-like events) only if the metallicity spread is  $\sigma_Z \lesssim 0.35$ .

By exploring 32 different models, we have varied only a small subset of all relevant model parameters, with sparse sampling of the many-dimensional space we considered. Hence, the effective uncertainty in the merger rate is likely higher than presented in our results. More exploration of the parameter space, and in particular of the  $\alpha$ –natal kick space, is desirable in the future, even if it represents a computational challenge for population-synthesis models (e.g., [Wong & Gerosa 2019](#)).

In summary, the uncertainties on both cosmic metallicity and binary evolution processes substantially affect the merger rate of BBHs and BHNSs. As shown in previous work (e.g.,

Rodriguez & Loeb, 2018; Santoliquido et al., 2020; Mapelli et al., 2020a), dynamics in dense star clusters represents another important source of uncertainty for the BBH merger rate.

In contrast, BNSs are not much affected by metallicity evolution and are not dramatically influenced by dynamics either, because they are significantly less massive than BBHs (Ye et al., 2020; Rastello et al., 2020; Santoliquido et al., 2020). Unlike BHs, for which the primordial BH formation channel has been proposed (Carr & Hawking, 1974; Carr et al., 2016), BNSs can originate only from the death of massive stars. This set of lucky circumstances gives us the opportunity to use the BNS merger rate to put constraints on some extremely uncertain binary evolution processes, such as mass transfer, common envelope and natal kicks.

Our results already point to an intriguing direction: only large values of  $\alpha$  ( $\geq 2$ ) and moderately low natal kicks (depending on the ejected mass and the SN mechanism) can match the cosmic merger rate inferred from GWTC-2. The growing sample of GW events will help us deciphering this puzzle.

# 4

## Modelling the host galaxies of binary compact object mergers with observational scaling relations

*The merger rate density evolution of binary compact objects and the properties of their host galaxies carry crucial information to understand the sources of gravitational waves. Here, we present GALAXYRATE , a new code that estimates the merger rate density of binary compact objects and the properties of their host galaxies, based on observational scaling relations. We generate our synthetic galaxies according to the galaxy stellar mass function. We estimate the metallicity according to both the mass-metallicity relation (MZR) and the fundamental metallicity relation (FMR). Also, we take into account galaxy-galaxy mergers and the evolution of the galaxy properties from the formation to the merger of the binary compact object. We find that the merger rate density changes dramatically depending on the choice of the star-forming galaxy main sequence, especially in the case of binary black holes (BBHs) and black hole neutron star systems (BHNSs). The slope of the merger rate density of BBHs and BHNSs is steeper if we assume the MZR with respect to the FMR, because the latter predicts a shallower decrease of metallicity with redshift. In contrast, binary neutron stars (BNSs) are only mildly affected by both the galaxy main sequence and metallicity relation. Overall, BBHs and BHNSs tend to form in low-mass metal-poor galaxies and merge in high-mass metal-rich galaxies, while BNSs form and merge in massive galaxies. We predict that passive galaxies host at least  $\sim 5 - 10\%$ ,  $\sim 15 - 25\%$ , and  $\sim 15 - 35\%$  of all BNS, BHNS and BBH mergers in the local Universe.*

Based on:

**Santoliquido F., Mapelli M., Artale M. C., Boco L., 2022, MNRAS, 516, 3297**

## 4.1 Introduction

The third gravitational wave transient catalog (GWTC-3) of the LIGO–Virgo–KAGRA collaboration (LVK) contains 90 gravitational-wave (GW) event candidates (Abbott et al., 2021a). From this growing number of detections, we can extract several astrophysical properties of binary compact objects (BCOs), such as their masses, spins and merger rates. From GWTC-3, the LVK inferred a local merger rate density  $\mathcal{R}_0^{\text{BBH}} = 16 - 61 \text{ Gpc}^{-3} \text{ yr}^{-1}$ ,  $\mathcal{R}_0^{\text{BHNS}} = 7.8 - 140 \text{ Gpc}^{-3} \text{ yr}^{-1}$  and  $\mathcal{R}_0^{\text{BNS}} = 10 - 1700 \text{ Gpc}^{-3} \text{ yr}^{-1}$  for binary black holes (BBHs), black hole-neutron star binaries (BHNSs) and binary neutron stars (BNSs), respectively (Abbott et al., 2020c). In the case of BBHs, it is even possible to reconstruct the evolution of the merger rate with redshift  $\mathcal{R}(z) \propto (1+z)^k$  with  $z \leq 1$ . Abbott et al. (2020c) find  $k > 0$  at 99.6% credibility, indicating that the BBH merger rate density increases with redshift. Thanks to the next-generation ground-based GW detectors, Einstein Telescope (Punturo et al., 2010) and Cosmic Explorer (Reitze et al., 2019), we will be able to reconstruct the redshift evolution of the BBH merger rate up to redshift  $z = 10$  or even higher (Kalogera et al., 2019, 2021; Maggiore et al., 2020).

While the merger rate provides crucial insights about the formation of BCOs (e.g., Dominik et al., 2013; Belczynski et al., 2016; Mapelli et al., 2017; Mapelli & Giacobbo, 2018; Baibhav et al., 2019; Neijssel et al., 2019), the properties of their host galaxies (HG)s represent another fundamental piece of information (e.g., Perna & Belczynski, 2002; Belczynski et al., 2006; O’Shaughnessy et al., 2010; Lamberts et al., 2016; Schneider et al., 2017; Mapelli et al., 2018; Artale et al., 2019, 2020a,b). Also, the identification of the host galaxy is crucial to reduce the uncertainties on the measure of the Hubble constant from GW sources (Abbott et al., 2017d; Fishbach et al., 2019; Gray et al., 2020; Jin et al., 2021; Leandro et al., 2022), and to successfully use BCOs as tracers of large scale structures (Vijaykumar et al., 2020; Adhikari et al., 2020; Libanore et al., 2021, 2022; Mukherjee et al., 2021; Cigarrán Díaz & Mukherjee, 2022).

At present, only the HG of the BNS merger GW170817 (Abbott et al., 2017c,f; Goldstein et al., 2017; Savchenko et al., 2017; Margutti et al., 2017; Coulter et al., 2017; Soares-Santos et al., 2017; Chornock et al., 2017; Cowperthwaite et al., 2017; Nicholl et al., 2017; Pian et al., 2017; Alexander et al., 2017), the elliptical galaxy NGC 4993, has been identified beyond any reasonable doubt (Levan et al., 2017; Im et al., 2017; Ebrová et al., 2020; Kilpatrick et al., 2022). The main obstacle to the successful identification of the HG is represented by the sky localisation uncertainties of GW detectors, currently being of the order of several ten square degrees (Abbott et al., 2018).

Several criteria to rank the galaxies within the sky localisation region have been proposed, in order to optimize the search for electromagnetic counterparts (e.g., Kopparapu et al., 2008; Arcavi et al., 2017; Ducoin et al., 2020; Stachie et al., 2020; Artale et al., 2020b; Ashkar et al., 2021a,b; Kovlakas et al., 2021; Perna et al., 2022). Furthermore, several authors studied the properties of the HGs on a theoretical ground; most of them interface the outputs of cosmological simulations with catalogs of compact objects, either obtained through population-synthesis or phenomenological models (e.g., O’Shaughnessy et al., 2017; Schneider et al., 2017; Mapelli et al., 2017; Toffano et al., 2019; Artale et al., 2019, 2020a,b; Adhikari et al., 2020; Mandhai et al., 2022; Chu et al., 2021; Rose et al., 2021; Perna et al.,

2022; Mukherjee & Moradinezhad Dizgah, 2021). These previous works suggest that the BCO merger rate per galaxy correlates with the stellar mass and star formation rate (SFR) of the HG (e.g., Artale et al., 2020a).

Here, we present a new fast numerical tool to estimate the cosmic merger rate density and to characterize the properties of the HGs of BCO mergers. Our new code `GALAXYRATE` exploits the main observational scaling relations (galaxy stellar mass function, SFR distribution, mass-metallicity relation, and fundamental-metallicity relation) to generate the distribution of galaxy masses, SFR and metallicity across cosmic time (Boco et al., 2019; Safarzadeh & Berger, 2019; Elbert et al., 2018; Chruslinska et al., 2019; Chruślińska et al., 2020, 2021). We derive the properties of the BCOs, and especially their delay times<sup>1</sup>  $t_{\text{del}}$ , from up-to-date binary population synthesis simulations (Santoliquido et al., 2021). `GALAXYRATE` is very flexible and can read catalogs from phenomenological models of BCO mergers as well.

Unlike models based on computationally expensive cosmological simulations, `GALAXYRATE` can be used to probe the parameter space of BCO mergers: a single model requires  $\sim 15$  CPU hours on a single core. With respect to similar codes based on observational scaling relations (e.g., Boco et al., 2019; Safarzadeh & Berger, 2019; Elbert et al., 2018), we have developed a new algorithm that is able to differentiate between the galaxy in which a BCO forms [hereafter, formation galaxy (FG)], and the galaxy where the BCO merges after the delay time [hereafter, host galaxy (HG)]. In fact, the properties of the FG and those of the HG can be very different from each other, not only because galaxies merge with other galaxies across the cosmic time, but also because the same galaxy can evolve significantly during the BCO delay time, changing its mass, SFR and metallicity. Our new algorithm evaluates a conditional probability that the HG of a BCO has mass  $M_{\text{host}}$  and star formation rate  $\text{SFR}_{\text{host}}$ , given the mass of the FG ( $M_{\text{form}}$ ), its SFR ( $\text{SFR}_{\text{form}}$ ), the formation and the merger redshift of the BCO ( $z_{\text{form}}$  and  $z_{\text{merg}}$ , respectively). To calculate this probability, we use the galaxy merger tree extracted from the EAGLE cosmological simulation with a  $(100 \text{ cMpc})^3$  volume (Schaye et al., 2015; Qu et al., 2017), but our formalism can be easily generalized to other merger trees.

This Chapter is organized as follows: in Section 4.2.1, we present the main formalism we adopted in our population-synthesis code MOBSE (Giacobbo & Mapelli, 2018); Section 4.2.2 describes the observational scaling relations adopted in `GALAXYRATE`; Sections 4.2.3 and 4.2.4 discuss the method to evaluate the merger rate density and the conditional probability, respectively. Section 4.3 presents our main results. We discuss the implications of our new methodology in Section 4.4, and draw our main conclusions in Section 4.5.

## 4.2 Methods

Here, we describe our new code `GALAXYRATE`, which calculates the merger rate evolution of BCOs and the properties of their host galaxies, based on population-synthesis simulations and observational scaling relations. `GALAXYRATE` is an upgrade of our code `COSMORATE` (Santoliquido et al., 2020, hereafter S20). Table 4.1 summarises the parameters included in

---

<sup>1</sup>We define the delay time as the time elapsed from the formation of the progenitor binary star to the merger of the BCO.

GALAXYRATE and discussed in the following sections.

### 4.2.1 Binary compact objects (BCOs)

The open-source population synthesis code MOBSE (Mapelli et al., 2017; Giacobbo & Mapelli, 2018) is an upgraded and customized version of BSE (Hurley et al., 2000, 2002). With respect to the original version of BSE, MOBSE includes an up-to-date formalism for stellar winds (Giacobbo & Mapelli, 2018), and several new models for the outcome of electron-capture (Giacobbo & Mapelli, 2019), core-collapse (Fryer et al., 2012) and pair-instability supernovae (Spera & Mapelli, 2017; Mapelli et al., 2020b). Here, we assume the rapid core-collapse supernova model (Fryer et al., 2012), which enforces a mass gap between the maximum mass of a neutron star ( $2 M_{\odot}$ ) and the minimum mass of a black hole ( $5 M_{\odot}$ ). Finally, we model natal kicks of compact remnants (both neutron stars and black holes) as  $v_{\text{kick}} \propto m_{\text{ej}}/m_{\text{rem}} v_{\text{H05}}$ , where  $m_{\text{rem}}$  is the mass of the compact object,  $m_{\text{ej}}$  is the mass of the ejecta, and  $v_{\text{H05}}$  is a random number following a Maxwellian distribution with one-dimensional root-mean square  $\sigma_{\text{H05}} = 265 \text{ km s}^{-1}$  (Giacobbo & Mapelli, 2020), inspired from the proper motions of Galactic young pulsars (Hobbs et al., 2005). MOBSE integrates the main binary evolution processes (wind mass transfer, Roche lobe overflow, common envelope, magnetic braking, equilibrium tides and GW decay) as described in Hurley et al. (2002). We refer to Giacobbo & Mapelli (2018) for further details on MOBSE.

For the runs presented in this Chapter, we have used three different models, with three different values of the common-envelope parameter  $\alpha = 1, 3$  and  $5$  (hereafter,  $\alpha 1$ ,  $\alpha 3$  and  $\alpha 5$ ). For each run, we have simulated 12 different metallicities:  $Z = 0.0002, 0.0004, 0.0008, 0.0012, 0.0016, 0.002, 0.004, 0.006, 0.008, 0.012, 0.016$ , and  $0.02$ . For metallicities  $Z \leq 0.002$  ( $Z > 0.002$ ), we have simulated  $10^7$  ( $2 \times 10^7$ ) massive binary stars per each model.

The primary mass of each binary star follows a Kroupa initial-mass function (IMF, Kroupa, 2001) with minimum (maximum) mass =  $5$  ( $150$ )  $M_{\odot}$ . We derive the mass ratio  $q = m_2/m_1$  as  $\mathcal{F}(q) \propto q^{-0.1}$  with  $q \in [0.1, 1]$ , the orbital period  $P$  from  $\mathcal{F}(P) \propto P^{-0.55}$  with  $P = \log_{10}(P/\text{day}) \in [0.15, 5.5]$  and the eccentricity  $e$  from  $\mathcal{F}(e) \propto e^{-0.42}$  with  $0 \leq e \leq 0.9$  (Sana et al., 2012). Appendix 4.6.1 discusses some of the main features of these population-synthesis simulations (merger efficiency and delay time distribution).

### 4.2.2 Observational scaling relations

Hereafter, we call formation galaxy (FG) the galaxy where the stellar progenitors of the BCO form, and host galaxy (HG) the galaxy where the BCO merges via GW emission. We describe each FG with three parameters: the galaxy stellar mass ( $M_*$ ), star-formation rate (SFR) and a log-normal distribution of metallicities. This is the minimum amount of information that allows us to understand the link between galaxy properties and compact object mergers. In order to create a population of star-forming galaxies in which our compact objects form, we sample  $M_*$ , SFR and the average galaxy metallicity from three different distributions, based on observational scaling relations.

## Stellar mass function of star-forming galaxies

The stellar mass function of star-forming galaxies is given in its simplest form as a Schechter function (Schechter, 1976):

$$\phi(M_*, z) dM_* = \phi^*(z) e^{-M_*/M_{\text{cut}}(z)} \left( \frac{M_*}{M_{\text{cut}}(z)} \right)^{\alpha_{\text{GSMF}}} dM_*, \quad (4.1)$$

where  $\phi^*(z)$  is the normalisation, and  $M_{\text{cut}}(z)$  is the stellar mass at which the Schechter function bends, changing from a single power law with slope  $\alpha_{\text{GSMF}}$  at low masses to an exponential cut-off at high masses. We adopted the galaxy stellar-mass function (GSMF) derived in Chruslinska et al. (2019), where the authors made an average of various GSMFs defined in the same redshift bin (see Table 1 of Chruslinska et al. 2019). Figure 4.1 (upper panel) shows the resulting GSMF.

At each formation redshift, we sample a number of star-forming galaxies proportional to the galaxy number density, defined as the numerical integral of the GSMF between a minimum and a maximum stellar mass. In this way, similarly to what happens in cosmological simulations, we fixed the comoving volume  $V = (100 \text{ cMpc})^3$ . We choose this volume as a good compromise between the computational cost of our models and the statistics of high-mass galaxies in the box. In Appendix 4.6.2, we discuss the impact of this choice on our results.

In the sampling procedure, we assume a maximum stellar mass  $M_{\text{max}} = 10^{12} M_\odot$ . The minimum stellar mass of the GSMF is highly uncertain, especially at high redshift (Conselice et al., 2016). To this regard, we varied the minimum stellar mass  $M_{\text{min}} = 10^6, 10^7, 10^8 M_\odot$  to explore the impact of this parameter on our results. In Appendix 4.6.3, we show that the minimum mass  $M_{\text{min}}$  has a mild impact on the merger rate density in the local Universe. For the following results, we adopted  $M_{\text{min}} = 10^7 M_\odot$  as a fiducial value. We consider the redshift range between  $z = 0$  and 8. At higher redshift, the observations are too scanty to confidently extrapolate the GSMF.

## Star formation rate (SFR)

Galaxies can be classified in three main groups based on their SFR. (i) The majority of galaxies belong to the so-called *galaxy main sequence*: they follow a tight relation between stellar mass and SFR at any redshift (Daddi et al., 2007; Speagle et al., 2014; Rodighiero et al., 2015; Schreiber et al., 2015; Pantoni et al., 2019; Lapi et al., 2020; Leja et al., 2021; Popesso et al., 2022). (ii) A second group of galaxies, the *starburst* galaxies, have higher SFR with respect to the main sequence (Rodighiero et al., 2011; Caputi et al., 2017). The main sequence and starburst galaxies form the population of star-forming galaxies. (iii) The third group of galaxies consists in the *passive* (or quenched) galaxies, which have, on average, a lower SFR with respect to the main sequence (Renzini & Peng, 2015; Bisigello et al., 2018; Santini et al., 2021). At low redshift, passive galaxies are the dominant population: they contain up to  $\sim 70\%$  of the total stellar mass in the local Universe (Moffett et al., 2016).

In GALAXYRATE, we describe the star-forming galaxy distribution in SFR at fixed redshift and stellar mass with a double log-normal distribution (Daddi et al., 2007; Rodighiero

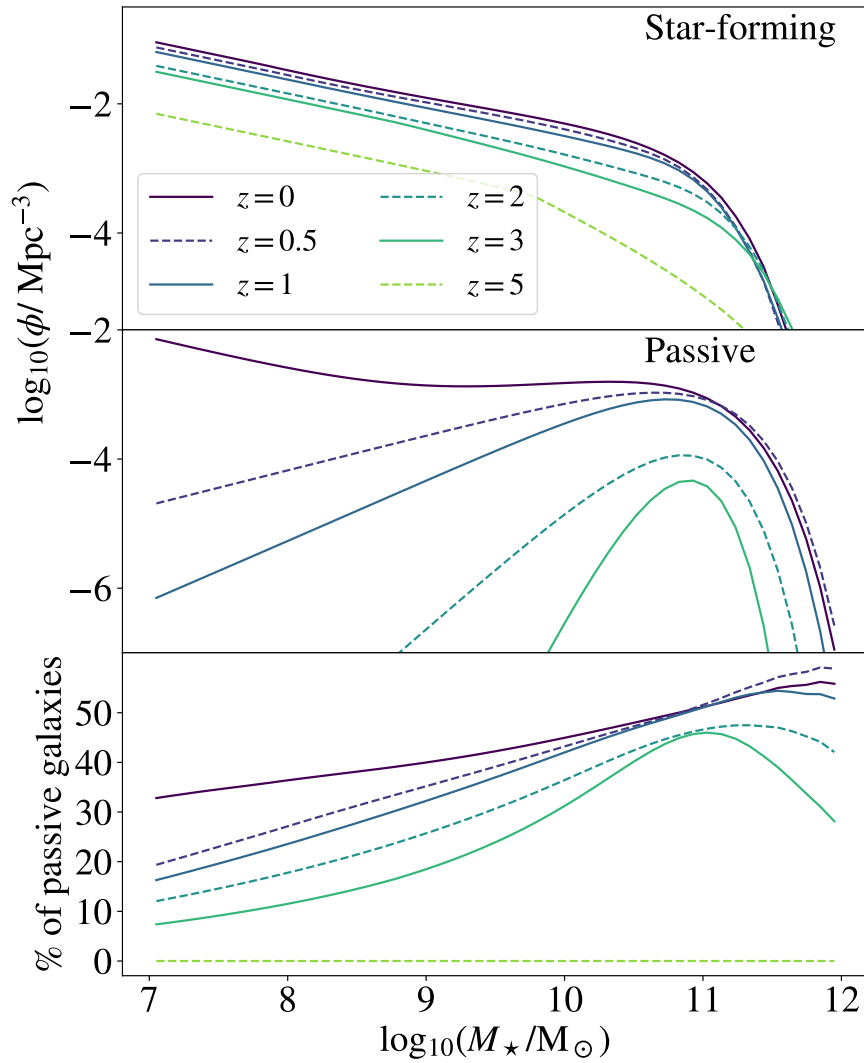


Figure 4.1: Upper panel: GSMF of star-forming galaxies from Chruslinska et al. (2019), shown at different redshifts. Middle panel: GSMF of passive galaxies from Ilbert et al. (2013). Lower panel: percentage of passive galaxies per stellar mass bin.

et al., 2011; Sargent et al., 2012; Béthermin et al., 2012; Schreiber et al., 2015; Ilbert et al., 2015; Schreiber et al., 2015). One of the two log-normal distributions is centered on the galaxy main sequence, the other on the starburst sequence (Boco et al., 2021):

$$\mathcal{P}(\log_{10} \text{SFR}|M_*, z) = A_{\text{MS}} \exp - \frac{(\log_{10} \text{SFR} - \langle \log_{10} \text{SFR} \rangle_{\text{MS}})^2}{2\sigma_{\text{MS}}^2} + \\ A_{\text{SB}} \exp - \frac{(\log_{10} \text{SFR} - \langle \log_{10} \text{SFR} \rangle_{\text{SB}})^2}{2\sigma_{\text{SB}}^2}, \quad (4.2)$$

where  $\langle \log_{10} \text{SFR} \rangle_{\text{MS}}$  ( $\langle \log_{10} \text{SFR} \rangle_{\text{SB}}$ ) is the average SFR of the main sequence (starburst galaxies),  $\sigma_{\text{MS}}$  ( $\sigma_{\text{SB}}$ ) is the standard deviation of the main sequence (starburst) galaxies,  $A_{\text{MS}} = 0.97$  and  $A_{\text{SB}} = 0.03$  (Sargent et al., 2012). We define the starburst sequence as  $\langle \log_{10} \text{SFR} \rangle_{\text{SB}} = \langle \log_{10} \text{SFR} \rangle_{\text{MS}} + 0.59$  with  $\sigma_{\text{SB}} = 0.243$  dex (Sargent et al., 2012). These values are obtained expressing the SFR in  $M_\odot \text{ yr}^{-1}$ .

We compared two definitions of the galaxy main sequence  $\langle \log_{10} \text{SFR} \rangle_{\text{MS}}$ : the definition given in Speagle et al. (2014, hereafter S14) and Boogaard et al. (2018, hereafter B18). The definition of galaxy main sequence by S14 is

$$\langle \log_{10} \text{SFR}(M_*, t) \rangle = (0.84 - 0.026 t) \log_{10} M_* - 6.51 - 0.11 t, \quad (4.3)$$

where  $t$  is age of the Universe in Gyr and  $M_*$  the galaxy stellar mass in  $M_\odot$ . The definition of B18 is

$$\langle \log_{10} \text{SFR}(M_*, z) \rangle = 0.83 \log_{10} \left( \frac{M_*}{M_0} \right) - 0.83 + 1.74 \log_{10} \left( \frac{1+z}{1+z_0} \right), \quad (4.4)$$

where  $M_0 = 10^{8.5} M_\odot$  and  $z_0 = 0.55$ . Equation 4.4 has been estimated considering the Chabrier IMF (Chabrier, 2003); thus, we shifted the SFR normalisation to make it consistent with our default Kroupa IMF (Kroupa 2001; see Table B1 in Chruslinska et al. 2019 for more details about the conversion). The dispersion around the main sequence is another debated quantity. We assume  $\sigma_{\text{MS}} = 0.188$  dex for S14 (Sargent et al., 2012) and  $\sigma_{\text{MS}} = 0.3$  dex for B18 (Chruslinska et al., 2019).

After sampling a number of galaxies from the GSMF and assigning them the SFR as described above, we can derive the total cosmic SFR density, by simply evaluating the average SFR over the population of galaxies and multiplying it by the galaxy number density at each redshift. Figure 4.2 shows different resulting cosmic SFR densities depending on the definition of the main sequence, and compares them to observational data. The star formation history we obtain adopting the results of S14 is in agreement with some of the most recent data points (Casey et al., 2018) and is slightly higher than the fit by Madau & Fragos (2017). In contrast, the results of B18 lie below most observational data in the redshift range  $z \in [1, 3]$ , across cosmic noon. Hence, the models by S14 and B18 allow us to compare two different evolutions of the star formation history, in terms of normalisation and redshift evolution. In the same figure, we also show the cosmic SFR density from the EAGLE cosmological simulation with a  $(100 \text{ cMpc})^3$  volume (Furlong et al., 2015). The cosmic SFR density obtained adopting the results of B18 is close to the one evaluated with the EAGLE especially at high redshift ( $z > 1$ ).

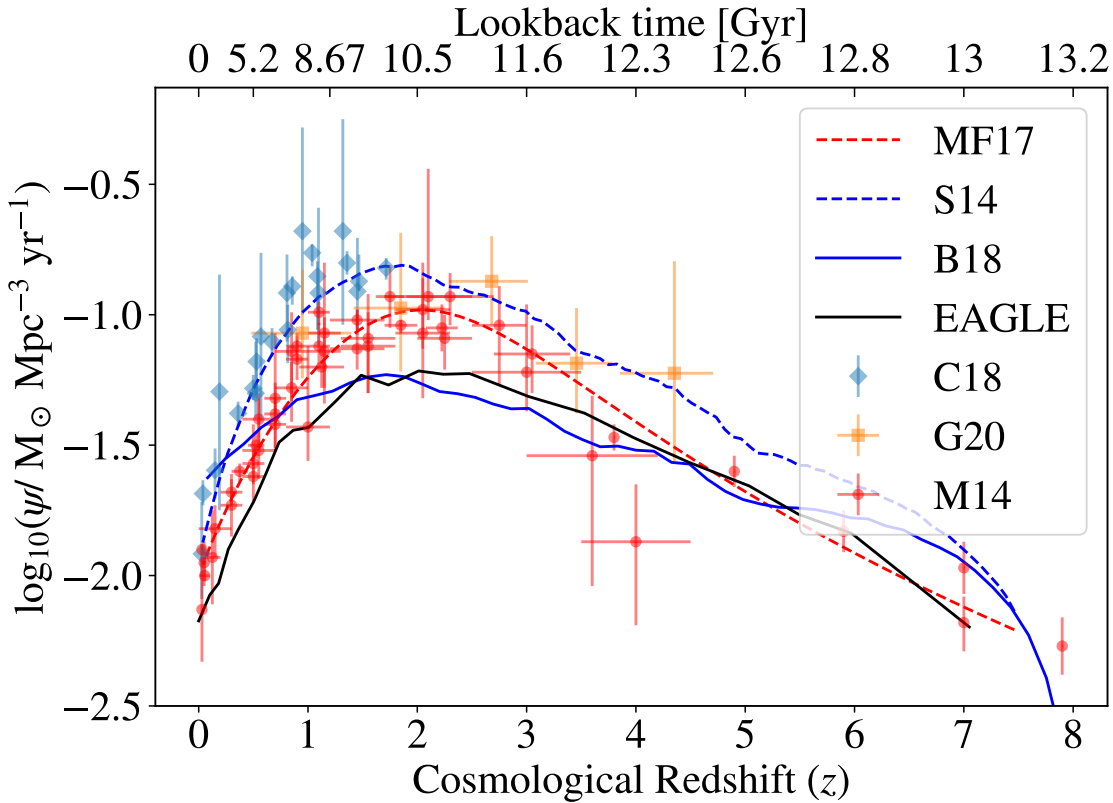


Figure 4.2: Cosmic SFR density,  $\psi(z)$ , as a function of redshift (lower  $x$ -axis) and lookback time (upper  $x$ -axis). The dashed and solid blue lines indicate the star-forming main sequence from Speagle et al. (2014, S14) and Boogaard et al. (2018, B18), respectively. The black line is the SFR density from the EAGLE box of  $(100 \text{ cMpc})^3$  (Schaye et al., 2015). The red dots are from Figure 9 of Madau & Dickinson (2014, M14) and the red line is the fit to the cosmic SFR density by Madau & Fragos (2017, MF17). The light blue dots are data points from Casey et al. (2018, C18) and the orange dots from Gruppioni et al. (2020, G20). All the data have been re-normalized to assume a Kroupa IMF (Kroupa, 2001).

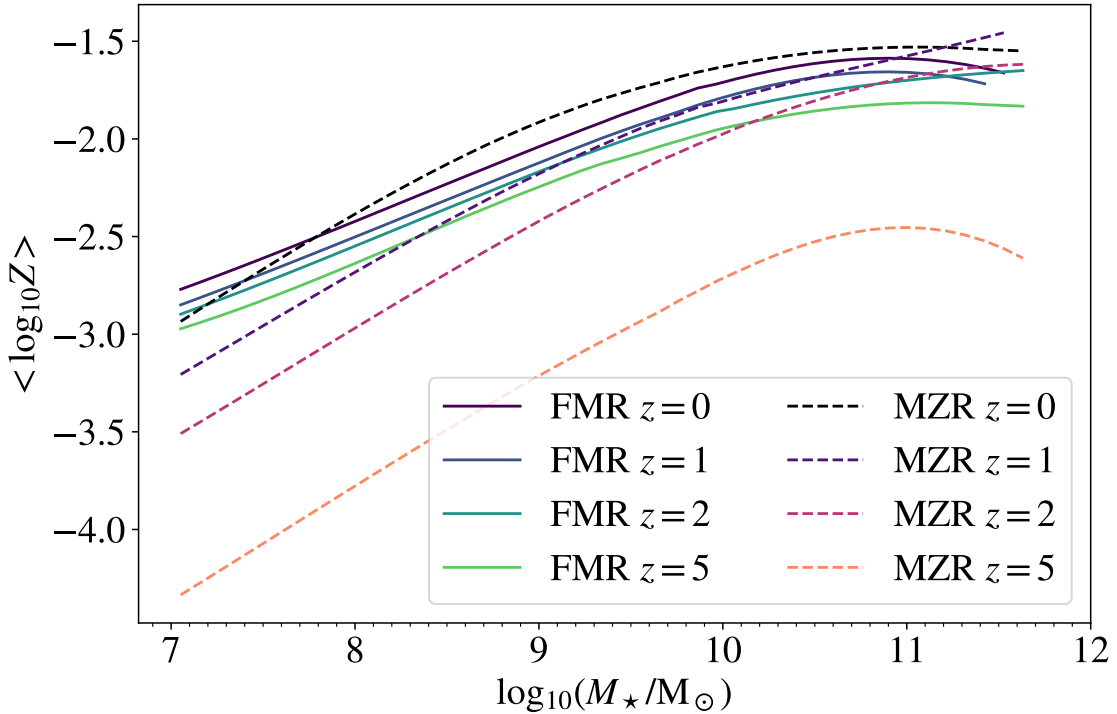


Figure 4.3: Average metallicity of star-forming galaxies obtained by sampling from the B18 main sequence and from the FMR (solid lines, [Mannucci et al., 2011](#)), compared with the MZR (dashed lines, [Chruslinska et al., 2019](#)), at different redshifts.

### Metallicity distribution

For each galaxy, we sample an average metallicity  $Z$  from observational scaling relations. Two main scaling relations have been proposed between the metallicity and other galaxy properties: the mass metallicity relation (MZR, [Tremonti et al., 2004](#); [Kewley & Ellison, 2008](#); [Maiolino et al., 2008](#); [Mannucci et al., 2009](#); [Magnelli et al., 2012](#); [Zahid et al., 2014](#); [Genzel et al., 2015](#); [Sanders et al., 2020](#)) and the fundamental metallicity relation (FMR, [Mannucci et al., 2010, 2011](#); [Hunt et al., 2012, 2016](#); [Curti et al., 2020](#); [Sanders et al., 2020](#)). The MZR is a correlation between metallicity and stellar mass, based on observations of galaxies with stellar mass in the range  $10^8 - 10^{12} \text{ M}_\odot$  and redshift  $z \sim 0 - 3.5$  ([Tremonti et al., 2004](#); [Zahid et al., 2014](#)). In general, at fixed stellar mass the MZR predicts a steep decline in  $Z$  towards higher redshifts. Some earlier works (e.g., [Maiolino et al., 2008](#); [Mannucci et al., 2009](#); [Magnelli et al., 2012](#)) found a slow evolution of the MZR out to  $z \sim 2$  but a very sharp decline of about 0.4 – 0.5 dex in  $Z$  between  $z = 2.5$  and  $3.5$ . Extrapolating this trend at  $z > 3.5$ , we expect a rapid decrease of the average galaxy metallicity in the early Universe.

The FMR is a three-parameter relation among stellar mass, SFR and metallicity. According to the FMR, the metallicity decreases at increasing SFR, for a fixed stellar mass ([Mannucci et al., 2010](#); [Hunt et al., 2016](#)). The FMR is thought to be almost redshift independent<sup>2</sup>, as confirmed by observations out to  $z \sim 3.5$  ([Mannucci et al., 2010](#)). The redshift

<sup>2</sup>Recent data from the Early Release Observations program of the James Webb Space Telescope suggest

$z$  is not a parameter of the FMR, and the metallicity evolution with redshift at fixed stellar mass is entirely explained with the redshift evolution of the SFR described by the main sequence (see Section 4.2.2). This results in a shallow decline of  $Z$  with redshift at fixed stellar mass. Therefore, while the redshift evolution of the FMR and MZR at  $z \lesssim 2$  is similar, the evolution of the two relations becomes completely different at  $z \gtrsim 3$  (Fig. 4.3). We refer to Section 3 of [Boco et al. \(2021\)](#) for a thorough discussion about the tension between the two metallicity distributions.

In the following, we will consider both MZR and FMR. To implement the MZR, we use the same definition as in Section 3.2 of [Chruslinska et al. \(2019\)](#). For the FMR, we use the definition in Equation 2 of [Mannucci et al. \(2011\)](#).

Both metallicity relations are usually expressed in terms of the relative abundance of oxygen and hydrogen,  $12 + \log_{10}(\text{O/H})$ . We need to convert this quantity to the total mass fraction of heavy elements  $Z$ , since our stellar-evolution models depend on  $Z$  (see Section 4.2.1). We assumed  $Z_\odot = 0.0153$  and  $12 + \log_{10}(\text{O/H})_\odot = 8.76$  ([Caffau et al., 2011](#)). Other choices of the solar metallicity value result in a different normalization of the merger rate density curve (Appendix 4.6.4).

Observations show that at a given stellar mass, there is an intrinsic scatter around both the MZR and FMR ([Tremonti et al., 2004](#); [Kewley & Ellison, 2008](#); [Zahid et al., 2014](#); [Chen et al., 2022](#)). Thus, we assumed a log-normally distributed scatter around the mean metallicity given by both the MZR and FMR. We considered a spread  $\sigma_0 = 0.15$  dex for both relations. Furthermore, we calculate the metallicity of single stars assuming a metallicity gradient inside each galaxy, that is the metallicity of single stars is log-normally distributed around the mean metallicity of the galaxy with  $\sigma_1 = 0.14$  dex ([Chruslinska et al. 2019](#); see also [Sánchez et al. 2014](#) and [Sánchez-Menguiano et al. 2016](#)).

Figure 4.3 shows the MZR and the FMR averaged over the SFR for six different redshift bins. While at  $z \lesssim 2$  the two relations give almost identical results, at  $z \gtrsim 3$  the MZR yields a rapid evolution of the metallicity, resulting in much lower values than those obtained from the FMR.

Figure 4.4 shows the resulting metallicity-dependent SFR density,  $\text{SFRD}(z, Z)$ , for each of the aforementioned models. Both the FMR and MZR produce a non-negligible fraction of metal-poor star formation ( $\log_{10} Z \leq -3$ ), both at high and low redshift. The fraction of metal-poor star formation increases if we assume lower values of  $M_{\min}$ , because smaller galaxies are also more metal poor. The metallicity associated with the highest value of the  $\text{SFRD}(z, Z)$  drops at high redshift if we assume the MZR or the metallicity model in [Santoliquido et al. \(2020\)](#), while it decreases very mildly for the FMR, in agreement with [Chruślińska et al. \(2021\)](#) and [Boco et al. \(2021\)](#).

---

that the FMR might hold up to redshift  $z \sim 8$  ([Curti et al., 2022](#)).

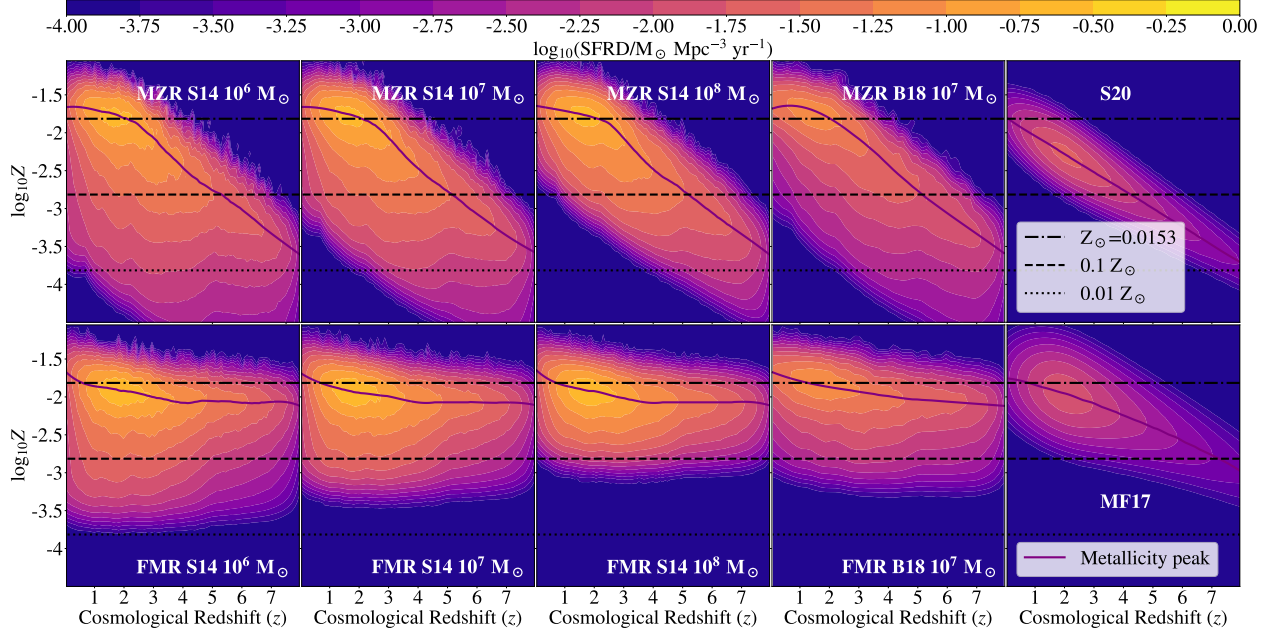


Figure 4.4: Distribution of the SFR density per metallicity bin,  $\text{SFRD}(z, Z)$ , resulting from GALAXY $\mathcal{R}$ ATE (Section 4.2.2) and COSMO $\mathcal{R}$ ATE . Starting from the left: the first, second and third columns show the  $\text{SFRD}(z, Z)$  obtained with S14, where we varied the minimum sampled stellar mass from the GMSF:  $M_{\min} = 10^6, 10^7$  and  $10^8 M_\odot$ , respectively. The fourth column shows the  $\text{SFRD}(z, Z)$  obtained with B18 and  $M_{\min} = 10^7 M_\odot$ . The four upper (lower) leftmost panels show the results obtained with the MZR (FMR). The rightmost column shows the  $\text{SFRD}(z, Z)$  obtained with COSMO $\mathcal{R}$ ATE , adopting the average metallicity evolution described in S20 and MF17 in the upper and lower panel, respectively. The purple solid line in all panels shows the metallicity associated with the highest value of the  $\text{SFRD}(z, Z)$  as a function of redshift.

## Passive galaxies

In our model, we generate the mass distribution of passive galaxies from the GSMF by Ilbert et al. (2013), by adopting a double Schechter function (Pozzetti et al., 2010):

$$\phi(M_*) dM_* = e^{-\frac{M_*}{M_{\text{cut}}}} \left[ \phi_1 \left( \frac{M_*}{M_{\text{cut}}} \right)^{\alpha_1} + \phi_2 \left( \frac{M_*}{M_{\text{cut}}} \right)^{\alpha_2} \right] \frac{dM_*}{M_{\text{cut}}}, \quad (4.5)$$

where the parameters  $M_{\text{cut}}$ ,  $\phi_1$ ,  $\alpha_1$ ,  $\phi_2$  and  $\alpha_2$  depend on redshift and are defined as in Table 2 of Ilbert et al. (2013). We linearly interpolated them between redshift bins at  $z \leq 3$ . Ilbert et al. (2013) show that the number density of passive galaxies rapidly drops at  $z \sim 3$ . Hence, in our model we assume that the number of passive galaxies is zero at  $z_{\text{max}}^{\text{pass}} = 3$ .

The middle panel of Figure 4.1 shows the stellar mass density of passive galaxies for some redshift bins. The lower panel of the same Figure shows the percentage of passive galaxies with respect to star-forming galaxies as a function of mass for the same redshift bins. Passive galaxies represent the majority of galaxies in the local Universe at high mass ( $M_* > 10^{11} M_\odot$ , Moffett et al. 2016; McLeod et al. 2021). There are several ways in the literature to define passive galaxies and the resulting population can show different properties based on the chosen definition (see, e.g., Donnari et al., 2021). In our fiducial definition, we assume that passive galaxies have a value of the SFR at least one dex below the main sequence, for a given stellar mass (Donnari et al., 2019). For each passive galaxy, we extract a SFR value uniformly distributed between  $\text{SFR}_{\text{min}}^{\text{pass}}$  and  $\text{SFR}_{\text{max}}^{\text{pass}}$ . We assume a fixed value for  $\text{SFR}_{\text{min}}^{\text{pass}} = 10^{-4} M_\odot \text{ yr}^{-1}$ , since it is unlikely that passive galaxies with  $M_* > 10^8 M_\odot$  have lower SFR (Renzini & Peng, 2015). We assume  $\log_{10} \text{SFR}_{\text{max}}^{\text{pass}} = \langle \log_{10} \text{SFR} \rangle_{\text{MS}} - N_{\text{pass}} \sigma_{\text{MS}}$ , where  $\langle \log_{10} \text{SFR} \rangle_{\text{MS}}$  is given by either Equation 4.3 (S14) or Equation 4.4 (B18) depending on which main sequence we assume,  $\sigma_{\text{MS}}$  is the dispersion around the main sequence, and  $N_{\text{pass}} = \text{int}(1/\sigma_{\text{MS}})$ . Thus in the case of S14 (B18)  $N_{\text{pass}} = 5$  (3). With this definition of  $\text{SFR}_{\text{max}}^{\text{pass}}$ , passive galaxies have maximum SFR  $\approx 1$  dex below the main sequence. We estimate the average metallicity of passive galaxies either with the MZR or the FMR.

Here, we assume for simplicity that a passive galaxy cannot be the FG of the stellar progenitors of BCO mergers. This is a reasonable assumption, because the total SFR happening in passive galaxies in the local Universe is  $< 3\%$  of the total SFR. However, BCO mergers can take place in passive galaxies, because the delay time  $t_{\text{del}}$  between the formation and the merger of a binary system can be several Gyr long: the FG might become a passive galaxy during  $t_{\text{del}}$  and/or might merge together with a passive galaxy.

### 4.2.3 Merger rate density

To evaluate the merger rate density we proceed in a similar way as in Mapelli et al. (2017) (see also Mapelli & Giacobbo 2018; Artale et al. 2019). At each time step  $\Delta t$ , we associate to each galaxy in our sample a total mass  $M_{\text{new}}(z) = \text{SFR}(z) \Delta t$  of newly formed stars, by randomly sampling a population of stars with total zero-age main sequence mass  $M_{\text{new}}$  from our population synthesis simulations. The metallicity distribution of these randomly

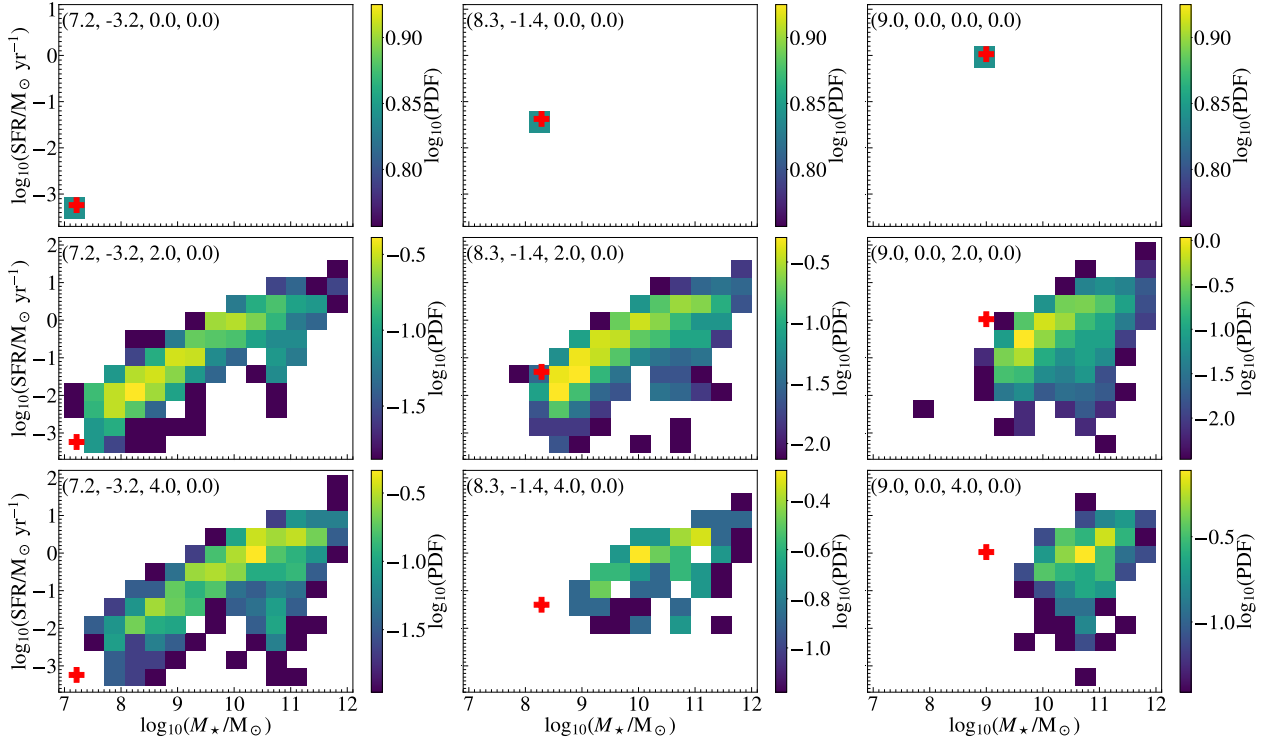


Figure 4.5: Conditional probability  $\mathcal{P}(\text{M}_{\text{host}}, \text{SFR}_{\text{host}} | \text{M}_{\text{form}}, \text{SFR}_{\text{form}}, z_{\text{form}}, z_{\text{merg}})$  evaluated adopting the merger tree of the EAGLE cosmological simulation, for various properties of the FGs, annotated at the top of each panel following the order  $(\log_{10}(\text{M}_{\text{form}}/\text{M}_{\odot}), \log_{10}(\text{SFR}_{\text{form}}/\text{M}_{\odot} \text{ yr}^{-1}), z_{\text{form}}, z_{\text{merg}})$ . The red cross marks the location of the FG at  $z_{\text{form}}$ . In this plot  $z_{\text{merg}} = 0$ .

sampled stars is the same as the metallicity distribution of the entire FG<sup>3</sup> at redshift  $z$ . This procedure allows us to associate the BCOs that form from this stellar population in our MOBSE simulations to their FG at a given formation redshift. Hereafter, we indicate with  $t_{\text{form}}$  ( $z_{\text{form}}$ ) the time (redshift) at which the progenitor stars of a BCO are associated with their FG. Each BCO merges at a time  $t_{\text{merg}}$ , which is estimated as  $t_{\text{merg}} = t_{\text{form}} - t_{\text{del}}$ . Here, both  $t_{\text{merg}}$  and  $t_{\text{form}}$  are expressed in terms of look-back times, while  $t_{\text{del}}$  is the delay time.

To evaluate the global cosmic merger rate density at a given redshift  $z_{\text{merg}}$ , we simply divide the total number of mergers happening at  $z_{\text{merg}}$  in all the considered galaxies, by the total comoving volume  $V$ . For each considered galaxy, we also calculate a merger rate per galaxy  $n_{\text{GW}}$ , i.e. the number of compact objects merging in that galaxy per unit time.

#### 4.2.4 Host galaxy (HG)

According to our definition, the HG of a BCO is the galaxy where the BCO merges. The HG can be the same as the FG, if the binary system forms and merges in the same galaxy,

<sup>3</sup>This might overestimate the contribution of metal-poor stars, as newly born stars are generally more metal-rich than previous star formation episodes (e.g., Peeples et al., 2014).

but it can also be different from the FG, if for example the FG has undergone galaxy-galaxy mergers by the time the two compact objects reach coalescence. Furthermore, even if the BCO forms and merges in the same galaxy, the mass, SFR and metallicity of the galaxy might change significantly after  $t_{\text{del}}$ .

To reconstruct the merger history of galaxies in `GALAXYRATE` we used the information from a merger tree. A merger tree encodes the entire assembly history and property evolution of each single galaxy across cosmic time (e.g., [McAlpine et al., 2016](#); [Qu et al., 2017](#)). Here, we show the results of the merger trees taken from the EAGLE cosmological simulation ([Schaye et al., 2015](#)), but `GALAXYRATE` can use any other possible merger trees obtained from cosmological simulations or semi-analytical models.

One of the main purposes of our new approach is to build a fast tool, thus we compressed the information contained in multiple merger trees, by evaluating the conditional probability  $\mathcal{P}(M_{\text{host}}, \text{SFR}_{\text{host}} | M_{\text{form}}, \text{SFR}_{\text{form}}, z_{\text{form}}, z_{\text{merg}})$ , i.e. the probability that the HG of the BCO merger has mass  $M_{\text{host}}$  and star formation rate  $\text{SFR}_{\text{host}}$ , given the mass ( $M_{\text{form}}$ ) and SFR ( $\text{SFR}_{\text{form}}$ ) of the FG, and given the formation ( $z_{\text{form}}$ ) and merger redshift ( $z_{\text{merg}}$ ) of the BCO. We evaluate the conditional probability

$\mathcal{P}(M_{\text{host}}, \text{SFR}_{\text{host}} | M_{\text{form}}, \text{SFR}_{\text{form}}, z_{\text{form}}, z_{\text{merg}})$  in an empirical way, directly from the merger trees. We count the number of galaxies at a fixed  $z_{\text{merg}}$  that are inside each bin in the  $(M_{\text{host}}, \text{SFR}_{\text{host}})$  plane, by keeping fixed the condition on  $M_{\text{form}}$ ,  $\text{SFR}_{\text{form}}$  and  $z_{\text{form}}$ . Figure 4.5 shows some examples of this conditional probability, in which we compare different values of the formation redshift  $z_{\text{form}}$  and different properties of the FGs. If the FG has no time to evolve between the formation and merger of the BCO (short  $t_{\text{del}}$ ), the properties of the HG remain the same (upper row) as those of the FG, while if the FG has more time to evolve (long  $t_{\text{del}}$ ) then the HG can be very different from the FG (lower rows).

Once we have defined the conditional probability, we sample one HG for each FG. Thereafter, we link each sampled HG from the merger trees to one and only one galaxy obtained through the observational scaling relations, considering both star-forming galaxies (Section 4.2.2) and passive galaxies (Section 4.2.2). Finally, to calculate the merger rate per galaxy at a given merger redshift  $z_{\text{merg}}$ , we sum up all the mergers of compact objects formed at any  $z_{\text{form}}$  and merging at  $z_{\text{merg}}$  in the same galaxy.

The conditional probabilities in Figure 4.5 show that, in some cases, the stellar mass of the HG might be smaller than the stellar mass of the FG. This happens for two reasons. In most cases, different physical mechanisms such as strong galactic outflows or galaxy interactions producing tidal stripping can reduce the stellar mass of the galaxies (see e.g., [Mac Low & Ferrara, 1999](#); [Efstathiou, 2000](#); [Hopkins et al., 2012](#)). In other cases, the subfind algorithm might misclassify the star particles belonging to a given galaxy. This issue is more common at the pericenter of a subhalo orbiting a larger halo (see e.g., [Muldrew et al., 2011](#); [Knebe et al., 2011](#)).

Section	Parameter/Model	Value(s)/Choice(s)	Reference(s)
<a href="#">4.2.1</a>	Core Collapse SN	Rapid	<a href="#">Fryer et al. (2012)</a>
	Natal Kicks	$v_{\text{kick}} \propto m_{\text{ej}}/m_{\text{rem}} v_{\text{H05}}$	<a href="#">Giacobbo &amp; Mapelli (2020)</a>
	$\alpha$ Common Envelope	1, 3 and 5	<a href="#">Webbink (1984)</a>
	$\lambda$ Common Envelope	Depends on star properties	<a href="#">Claeys et al. (2014)</a>
	Primary star IMF	Kroupa with $M \in [5, 150] M_{\odot}$	<a href="#">Kroupa (2001)</a>
	Mass ratio	$\mathcal{F}(q) \propto q^{-0.1}$	<a href="#">Sana et al. (2012)</a>
	Orbital period	$\mathcal{F}(\Pi) \propto \Pi^{-0.55}$	<a href="#">Sana et al. (2012)</a>
	Eccentricity	$\mathcal{F}(e) \propto e^{-0.42}$	<a href="#">Sana et al. (2012)</a>
	Progenitor metallicity	$Z \in [0.0002, 0.02]$	<a href="#">Giacobbo &amp; Mapelli (2018)</a>
<a href="#">4.2.2</a>	Star-forming GSMF	Single Schechter	<a href="#">Chruslinska et al. (2019)</a>
	$M_{\min}$	$10^6, 10^7, 10^8 M_{\odot}$	<a href="#">Conselice et al. (2016)</a>
	$\alpha_{\text{GSMF}}$	constant, varying with $z$	<a href="#">Chruslinska et al. (2019)</a>
	$z_{\max}$	8	<a href="#">Ilbert et al. (2013)</a>
<a href="#">4.2.2</a>	$A_{\text{MS}}$	$0.969^{+0.004}_{-0.006}$	<a href="#">Sargent et al. (2012)</a>
	$\langle \log_{10} \text{SFR} \rangle_{\text{MS}}$	S14; B18	<a href="#">Speagle et al. (2014); Boogaard et al. (2018)</a>
	$\sigma_{\text{MS}}$	$0.188^{+0.003}_{-0.003}, 0.3$	<a href="#">Sargent et al. (2012); Chruslinska et al. (2019)</a>
	$A_{\text{SB}}$	$0.031^{+0.006}_{-0.004}$	<a href="#">Sargent et al. (2012)</a>
	$\langle \log_{10} \text{SFR} \rangle_{\text{SB}}$	$\langle \log_{10} \text{SFR} \rangle_{\text{MS}} + 0.59^{+0.06}_{-0.13}$	<a href="#">Sargent et al. (2012)</a>
	$\sigma_{\text{SB}}$	$0.243^{+0.078}_{-0.047}$	<a href="#">Sargent et al. (2012)</a>
<a href="#">4.2.2</a>	Metallicity relation	MZR; FMR	<a href="#">Chruslinska et al. (2019); Mannucci et al. (2011)</a>
	$Z_{\odot}$	0.0153	<a href="#">Caffau et al. (2011)</a>
	$\sigma_0$	0.05; 0.15; 0.30	<a href="#">Boco et al. (2021)</a>
	$\sigma_1$	0.00001; 0.14; 0.30	<a href="#">Chruslinska et al. (2019)</a>
	Metallicity calibration	Photoionization models; $T_e$ -based	<a href="#">Maiolino et al. (2008); Curti et al. (2020)</a>
<a href="#">4.2.2</a>	Passive GSMF	Double Schechter	<a href="#">Ilbert et al. (2013)</a>
	$z_{\max}^{\text{pass}}$	3	<a href="#">Ilbert et al. (2013)</a>
	$\text{SFR}_{\max}^{\text{pass}}$	1 dex below the adopted MS	<a href="#">Donnari et al. (2019)</a>
	$\text{SFR}_{\min}^{\text{pass}}$	$10^{-4} M_{\odot} \text{ yr}^{-1}$	<a href="#">Renzini &amp; Peng (2015)</a>
<a href="#">4.2.4</a>	Merger trees	EAGLE	<a href="#">Schaye et al. (2015)</a>

Table 4.1: Parameters and models adopted in this version of GALAXYRATE. S14 and B18 refer to [Speagle et al. \(2014\)](#) and [Boogaard et al. \(2018\)](#), respectively. For the MZR we adopt the definition in [Mannucci et al. \(2009\)](#) and [Chruslinska et al. \(2019\)](#). For the FMR, we adopt the definition in [Mannucci et al. \(2011\)](#).

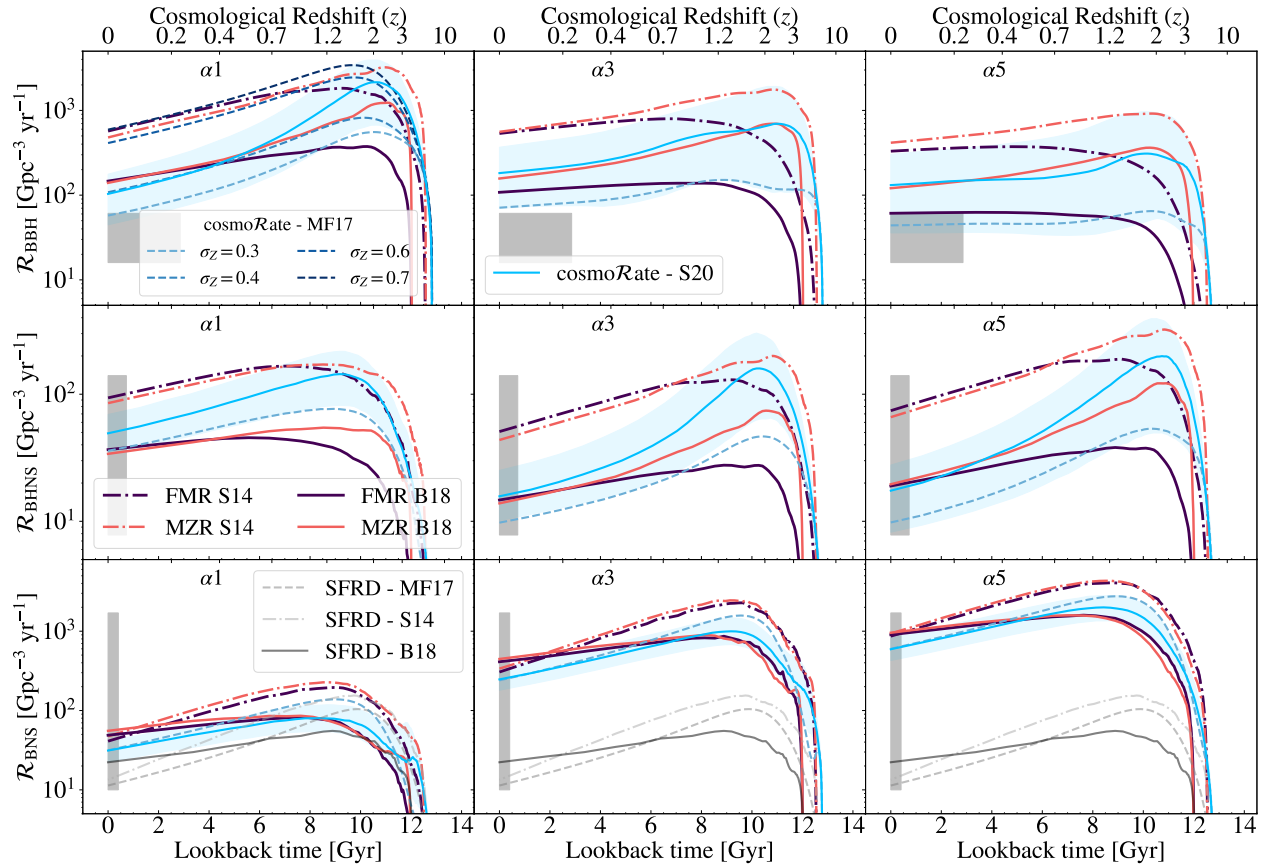


Figure 4.6: Evolution of the merger rate density  $\mathcal{R}(z)$  in the comoving frame as a function of the look-back time (lower  $x$ -axis) and of the cosmological redshift (upper  $x$ -axis), for  $\alpha = 1, 3, 5$  (columns) and for BBHs, BHNSs and BNSs (rows). Here, we show the results obtained with  $M_{\min} = 10^7 M_{\odot}$  for two different metallicity evolution models (MZR in red and FMR in blue) and for two definitions of the star-forming main sequence (B18, solid lines, and S14, dash-dotted lines). The solid and dashed light blue lines are the merger rate densities obtained with `COSMO RATE`, assuming the average metallicity evolution in S20 and MF17, respectively. For the model MF17 with  $\alpha = 1$ , we evaluated the merger rate density of BBHs (upper left-hand panel) with different values of  $\sigma_Z = 0.3, 0.4, 0.6$  and  $0.7$ . In the other panels, we fix  $\sigma_Z = 0.3$  for the model M17. The shaded light-blue areas are the 50% credible intervals of the S20 model considering the uncertainties on metallicity. For BBHs, BHNSs and BNSs the gray shaded areas shows the 90% credible interval of the local merger rate density (Abbott et al., 2021b). The width of the shaded areas on the  $x$ -axis corresponds to the instrumental horizon obtained by assuming BBHs, BHNS, BNSs of mass  $(30, 30)$ ,  $(10, 1.4)$  and  $(1.4, 1.4) M_{\odot}$ , respectively, and O3 sensitivity (Abbott et al., 2018). The dashed gray line in the lower panels is the total cosmic SFR density from MF17. The solid and dashed-dotted gray lines are the cosmic SFR densities derived from B18 and S14 star-forming main sequences, respectively.

## 4.3 Results

### 4.3.1 Merger rate density

Figure 4.6 shows the evolution of the merger rate density  $\mathcal{R}(z)$  for three different values of the  $\alpha$  parameter, for the two main sequence models (B18 and S14) and for the two metallicity relations (FMR and MZR). In this Figure, we also compare the results obtained with `COSMORATE` and those obtained with the new code `GALAXYRATE`. For each value of the common envelope efficiency  $\alpha$ , `GALAXYRATE` produces a higher local merger rate density of BBHs and BHNSs with respect to the model MF17, that we obtained with `COSMORATE` assuming the average metallicity evolution from [Madau & Fragos \(2017\)](#) and a metallicity spread  $\sigma_Z = 0.3$ . This springs from the interplay of two factors. First, BBHs and BHNSs merge more efficiently if they have metal-poor progenitors in our population-synthesis models (Appendix 4.6.1). Second, the SFRD( $z, Z$ ) distribution of `GALAXYRATE` yields a longer tail of low-metallicity star formation at different redshifts with respect to `COSMORATE` (Figure 4.4). The differences between the BBH merger rate density obtained with `GALAXYRATE` and `COSMORATE` (model M17) can be reconciled by assuming a larger metallicity spread  $\sigma_Z > 0.4$  in `COSMORATE`.

The dependence of the BBH/BHNS merger rate on metallicity also appears when we vary both the main sequence definition and the metallicity relation. We have already seen that with B18 the SFR density at redshift  $z \sim 2$  is  $\sim 0.5$  dex lower with respect to S14 (Figure 4.2). Thus, B18 quenches the formation of BBHs and BHNSs at high redshift. As a result, the merger rate density of BBHs evaluated with B18 and  $\alpha = 1$  is  $\sim 4$  times lower with respect to S14 in the local Universe.

The merger rate density of BBHs and BHNSs in the local Universe is almost the same if we adopt the MZR or the FMR. However, the two scaling relations (MZR and FMR) produce a completely different slope of the merger rate density of BBHs at  $z \gtrsim 1$ . For  $\alpha = 5$ , the merger rate density of BBHs almost decreases between  $0 < z < 2$ , if we assume the FMR. This happens because the case with  $\alpha = 5$  has the longest delay times (Appendix 4.6.1) and the FMR yields only a mild decrease of the average metallicity with redshift (Figure 4.3).

In contrast, the merger rate density of BNSs does not depend on the adopted metallicity relation. Figure 4.6 (lower panel) shows the three cosmic SFR densities we took in account in this work. The merger rate density of BNSs approximately scales with the adopted cosmic SFR density, because in our population-synthesis models the BNSs are almost independent of metallicity and their delay times are predominantly short (e.g., [Dominik et al., 2012, 2013](#); [Klencki et al., 2018](#); [Mapelli & Giacobbo, 2018](#); [Mapelli et al., 2019](#); [Neijssel et al., 2019](#); [Santoliquido et al., 2021](#)). In Appendix 4.6.3, we also discuss the impact of the minimum galaxy stellar mass on the merger rate density.

The merger rate density of BNSs and BHNSs is within the 90% credible interval estimated by the LVK with GWTC-3 ([Abbott et al., 2021b](#)) for all considered assumptions, while the merger rate density of BBHs predicted by our models is higher than the LVK range. This discrepancy is the consequence of several factors. Firstly, here we assumed that all BBHs form via unperturbed binary evolution. Considering alternative channels might significantly affect the merger rate evolution (e.g., [Mapelli et al., 2022](#)). Furthermore, current binary evo-

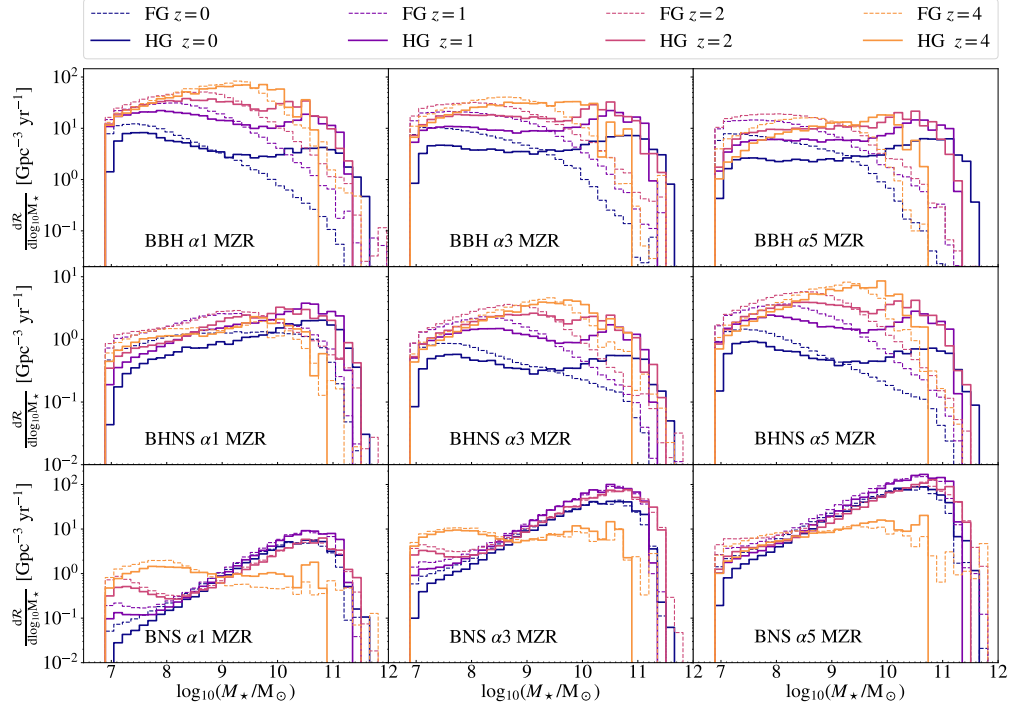


Figure 4.7: Distribution of the merger rate density for four different redshifts as a function of the formation galaxy (FG) mass (dashed lines) and host galaxy (HG) mass (solid lines), assuming the MZR. The different colours refer to redshift  $z = 0, 1, 2$ , and  $4$ .

lution models might overestimate the merger rate of BBHs and its dependence on metallicity, because of the large uncertainties they are affected by (e.g., Gallegos-Garcia et al., 2021; Belczynski et al., 2022). Finally, the measurement of gas and star metallicity is affected by large uncertainties, especially at high redshift (e.g., Maiolino & Mannucci, 2019).

The merger rate density of BCOs likely extends to a redshift higher than the maximum value we considered in this work ( $z_{\text{max}} = 8$ ). Here, we do not consider  $z > 8$  because we prefer to avoid to arbitrarily extrapolate the observational relationships at higher redshift. Furthermore, the merger rate density at  $z \gtrsim 8$  is likely dominated by population III stars (e.g., Inayoshi et al., 2017; Liu & Bromm, 2021; Ng et al., 2021; Tanikawa et al., 2021b), which are not included in our formalism. We will include them in a follow-up study.

### 4.3.2 Formation and host galaxies across cosmic time

In this Section, we look at the distribution of HG properties, namely stellar mass, SFR and metallicity. We compare them with the distribution of FGs. For the sake of brevity, we show the results only for the definition of galaxy main sequence in B18.

#### Stellar Mass

Figures 4.7 and 4.8 show the mass distribution of FGs (dashed lines) and HGs (solid lines) for the MZR and the FMR, respectively. The time elapsed between compact-object formation

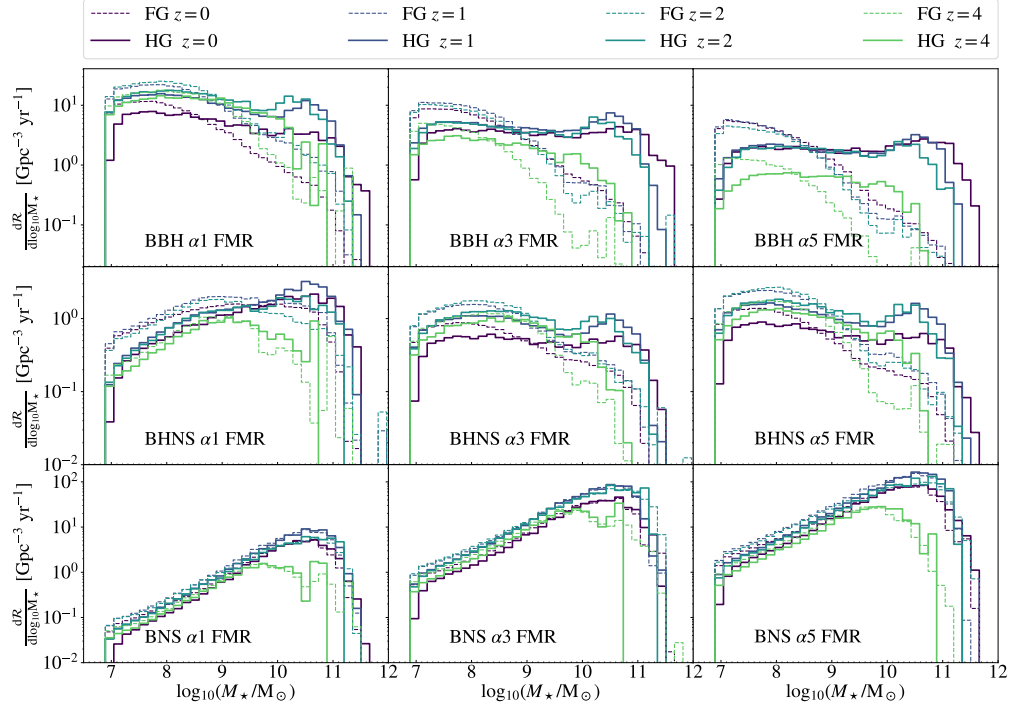


Figure 4.8: Same as Fig. 4.7, but for the FMR.

and merger spans from a few Myr to several Gyr (Appendix 4.6.1). Hence, the HG might show significantly different properties with respect to the FG, not only because the original FG might have merged into a larger galaxy, but also because the FG might have drastically evolved (in terms of mass, SFR and metallicity) from the formation to the merger epoch of the BCO.

In the case of BNSs, the mass of the HG is always very similar to that of the FG, because BNSs merge with a short delay time and are not affected by metallicity. In contrast, the FGs of BBHs and BHNSs tend to be less massive than the HGs. This happens because many FGs merge with other galaxies by the time of the BBH/BHNS coalescence. The HGs in the local Universe are more massive than in any other previous epochs.

The fraction of high-mass HGs increases with increasing  $\alpha$ . In fact,  $\alpha = 5$  corresponds to longer delay times on average. If the delay times are longer, the FGs have more time to merge with other galaxies and form more massive HGs. On the other hand, both Figure 4.7 and 4.8 show that a large fraction of BBH HGs are low-mass galaxies. This is more important for  $\alpha = 1$ , which corresponds to shorter delay times. Hence, the HG mass distribution is shaped by the delay time distribution of compact objects, consistently with the result of previous authors (e.g., Mapelli & Giacobbo, 2018; Artale et al., 2019, 2020a; McCarthy et al., 2020).

The HG mass distributions of both BBHs and BHNSs depend on the adopted metallicity model. At  $z \gtrsim 2$  the normalisation of the distribution is higher if we consider the MZR. This was also evident by looking at Figure 4.6, where at  $z \gtrsim 2$  the MZR yields many more BBH mergers than the FMR.

Finally, the HGs of BNSs tend to be more massive than the HGs of both BHNSs and

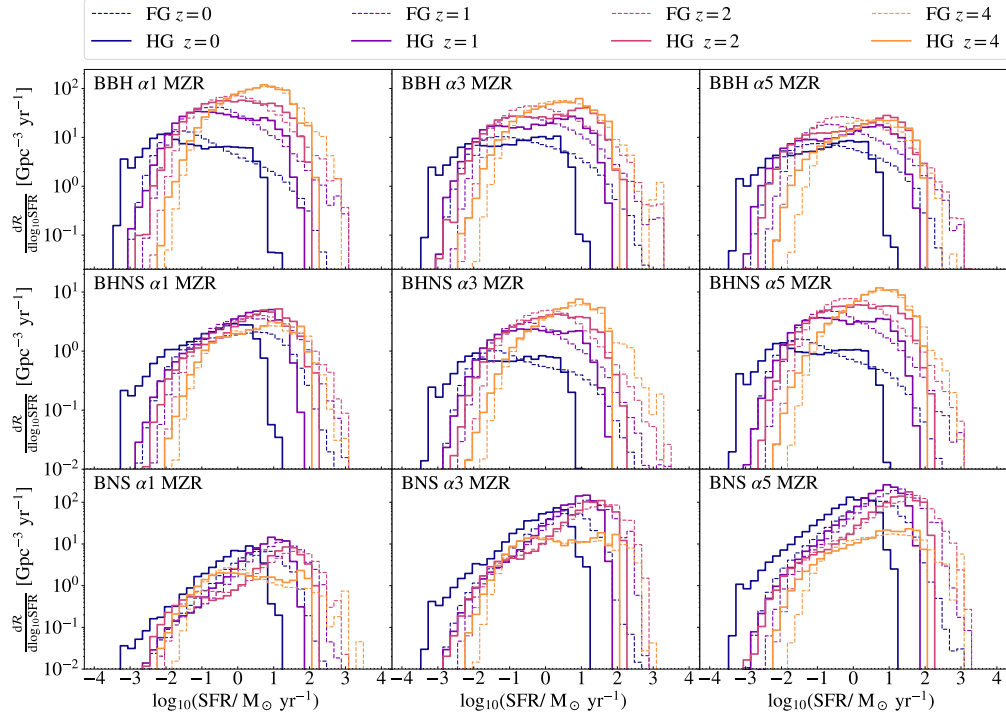


Figure 4.9: Distribution of the merger rate density for four different redshifts ( $z = 0, 1, 2$  and  $4$ ) as a function of the SFR of the FGs (dashed lines) and HGs (solid lines), assuming the MZR.

BBHs, at least at  $z < 4$ . The reason is that BNSs are insensitive to metallicity, while BHNSs and BBHs form predominantly in metal-poor (hence, smaller) galaxies. Both the FMR and the MZR predict that metal-poor galaxies are generally less massive than metal-rich ones.

### Star formation rate (SFR)

We show the SFR distribution of FGs and HGs in Figure 4.9 for the MZR and Figure 4.10 for the FMR. At lower redshifts, compact objects tend to form and merge in galaxies with lower SFR. The reason is that low-redshift galaxies have lower SFR on average, as shown in Figure 4.2. At higher redshift ( $z > 1$ ), the SFR distribution of FGs and HGs are very similar, since the delay times are short.

At  $z = 4$ , the SFR of FGs and HGs of BBHs peaks at lower values when we assume the FMR than in the case of the MZR. The reason is that the metallicity of massive and high star-forming galaxies is high enough to quench the formation of BBHs already at high redshift, if we assume the FMR. The common envelope parameter  $\alpha$  affects only the normalisation of the distributions.

### Metallicity

Figure 4.11 (Figure 4.12) shows the metallicity distribution of FGs and HGs we obtain if we adopt the MZR (FMR). The main difference between Figure 4.11 and 4.12 is that the

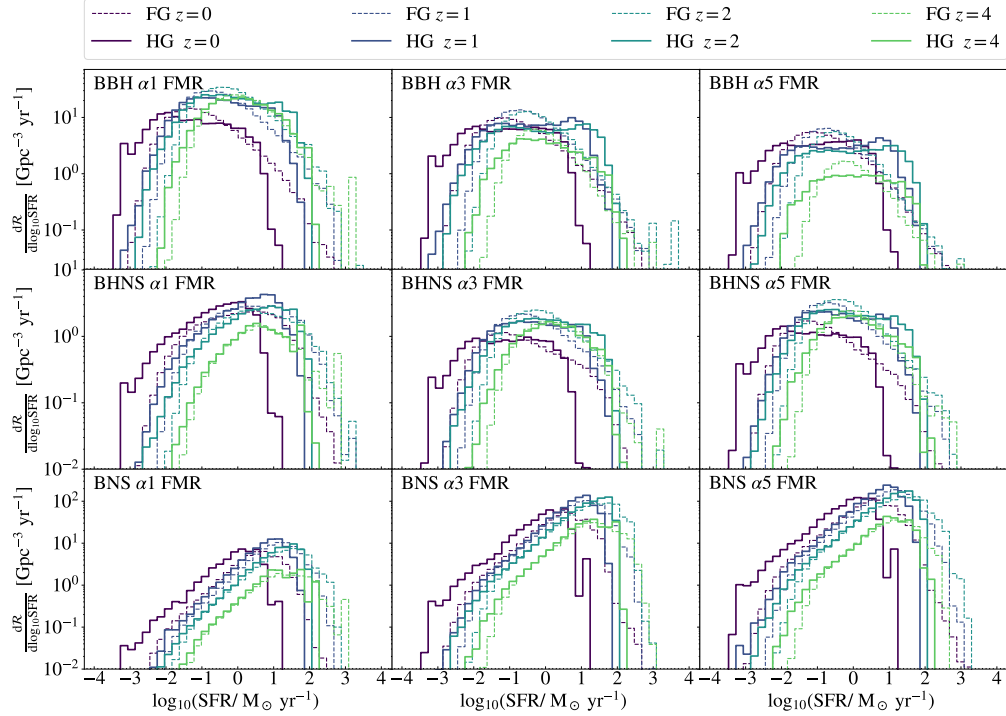


Figure 4.10: Same as Fig. 4.9, but for the FMR.

distributions of both FGs and HGs extend to very low-metallicity tails in the case of the MZR, while they are truncated at  $\log_{10} Z \approx -3.5$  in the case of the FMR.

For both the MZR (Figure 4.11) and FMR (Figure 4.12), the metallicity of the HG tends to be higher than the metallicity of the FG, because the average metallicity of the Universe increases as redshift decreases (Figure 4.4). The metallicity difference between HGs and FGs is particularly large for BBHs and BHNSs, which merger efficiency depends on metallicity, while it is negligible for BNSs.

Overall, BBHs tend to form in metal-poor galaxies and merge in metal-rich galaxies. This is particularly evident in the local Universe. In the case of BNSs, the peak of the metallicity distribution of FGs and HGs almost coincide.

### 4.3.3 Merger rate per galaxy

Figure 4.13 shows the merger rate per galaxy  $n_{\text{GW}}$  as function of the stellar mass. We compare our results to those of Artale et al. (2019) and Artale et al. (2020a), who adopt the EAGLE cosmological simulation to retrieve this information. The merger rate of BNSs strongly correlates with the stellar mass of the HG. The correlation slope (Table 4.2) is consistent with that obtained by Artale et al. (2020a) with cosmological simulations in the case of BNSs. To interpret this result, in Figure 4.13 we show the main sequence definition by B18, with an arbitrary normalisation. It is apparent that the correlation of  $n_{\text{GW}}$  with the stellar mass is mainly a consequence of the main sequence of star-forming galaxies.

Deviations from the main sequence are particularly evident in the case of BBHs and

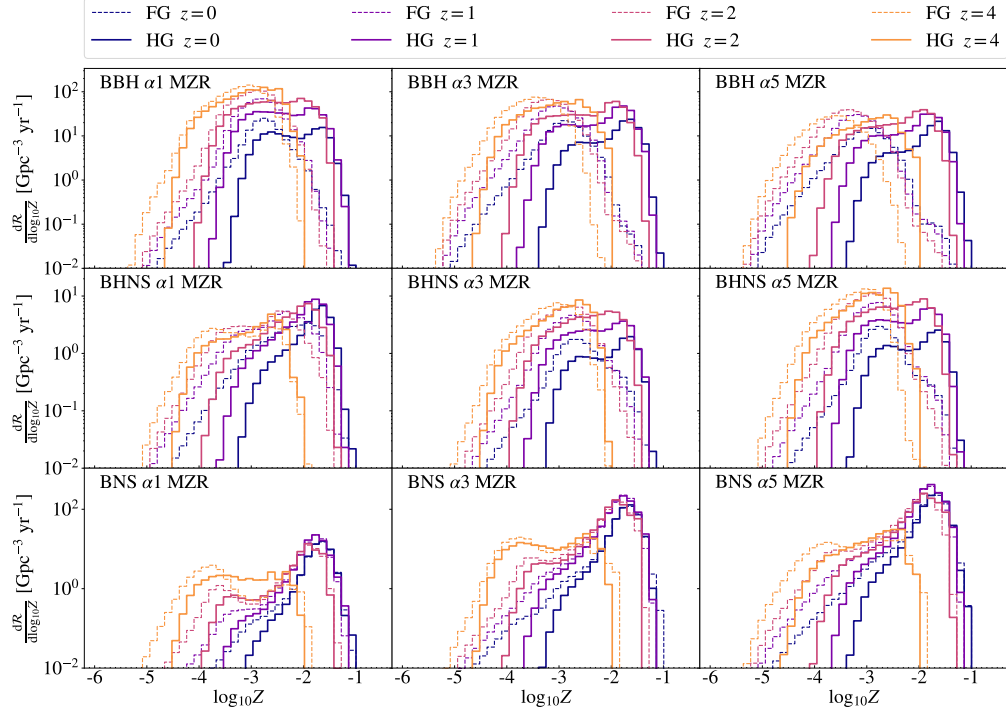


Figure 4.11: Distribution of the merger rate density for four different redshifts ( $z = 0, 1, 2$ , and  $4$ ) as a function of the FG metallicity (dashed lines) and HG metallicity (solid lines), assuming the MZR.

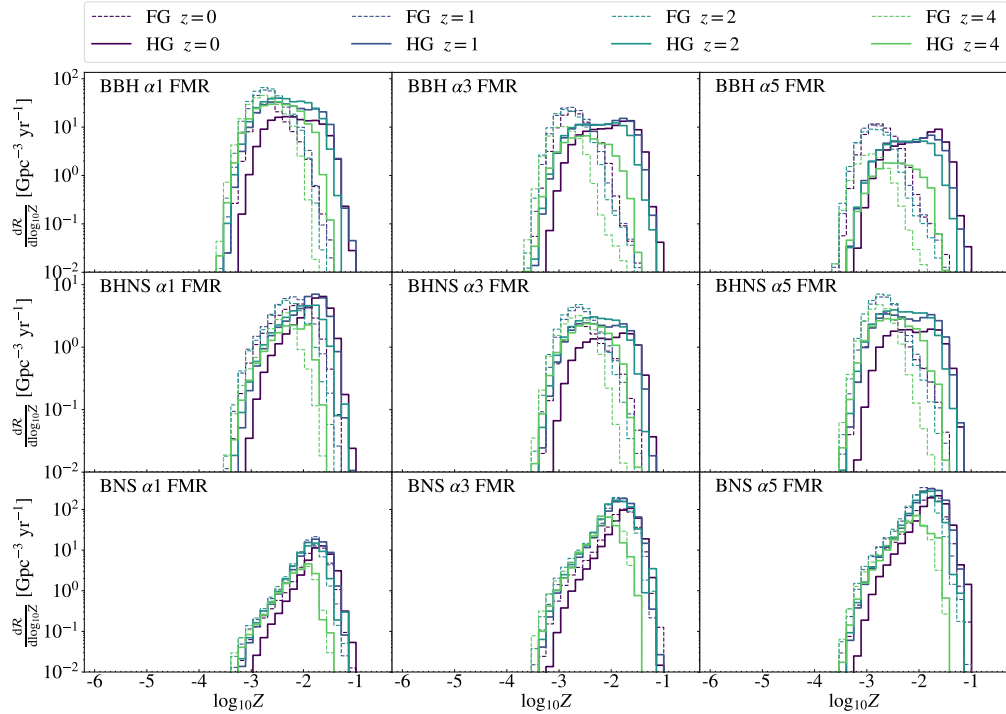


Figure 4.12: Same as Fig. 4.11 but for the FMR.

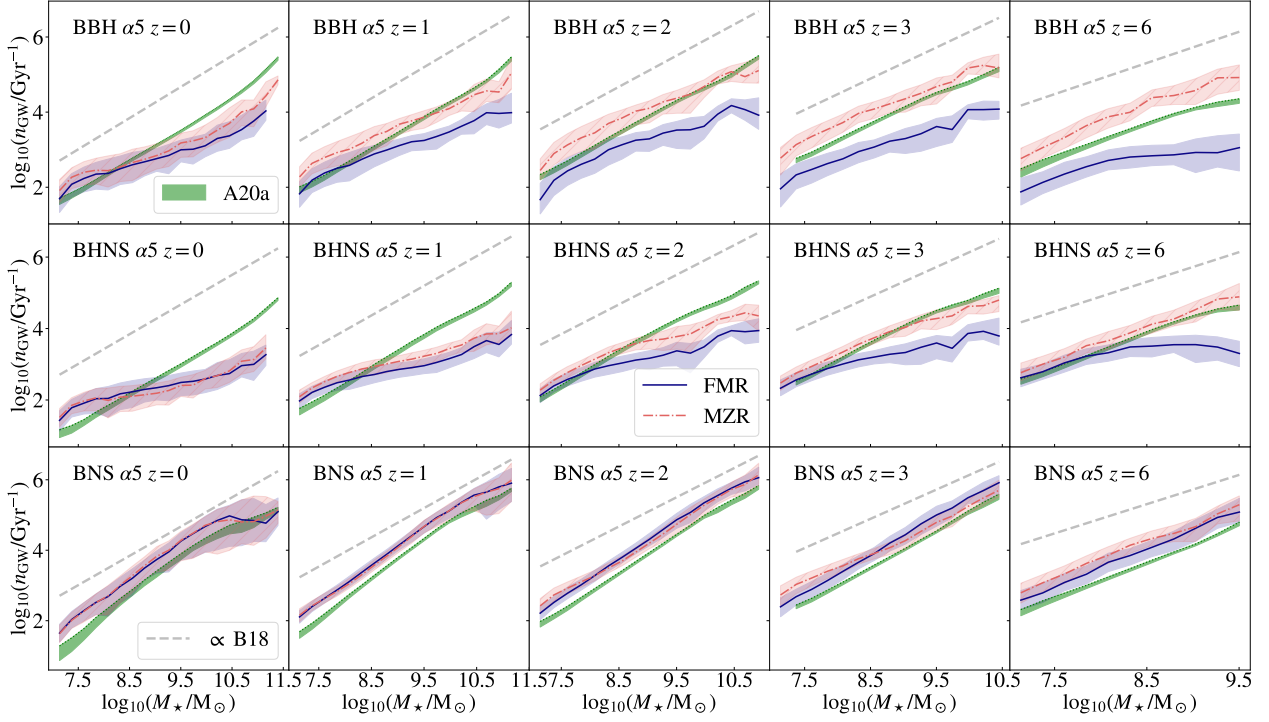


Figure 4.13: From left to right: median value of the merger rate per galaxy ( $n_{\text{GW}}$ ) as a function of the stellar mass  $M_*$  for the HGs of BBHs (upper panels), BHNSs (middle panels) and BNSs (lower panels), for  $z_{\text{merg}} = 0, 1, 2, 3$  and 6. The MZR and FMR are shown in red and blue, respectively. The shaded areas are the 75th and 25th percentiles of the distribution of  $n_{\text{GW}}$  for each stellar mass bin. The dashed gray lines show the B18 main sequence definition with arbitrary normalisation. The green shaded areas are the results of Artale et al. (2020a, A20a).

		$z = 0$		$z = 1.0$		$z = 2.0$		$z = 3.0$		$z = 6.0$	
		$a$	$b$	$a$	$b$	$a$	$b$	$a$	$b$	$a$	$b$
BBH	FMR	-1.5 ± 0.2	0.47 ± 0.02	-1.5 ± 0.2	0.50 ± 0.02	-1.9 ± 0.4	0.56 ± 0.04	-2.2 ± 0.2	0.61 ± 0.03	-1.0 ± 0.5	0.44 ± 0.06
	MZR	-2.3 ± 0.3	0.58 ± 0.03	-1.8 ± 0.2	0.60 ± 0.02	-1.9 ± 0.3	0.66 ± 0.03	-2.2 ± 0.2	0.72 ± 0.03	-3.7 ± 0.4	0.93 ± 0.04
	A20a	-4.5 ± 0.2	0.85 ± 0.02	-4.1 ± 0.1	0.84 ± 0.01	-3.56 ± 0.05	0.83 ± 0.01	-3.1 ± 0.1	0.79 ± 0.01	-3.2 ± 0.2	0.81 ± 0.02
BHNS	FMR	-0.9 ± 0.2	0.36 ± 0.02	-0.8 ± 0.2	0.40 ± 0.02	-0.8 ± 0.2	0.45 ± 0.02	-0.60 ± 0.2	0.44 ± 0.03	0.54 ± 0.66	0.33 ± 0.08
	MZR	-1.1 ± 0.3	0.38 ± 0.03	-0.8 ± 0.1	0.43 ± 0.01	-1.3 ± 0.2	0.53 ± 0.03	-2.2 ± 0.2	0.68 ± 0.03	-3.7 ± 0.2	0.91 ± 0.02
	A20a	-5.0 ± 0.1	0.85 ± 0.01	-4.41 ± 0.07	0.86 ± 0.01	-3.9 ± 0.1	0.85 ± 0.01	-3.7 ± 0.2	0.86 ± 0.02	-3.9 ± 0.2	0.92 ± 0.02
BNS	FMR	-3.9 ± 0.5	0.82 ± 0.05	-4.8 ± 0.2	0.98 ± 0.02	-5.1 ± 0.1	1.04 ± 0.02	-5.29 ± 0.07	1.08 ± 0.01	-5.1 ± 0.1	1.08 ± 0.02
	MZR	-3.9 ± 0.4	0.83 ± 0.05	-4.9 ± 0.2	0.99 ± 0.02	-4.7 ± 0.1	0.99 ± 0.01	-3.5 ± 0.2	0.87 ± 0.02	-4.4 ± 0.2	1.02 ± 0.02
	A20a	-5.3 ± 0.3	0.95 ± 0.03	-5.6 ± 0.2	1.04 ± 0.02	-5.53 ± 0.07	1.05 ± 0.01	-5.27 ± 0.09	1.04 ± 0.01	-5.0 ± 0.1	1.02 ± 0.02

Table 4.2: Fits of the merger rate per galaxy  $\log_{10}(n_{\text{GW}}/\text{Gyr}^{-1}) = a + b \log_{10}(M_*/\text{M}_\odot)$  at  $z = 0, 1, 2, 3$  and 6 for the models shown in Figure 4.13.

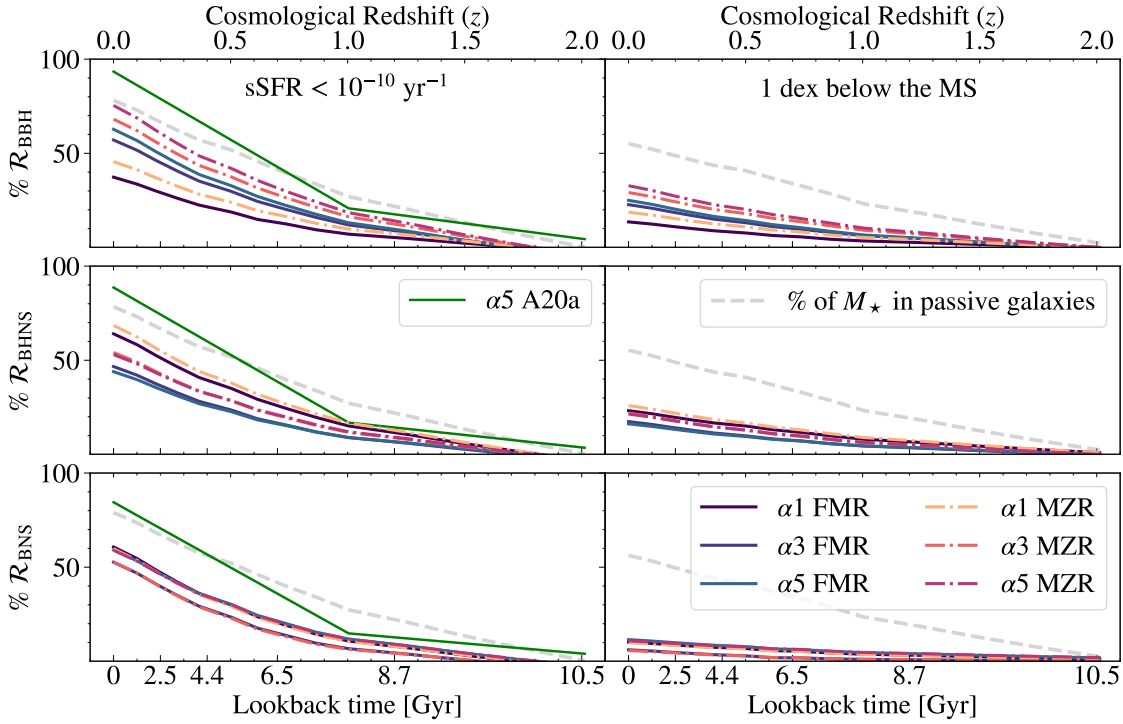


Figure 4.14: Percentage of compact object mergers in passive galaxies for the models considered in this work. Upper, middle and lower panel: BBHs, BHNSs and BNSs. Left-hand column: definition of passive galaxies from Artale et al. (2020a, A20a), i.e. passive galaxies have  $\text{sSFR} < 10^{-10} \text{ yr}^{-1}$ . Green solid line: results from A20a. Right-hand column: our definition of passive galaxies (i.e., galaxies with SFR at least 1 dex below the star-forming main sequence, Section 4.2.2). The grey dashed line is the percentage of stellar mass ( $M_*$ ) stored in passive galaxies as function of redshift, according to the two above-mentioned definitions.

BHNSs. In fact, the merger rate per galaxy of BBHs and BHNSs also depends on the chosen metallicity relation. The merger rates per galaxy obtained with the MZR or FMR are almost identical in the local Universe, but become dramatically different at redshift  $z \gtrsim 1$ , in terms of both slope and normalization. This happens because the differences between FMR and MZR increase with redshift (Figure 4.3). In fact, in the case of the FMR the formation of BBHs and BHNSs drops in galaxies with  $M_* > 10^9 M_\odot$  at  $z \geq 4$  (Figure 4.8). As a result, the BBH merger rate per galaxy at  $z = 6$  has a much shallower trend with  $M_*$  in the case of the FMR with respect to the MZR.

#### 4.3.4 Role of passive galaxies

Figure 4.14 shows the percentage of compact object mergers in passive galaxies. Besides our definition of passive galaxies (Section 4.2.2), we also show the definition adopted by Artale et al. (2019), for comparison. According to the definition in Artale et al. (2019), passive galaxies are galaxies with specific SFR (sSFR)  $< 10^{-10} \text{ yr}^{-1}$ . Figure 4.14 shows that the contribution of passive galaxies to the merger rate increases as redshift decreases, for both

definitions. This happens because the percentage of stellar mass stored in passive galaxies increases as we approach the local Universe.

With common envelope efficiency  $\alpha = 5$ , which corresponds to longer delay times, the fraction of BBH mergers in passive galaxies is higher with respect to lower values of  $\alpha$ . The MZR predicts more BBH mergers in passive galaxies at fixed redshift with respect to the FMR, while the fraction of BNS mergers in passive galaxies does not depend on the chosen metallicity evolution.

Figure 4.14 also shows the impact of different definitions of passive galaxies: with the definition adopted in this work, we estimate less than a half (a fifth) of BBH (BNS) mergers in passive galaxies with respect to [Artale et al. \(2020a\)](#).

## 4.4 Discussion

Here, we discuss some of the main assumptions we made in our model and their impact on our results. We will not consider the impact of binary population synthesis parameters, which we have already described in [Santoliquido et al. \(2021\)](#).

### 4.4.1 Constant versus variable GSMF

We assumed that the slope of the GSMF ( $\alpha_{\text{GSMF}}$ ) is constant with redshift. [Chruslinska et al. \(2019\)](#) pointed out that the slope of the low-mass end of the GSMF is weakly constrained. Although the low-mass galaxies are overall the most abundant, they are also the faintest and most difficult to observe, especially at high redshift. Table 1 in [Chruslinska et al. \(2019\)](#) shows that the low-mass slope tends to steepen with redshift. In other words,  $\alpha_{\text{GSMF}}$  in Equation 4.1 becomes more negative at increasing redshift (Figure 3 of [Chruslinska et al. 2019](#)). Figure 4.15 shows the impact of the evolving low-mass slope of GSMF with redshift,  $\alpha_{\text{GSMF}}(z)$ , on the cosmic SFR density and on the merger rate density. For the latter, we show the case of BBHs,  $\alpha = 5$  and MZR to maximise the impact of a higher fraction of metal-poor low-mass galaxies on the merger rate density. The cosmic SFRD varies at most by a factor of 4 at  $z \sim 6$ , resulting in a similar difference at  $z \sim 3.5$  in the merger rate density.

### 4.4.2 Main sequence of star forming and starburst galaxies

We assumed that the star-forming main sequence has no flattening at high masses, i.e. the linear relation is preserved at any value of stellar mass (equations 4.3 and 4.4). [Chruslinska et al. \(2019\)](#) show that there can be two main variations with respect to this assumption. The first variation is referred to as *moderate flattening*. In this case the high-mass end of the main sequence is less steep than that of the low-mass end, and can also evolve with redshift becoming steeper with increasing  $z$  ([Speagle et al., 2014](#); [Boogaard et al., 2018](#); [Popesso et al., 2019](#)). The second variation is called *sharp flattening* and the main sequence has an even sharper flattening at high masses ([Tomczak et al., 2016](#)). The resulting SFR is almost constant with increasing stellar mass (Figure 5 of [Chruslinska et al. 2019](#)). We expect that the impact on our results of the moderate and sharp flattening of the main sequence of

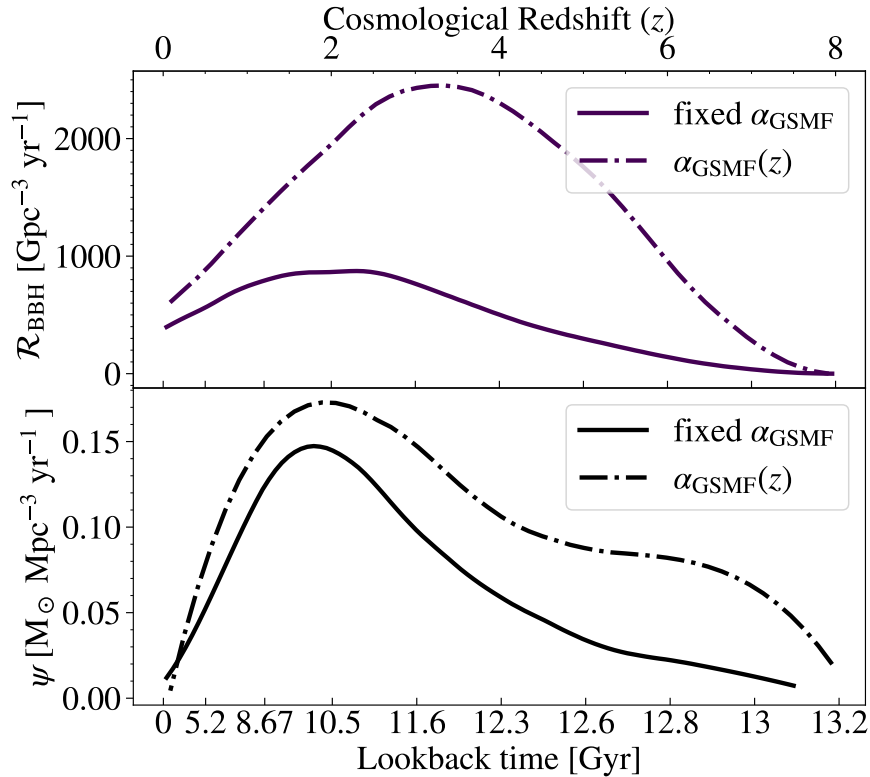


Figure 4.15: Upper panel: Evolution of the BBH merger rate density  $\mathcal{R}_{\text{BBH}}(z)$  calculated with a constant value of  $\alpha_{\text{GSMF}}$  (solid line) and with the value  $\alpha_{\text{GSMF}}(z)$  proposed by [Chruslinska et al. \(2019\)](#) (dot-dashed line). In both cases, we assume  $\alpha = 5$ , MZR, S14 and  $M_{\min} = 10^7 \text{ M}_\odot$ . Lower panel: cosmic SFR density  $\psi(z)$  obtained adopting the two different GSMFs shown in the upper panel.

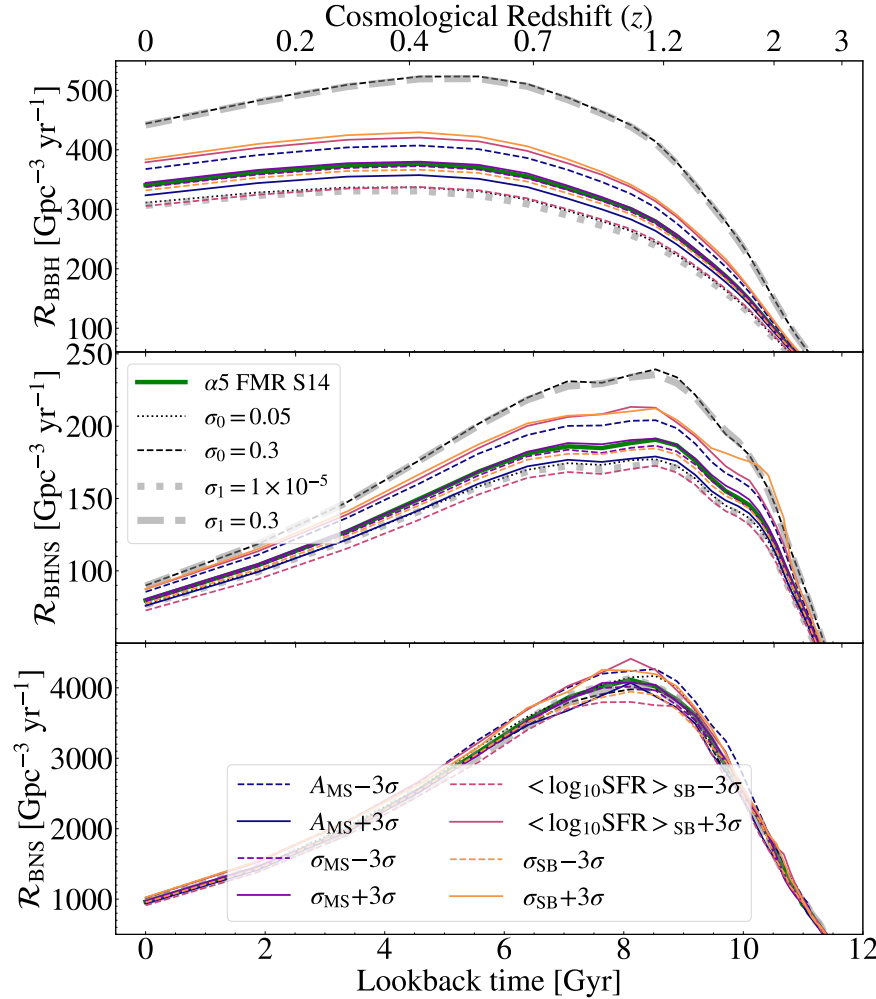


Figure 4.16: Impact of  $\pm 3\sigma$  variation of the parameters in Equation 4.2 on the merger rate density  $\mathcal{R}(z)$  of BBHs (upper panel), BHNSs (middle panel), and BNSs (lower panel). We assume, as reference,  $\alpha = 5$ , FMR, S14 and  $M_{\min} = 10^7 M_\odot$  with  $\sigma_0 = 0.15$  and  $\sigma_1 = 0.14$  (thin green line). Solid and dashed dark-blue lines:  $A_{\text{MS}} \pm 3\sigma$ ; solid and dashed violet lines:  $\sigma_{\text{MS}} \pm 3\sigma$ ; solid and dashed pink lines:  $\langle \log_{10} \text{SFR} \rangle_{\text{SB}} \pm 3\sigma$ ; solid and dashed orange lines:  $\sigma_{\text{SB}} \pm 3\sigma$ ; thin dotted and dashed black lines:  $\sigma_0 = 0.05$  and  $0.3$ ; thick dotted and dashed grey lines:  $\sigma_1 = 10^{-5}$  and  $0.3$

massive galaxies is lower with respect to changing the definition of the main sequence itself (i.e., considering both S14 and B18).

The distribution of star-forming galaxies at fixed mass (Equation 4.2) also relies on a number of parameters affected by observational uncertainties:  $A_{\text{MS}}$ ,  $A_{\text{SB}}$ ,  $\sigma_{\text{MS}}$ ,  $\sigma_{\text{SB}}$ ,  $\langle \log_{10} \text{SFR} \rangle_{\text{MS}}$  and  $\langle \log_{10} \text{SFR} \rangle_{\text{SB}}$  (see Table 4.1 and Section 4.2.2 for details). Figure 4.16 shows the impact of  $\pm 3\sigma$  variations of these parameters on the merger rate density. The shift between starburst galaxies and main sequence (i.e., the definition of  $\langle \log_{10} \text{SFR} \rangle_{\text{SB}}$ ) yields the largest differences ( $\pm 10\%$ ) on the merger rate density of BBHs at  $z = 0$ . Overall, BNSs are less affected by these parameters than both BBHs and BHNSs, because they are less sensitive to metal-dependent star formation.

Recent papers (e.g. Caputi et al. 2017 and Bisigello et al. 2018) show that the percentage of starburst galaxies with respect to all star-forming galaxies might increase towards lower stellar masses and with redshift. This suggests that the contribution of starburst galaxies to the total cosmic SFR density is higher than our main assumption (Section 4.2.2). To see an example of the impact of this treatment of starburst galaxies on the SFRD( $z, Z$ ), we refer to Chruślińska et al. (2021) (Figure 10). We will include the impact of this treatment of starburst galaxies in a follow-up study.

#### 4.4.3 Metallicity relationships

The intrinsic scatter around both the MZR and the FMR is also uncertain, as well as the metallicity gradient within each galaxy, described by  $\sigma_0$  and  $\sigma_1$ , respectively (Section 4.2.2). We varied these parameters to assess their impact on the merger rate density, as shown in Figure 4.16. In the local Universe, the merger rate density of BBHs varies at most by  $-5(+15)\%$  and  $-5(+19)\%$  if we consider  $\sigma_0$  ( $\sigma_1$ ) = 0.05 ( $1 \times 10^{-5}$ ) and 0.30 (0.30), respectively.

Previous works have proposed a third observational relation to describe the metallicity evolution of galaxies: the fundamental plane (Lara-López et al., 2010; Hunt et al., 2012, 2016). Similarly to the FMR, the fundamental plane is independent of redshift, and relates metallicity, SFR and stellar mass. However, in the case of the fundamental plane these three quantities are linked in a two-dimensional plane. In this way, the value of the galaxy metallicity can be expressed as (Hunt et al., 2016):

$$12 + \log_{10}(\text{O/H}) = -0.14 \log_{10} \text{SFR} + 0.37 \log_{10} M_* + 4.82. \quad (4.6)$$

As a result, at high mass there is no bending after the turn-over mass and thus the metallicity does not converge to an asymptotic value. At low mass instead, Equation 4.6 yields an even flatter trend with stellar mass at fixed SFR with respect to the FMR. Thanks to this behaviour, the fundamental plane yields a merger rate density evolution in between the FMR and the MZR.

One last caveat concerns the calibration of metallicity in the adopted scaling relations. Empirical metallicity calibrations are one of the main sources of uncertainty in determining the metallicity of galaxies (Kewley & Ellison, 2008; Maiolino & Mannucci, 2019; Curti et al., 2020). In fact, different metallicity calibrations can give rise to different a normalisation (up to  $\sim 0.6$  dex) and shape of the MZR (see, for example, Figure 4 of Chruslinska et al. 2019).

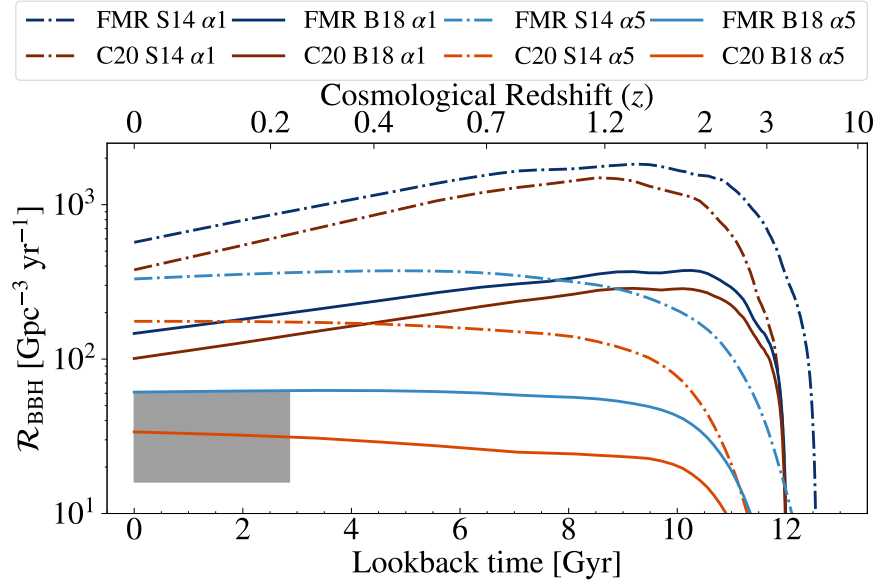


Figure 4.17: Evolution of the BBH merger rate density  $\mathcal{R}_{\text{BBH}}(z)$  obtained with the fundamental metallicity relation defined in [Curti et al. \(2020, C20\)](#) and [Mannucci et al. \(2011, FMR\)](#) for  $\alpha = 1$  and  $5$ . Solid and dash-dotted lines refer to B18 and S14, respectively. The gray shaded area shows the 90% credible interval of the local BBH merger rate density ([Abbott et al., 2021b](#)).

To assess the impact of a different metallicity calibration on our results, we evaluated the BBH merger rate density with the new definition of FMR given in Equation 5 of [Curti et al. \(2020\)](#), hereafter C20. The main difference between the FMR we adopted in our work and the FMR derived by C20 is that the latter has a shallower slope for galaxies less massive than the turnover mass ( $M_0 = 10^{10.02 \pm 0.09} M_\odot$ ); in other words, galaxies with  $M \lesssim 10^8 M_\odot$  have higher metallicity at any SFR (lower panel of Figure 3 of C20). Figure 4.17 shows that the overall evolution of the BBH merger rate density with redshift is not heavily affected by this different metallicity calibration. On the other hand, the BBH merger rate density in the local Universe resulting from the FMR reported by C20 is a factor  $\sim 1.2 - 2$  lower with respect to the FMR adopted in this work.

## 4.5 Conclusions

We developed the new code `GALAXYRATE`, which estimates the merger rate density of binary compact objects (BCOs) and the properties of their host galaxies (HG), based on observational scaling relations. With `GALAXYRATE`, we can perform many realizations of the merger rate density and HG properties across the cosmic time, in order to bracket the main uncertainties springing from both BCO formation and galaxy evolution.

Here, we have adopted three BCO catalogues generated with the population-synthesis code MOBSE ([Giacobbo & Mapelli, 2018](#)). In each catalogue, we vary the common-envelope efficiency parameter  $\alpha = 1, 3$  and  $5$ . This parameter is one of the main sources of uncertainty

among binary evolution processes (Santoliquido et al., 2021) and has a great impact on the delay time distribution of BCOs (Appendix 4.6.1).

`GALAXYRATE` first generates the formation galaxy (FG) of each BCO, i.e. the galaxy in which the progenitor stars of the BCO form. Each FG is described by its stellar mass, SFR and metallicity. We extract these properties from observational relations: the galaxy stellar mass function, the SFR distribution of star-forming and starburst galaxies, the mass-metallicity relation (MZR), and the fundamental metallicity relation (FMR). Given the large observational uncertainties, we explored the parameter space (Section 4.2.2) that mostly affects our results. For instance, we considered two galaxy main sequence definitions (S14 and B18). We also compared the metallicity evolution obtained with the MZR and FMR.

The HG (i.e., the galaxy in which the BCO merges) can be different from the FG for several reasons: the FG might have merged with other galaxies by the time the BCO reaches coalescence, or it might have evolved changing its mass, SFR and metallicity. We thus assign a HG to each BCO based on the conditional probability  $\mathcal{P}(M_{\text{host}}, \text{SFR}_{\text{host}} | M_{\text{form}}, \text{SFR}_{\text{form}}, z_{\text{form}}, z_{\text{merg}})$ , i.e. the probability that the HG has mass  $M_{\text{host}}$  and star formation rate  $\text{SFR}_{\text{host}}$ , given the mass ( $M_{\text{form}}$ ) and SFR ( $\text{SFR}_{\text{form}}$ ) of the FG, and given the formation ( $z_{\text{form}}$ ) and merger redshift ( $z_{\text{merg}}$ ) of the BCO (Section 4.2.4). Here, we calculate this probability in an empirical way by using the merger trees from the EAGLE cosmological simulation (Schaye et al., 2015; Qu et al., 2017).

We found that the merger rate density evolution with redshift changes dramatically depending on the choice of the star-forming galaxy main sequence, especially in the case of BBHs and BHNSs. The local merger rate density of BBHs and BHNSs is  $\sim 3 - 4$  times higher if we assume the star-forming main sequence from S14 with respect to B18. This happens because the S14 main sequence predicts a significantly higher SFR density at high redshift with respect to B18 (Figure 4.2). BBHs and BHNSs are strongly affected by this difference, because their merger rate depends on metallicity and newly born stars at high redshift are preferentially metal-poor. In contrast, BNSs are marginally affected, because their merger rate does not depend on metallicity (Figure 4.6).

The choice of the metallicity evolution has an important effect on the slope of the merger rate density of BBHs and BHNSs. The slope of the merger rate density evolution of BBHs and BHNSs is steeper if we assume the MZR with respect to the FMR, because the latter predicts a shallower decrease of metallicity with redshift (Figure 4.6). In contrast, BNSs are not affected by the choice of the metallicity relation.

Also, we compared the merger rate density obtained with `GALAXYRATE` (Section 4.2.3) with that obtained with `COSMORATE`, which evaluates the merger rate density by assuming the average SFR density and metallicity evolution of the Universe, i.e. without information about the galaxies (Santoliquido et al., 2021). We found that the merger rate density evolution of BNSs obtained with `COSMORATE` and `GALAXYRATE` are in good agreement, while the BBH and BHNS merger rate densities evaluated with `GALAXYRATE` are higher than those obtained with `COSMORATE`, if we assume the fitting formulas from Madau & Fragos (2017) and a metallicity spread  $\sigma_Z = 0.3$  (Figure 4.6). The main reason is that the  $\text{SFRD}(z, Z)$  we obtain from the observational scaling relations supports a larger population of metal-poor stars with respect to the Madau & Fragos (2017) fitting formulas with  $\sigma_Z = 0.3$ . The differences between the BBH merger rate density obtained with

`GALAXYRATE` and `COSMORATE` can be reconciled by assuming a larger metallicity spread  $\sigma_Z > 0.4$  in `COSMORATE`.

The merger rate density of BNSs and BHNSs is within the 90% credible interval estimated by the LVK with GWTC-3 (Abbott et al., 2021b) for all considered assumptions, while the merger rate density of BBHs predicted by our models is higher than the LVK range. This discrepancy most likely originates from the interplay of several different sources of uncertainty. Firstly, we considered only the formation of BBHs from binary evolution, and neglected the dynamical formation channel, which is more effective for BBHs than for the other families of BCOs. Current models of binary evolution predict an extremely strong dependence of the BBH merger rate density on metallicity, while this dependence is quenched by most dynamical formation channels (e.g., Mapelli et al., 2022). It might be that the dependence of the BBH merger rate on metallicity is overestimated by current binary evolution models, or that most BBHs do not form via this channel. In a follow-up study, we will consider alternative formation channels for BBHs. Secondly, current models of binary evolution might overestimate the BBH merger rate because of our poor knowledge of several binary evolution processes, such as common envelope and the stability of Roche lobe (Marchant et al., 2021; Klencki et al., 2021; Gallegos-Garcia et al., 2021; Belczynski et al., 2022). Thirdly, the evolution of stellar metallicity across cosmic time is one of the most disputed aspects of galaxy evolution, because all the metallicity calibrations are affected by large (and sometimes systematic) uncertainties (Maiolino & Mannucci, 2019).

Overall, the HGs of BBHs and BHNSs are more massive than their FGs (both assuming the MZR and the FMR), because both BBHs and BHNSs tend to form in smaller metal-poor galaxies and to merge in larger metal-rich galaxies. In contrast, the FGs and HGs of BNSs are very similar to each other (Figures 4.7 and 4.8).

The mass distribution of HGs is affected by the delay time distribution. In our models, different values of the common-envelope efficiency  $\alpha$  result in different distributions of the delay time (Appendix 4.6.1), with larger values of  $\alpha$  being associated with longer delay times. Figures 4.7 and 4.8 show that the contribution of high-mass galaxies increases with  $\alpha$ . In fact, with  $\alpha = 5$  (longer delay times), the FG has more time to merge with other galaxies and form a more massive HG. On the other hand, for  $\alpha = 1$  (shorter delay times), a large fraction of BBHs are hosted in low-mass galaxies.

In the high-redshift Universe ( $z = 4$ ) both the FGs and HGs of BCOs have a higher SFR than in the local Universe (Figures 4.9 and 4.10). Different values of  $\alpha$  have a mild impact on the shape of the SFR distribution of HGs. On the other hand, the FMR favours HGs with lower SFR with respect to the MZR in the case of BBHs at  $z \geq 4$ .

The FGs of BBHs and BHNSs tend to have a lower metallicity than their HGs, in the case of both MZR and FMR (Figures 4.11 and 4.12). However, the metallicity distributions of both FGs and HGs strongly depend on the choice of the metallicity relation. If we assume the MZR, the HGs and especially the FGs extend to lower metallicity at high redshift than in the local Universe. In contrast, the FMR predicts relatively high metallicities for both FGs and HGs and no significant trend with redshift.

We found a strong correlation between the BNS merger rate per galaxy ( $n_{\text{GW}}$ ) and the stellar mass of the HG (Figure 4.13). This correlation is less tight for BBHs and BHNSs, especially if we assume the FMR (Table 4.2).

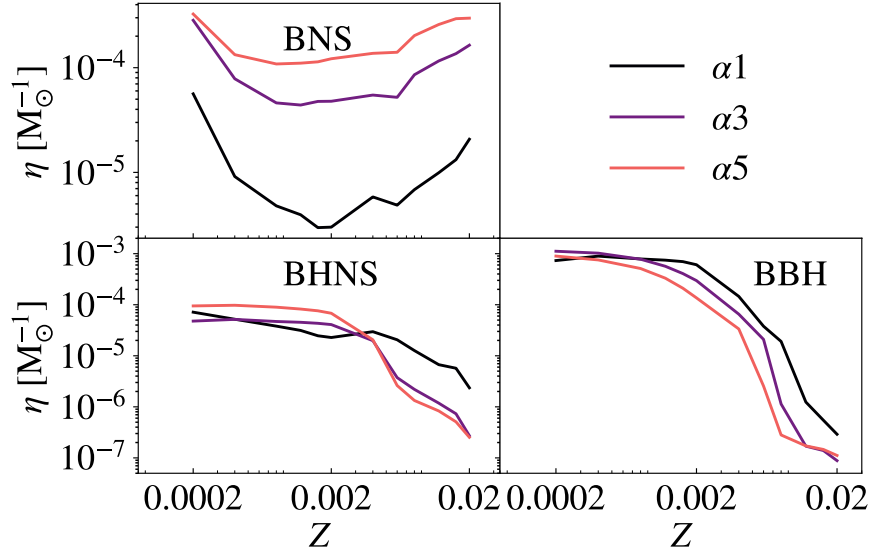


Figure 4.18: Merger efficiency  $\eta$  as a function of progenitor metallicity for models  $\alpha = 1, 3$  and  $5$ .

Passive galaxies can host compact objects mergers (Figure 4.14). Their contribution increases as approaching the local Universe, regardless of the adopted passive galaxy definition. However, the percentage of mergers hosted in passive galaxies crucially depends on this definition. If all the galaxies with  $\text{sSFR} < 10^{-10} \text{ yr}^{-1}$  are considered passive galaxies, we find that  $\sim 50 - 60\%$ ,  $\sim 45 - 70\%$  and  $\sim 40 - 75\%$  of all BNS, BHNS and BBH mergers in the local Universe are associated with a passive galaxy, respectively. In contrast, if we define passive galaxies as those galaxies with SFR at least 1 dex below the star-forming main sequence, only  $\sim 5 - 10\%$ ,  $\sim 15 - 25\%$  and  $\sim 15 - 35\%$  of all BNS, BHNS and BBH mergers in the local Universe are associated with a passive galaxy, respectively. Overall, BCOs have more chances to be hosted in passive galaxies if their delay time distribution is longer.

## 4.6 Appendix

### 4.6.1 Delay time distributions and merger efficiency

The merger efficiency and delay time distribution of BBHs strongly depend on metallicity and  $\alpha$ . Figure 4.18 show the merger efficiency  $\eta(Z)$ , defined as:

$$\eta(Z) = f_{\text{bin}} f_{\text{IMF}} \frac{\mathcal{N}_{\text{TOT}}(Z)}{M_*(Z)}, \quad (4.7)$$

where  $f_{\text{bin}} = 0.5$  is the binary fraction (Sana et al., 2012), and  $f_{\text{IMF}}$  is a correction factor taking into account that we simulated only stars with mass  $m > 5 M_{\odot}$  with MOBSE. Thus, assuming a Kroupa IMF (Kroupa, 2001),  $f_{\text{IMF}} = 0.285$ .

Figure 4.18 shows that the merger efficiency decreases by four orders of magnitude if we vary  $Z = 0.0002$  to  $Z = 0.02$ . This strong dependence of  $\eta$  on  $Z$  has been already widely

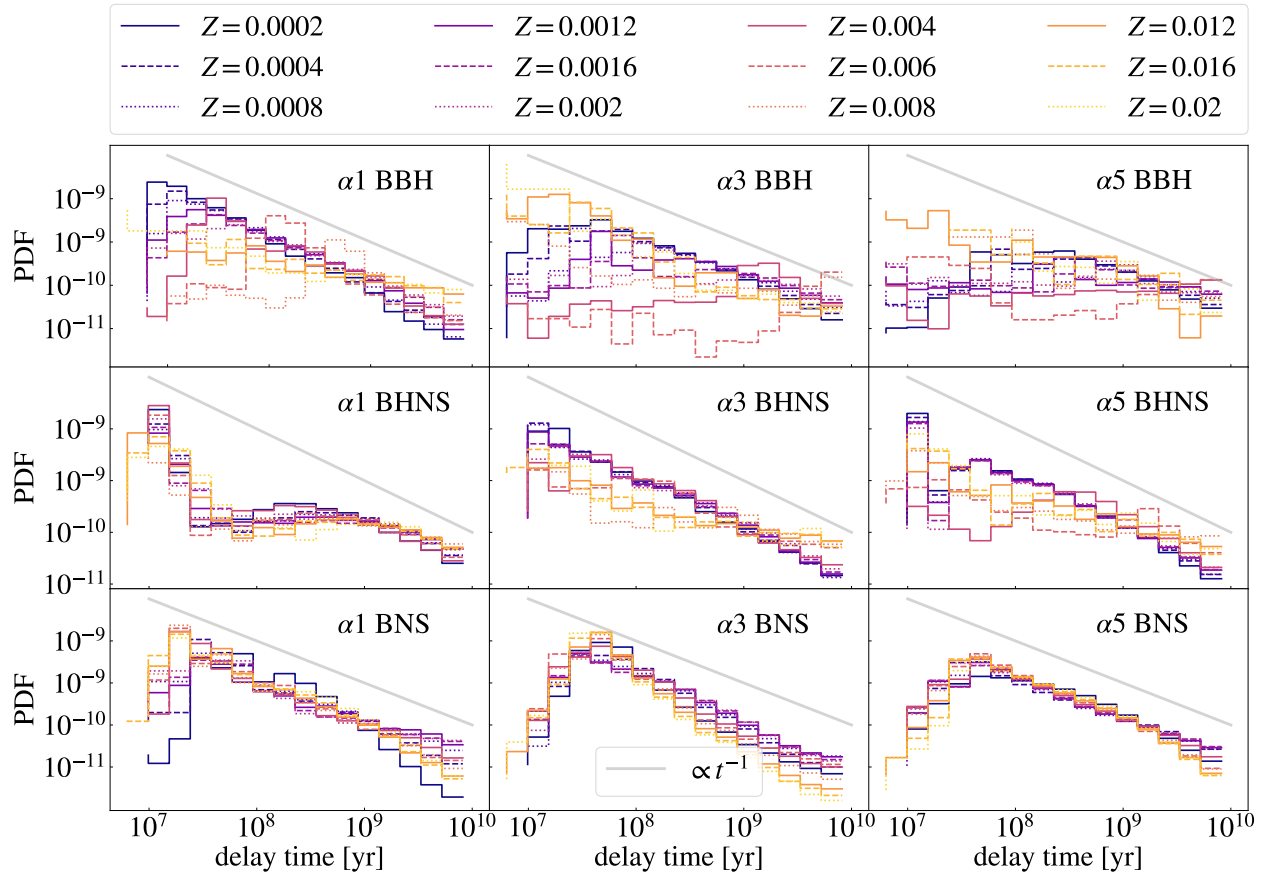


Figure 4.19: From left to right: delay time distributions for  $\alpha = 1, 3$  and  $5$  for BBHs (upper panels), BHNSs (middle) and BNSs (lower panels). Each color refers to a different progenitor's metallicity. The grey line is  $\propto t_{\text{del}}^{-1}$  with arbitrary normalisation.

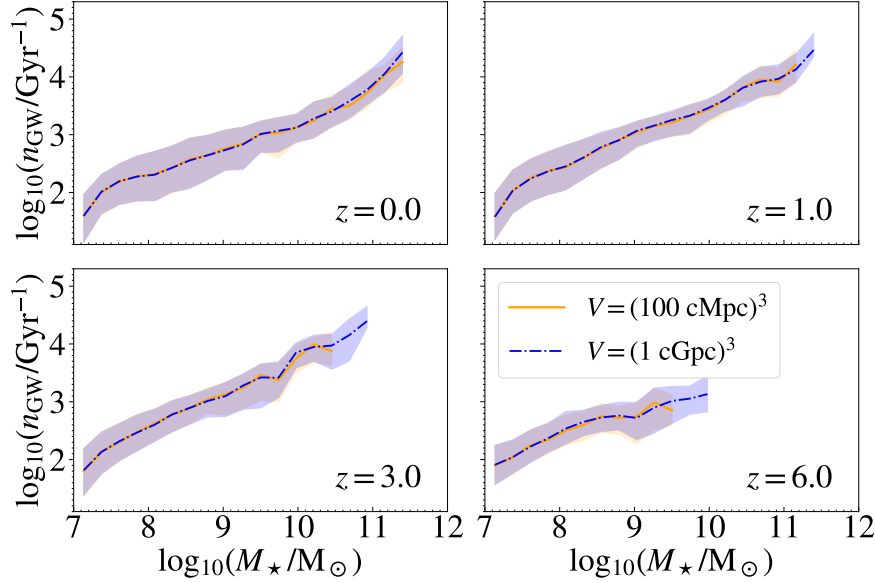


Figure 4.20: BBH merger rate per galaxy ( $n_{\text{GW}}$ ) as function of stellar mass ( $M_*$ ) for two different values of the comoving volume:  $V = (100 \text{ cMpc})^3$  and  $V = (1 \text{ cGpc})^3$ . We assume  $\alpha = 5$ , FMR and B18.

described in the literature and is common to very different population-synthesis codes (e.g. Dominik et al. 2012; Giacobbo & Mapelli 2018; Klencki et al. 2018; Neijssel et al. 2019; Spera et al. 2019). It is a consequence of stellar winds: metal-poor stars retain larger masses during their lives and grow larger radii than metal-rich ones. This enhances their chances to undergo mass transfer with companion stars and produce tight BBHs.

The merger efficiency of BNSs varies much less with  $Z$  but is heavily affected by  $\alpha$ . The parameter  $\alpha$  also shapes the distribution of delay times. Figure 4.19 shows that if  $\alpha = 1$  the delay time distribution peaks at shorter delay times than for larger values of  $\alpha$ . Smaller values of  $\alpha$  correspond to shorter delay times, because a small value of  $\alpha$  implies a more effective shrinking of the progenitor binary during common envelope. Hence, binary compact objects tend to form with shorter orbital separation if we assume a lower value of  $\alpha$ . Also, Figure 4.19 shows that  $dN/dt_{\text{del}} \propto t_{\text{del}}^{-1}$  for long delay times.

#### 4.6.2 Impact of the comoving volume on the merger rate

We assumed a comoving volume  $V = (100 \text{ cMpc})^3$  to obtain the results presented in the main text. This choice is a compromise between the need to sample a large volume and the computational cost: it takes  $\sim 15$  and  $\sim 2.5 \times 10^2$  CPU hours to simulate a volume  $V = (100 \text{ cMpc})^3$  and  $V = (1 \text{ cGpc})^3$ , respectively. Figure 4.20 compares the case in which we assume  $V = (100 \text{ cMpc})^3$  and  $(1 \text{ cGpc})^3$  for one test case (with  $\alpha = 5$ , FMR and B18). We find statistically no differences between the two volumes at redshift  $z = 0$ , while at higher redshift considering a large volume allows us to include more massive galaxies. Overall, we find no differences in the mass range we considered in this study, and our main results can

Reference		$Z_{\odot}$	$12 + \log_{10}(\text{O/H})_{\odot}$
Asplund et al. (2009)	A09	0.0134	8.69
Caffau et al. (2011)	C11	0.0153	8.76
Anders & Grevesse (1989)	AG89	0.017	8.83
Villante et al. (2014)	V14	0.019	8.85
Grevesse & Sauval (1998)	GS98	0.0201	8.93

Table 4.3: Solar metallicity measures from different authors.

be easily extrapolated to larger galaxy masses.

#### 4.6.3 Impact of the minimum galaxy mass on the merger rate

In our main text, we adopted a value  $M_{\min} = 10^7 M_{\odot}$  for the minimum galaxy stellar mass. In the local Universe, we see galaxies with mass lower than  $10^7 M_{\odot}$ , but it is not clear if we can extrapolate the main scaling relations (GSMF, SFR, MZR and FMR) down to such small masses. Actually, there is a mild evidence that the lowest mass star forming galaxies deviate from the main observational scaling relations (e.g., Hunt et al., 2012).

Figure 4.21 shows the impact of two other choices of the minimum galaxy stellar masses, namely  $10^6$ , and  $10^8 M_{\odot}$ . In particular, we show the ratio of the merger rate density we obtain by varying the minimum galaxy stellar mass to the merger rate density we obtain for the fiducial value  $M_{\min} = 10^7 M_{\odot}$ .

A lower (higher) value of  $M_{\min}$  implies a higher (lower) merger rate density for both BBHs and BHNSs, because of their dependence on the metallicity of the progenitor stars. We find a maximum difference of a factor of two between the BBH merger rate density with  $M_{\min} = 10^6 M_{\odot}$  and  $10^7 M_{\odot}$ . This difference is nearly constant across redshift for the FMR, while it becomes smaller at high redshift for the MZR. In contrast, BNSs are not affected by the choice of  $M_{\min}$ .

#### 4.6.4 Impact of the solar metallicity on the merger rate density

Both the MZR and FMR are expressed in terms of the relative abundance of oxygen and hydrogen  $12 + \log_{10}(\text{O/H})$ . In order to convert this quantity to the mass fraction of all elements heavier than helium  $Z$ , we assumed, as commonly done in literature (e.g. Maiolino & Mannucci, 2019), that the latter scales linearly with the measured  $12 + \log_{10}(\text{O/H})$ . In other words, we assumed that  $Z$  maintains the solar abundance ratio, as expressed by the following equation:

$$\log_{10} Z = \log_{10} Z_{\odot} + \log_{10}(\text{O/H}) - \log_{10}(\text{O/H})_{\odot}. \quad (4.8)$$

Figure 4.22 shows the impact of different definitions of the solar metallicity (Table 4.3) on the merger rate density of BBHs, which are the most affected by metallicity variations among BCOs. We show only the local merger rate density since changing the definition of the solar metallicity only affects the normalisation of the merger rate density.

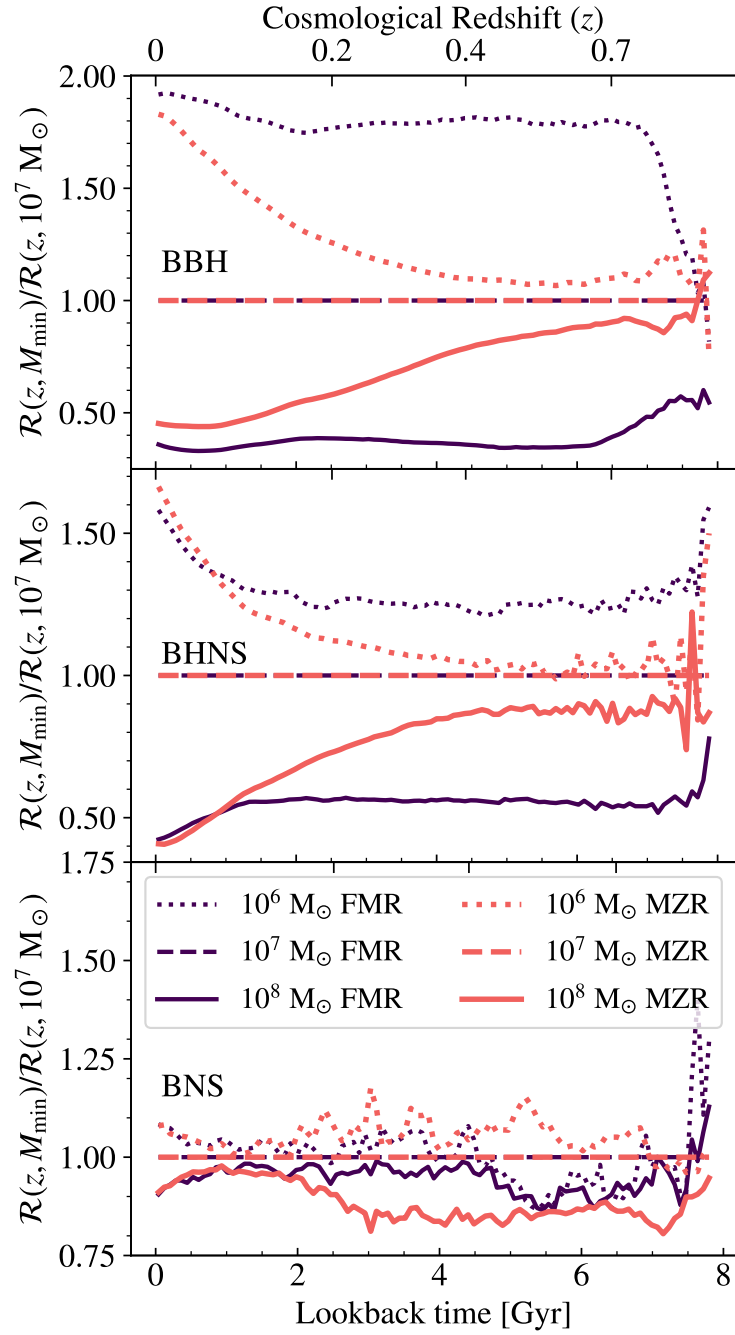


Figure 4.21: Impact of the choice of the minimum galaxy stellar mass ( $M_{\min}$ ) on the merger rate density of BBHs (upper panel), BHNSs (middle) and BNSs (lower). Each line is the ratio of the merger rate density  $\mathcal{R}(z)$  we estimate assuming  $M_{\min} = 10^6$  (dotted line),  $10^7$  (dashed line), and  $10^8 \text{ M}_\odot$  (solid line) to the merger rate density obtained for our fiducial value  $M_{\min} = 10^7 \text{ M}_\odot$ . Blue lines: FMR. Pink lines: MZR. We show the case with  $\alpha = 5$  and for S14.

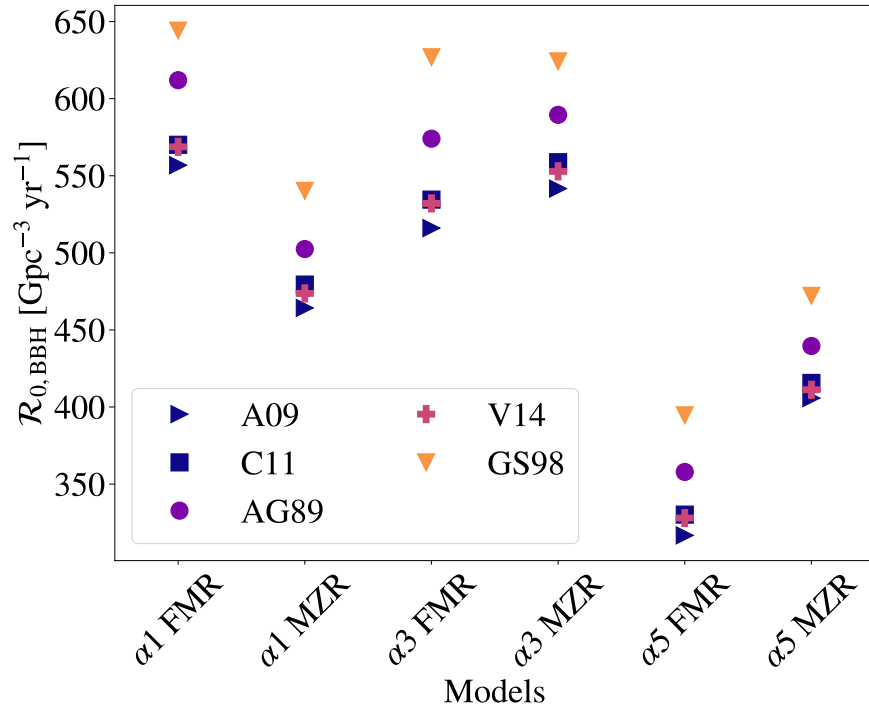


Figure 4.22: BBH merger rate density in the local Universe evaluated with different definitions of solar metallicity: A09 refers to [Asplund et al. \(2009\)](#), V14 to [Villante et al. \(2014\)](#), C11 to [Caffau et al. \(2011\)](#), GS98 to [Grevesse & Sauval \(1998\)](#) and AG89 to [Anders & Grevesse \(1989\)](#). See Table 4.3 for more details. We show the results for  $\alpha = 1, 3, 5$ , and for both the MZR and FMR, assuming the main sequence definition from S14.

# 5

## Binary black hole mergers from Population III stars: uncertainties from star formation and binary star properties

*Population III (Pop. III) binary stars likely produced the first stellar-born binary black hole (BBH) mergers in the Universe. Here, we quantify the main sources of uncertainty of the merger rate density evolution and mass spectrum of Pop. III BBHs by considering four different star formation histories of Pop. III stars and 11 different configurations of the initial orbital properties of our binary systems. The uncertainty on the orbital properties affects the BBH merger rate density by up to two orders of magnitude; models with shorter initial orbital periods lead to higher BBH merger rates, because they favour the merger via stable mass transfer episodes. The uncertainty on the star formation history has a substantial impact on both the shape and the normalization of the BBH merger rate density: the peak of the merger rate density shifts from  $z \sim 8$  up to  $z \sim 16$  depending on the assumed star formation rate, while the maximum rate for our fiducial binary population model spans from  $\sim 2$  to  $\sim 30 \text{ Gpc}^{-3} \text{ yr}^{-1}$ . The typical BBH masses are not affected by the star formation rate model and only mildly affected by the binary population parameters. The primary black holes born from Pop. III stars tend to be rather massive ( $30 - 40 M_{\odot}$ ) with respect to those born from metal-rich stars ( $8 - 10 M_{\odot}$ ). On the other hand, we expect that Pop. III BBH mergers with primary mass  $m_1 > 60 M_{\odot}$  are extremely rare ( $< 10^{-2} \text{ Gpc}^{-3} \text{ yr}^{-1}$ ).*

Based on:

Santoliquido F. et al., 2023, in preparation

### 5.1 Introduction

The third-generation ground-based gravitational-wave interferometers, the Einstein Telescope (Punturo et al., 2010) and Cosmic Explorer (Reitze et al., 2019), will capture binary BBH mergers up to a redshift  $z \sim 100$  (Maggiore et al., 2020; Ng et al., 2021, 2022b), with a factor

of  $\sim 100$  higher sensitivity at 10 Hz with respect to current detectors (Maggiore et al., 2020; Kalogera et al., 2021). Hence, they will be the ideal observatories to probe the merger of stellar-sized black holes (BHs) in the early Universe (e.g., Ng et al., 2021; Singh et al., 2022; Ng et al., 2022a), such as primordial BHs, and BHs born from Population III (hereafter, Pop. III) stars.

Here, we will focus on BHs born from the collapse of Pop. III stars, i.e. the first, metal-free stars (Haiman et al., 1996; Tegmark et al., 1997; Yoshida et al., 2003). While we have not directly observed them yet, we expect that Pop. III stars gave a key contribution to the reionization of the Universe (Kitayama et al., 2004; Alvarez et al., 2006; Johnson et al., 2007) and to the enrichment of the intergalactic medium, by spreading metals heavier than He through supernova explosions (e.g., Madau & Rees, 2001; Bromm & Loeb, 2003; Tornatore et al., 2007; Karlsson et al., 2008; Bromm et al., 2009; Karlsson et al., 2013).

Mergers of BHs from Pop. III stars have attracted a considerable interest (e.g., Kinugawa et al., 2016; Hartwig et al., 2016; Belczynski et al., 2017b; Tanikawa et al., 2022a) since the first LIGO–Virgo detection of a BBH merger, GW150914, with a total mass of  $65.3^{+4.1}_{-3.4} \text{ M}_\odot$  in the source frame (Abbott et al., 2016b; Abbott et al., 2016e). In fact, BHs from Pop. III stars are expected to extend to higher masses than the compact remnants of Population I stars (hereafter, Pop. I stars, i.e. metal-rich stars like our Sun) because mass loss by stellar winds is drastically quenched in metal-free stars (e.g., Madau & Rees, 2001; Heger et al., 2002; Woosley et al., 2002; Schneider et al., 2002; Kinugawa et al., 2014; Volpato et al., 2022). Moreover, the initial mass function of Pop. III stars is commonly believed to be more top heavy than that of Pop. I stars (e.g., Abel et al., 2002; Bromm & Larson, 2004; Schneider et al., 2006; Yoshida et al., 2006; Stacy & Bromm, 2013; Bromm, 2013; Glover, 2013; Susa et al., 2014; Hirano et al., 2014, 2015; Wollenberg et al., 2020; Chon et al., 2021; Tanikawa et al., 2021b; Jaura et al., 2022; Prole et al., 2022), increasing the efficiency of BH formation. Also, Pop. III binary stars tend to produce massive BBHs because they are more likely to experience stable mass transfer than Pop. I binary stars. In fact, massive Pop. III stars tend to have radiative envelopes for most of their life, avoiding common-envelope episodes (Kinugawa et al., 2016; Inayoshi et al., 2017).

For the above reasons, Pop. III stars are among the main suspects for the formation of BHs inside or above the pair-instability mass gap (e.g., Liu & Bromm, 2020c; Farrell et al., 2021; Kinugawa et al., 2021; Tanikawa et al., 2021b, 2022a), possibly explaining the formation of the peculiar merger GW190521, with primary (secondary) BH mass  $85^{+21}_{-14}$  ( $66^{+17}_{-18}$ )  $\text{M}_\odot$  (Abbott et al., 2020d,f).

Despite this revived interest in Pop. III stars and their remnants, the actual merger rate density and mass spectrum of Pop. III black holes are still debated (e.g., Kinugawa et al., 2016; Belczynski et al., 2017b; Kinugawa et al., 2020), mostly because of the absence of direct evidence for Pop. III stars. Current predictions yield a local merger rate density of Pop. III BBHs ranging from  $\sim 10^{-1}$  to  $\sim 10^2 \text{ Gpc}^{-3} \text{ yr}^{-1}$  (Kinugawa et al., 2014; Belczynski et al., 2017b; Liu & Bromm, 2020a; Tanikawa et al., 2022a). This uncertainty comes from different assumptions regarding the initial binary properties, star and binary evolution processes, and star formation rate history. Moreover, dynamical interactions of Pop. III BHs might also contribute to the merger rate (e.g., Liu & Bromm, 2020a; Wang et al., 2022). All of these uncertainties also propagate onto the evolution with redshift of the mass spectrum and merger

rate.

Here, we quantify the current uncertainties on the merger rate density and mass spectrum of BBH mergers from Pop. III stars by considering a wide range of assumptions for the star formation history of metal-free stars (Jaacks et al., 2019; Liu & Bromm, 2020a; Hartwig et al., 2022), for their initial binary properties (e.g., Larson, 1998; Stacy & Bromm, 2013; Stacy et al., 2016; Tanikawa et al., 2022a), and binary evolution (e.g., Costa & et al., 2023, and references therein), by adopting the SEVN binary population synthesis code (Spera et al., 2019; Mapelli et al., 2020b; Iorio et al., 2022).

## 5.2 Methods

### 5.2.1 Population synthesis with SEVN

We derived our BBH merger catalogues with the binary population synthesis code SEVN, which integrates single and binary evolution by interpolating a set of pre-computed single stellar-evolution tracks, as described in Iorio et al. (2022). Here, we adopt the following set up of SEVN.

We calculated the Pop. III stellar tracks with the PARSEC code (Bressan et al., 2012; Costa et al., 2021; Nguyen et al., 2022) at metallicity  $Z = 10^{-11}$ . This value of  $Z$  is equivalent to considering a metal-free composition (e.g., Marigo et al., 2001; Tanikawa et al., 2021b). Their zero-age main sequence mass (ZAMS) ranges from 2 to  $600 M_{\odot}$ . All tracks evolve until the end of the core He burning and reach the early asymptotic giant branch phase (stars with  $2 < M_{\text{ZAMS}}/M_{\odot} < 8$ ), or the beginning of the core O burning phase (stars with  $M_{\text{ZAMS}} > 8 M_{\odot}$ ). For more details on these tracks, we refer to Costa & et al. (2023).

We remap the final properties of the stars (in particular, final total mass and CO core mass) into BH masses by adopting the rapid model for core-collapse supernovae (Fryer et al., 2012). Furthermore, we implement the outcome of electron-capture supernovae, as detailed in Giacobbo & Mapelli (2019). For (pulsational) pair-instability supernovae, we adopt the model presented in Mapelli et al. (2020b). In this model, based on the hydro-dynamical calculation by Woosley (2017) (see also Spera & Mapelli 2017), a star undergoes pulsational pair instability if the pre-supernova He-core mass,  $M_{\text{He}}$ , is between 32 and  $64 M_{\odot}$ . The mass of the BH after pulsational pair instability is:

$$M_{\text{BH}} = \begin{cases} \alpha_P M_{\text{CCSN}} & \text{if } (\alpha_P M_{\text{CCSN}}) \geq 4.5 M_{\odot} \\ 0 & \text{if } (\alpha_P M_{\text{CCSN}}) < 4.5 M_{\odot}, \end{cases} \quad (5.1)$$

where  $M_{\text{CCSN}}$  is the mass of the BH after a core-collapse supernova (without pulsational pair instability) and  $\alpha_P$  is a dimensionless correction factor between 0 and 1. The dimensionless factor  $\alpha_P$  depends on  $M_{\text{He}}$  and the pre-supernova mass ratio between the mass of the He core and the total stellar mass (see Equations 4 and 5 in the Appendix of Mapelli et al. 2020b). For  $M_{\text{He}} > 64 M_{\odot}$ , the star enters the pair-instability regime.

When a star enters the pair-instability regime, we assume that (i) the star is completely disrupted and leaves no compact remnant for  $M_{\text{He}} \leq 135 M_{\odot}$ ; (ii) the star directly collapses

to a BH for a larger final He mass (see [Costa & et al. 2023](#) and [Iorio et al. 2022](#) for more details on these assumptions).

Here, we draw BH natal kicks from two different distributions. In our fiducial case, we adopt the formalism by [Giacobbo & Mapelli \(2020\)](#), hereafter GM20):

$$V_{\text{kick}} = f_{\text{H05}} \frac{\langle M_{\text{NS}} \rangle}{M_{\text{rem}}} \frac{M_{\text{ej}}}{\langle M_{\text{ej}} \rangle}, \quad (5.2)$$

where  $\langle M_{\text{NS}} \rangle$  and  $\langle M_{\text{ej}} \rangle$  are the average NS mass and ejecta mass from single stellar evolution, respectively, while  $M_{\text{rem}}$  and  $M_{\text{ej}}$  are the compact object mass and the ejecta mass ([Giacobbo & Mapelli, 2020](#)). The term  $f_{\text{H05}}$  is a random number drawn from a Maxwellian distribution with one-dimensional root mean square  $\sigma_{\text{kick}} = 265 \text{ km s}^{-1}$ , coming from a fit to the proper motions of 73 young pulsars ( $< 3 \text{ Myr}$ ) in the Milky Way ([Hobbs et al., 2005](#)). In this formalism, stripped and ultra-stripped supernovae result in lower kicks with respect to the other explosions, owing to the lower amount of ejected mass  $M_{\text{ej}}$  ([Bray & Eldridge, 2016, 2018](#)). BHs originating from a direct collapse receive zero natal kicks from this mechanism.

In the alternative model we present in Section 5.5, we randomly draw the BH natal kicks from a Maxwellian distribution with one dimensional root mean square  $\sigma_{\text{kick}} = 150 \text{ km s}^{-1}$  (hereafter  $\sigma_{150}$ ). This model matches the BH kicks inferred by [Atri et al. \(2019\)](#), based on the proper motions of 16 BH X-ray binaries in the Milky Way. The two models GM20 and  $\sigma_{150}$  bracket the uncertainties on BH natal kicks, but while the latter is independent of the mass of the BH, the former introduces a strong dependence on both the mass of the compact remnant ( $M_{\text{rem}}$ ) and the evolution of the progenitor star (encoded in  $M_{\text{ej}}$ ).

In addition to the natal kick, we also calculate a Blaauw kick ([Blaauw, 1961](#)) resulting from the instantaneous mass loss in a binary system triggered by a supernova explosion. We use the same formalism as described in Appendix A of [Hurley et al. \(2002\)](#).

Finally, SEVN integrates the following binary evolution processes: wind mass transfer, stable Roche-lobe overflow, common envelope evolution (adopting the  $\alpha$  formalism, [Hurley et al. 2002](#)), tidal evolution, stellar collisions, magnetic braking, and gravitational-wave decay, as discussed in [Iorio et al. \(2022\)](#).

Here, we use the same set up as the fiducial model of [Iorio et al. \(2022\)](#), adopting the default values for all relevant parameters (Section 3.2 of [Iorio et al. 2022](#)): mass transfer is always stable for main sequence and Hertzsprung-gap donor stars, while we follow the prescriptions by [Hurley et al. \(2002\)](#) in all the other cases. We set the Roche-lobe overflow mass accretion efficiency to 0.5 (for a non-degenerate accretor), and assume that the mass which is not accreted is lost from the vicinity of the accretor as an isotropic wind (isotropic re-emission). At the onset of the Roche-lobe overflow, SEVN circularises the orbit at the periastron. During common envelope, we estimate the envelope binding energy using the same formalism as in [Claeys et al. \(2014\)](#). We adopt  $\alpha = 1$  for the common-envelope efficiency parameter, i.e. we assume that all the kinetic energy lost from the system contributes to unbinding the common-envelope.

### 5.2.2 Initial conditions for Pop. III binary systems

We use the same binary-population synthesis simulations as in Costa & et al. (2023). We summarize their initial conditions here below and in Table 5.1.

#### Initial mass function (IMF)

We consider the following four distributions for the initial mass function (IMF), in order to account for the uncertainties on the IMF of Pop. III stars (e.g., Bromm & Larson, 2004; Yoshida et al., 2006; Bromm, 2013; Glover, 2013).

- A flat-in-log distribution (see e.g., Stacy & Bromm, 2013; Susa et al., 2014; Hirano et al., 2014, 2015; Wollenberg et al., 2020; Chon et al., 2021; Tanikawa et al., 2021b; Jaura et al., 2022; Prole et al., 2022)):

$$\xi(M_{\text{ZAMS}}) \propto M_{\text{ZAMS}}^{-1}. \quad (5.3)$$

- A Kroupa (2001) distribution (hereafter, K01):

$$\xi(M_{\text{ZAMS}}) \propto M_{\text{ZAMS}}^{-2.3}. \quad (5.4)$$

With respect to the original K01, which has a flatter slope for  $M_{\text{ZAMS}} < 0.5 M_{\odot}$ , here we assume a single slope because we do not generate ZAMS masses  $< 5 M_{\odot}$  from this distribution.

- A Larson (1998) distribution (hereafter, L98):

$$\xi(M_{\text{ZAMS}}) \propto M_{\text{ZAMS}}^{-2.35} e^{-M_{\text{cut1}}/M_{\text{ZAMS}}}, \quad (5.5)$$

where  $M_{\text{cut1}} = 20 M_{\odot}$  (Valiante et al., 2016).

- A top-heavy distribution (hereafter, TOP), following Stacy & Bromm (2013), Jaacks et al. (2019), and Liu & Bromm (2020a):

$$\xi(M_{\text{ZAMS}}) \propto M_{\text{ZAMS}}^{-0.17} e^{-M_{\text{cut2}}^2/M_{\text{ZAMS}}^2}, \quad (5.6)$$

where  $M_{\text{cut2}} = 20 M_{\odot}$ .

In the following, we name LOG, KRO, LAR, and TOP our models adopting the flat-in-log, K01, L98, and top-heavy IMFs (Table 5.1).

In all of our models but LOG3 (Table 5.1), we use the aforementioned IMFs to generate the ZAMS mass of the primary star  $M_{\text{ZAMS},1}$  (i.e., the most massive component of the binary star) in the range  $[5, 550] M_{\odot}$ . In model LOG3, we instead randomly sample the entire IMF (both primary and secondary stars) in the range  $M_{\text{ZAMS}} \in [5, 550] M_{\odot}$  according to the LOG IMF.

## Mass ratio and secondary mass

We draw the mass of the secondary star ( $M_{\text{ZAMS},2}$ ) according to three different distributions.

- We use the distribution of the mass ratio  $q = M_{\text{ZAMS},2}/M_{\text{ZAMS},1}$  from [Sana et al. \(2012\)](#), hereafter S12:

$$\xi(q) \propto q^{-0.1} \text{ with } q \in [0.1, 1] \text{ and } M_{\text{ZAMS},2} \geq 2.2 \text{ M}_\odot. \quad (5.7)$$

This distribution is a fit to the mass ratio of O- and B-type binary stars in the local Universe ([Sana et al., 2012](#)).

- In the sorted distribution, we draw the ZAMS mass of the entire stellar population from the same IMF, and then we randomly pair two stars from this distribution, imposing that  $M_{\text{ZAMS},2} \leq M_{\text{ZAMS},1}$ . In this model, the minimum mass of the secondary is equal to that of the primary ( $5 \text{ M}_\odot$ ) by construction, and there is no minimum mass ratio.
- The mass ratio distribution by [Stacy & Bromm \(2013\)](#), hereafter SB13):

$$\xi(q) \propto q^{-0.55} \text{ with } q \in [0.1, 1] \text{ and } M_{\text{ZAMS},2} \geq 2.2 \text{ M}_\odot. \quad (5.8)$$

This distribution was obtained from a fit to Pop. III stars formed in cosmological simulations (SB13).

## Orbital period

We consider two different distributions for the orbital period ( $P$ ):

- The distribution derived by S12 for O- and B- stars in the local Universe:

$$\xi(\pi) \propto \pi^{-0.55} \text{ with } \pi = \log(P/\text{day}) \in [0.15, 5.5]. \quad (5.9)$$

- A Gaussian distribution

$$\xi(\pi) \propto \exp [-(\pi - \mu)^2 / (2\sigma^2)] \quad (5.10)$$

with  $\mu = 5.5$ , and  $\sigma = 0.85$ , as derived from SB13 based on cosmological simulations. While this distribution is likely affected by the numerical resolution of the original simulations, which suppresses the formation of systems with short orbital periods, we decide to consider it as a robust upper limit to the orbital period of Pop. III and Pop. II binary stars.

## Eccentricity

We compare two distributions for the orbital eccentricity:

- The distribution obtained by S12 and based on a sample of O- and B-type stars in the local Universe:

$$\xi(e) \propto e^{-0.42} \text{ with } e \in [0, 1]. \quad (5.11)$$

- The thermal distribution, adopted for Pop. III binaries by, e.g., [Kinugawa et al. \(2014\)](#); [Hartwig et al. \(2016\)](#); [Tanikawa et al. \(2021b\)](#):

$$\xi(e) = 2e \text{ with } e \in [0, 1] \quad (5.12)$$

Table 5.1: Initial conditions.

Model	$M_{\text{ZAMS},1}$	$M_{\text{ZAMS}}$	$q$	$P$	$e$
LOG1	Flat in log	–	S12	S12	S12
LOG2	Flat in log	–	S12	SB13	Thermal
LOG3	–	Flat in log	Sorted	S12	S12
LOG4	Flat in log	–	SB13	S12	Thermal
LOG5	Flat in log	–	SB13	SB13	Thermal
KRO1	K01	–	S12	S12	S12
KRO5	K01	–	SB13	SB13	Thermal
LAR1	L98	–	S12	S12	S12
LAR5	L98	–	SB13	SB13	Thermal
TOP1	Top heavy	–	S12	S12	S12
TOP5	Top heavy	–	SB13	SB13	Thermal

Column 1 reports the model name. Columns 2 describes how we generate the ZAMS mass of the primary star (i.e., the most massive of the two members of the binary system). Column 3 describes how we generate the ZAMS mass of the overall stellar population (without differentiating between primary and secondary stars). We follow this procedure only for model LOG3 (see the text for details). Columns 4, 5, and 6 specify the distributions we used to generate the mass ratios  $q$ , the orbital periods  $P$  and the orbital eccentricity  $e$ . See Section 5.2.2 for a detailed description of these distributions.

### Input catalogues

We build 11 different input catalogues by varying the aforementioned distributions of the IMF,  $q$ ,  $P$ , and  $e$ . We set the total number of generated binaries to obtain  $10^7$  binaries in the high-mass regime ( $M_{\text{ZAMS},2} \geq 10 M_\odot$ , and  $M_{\text{ZAMS},1} \geq 10 M_\odot$  by construction). This ensures a good sampling of the high-mass regime and reduces the stochastic fluctuations (e.g., Iorio et al., 2022). Table 5.1 lists the properties of our input catalogues. We refer to Costa & et al. (2023) for more details.

### 5.2.3 Formation history of Pop. III stars

We consider four independent estimates of the Pop. III star formation rate density (SFRD), to quantify the main differences among models. Figure 5.1 shows these four star formation rate histories, which come from Hartwig et al. (2022, hereafter H22), Jaacks et al. (2019, hereafter J19), Liu & Bromm (2020b, hereafter LB20), and Skinner & Wise (2020, hereafter SW20). All of them match the value of the Thomson scattering optical depth estimated by the Planck Collaboration (i.e.  $\tau_e = 0.0544 \pm 0.0073$ , Ade et al., 2016). The peak of the SFRD is remarkably different in these four models, ranging from  $z \approx 8$  (J19) to  $z \approx 20$  (SW20). By selecting these four SFRDs, we account for both differences in the underlying physics assumptions and the cosmic variance, since these models rely on cosmological boxes with length spanning from 1 to  $8 h^{-1}$  comoving Mpc.

All of these SFRDs come from semi-analytic models or cosmological simulations that

assume their own IMF for Pop. III stars. Thus, we introduce an inconsistency whenever we combine a given SFRD model with a binary population synthesis catalogue generated with a different IMF. The impact of this assumption on our results is negligible with respect to other sources of uncertainty considered in this work (e.g., [Crosby et al., 2013](#)).

## H22

A-SLOTH is the only semi-analytic model that samples and traces individual Pop. III and II stars, and is calibrated on several observables from the local and high-redshift Universe ([Hartwig et al., 2022](#); [Uysal & Hartwig, 2023](#)). It can take the input dark-matter halo merger trees either from cosmological simulations or from an extended Press-Schechter formalism. Here, we use the results obtained with the merger tree from [Ishiyama et al. \(2016\)](#), who simulated a  $(8 h^{-1} \text{ Mpc})^3$  box down to a redshift  $z = 4$ . In Fig. 5.1 and in the rest of the paper we use a linear extrapolation of the H22 SFRD down to redshift  $z = 0$ .

With A-SLOTH, it is possible to propagate the uncertainties in the underlying input physics (such as Pop. III IMF or star formation efficiency) on the resulting SFRD. Figure 5.1 shows the 95% credible interval evaluated by taking into account these uncertainties (Hartwig et al., in prep.).

## J19

[Jaacks et al. \(2019\)](#) used the hydro-dynamical/ $N$ -body code GIZMO ([Hopkins, 2015](#)) coupled with a custom sub-grid physics, accounting for both the chemical and radiative feedback from core-collapse and pair-instability supernovae. The simulation has been run down to redshift 7.5 with a comoving box length of  $4 h^{-1} \text{ Mpc}$ . In this case, we do not extrapolate the Pop. III SFRD down to redshift zero, but we assume that it just stops at  $z = 7.5$ .

## LB20

[Liu & Bromm \(2020b\)](#) also ran a cosmological simulation with GIZMO, but assumed different sub-grid prescriptions with respect to [Jaacks et al. \(2019\)](#), resulting in a lower Pop. III SFRD with respect to [Jaacks et al. \(2019\)](#). They simulated a comoving cubic box of  $(4 h^{-1} \text{ Mpc})^3$  down to redshift  $z = 4$ , and then extrapolate the results down to  $z = 0$  with additional semi-analytical modelling. They parameterised their Pop. III SFRD evolution with the same functional form as [Madau & Dickinson \(2014\)](#)

$$\psi(z) = \frac{a(1+z)^b}{1 + [(1+z)/c]^d} [\text{M}_\odot \text{ yr}^{-1} \text{ Mpc}^{-3}], \quad (5.13)$$

and obtained best-fit parameters  $a = 756.7 \text{ M}_\odot \text{ yr}^{-1} \text{ Mpc}^{-3}$ ,  $b = -5.92$ ,  $c = 12.83$ , and  $d = -8.55$  [Liu & Bromm \(2020b\)](#). In our analysis, we use this best fit.

## SW20

[Skinner & Wise \(2020\)](#) ran a hydro-dynamical cosmological simulation with the adaptive mesh refinement code ENZO ([Bryan et al., 2014](#)). They simulate a  $(1 h^{-1} \text{ Mpc})^3$  comoving

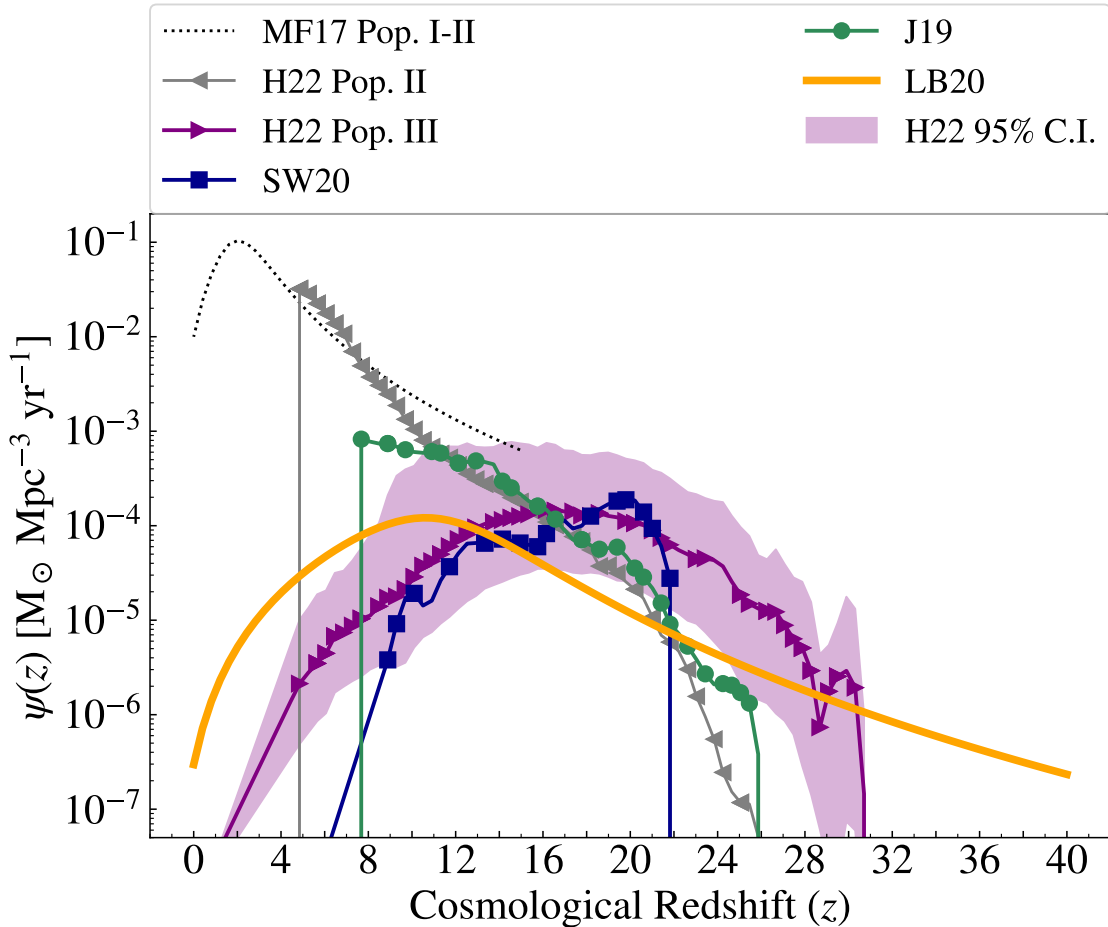


Figure 5.1: Star formation rate density ( $\psi(z)$ ) of Pop. III stars. Purple line: (Hartwig et al., 2022) (H22); blue line: Skinner & Wise (2020) (SW20); green line: Jaacks et al. (2019) (J19); orange line Liu & Bromm (2020a) (LB20). The shaded area shows the 95% credible interval for the H22 model. The grey line is the star formation rate density of Pop. II stars from A-SLOTH. The thin dashed black line is the star formation rate density of Pop. I-II stars from Madau & Fragos (2017) (MF17).

box with a  $256^3$  base grid resolution and a dark-matter particle mass of  $2001 \text{ M}_\odot$ . This simulation has been run down to  $z = 9.32$ . In Figure 5.1 and in the rest of the paper, we linearly extrapolate their SFRD down to redshift zero.

### 5.3 COSMORATE

We estimate the merger rate density evolution of BBHs with the semi-analytic code COSMORATE (Santoliquido et al., 2020, 2021), which interfaces catalogues of simulated BBH mergers with a metallicity-dependent SFRD model. The merger rate density in the comoving frame is given by

$$\mathcal{R}(z) = \int_{z_{\min}}^z \left[ \int_{Z_{\min}}^{Z_{\max}} \text{SFRD}(z', Z) \mathcal{F}(z', z, Z) dZ \right] \frac{dt(z')}{dz'} dz', \quad (5.14)$$

where  $\text{SFRD}(z', Z) = \psi(z') p(z', Z)$ . Here,  $\psi(z)$  is the adopted star formation rate density evolution (chosen among the ones presented in Figure 5.1), and  $p(z', Z)$  is the distribution of metallicity  $Z$  at fixed formation redshift  $z'$ . Since Pop. III stars are modelled with a single metallicity ( $Z = 10^{-11}$ ), for them  $p(z', Z)$  is defined as a delta function, different from zero only if  $Z = 10^{-11}$ . In Equation 5.14,  $dt(z')/dz' = H_0^{-1} (1+z')^{-1} [(1+z')^3 \Omega_M + \Omega_\Lambda]^{-1/2}$ , where  $H_0$  is the Hubble constant,  $\Omega_M$  and  $\Omega_\Lambda$  are the matter and energy density, respectively. We adopt the values in Planck Collaboration et al. (2020). The term  $\mathcal{F}(z', z, Z)$  in Equation 5.14 is given by:

$$\mathcal{F}(z', z, Z) = \frac{1}{\mathcal{M}_{\text{TOT}}(Z)} \frac{d\mathcal{N}(z', z, Z)}{dt(z)}, \quad (5.15)$$

where  $\mathcal{M}_{\text{TOT}}(Z)$  is the total simulated initial stellar mass in our binary population-synthesis simulations, and  $d\mathcal{N}(z', z, Z)/dt(z)$  is the rate of BBHs that form from progenitor metallicity  $Z$  at redshift  $z'$  and merge at  $z$ , extracted from our population-synthesis catalogues.

For all the Pop. III models shown in this work, we assume that the binary fraction is  $f_{\text{bin}} = 1$ , and we do not apply correction for sampling stars with mass  $> 5 \text{ M}_\odot$ . We make this simplifying assumption because we do not know the minimum mass and binary fraction of Pop. III stars. Assuming a lower binary fraction and a lower minimum mass than  $m_{\min} = 5 \text{ M}_\odot$  translates into a simple shift of our merger rate by a constant numerical factor (unless we assume the minimum mass and the binary fraction depend on either redshift or metallicity).

## 5.4 Results

### 5.4.1 Merger rate density of BBHs born from Pop. III stars

Figure 5.2 shows the merger rate density evolution of Pop. III BBHs assuming the SFRD from H22. The merger rate density changes by about one order of magnitude within the 95% credible interval of the Pop. III SFRD estimated by H22. Uncertainties on the initial conditions of binary systems (Table 5.1) impact the merger rate density of Pop. III BBHs by up to two orders of magnitude, for a fixed SFRD model. The models adopting a SB13 distribution for the initial orbital periods (LOG2, LOG5, KRO5, LAR5, and TOP5) have

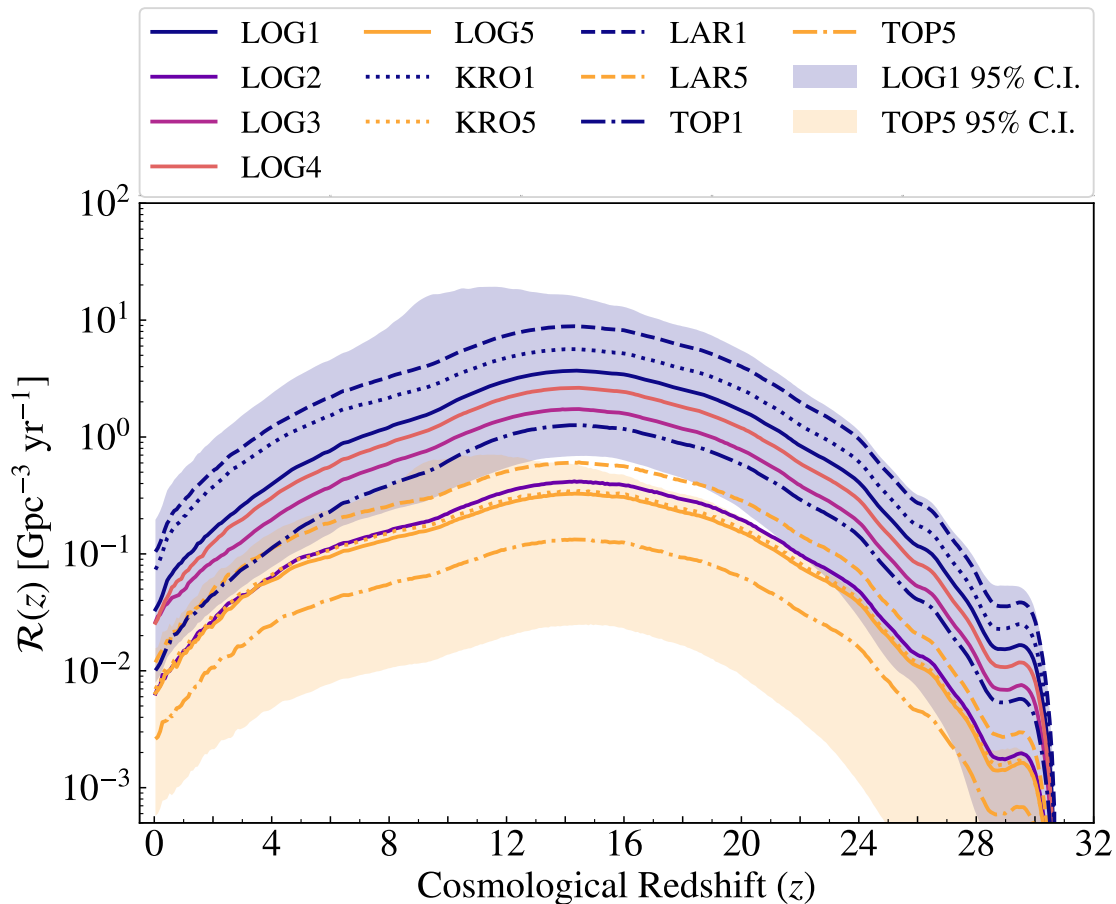


Figure 5.2: Evolution of the BBH merger rate density with redshift  $\mathcal{R}(z)$ . Solid lines: models with a flat-in-log IMF (LOG). Dotted lines: models with a Kroupa IMF (KRO). Dashed lines: models with a Larson IMF (LAR). Shaded areas are 95% credible interval evaluated considering input uncertainty in A-SLOTH (see Figure 5.1) for LOG1 and TOP5 models.

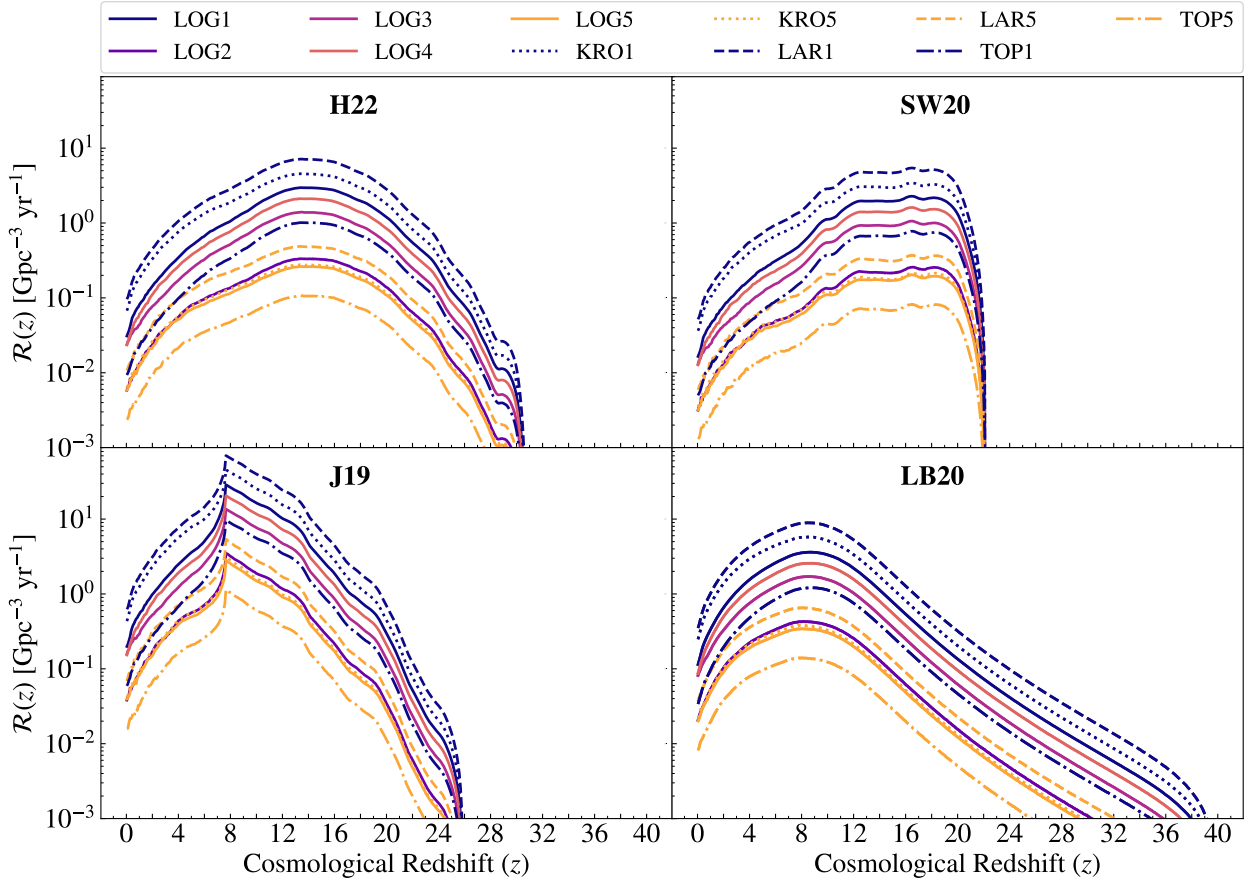


Figure 5.3: Evolution of the BBH merger rate density with redshift  $\mathcal{R}(z)$  for all the 44 models considered in this work. Solid lines: models with a flat-in-log IMF (LOG). Dotted lines: models with a Kroupa IMF (KRO). Dashed lines: models with a Larson IMF (LAR). Upper left plot: H22 star formation history, upper right: SW10, lower left: J19, and lower right: LB20.

lower merger rate densities than models adopting the distribution by S12 (all the other models). The reason is that short orbital periods, as in the case of S12, favour the merger of BBHs via stable mass transfer episodes between the progenitor stars.

Figure 5.3 shows the merger rate density for all the SFRD models considered in this work. The star formation rate history affects both the shape and the normalisation of the BBH merger rate density. Our merger rate density curves (Fig. 5.3) are similar in shape to the SFRD curves (Fig. 5.1), with just a shift to lower redshift because of the delay time, i.e. the time between the formation of a BBH-progenitor binary system and the merger of the two BHs. Hence, the peak of the merger rate density spans from  $z \approx 16$  to  $z \approx 8$  depending on the SFRD model. For all the considered star formation rate histories and binary models, the BBH merger rate density peaks well inside the instrumental horizon of the Einstein Telescope (Maggiore et al., 2020; Kalogera et al., 2021).

#### 5.4.2 Evolution of BH mass with redshift

Figure 5.4 shows that the median value of the primary BH mass (i.e., the most massive between the two merging BHs) does not change significantly with redshift, considering the entire ensemble of our models. On the other hand, the median mass of the secondary BH mass does decrease at lower redshift (Figure 5.5). This trend of the secondary BH mass is more evident when the SFRD of Pop. III becomes negligible.

As a consequence of this trend, the mass ratio of Pop. III BBHs (Figure 5.6) decreases from  $q \gtrsim 0.9$  at  $z \sim 15$  to  $q \sim 0.5 - 0.7$  at  $z \leq 4$ . In contrast, the mass ratio of Pop. I-II BBHs remains nearly constant  $q \gtrsim 0.9$  across all redshifts.

Figures 5.7 and 5.8 show the whole distribution of primary and secondary masses of Pop. III BHs, respectively, at redshift  $z = 0, 2$ , and  $10$ . The percentage of Pop. III systems with  $m_2 \geq 25 M_\odot$  is  $\sim 60 - 80\%$  at  $z = 10$  and only  $\sim 25 - 40\%$  at  $z = 0$  (depending on the chosen model). This change of the shape springs from the different distribution of delay time. In fact, when the formation rate of Pop. III stars becomes negligible, we expect to see only mergers of Pop. III BBHs with long delay times. We further discuss this feature in Section 5.5.1, considering the impact of the various formation channels.

Figures 5.7 and 5.8 also show that the range of primary (secondary) BH masses from Pop. I-II stars becomes narrower at  $z < 10$ : the percentage of BHs with primary mass  $> 30 M_\odot$  is  $\sim 10.6\%$  ( $\sim 5\%$ ) at  $z = 10$  and only  $\sim 0.3\%$  ( $\sim 0.09\%$ ) at  $z = 0$ . This happens because at lower redshift most BBH mergers have metal-rich progenitors, and strongly depends on the assumed metallicity spread (Santoliquido et al., 2021, 2022).

At low redshift, our metal-rich ( $Z \geq 10^{-3}$ ) binary stars produce a main peak in the primary BH mass distribution at  $8 - 10 M_\odot$ , similar to the main peak inferred from the LVK data (Abbott et al., 2019b, 2020c, 2021b; Farah et al., 2023; Callister & Farr, 2023). Instead, primary BHs born from Pop. III stars have a preference for a mass  $m_1 \approx 30 - 35 M_\odot$ , which is in the range of the secondary peak inferred from the LVK data (Abbott et al., 2019b, 2020c, 2021b; Farah et al., 2023; Callister & Farr, 2023). The secondary peak has usually been interpreted as a signature of the pair-instability mass gap, but recently this interpretation has been put into question because the lower edge of the gap should be at higher masses ( $> 50 M_\odot$ , e.g., Farmer et al., 2020; Costa et al., 2021; Woosley & Heger, 2021;

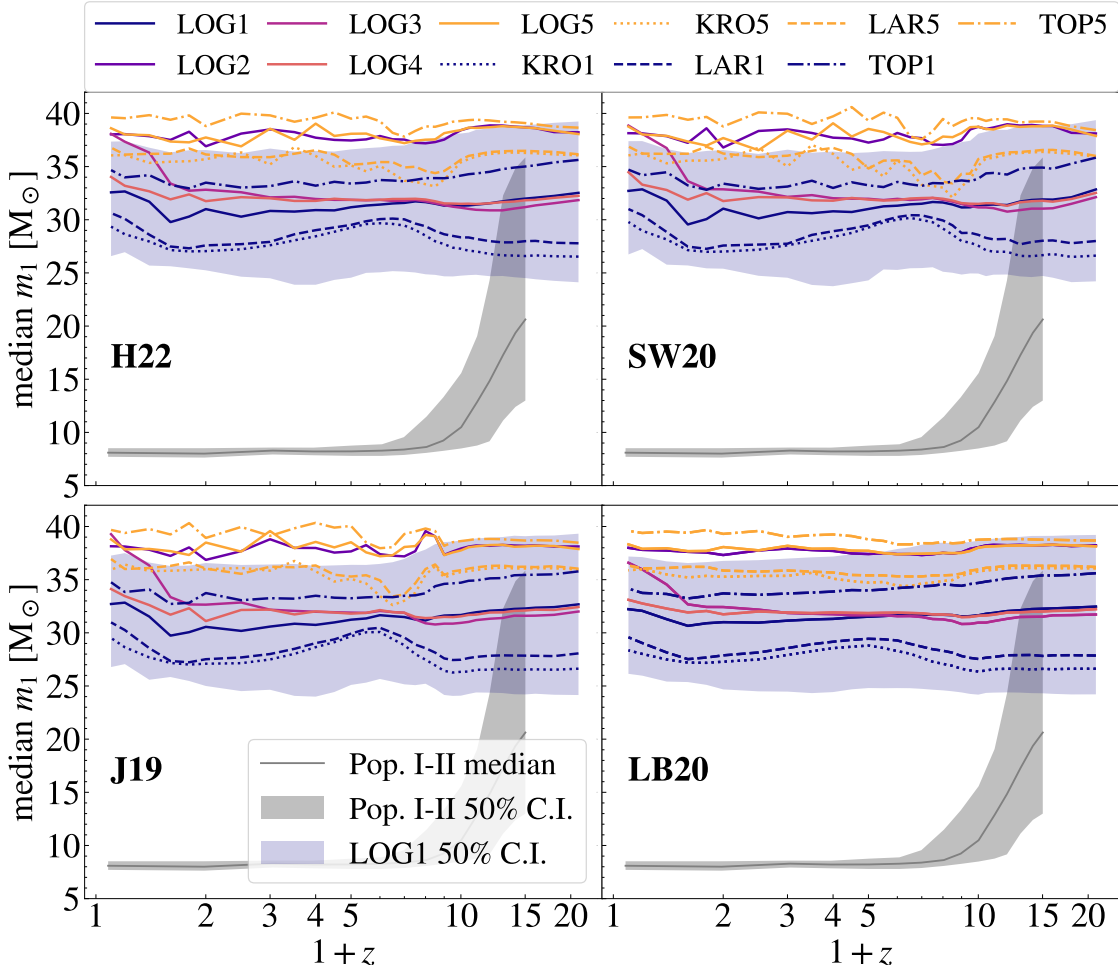


Figure 5.4: Median primary BH mass  $m_1$  as a function of redshift, for all the models considered in this work. The blue shaded area is the interval from the 25th to the 75th percentile of the primary BH mass distribution for the LOG1 model. Upper left-hand panel: H22 SFRD model, upper right-hand panel: SW20, lower left-hand panel: J19, and lower right-hand panel: LB20. The black thin solid line shows the median primary mass of Pop. I-II BBHs in our fiducial model (Appendix 5.8). The shaded grey area is the corresponding 50% credible interval.

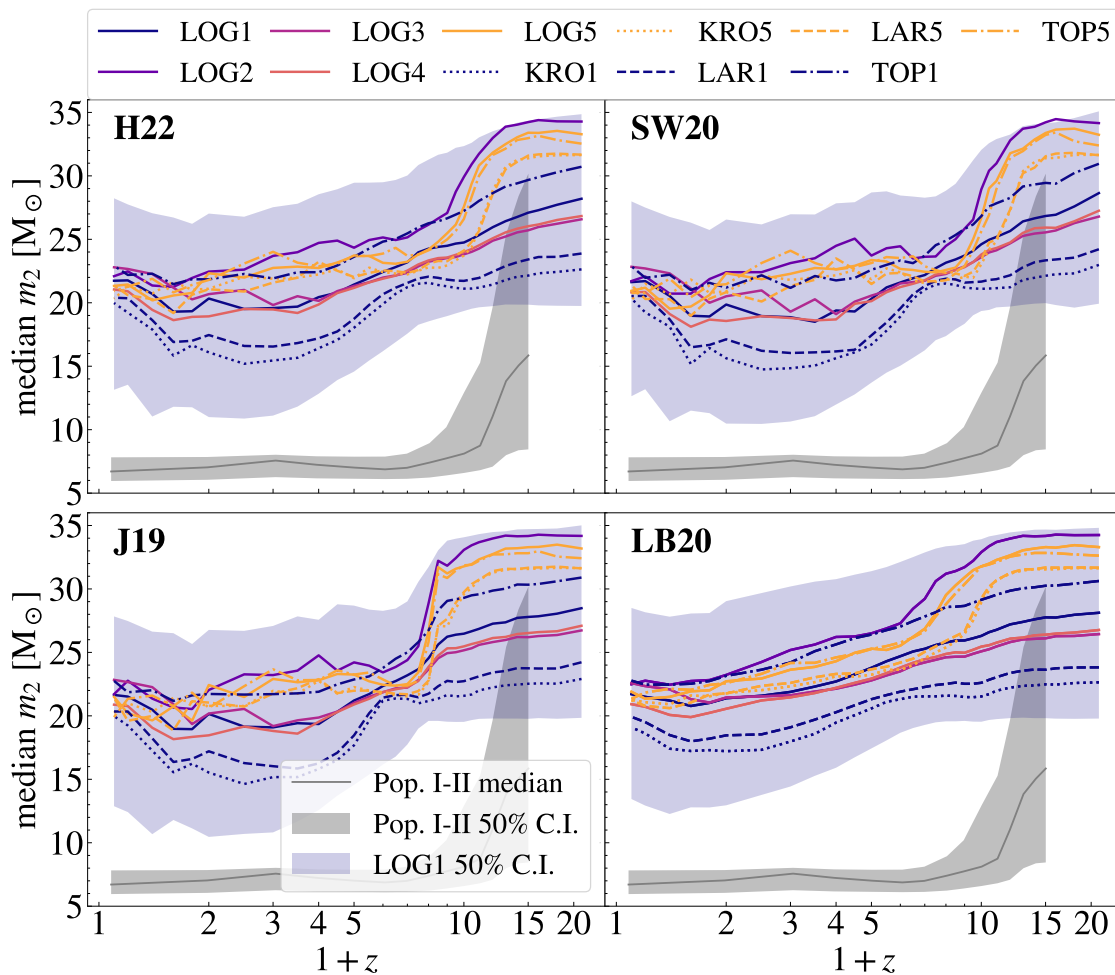


Figure 5.5: Same as Figure 5.4 but for the secondary BH mass  $m_2$ .

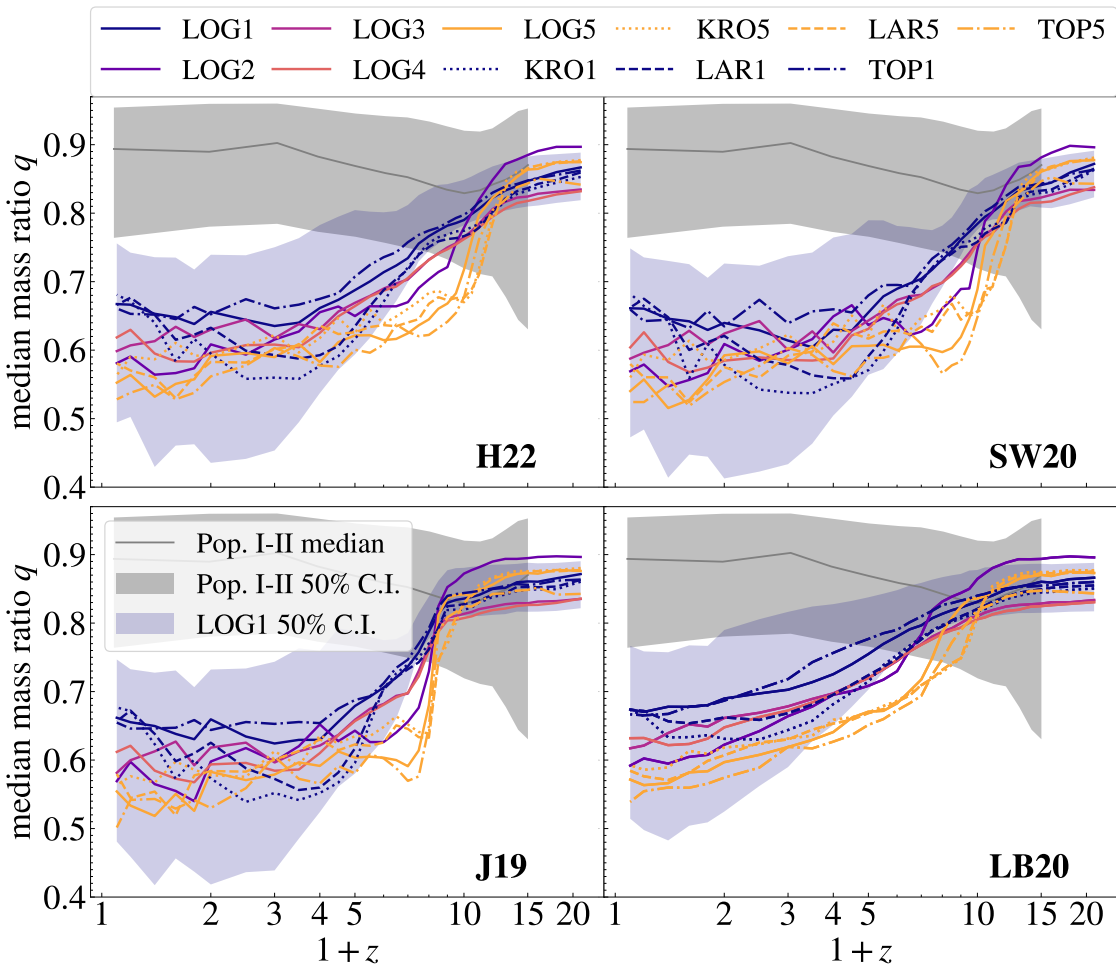


Figure 5.6: Same as Figure 5.4 but for the BH mass ratio  $q$ .

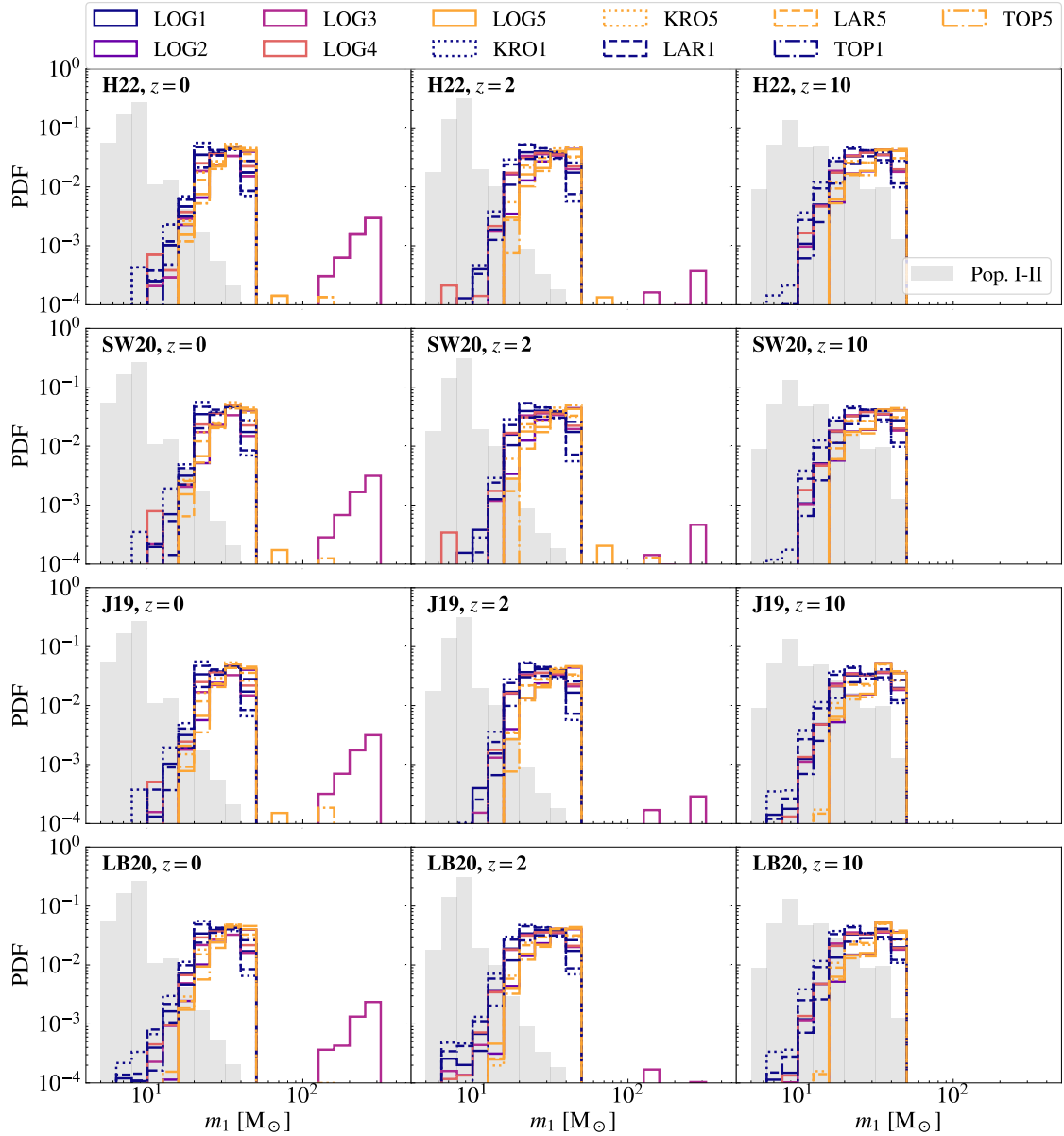


Figure 5.7: Primary BH mass distribution  $m_1$  for three different redshift bins (*in columns*:  $z = 0, 2$  and  $10$ ) and the four SFRD models considered in this work (*in rows*: H22, SW20, J19 and LB20).

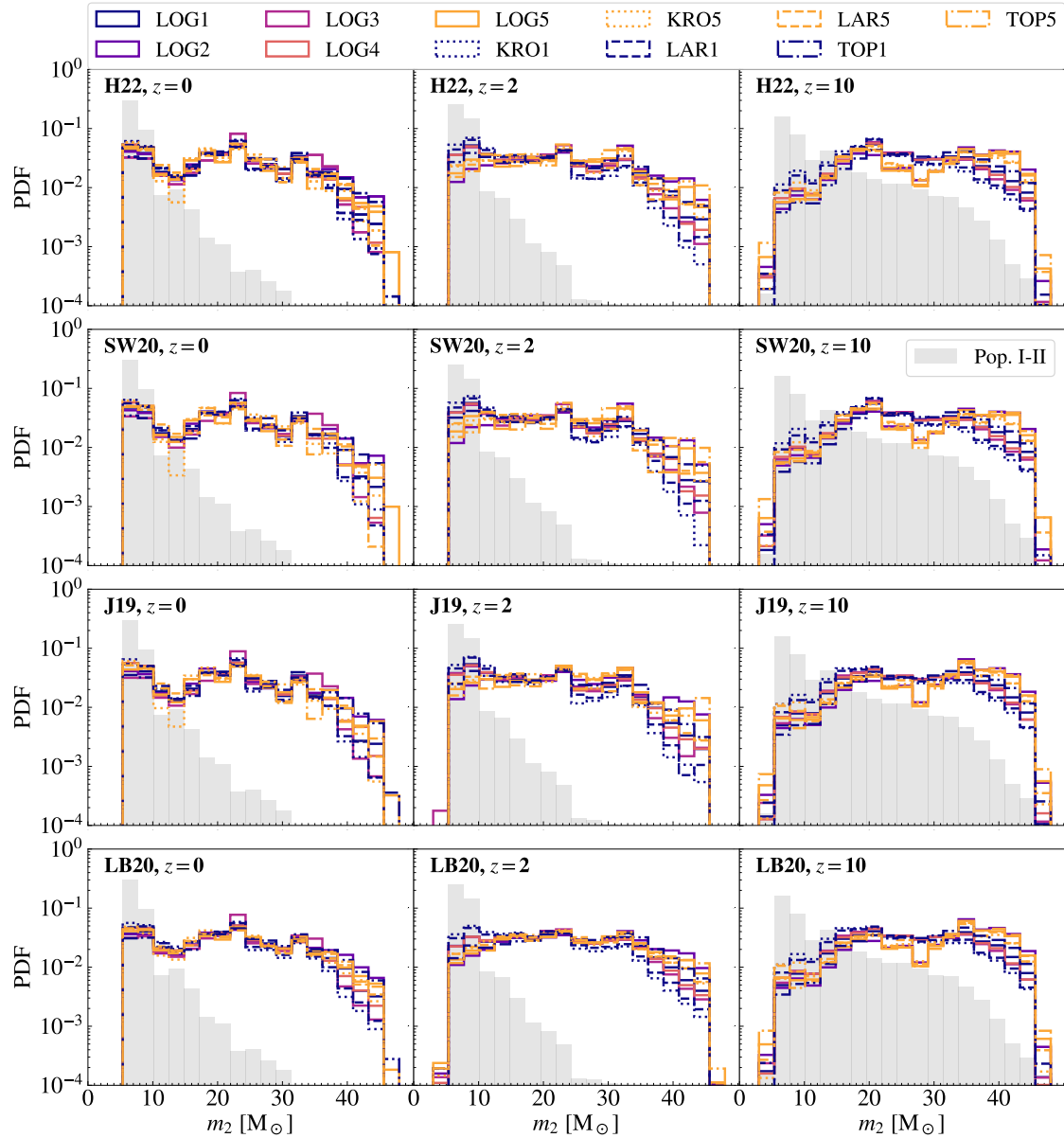


Figure 5.8: Same as Figure 5.7 but for the secondary BH mass  $m_2$ .

Vink et al., 2021; Farag et al., 2022). Our results indicate that the secondary peak at  $\sim 35 M_{\odot}$  might rather be a signature of the progenitor’s metallicity: metal-poor and metal-free stars in tight binary systems tend to end their life as naked helium cores with a mass of  $\sim 30 - 40 M_{\odot}$ , favouring a sub-population of BBHs in this mass range (Iorio et al., 2022; van Son et al., 2022a).

## 5.5 Discussion

### 5.5.1 The formation channels

To better understand the behaviour of Pop. III BBHs, we divide our sample into the four formation channels we already discussed in Iorio et al. (2022). Channel I includes all the systems that undergo a stable mass transfer before the first BH formation, and later evolve through at least one common-envelope phase. Channel II comprises the systems that interact through at least one stable mass transfer episode, without common envelopes.

Channel III and IV both include systems that undergo at least one common-envelope before the formation of the first BH. The only difference between these two channels is that in channel III one of the two components of the binary system still retains a residual fraction of its H-rich envelope at the time of the first BH formation, while in channel IV both stars have already lost their H-rich envelope at the time of the first BH formation.

Figure 5.9 shows the percentage of Pop. III binary stars evolving through each of the four channels and resulting in BBH mergers at  $z = 10$  (upper panel) and  $z = 0.1$  (lower panel). Channel I, which is commonly believed to be the main formation pathway for BBH mergers (e.g., Tauris & van den Heuvel, 2006; Belczynski et al., 2017a; Neijssel et al., 2019; Mandel & Müller, 2020; Broekgaarden et al., 2021), has marginal importance ( $\leq 7\%$ ) for Pop. III BBHs, regardless of the chosen initial conditions. This happens because mass transfer tends to remain stable in the late evolutionary stages, when the system is composed of a BH and a companion star, given the relative compactness of Pop. III stars with respect to Pop. I and II stars (Tanikawa et al., 2021b).

Channel II (stable mass transfer) is the dominant channel ( $\geq 50\%$ ) for most of our initial conditions, with the exception of LOG2, LOG5, KRO5, LAR5, and TOP5, for which channel II represents only 1 – 2% of all the mergers. The latter five models are the only ones in our sample adopting the SB13 distribution for the orbital periods, which are significantly longer than the S12 orbital periods. Indeed, the stable mass transfer channel favours high-mass binary stars that start with a short orbital separation ( $\leq 10^3 R_{\odot}$ ) and undergo a stable mass transfer early in their main sequence or Hertzsprung-gap phase (e.g., Pavlovskii et al., 2017; van den Heuvel et al., 2017; Giacobbo & Mapelli, 2018; Neijssel et al., 2019; Mandel & Müller, 2020; Marchant et al., 2021; Gallegos-Garcia et al., 2021). This predominance of the stable mass transfer in the case of Pop. III star BHs is in agreement with Kinugawa et al. (2016) and Inayoshi et al. (2017). The large orbital periods in SB13 suppress this channel, because they prevent the formation of binary systems with initial orbital separation  $< 10^3 R_{\odot}$ .

Channel III and IV are complementary to channel II: they contribute together to  $\sim 9 - 47\%$  of the BBH mergers when channel II is the dominant one and to  $> 90\%$  when

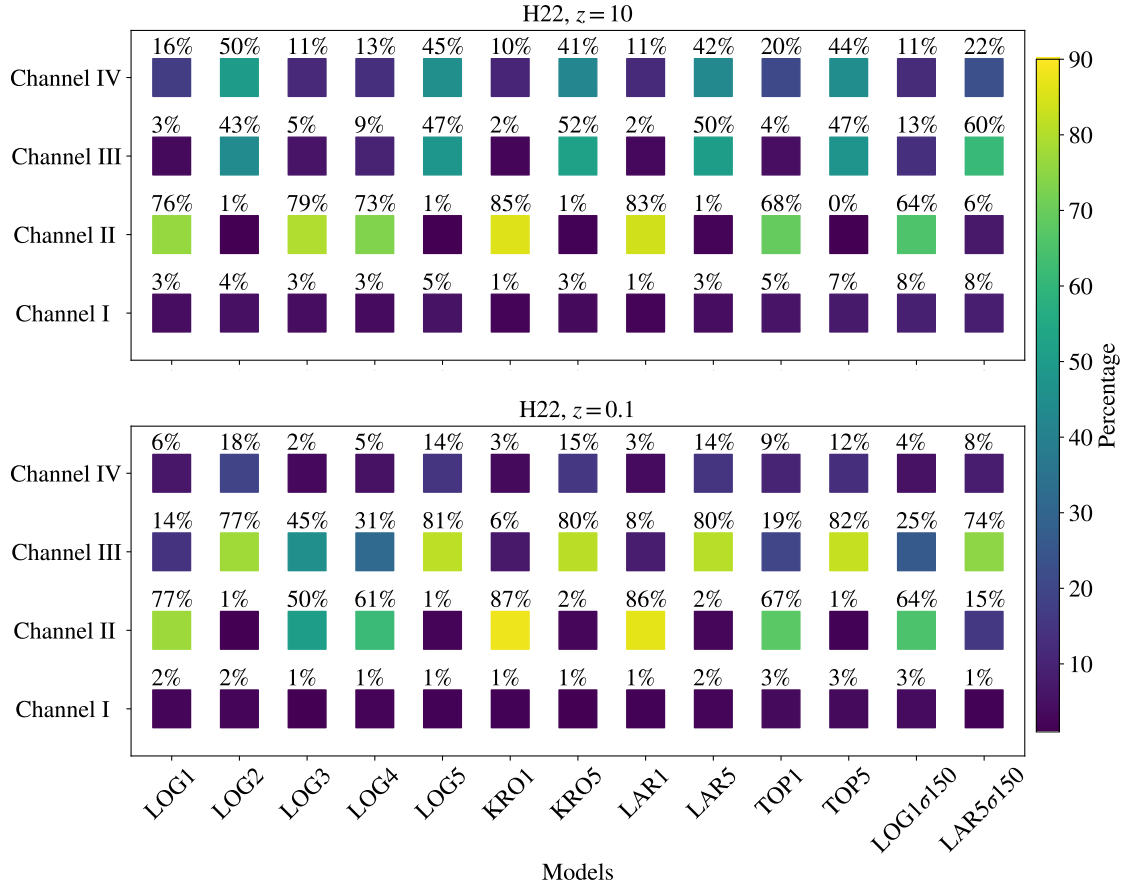


Figure 5.9: Percentage distribution of formation channels for all the models adopted in this work. Upper (lower) panel: Pop. III BBHs that merge at  $z = 10$  ( $z = 0.1$ ). *Channel I* includes all the systems that undergo a stable mass transfer before the first BH forms, and later evolve through at least one common-envelope phase. *Channel II* encompasses systems that interact only via stable mass transfer (no common envelopes). *Channels III* and *IV* consist in systems that experience at least one common envelope before the formation of the first BH. The only difference between them is that one of the two stars retains a fraction of its H-rich envelope until the formation of the first BH in *channel III*, while both stars have lost their envelope by the formation of the first BH in *channel IV*.

channel II is suppressed, i.e. for models LOG2, LOG5, KRO5, LAR5, and TOP5. In the latter five cases, the initial orbital periods are sufficiently large that the two stars start mass transfer only when their radii are significantly expanded, i.e. in the red giant phase. Because of their convective envelope, such mass transfer becomes unstable and triggers one or more common envelopes.

Channel III has generally longer delay times than channel IV (Figure 5.10) because it takes place in systems with low initial mass ratios the secondary star is generally less massive than the BH produced by the primary star and mass transfer episodes after the formation of the first BH do not shrink the orbit. The long delay times of channel III explain why it becomes more important at  $z = 0.1$  with respect to the high redshift.

### 5.5.2 The evolution of the secondary mass

Our models calculated with the distribution by GM20 for natal kicks show that the median secondary mass of Pop. III BBH mergers in the local Universe is significantly lower than that of Pop. III BBHs in the early Universe. This leads to a sub-population of unequal-mass BBHs ( $q \sim 0.1 - 0.7$ ), which might help us to identify Pop. III BBHs among the other LVK mergers, since most BBHs born from Pop. I-II stars are nearly equal mass in our simulations (Santoliquido et al., 2021; Iorio et al., 2022). Also, most LVK systems are nearly equal mass (Abbott et al., 2021b).

Figures 5.10 and 5.11 show that this trend is an effect of delay time: the majority of the unequal mass BBHs (i.e., with low-mass secondary BHs) come from channel II and III. These Figures show that low-mass secondary BHs have longer delay times in both channel II and III.

### 5.5.3 The effect of natal kicks

All the models we discussed so far adopt the natal kick model from GM20. This is our fiducial kick model because it naturally accounts for the claimed lower kicks in stripped and ultra-stripped supernovae (e.g., Bray & Eldridge, 2016; Tauris et al., 2017; Kruckow et al., 2018; Bray & Eldridge, 2018). On the other hand, model GM20 has a major impact on the formation channels, because it introduces a dependence of the kick on the BH and ejecta mass.

Here, we consider an alternative model  $\sigma 150$  (Section 5.2.1), in which the natal kicks have been randomly drawn from a Maxwellian distribution with parameter  $\sigma = 150 \text{ km s}^{-1}$ . In this alternative model, the natal kicks do not depend on the properties of the system. This implies that the  $\sigma 150$  kicks are generally larger for stripped/ultra-stripped binaries and for high-mass BHs than the GM20 kicks. This difference has a substantial impact on channel III.

Figure 5.10 shows the delay time distribution for four models: KRO1 and LAR5 adopt the kick distribution by GM20, while KRO1 $\sigma 150$  and LAR5 $\sigma 150$  adopt the  $\sigma 150$  model. We distinguish the delay times of the four channels. The kick model barely affects channels II and IV, while it has a strong impact on channels I and III. Model  $\sigma 150$  slightly increases the number of channel I BBH mergers, from nearly 0 to a few per cent. Most importantly, model

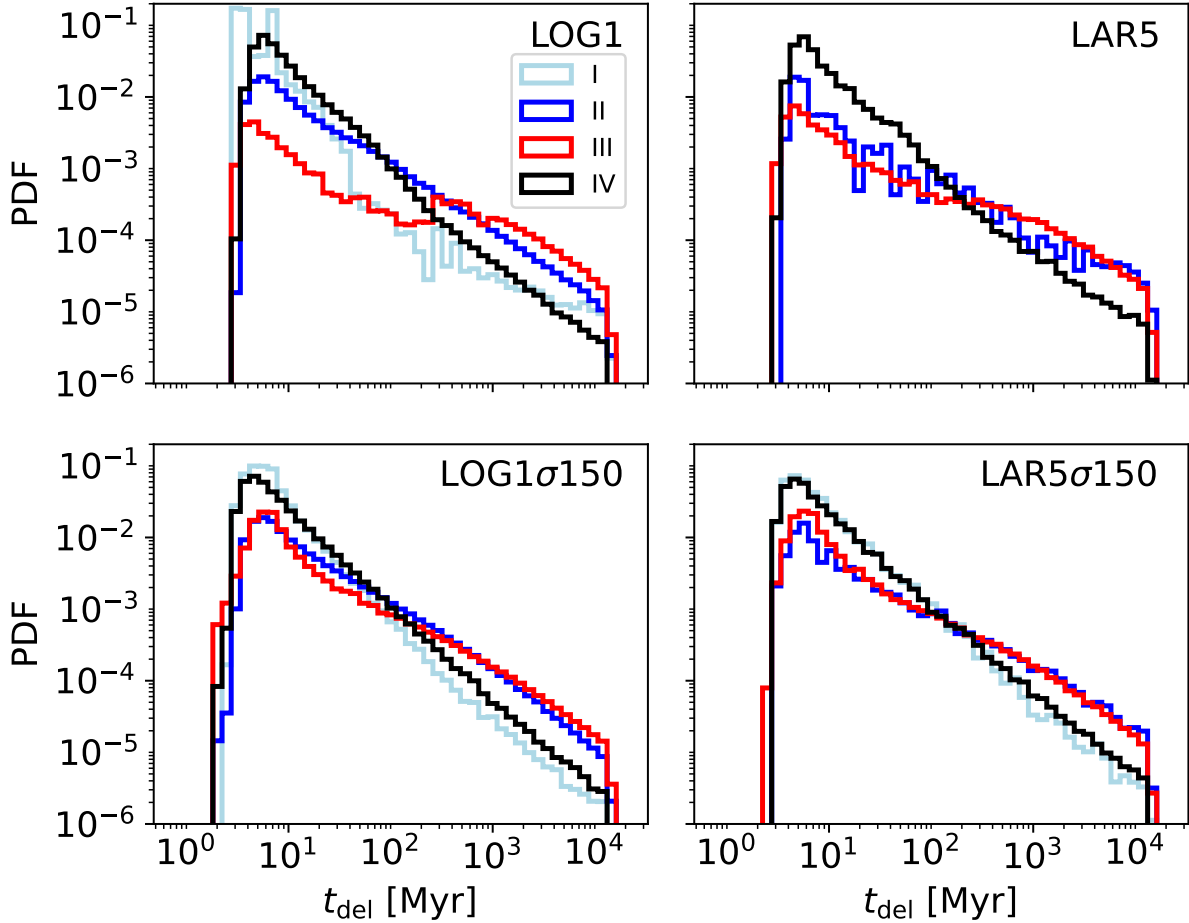


Figure 5.10: Distribution of delay times for models LOG1, LAR5, LOG1 $\sigma$ 150 and LAR5 $\sigma$ 150. Light-blue line: channel I; blue line: channel II; red line: channel III; black line: channel IV. Channel I is not shown in the case of LAR5 because of the low number of systems. These data come directly from the SEVN catalogues and are not convolved with redshift evolution.

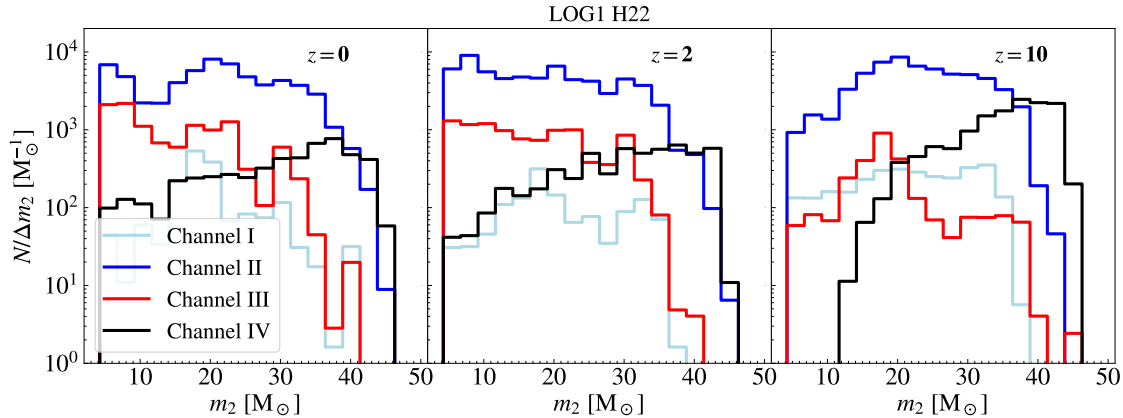


Figure 5.11: Secondary BH mass distribution  $m_2$  for three different redshift bins (from left to right:  $z = 0, 2$ , and  $10$ ). Light-blue line: channel I; blue line: channel II; red line: channel III; black line: channel IV.

$\sigma 150$  wildly changes the delay-time distribution of channel III mergers, populating the region of short delay times.

This difference springs from the impact of the natal kick on the orbital eccentricity. A larger kick either splits the binary, or increases its orbital eccentricity. Since the time of gravitational decay  $t_{\text{GW}} \propto (1 - e^2)^{7/2}$  (Peters, 1964), a large eccentricity speeds up the BBH merger significantly. This effect is particularly important for channel III BBHs because they start from a large initial semi-major axis of the progenitor binary ( $10^2 - 10^5 R_\odot$ ) and have lower secondary BH masses than the other channels (Costa & et al., 2023).

The different delay time distribution of channel III has an obvious impact on the median mass of the secondary BH. Figure 5.12 shows the evolution of the median secondary BH mass for models KRO1, LAR5, KRO1 $\sigma 150$ , and LAR5 $\sigma 150$  (the same models as in Figure 5.10). The decrease of the median secondary BH mass with redshift almost completely disappears in the models with  $\sigma 150$ , because of the larger number of channel III mergers and of their different delay time distribution.

Still, the SN kick does not have a large impact on the merger rate density evolution of Pop. III BBHs, as shown in Fig. 5.13. The merger rate density of model LAR5 $\sigma 150$  is higher by a factor of two at the peak redshift ( $z = 13$ ), where the variation of the number of channel III mergers is larger.

#### 5.5.4 BBH mergers above the mass gap

The long delay times of channel III explain why we have BBH mergers with primary BH mass above the mass gap ( $> 120 M_\odot$ ) only at low redshift in Figure 5.7, mainly in model LOG3. This model is the only one adopting a sorted distribution to pair up the progenitor stars. Hence, it is the one with the lowest initial mass ratios ( $M_{\text{ZAMS},1}/M_{\text{ZAMS},2}$ ). Systems with  $M_{\text{ZAMS},1} \geq 250 M_\odot$  and initial semi-major axis  $a_{\text{initial}} \in [10^3, 1.5 \times 10^5] R_\odot$  evolve nearly unperturbed until the primary star becomes a giant star and fills its Roche lobe (Figure 5.14). In channel III, the Roche lobe overflow becomes unstable and triggers a common envelope

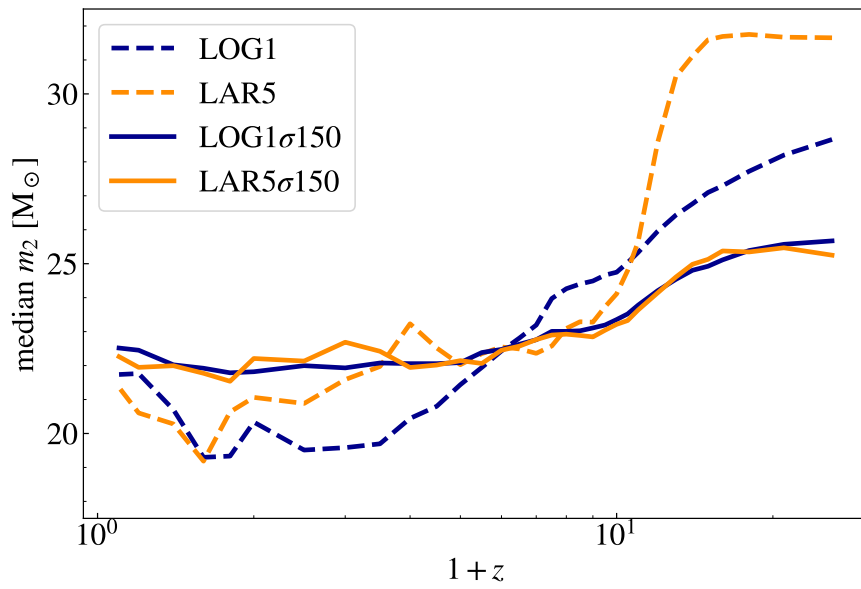


Figure 5.12: Evolution of the median secondary BH mass  $m_2$  as a function of redshift, for KRO1 and LAR5, with the H22 star formation rate. Solid (dashed) line: natal kicks drawn from model  $\sigma$ 150 (GM20).

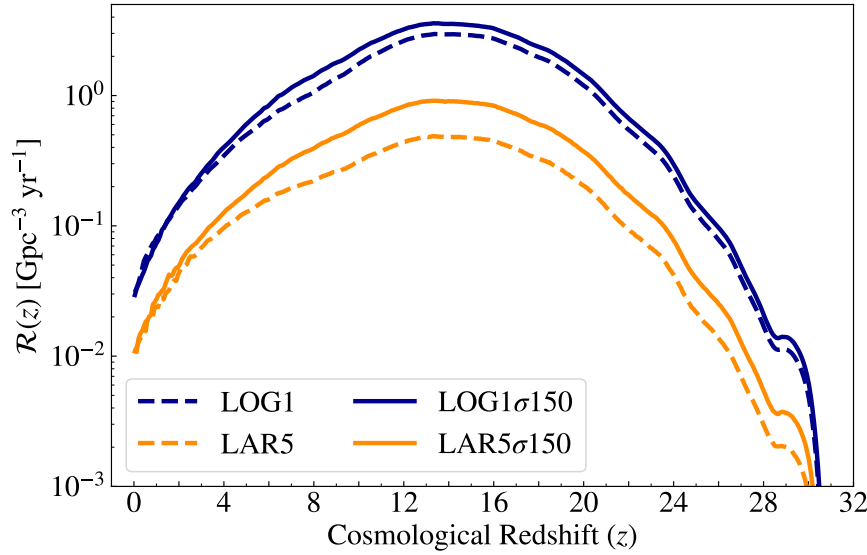


Figure 5.13: Evolution of the merger rate density with redshift  $\mathcal{R}(z)$  for KRO1 and LAR5, with the H22 star formation rate. Solid (dashed) line: natal kicks from model  $\sigma$ 150 (GM20).

which removes the H-rich envelope of the primary star. Short after the common envelope, the primary star collapses to a BH above the pair-instability mass gap. Then, the binary evolves nearly unperturbed until the secondary star also becomes a BH. Given the large semi-major axis at the time of formation of the secondary BH ( $\approx 100 R_\odot$ ) and the relatively low mass of the secondary BH ( $m_2 \sim 10 - 30 M_\odot$ ), such binaries have a long delay time, of the order of 5 – 12 Gyr (Figure 5.14).

### 5.5.5 Merger Rate Density of BBHs born from Pop. II stars

Here, we compare the merger rate density of BBHs born from Pop. II and Pop. III stars (Figure 5.15). For both Pop. II and III stars we adopt the SFRDs from H22 (grey and purple lines in Figure 5.1). We linearly extrapolate the SFRD of Pop. III stars derived by H22 down to redshift  $z = 0$ , whereas we assume that the SFRD of Pop. II stars becomes zero for  $z < 4$ . This gives us a lower limit to the contribution of Pop. II binary stars to the present day BBH merger rate density. For the input BBH catalogues of Pop. II stars, we use the SEVN runs by Costa & et al. (2023) at  $Z = 10^{-4}$ . Our fiducial model in the case of Pop. II stars is KRO1, adopting the K01 IMF and the orbital properties from Sana et al. (2012). We assume that the IMF of Pop. II stars extends down to  $0.1 M_\odot$ . Since we simulated only stars with primary mass  $m_1 > 5 M_\odot$ , we introduce a correction to the merger rate density, in order to account for the contribution of the low-mass Pop. II stars to the total initial stellar mass (Appendix 5.8). We do not apply such correction to the merger rate density of Pop. III BBHs, because we do not know what is the minimum mass of Pop. III stars.

We find that the merger rate density of Pop. II BBHs is at least one order of magnitude more important than that of Pop. III BBHs within the instrumental horizon of LIGO and Virgo, even if we make very conservative assumptions for Pop. II stars (e.g., we assume that the SFRD of Pop. II stars becomes zero at  $z < 4$ ). The merger rate density of Pop. III BBHs becomes higher than that of Pop. II BBHs only at high redshift. For example, if we assume the KRO1 model for Pop. II stars and the LOG1 model for Pop. III stars, the two merger rate density become equal only at  $z \approx 20$ .

The lower panel of Figure 5.15 shows that our Pop. III binary stars produce a very low merger rate density of BBHs with primary BH mass<sup>1</sup>  $m_1 > 60 M_\odot$  in the local Volume [ $\mathcal{R}(m_1 > 60 M_\odot, z = 0) < 10^{-4} \text{ Gpc}^{-3} \text{ yr}^{-1}$ ], apart from the LOG3 model [ $\mathcal{R}(m_1 > 60 M_\odot, z = 0) \approx 4 \times 10^{-3} \text{ Gpc}^{-3} \text{ yr}^{-1}$ ].

For all the other models, we expect that Pop. II stars give a larger contribution to the merger rate density of BBH mergers with primary BH mass  $m_1 > 60 M_\odot$  in the low-redshift Universe, with a  $\mathcal{R}(m_1 > 60 M_\odot, z = 0) = 10^{-3} - 10^{-1} \text{ Gpc}^{-3} \text{ yr}^{-1}$ , if we adopt the SFRD of Pop. II stars from H22.

Figure 5.15 highlights one important issue that has already been discussed in several manuscripts and is common to different binary population synthesis codes: the more we improve our assumptions about the evolution of metallicity and SFRD in the Universe (e.g., Boco et al., 2019; Eldridge et al., 2019; Santoliquido et al., 2022; Mandel & Broekgaarden, 2022), the poorer is the agreement between the merger rate density of BBHs from the isolated

<sup>1</sup>Here, we consider  $m_1 = 60 M_\odot$  as the lower edge of the pair-instability mass gap, because this is the most common value adopted in the literature (e.g., Abbott et al., 2020f).

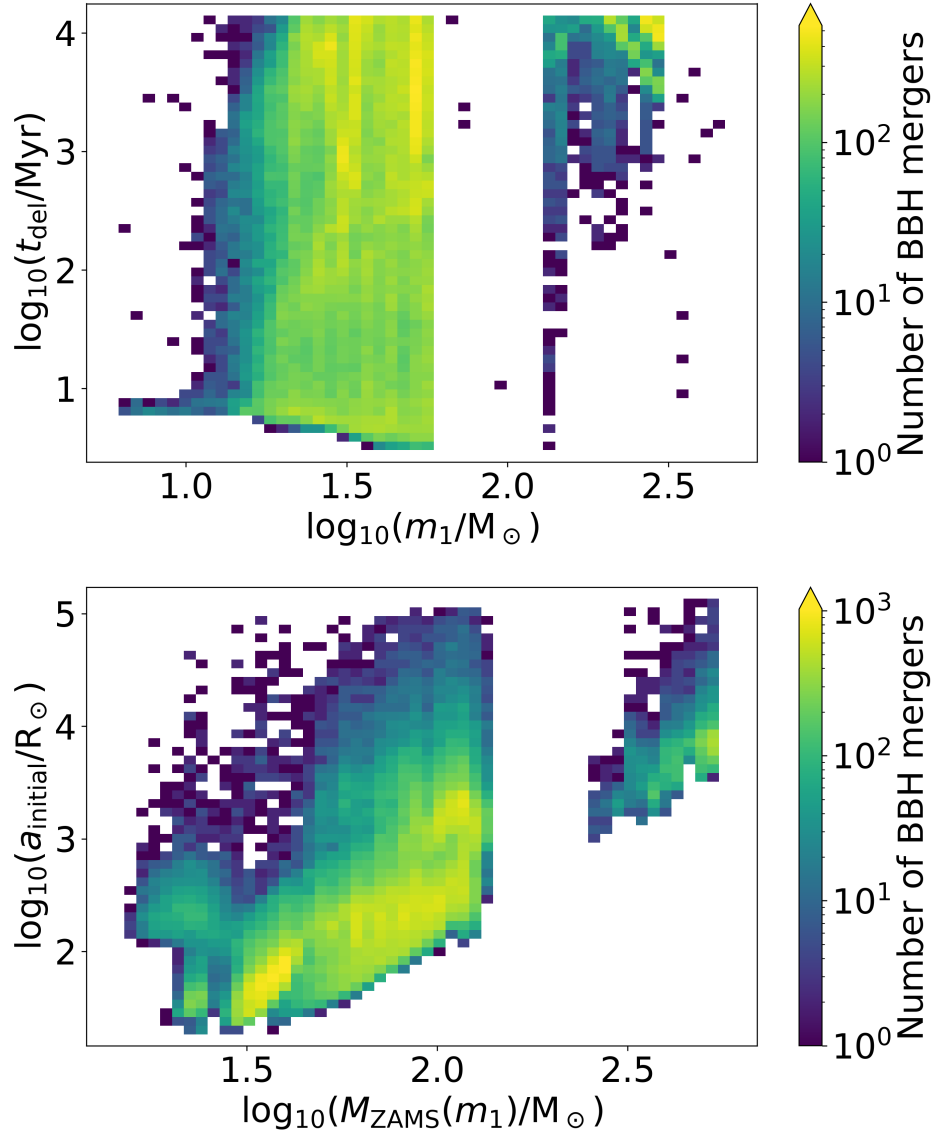


Figure 5.14: Properties of Pop. III BBH mergers and their progenitors in model LOG3. Upper panel: delay time  $t_{\text{del}}$  as a function of the primary BH mass  $m_1$ . Lower panel: initial semi-major axis of the progenitor binary star  $a_{\text{initial}}$  versus ZAMS mass of the progenitor of the primary BH  $M_{\text{ZAMS}}(m_1)$ . These data come directly from the SEVN catalogues and are not convolved with redshift evolution.

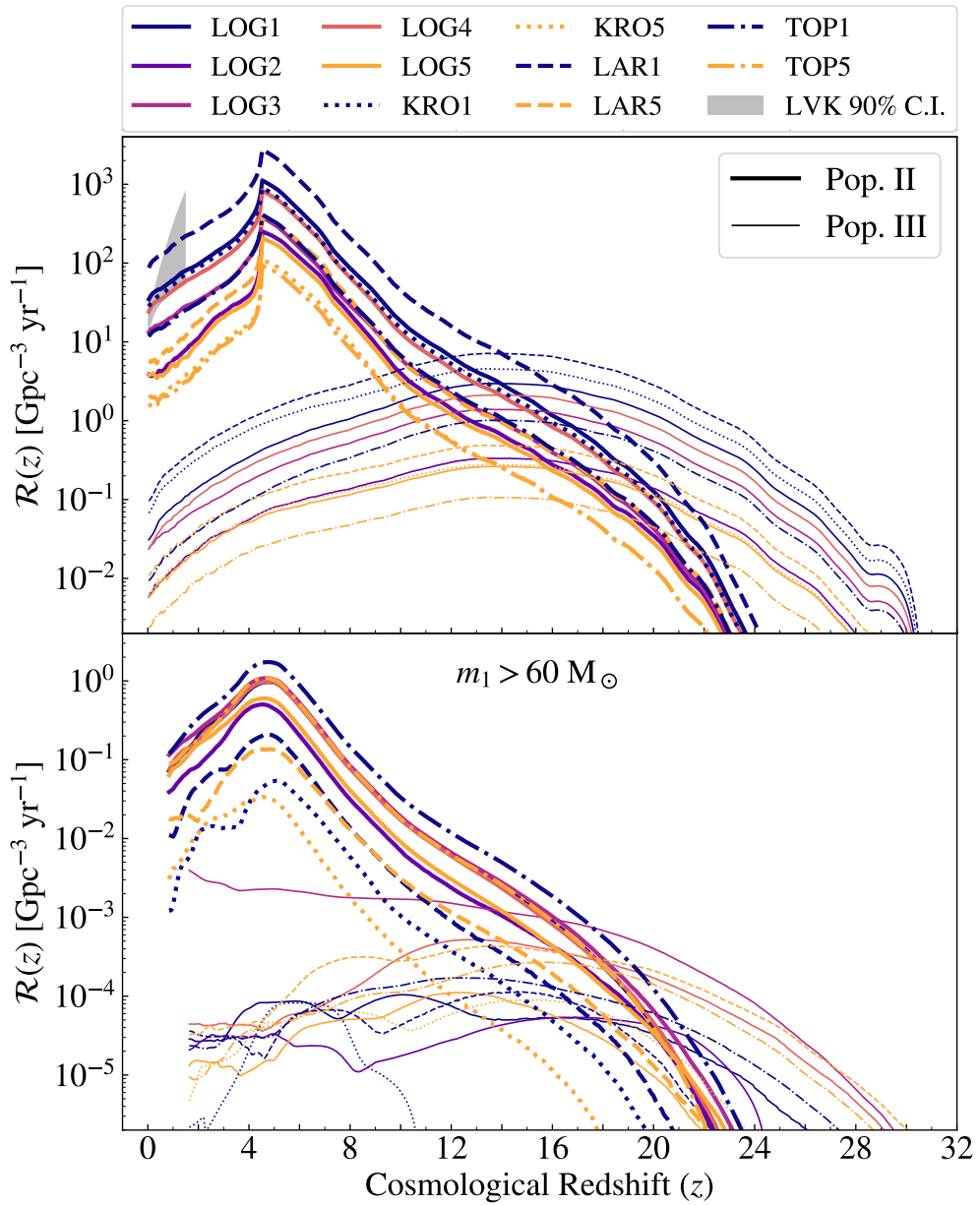


Figure 5.15: Upper panel: merger rate density evolution with redshift of BBHs born from Pop. II stars (thick lines) compared to BBHs from Pop. III stars (thin lines). For Pop. II and Pop. III stars we use the corresponding SFRD from H22 (Figure 5.1). The colours and line types refer to the same initial orbital parameters for both Pop. II and III stars (Table 5.1). The grey shaded area is the 90% credible interval inferred by the LIGO-Virgo-KAGRA collaboration (Abbott et al., 2021b). Lower panel: same as in the upper panel but for BBHs with primary mass  $m_1 > 60 M_\odot$ .

binary evolution channel and the values inferred by LVK (Abbott et al., 2021b). In particular, the present-day BBH merger rate density tends to be too high because of the high efficiency of BBH mergers from metal-poor progenitors (e.g., Klencki et al., 2018), so that even a small sub-population of metal-poor binary stars in the local Universe can lead to a very high present-day BBH merger rate density (e.g., Chruslinska et al., 2019; Chruślińska et al., 2020; Chruślińska, 2022). In our fiducial model, the present-day merger rate density of Pop. II BBHs is sufficient to explain the LVK rate, even if we assume that Pop. II formation stops at  $z = 4$ . Furthermore, here we are not considering the contribution to the merger rate density of the dynamical formation channels (e.g., Rodriguez et al., 2018; Santoliquido et al., 2020). We caution that this result strongly depends on many assumptions about the stellar-evolution model and stable/unstable mass transfer (e.g., Iorio et al., 2022).

### 5.5.6 Comparison with previous work

We do not find any BBH mergers with primary mass inside the pair-instability gap, while Tanikawa et al. (2022b) find this sub-population of mergers in their fiducial model. This is mainly an effect of the different stellar radii. Tanikawa et al. (2022b) produce this sub-population of BBH mergers from binary stars with primary ZAMS mass  $\sim 65 - 90 M_{\odot}$ . In their fiducial model, such stars have radii  $R < 100 R_{\odot}$  for their entire life, while in our models they expand much more during the end of the main sequence and the red giant phase (Costa & et al., 2023). This springs from the choice of core overshooting: we assume an overshooting parameter  $\Lambda_{ov} = 0.5$  Hp, which corresponds to  $f_{ov} = 0.025$  in the formalism adopted by Tanikawa et al. (2022b), while they assume  $f_{ov} = 0.01$  in the fiducial model (M-model). Indeed, our models are similar to the L-std model by Tanikawa et al. (2022b), with  $f_{ov} = 0.03$ . Indeed, in the L-std model, they find no mergers with primary BH mass inside the mass gap (Fig. 6 of Tanikawa et al. 2022b).

Tanikawa et al. (2022b) merger rate density of Pop. III BBHs reaches a maximum of  $R(z \sim 10) \approx 20 \text{ Gpc}^{-3} \text{ yr}^{-1}$ . For initial orbital parameters, their model is almost identical to our LOG1 model. They use the SFRD by Skinner & Wise (2020), which is similar to A-SLOTH (within a factor of two) and peaks at  $z \sim 20$ . In our model LOG1 the merger rate peaks at  $z \sim 15$  and  $R(z \sim 15) \approx 3.5 \text{ Gpc}^{-3} \text{ yr}^{-1}$ . The difference in the redshift of the peak, which is  $z \sim 15$  and 10 between us and Tanikawa et al. (2022b) with the SW20 SFRD, is a consequence of the delay time distribution. Tanikawa et al. (2022b) have significantly longer delay times, even for their model L-std (see Figure 3 from Tanikawa et al., 2021a). The large difference in the normalization of the peak between our work and Tanikawa et al. (2022b) is a consequence of the differences in our stellar and binary evolution models. In particular, our larger stellar radii increase the risk that two possible progenitor stars collide leaving just one single star, before they become a BBH.

## 5.6 Summary and conclusions

We estimated the merger rate density evolution of binary black holes (BBHs) born from Pop. III stars (Figure 5.3) by means of our code COSMORATE (Santoliquido et al., 2021). To

evaluate the main uncertainties affecting the merger rate density, we explored a large portion of the parameter space, consisting of four different models for the formation history of Pop. III stars (from Jaacks et al. 2019, J19, Liu & Bromm 2020b, LB20, Skinner & Wise 2020, SW20, and Hartwig et al. 2022, H22), and eleven different configurations of the initial orbital properties of Pop. III binary stars. In particular, we probe different IMFs (flat-in-log, K01, L98, and top-heavy), mass ratios (S12, sorted), orbital period distributions (S12, SB13), and eccentricity distributions (S12, thermal), as described in Table 5.1. We generated the catalogues of Pop. III BBHs with our binary population-synthesis simulation code SEVN (Iorio et al., 2022), based on a new set of Pop. III stellar tracks with metallicity  $Z = 10^{-11}$  and ZAMS mass  $m_{\text{ZAMS}} \in [2.2, 600] \text{ M}_\odot$  (Costa & et al., 2023).

The assumed star formation rate history of Pop. III stars affects both the normalisation and the shape of the BBH merger rate density evolution with redshift (Fig. 5.3):  $\mathcal{R}(z)$  peaks at  $z_p \approx 8 - 10$  for the models by J19 and LB20, and at  $z_p \approx 12 - 16$  for H22 and SW20. For our fiducial model LOG1, the maximum merger rate density ranges from  $\mathcal{R}(z_p) \approx 30 \text{ Gpc}^{-3} \text{ yr}^{-1}$  for the star formation rate density (SFRD) by J19 down to  $\mathcal{R}(z_p) \approx 2 - 4 \text{ Gpc}^{-3} \text{ yr}^{-1}$  for the SFRDs by SW20, H22, and LB20. At redshift  $z = 0$ , all the considered SFRD models yield  $\mathcal{R}(0) \leq 2 \times 10^{-1} \text{ Gpc}^{-3} \text{ yr}^{-1}$  in our fiducial model LOG1, about two orders of magnitude lower than the local BBH merger rate density inferred from LVK data (Abbott et al., 2021b). Overall, changing the SFRD model for Pop. III stars affects the BBH merger rate density by up to about one order of magnitude. In the case of the SFRD derived by H22, we can also account for the intrinsic uncertainties of the SFRD calibration on data. We find that the merger rate density changes by about one order of magnitude within the 95% credible interval of the Pop. III SFRD estimated by H22 (Fig. 5.2).

The initial orbital properties of our Pop. III binary systems have an even larger impact on the BBH merger rate density, up to two orders of magnitude (Fig. 5.3). The models adopting a SB13 distribution for the initial orbital periods (LOG2, LOG5, KRO5, LAR5, and TOP5) have lower merger rate densities than models adopting the distribution by S12 (LOG1, LOG3, LOG4, KRO1, LAR1, and TOP1). The reason is that short orbital periods, as in the case of S12, favour the merger of BBHs via stable mass transfer episodes between the progenitor stars, while large orbital periods (SB13) suppress these systems.

We estimated the mass distribution of Pop. III BBHs for all of our models and as a function of redshift. Both the primary and secondary BH (i.e., the most and least massive member of a BBH) born from a Pop. III binary star tend to be substantially more massive than the primary and secondary BH born from a metal-rich binary star (Figs. 5.7, 5.8). This happens mainly because stellar winds are suppressed at low  $Z$ . The median mass of the primary BHs born from Pop. III stars is  $m_1 \approx 30 - 40 \text{ M}_\odot$  across the entire redshift range, while the median mass of primary BHs born from metal-rich stars is  $m_1 \approx 8 \text{ M}_\odot$  (Fig. 5.4). This result does not depend on the adopted SFRD and is only mildly sensitive to the initial orbital properties of Pop. III binary stars.

The mass spectrum of primary BHs inferred by the LVK (Abbott et al., 2021b) is characterised by two peaks, the main one at  $8 - 10 \text{ M}_\odot$  and the other at  $\sim 35 \text{ M}_\odot$ . The location of these two peaks is remarkably similar to the median mass of the primary BHs born from metal-rich and metal-free/metal-poor stars in our simulations.

The mass ratio  $q$  between the secondary and primary BH is another feature that dis-

tinguishes BBHs born from Pop. III and metal-rich binary stars (Fig. 5.6). At low redshift ( $z \leq 4$ ), BBH mergers from Pop. III stars have low mass ratios (median values  $q \approx 0.5 - 0.7$ ) with respect to BBH mergers from metal-rich stars (median values  $q \approx 0.9$ ). In contrast, at high redshift even BBH mergers from Pop. III stars have a typical  $q \sim 0.9$ . This happens because the median secondary BH mass of Pop. III BBH mergers decreases with redshift. This feature is a consequence of the delay time distribution: Pop. III BBHs with relatively small secondary BH mass are associated with longer delay times than Pop. III BBHs with equal mass BHs (Fig. 5.10). This dependence of the delay time on the secondary BH mass is a consequence of the formation channels of our Pop. III BBHs. It is not affected by the adopted SFRD and is only mildly sensitive to the initial orbital properties of Pop. III binary stars, but it is highly sensitive to the assumed natal kick distribution. In our fiducial models, we assume that natal kicks are lower for more massive BHs and for (ultra-)stripped binary systems. If we instead use a natal kick model in which the kick magnitude does not depend on the properties of the system, the decrease of the median secondary BH mass with redshift almost disappears.

In our fiducial model (LOG1) and all the other models assuming the initial orbital period distribution by S12, most ( $> 50\%$ ) of our Pop. III BBHs evolve via stable mass transfer episodes, without common envelope phases. This is a consequence of the rather compact radii of our Pop. III stars and of our assumption that mass transfer is always stable during the main sequence and Hertzsprung gap phases.

Even if most of our BBH mergers from Pop. III stars are rather massive ( $m_1 \approx 30 - 40 M_\odot$ ), BBHs with mass above or inside the pair-instability mass gap are extremely rare in our models. For example, assuming the SFRD by H22, we find that the local merger rate of Pop. III BBHs with primary BH mass  $m_1 > 60 M_\odot$  is  $< 10^{-4} \text{ Gpc}^{-3} \text{ yr}^{-1}$  in all of our models but LOG3, for which we find  $\approx 4 \times 10^{-3} \text{ Gpc}^{-3} \text{ yr}^{-1}$ . For comparison, the local merger rate density of BBHs with primary BH mass  $m_1 > 60 M_\odot$  born from Pop. II stars ( $Z = 10^{-4}$  in our models) is  $\gtrsim 10^{-3} \text{ Gpc}^{-3} \text{ yr}^{-1}$ , about one order of magnitude higher than our fiducial model for Pop. III stars (LOG1).

Our results show that the overall uncertainty on the merger rate density evolution of Pop. III BBHs mergers spans at least two orders of magnitude and depends on the SFRD model, initial orbital properties of Pop. III binary stars, and stellar/binary evolution physics. Future work should further explore the impact of stellar evolution (e.g., rotation, chemically homogeneous evolution, core overshooting) and different assumptions for mass and angular momentum evolution during mass transfer.

## 5.7 Appendix

## 5.8 Comparison sample of BBHs from Pop. I–II stars

In Figures 5.4–5.8, we compare the masses of Pop. III BBHs with those of Pop. I+II BBHs. The latter are the fiducial model presented in [Iorio et al. \(2022\)](#). Here, we briefly summarise their main features but we refer to [Iorio et al. \(2022\)](#) for more details. We simulated 5M

binary star systems<sup>2</sup> for each of the following 15 metallicities:  $Z = 10^{-4}, 2 \times 10^{-4}, 4 \times 10^{-4}, 6 \times 10^{-4}, 8 \times 10^{-4}, 10^{-3}, 2 \times 10^{-3}, 4 \times 10^{-3}, 6 \times 10^{-3}, 8 \times 10^{-3}, 10^{-2}, 1.4 \times 10^{-2}, 1.7 \times 10^{-2}, 2 \times 10^{-2}, 3 \times 10^{-2}$ . The total number of simulated binary systems is thus 75M, ensuring that stochastic fluctuations are not important (Iorio et al., 2022).

The set-up of these simulations is the same as model KRO1, apart from the IMF mass range. In fact, we randomly drew the initial ZAMS mass of primary stars from a K01 IMF with  $M_{\text{ZAMS},1} \in [5, 150] M_{\odot}$  instead of  $[5, 550] M_{\odot}$ . We randomly selected the masses of secondary stars assuming the distribution of mass ratios from Sana et al. (2012) with a lower mass limit of  $M_{\text{ZAMS},2} = 2.2 M_{\odot}$ . The initial orbital periods and eccentricities have also been generated according to the distributions by Sana et al. (2012). The set-up of SEVN is the same as we describe in Section 5.2.1.

From these simulations we extract our catalogues of Pop I and II BBH mergers, which we use as input conditions for COSMORATE. We calculate the merger rate density of these metal-rich BBHs in the same way as described in Section 5.3, and in particular in Eq. 2.1. To calculate  $\text{SFRD}(z', Z) = \psi(z') p(z', Z)$ , in this case we use

$$\psi(z) = a \frac{(1+z)^b}{1 + [(1+z)/c]^d} [\text{M}_{\odot} \text{ yr}^{-1} \text{ Mpc}^{-3}], \quad (5.16)$$

where  $a = 0.01 \text{ M}_{\odot} \text{ Mpc}^{-3} \text{ yr}^{-1}$  (for a K01 IMF),  $b = 2.6$ ,  $c = 3.2$  and  $d = 6.2$ , from Madau & Fragos (2017).

We also assume an average metallicity evolution from Madau & Fragos (2017):

$$p(z', Z) = \frac{1}{\sqrt{2\pi}\sigma_Z^2} \exp \left\{ - \frac{[\log(Z(z')/Z_{\odot}) - \langle \log Z(z')/Z_{\odot} \rangle]^2}{2\sigma_Z^2} \right\}, \quad (5.17)$$

where  $\langle \log Z(z')/Z_{\odot} \rangle = \log \langle Z(z')/Z_{\odot} \rangle - \ln(10)\sigma_Z^2/2$  and  $\sigma_Z = 0.2$  (Bouffanais et al., 2021). Finally, in the calculation of the total initial stellar mass  $M_{\text{TOT}}$ , we introduce a term  $M_{\text{TOT}} = M_{\text{sim}}/f_{\text{IMF}}$ , where  $M_{\text{sim}}$  is the total initial simulated stellar mass and  $f_{\text{IMF}} = 0.285$ , to account for the fact that we simulate only stars with  $M_{\text{ZAMS},1} > 5 M_{\odot}$  and  $M_{\text{ZAMS},2} > 2.2 M_{\odot}$ , but we expect the K01 IMF to extend down to  $0.1 M_{\odot}$ .

In, Fig. 5.15 we show the BBH merger rate density produced by Pop. II alone. In this case, instead of using  $\psi(z)$  from Eq. 5.16, which is the total cosmic star formation rate density regardless of the metallicity, we adopt the star formation rate density  $\psi(z)$  for Pop. II stars from H22. We also assume that all Pop. II stars have metallicity  $Z = 10^{-4}$  and use the catalogues by Costa & et al. (2023), which have exactly the same set up as the Pop. III initial conditions in Table 5.1. This assumption is to have a fair comparison between the merger rate density of Pop. III BBHs and Pop. II BBHs, both adopting the SFRDs from H22.

---

<sup>2</sup>The fiducial model by Iorio et al. (2022) only contains 1M binary star systems for each metallicity. Here, we have rerun the same model with a  $5 \times$  higher statistics, to filter out stochastic fluctuations.

# 6

## Conclusions

GW astrophysics revolutionised our understanding of compact objects in the last seven years. By detecting and studying GWs, we learn more about the origins and the evolution of exotic objects, such as black holes and neutron stars. Since 2015, the LIGO-Virgo-KAGRA collaboration released an ever increasing number of GW event candidates.

The third gravitational-wave transient catalogue (GWTC-3, Abbott et al., 2021b) includes all the GW candidates from the first three observing runs (O1, O2, and O3, Abbott et al., 2016a, 2019a, 2020b) with probability of astrophysical origin  $p_{\text{astro}} > 0.5$ . Among them, the LVK collaboration selected 56 low false-alarm rate candidates and used them to infer the properties of the underlying astrophysical population of BBHs, BHNSs and BNSs. By taking the lowest 5% and highest 95% credible interval, they inferred the merger rate density in the local Universe to be within  $16 \text{ Gpc}^{-3} \text{ yr}^{-1} - 61 \text{ Gpc}^{-3} \text{ yr}^{-1}$  for BBHs,  $7.8 \text{ Gpc}^{-3} \text{ yr}^{-1} - 140 \text{ Gpc}^{-3} \text{ yr}^{-1}$  for BHNSs and  $10 \text{ Gpc}^{-3} \text{ yr}^{-1} - 1700 \text{ Gpc}^{-3} \text{ yr}^{-1}$  for BNSs (see Section 1.1.2 for more details).

One of the main open questions that stems from looking at the ensemble of detections is the interpretation of the astrophysical merger rates of gravitational wave sources. In this Thesis, I thoroughly explore this issue, by predicting the merger rate density of compact object across cosmic time. In the future, the next generation of ground-based gravitational-wave interferometers, namely the Einstein Telescope (Punturo et al., 2010) and Cosmic Explorer (Reitze et al., 2019), will observe BBH mergers out to  $z \sim 100$  (Maggiore et al., 2020; Ng et al., 2021, 2022b) as well as BNS mergers at  $z \sim 2$  (Kalogera et al., 2021), allowing us to probe the redshift distribution of compact objects.

The exploration of the properties of the host galaxies of compact object mergers is another importance piece of the debate around gravitational-wave astrophysics. In fact, in 2017 the first and (so far) only combined detection of a BNS merger and its electromagnetic counterpart allowed the identification of the host galaxy (Abbott et al., 2017d). The importance of the information carried by host galaxies identification, in understating the sources of gravitational waves, is also expected to increase with the next-generation observatories. In this Thesis, I thus show the results I obtained by developing two codes: COSMO $\mathcal{R}$ ATE and GALAXY $\mathcal{R}$ ATE (Santoliquido et al., 2020, 2021, 2022). COSMO $\mathcal{R}$ ATE evaluates the merger rate density by combining catalogues of merging compact objects with the SFR density (Madau & Fragos, 2017) and the evolution of metallicity with redshift (De Cia et al., 2018;

(Gallazzi et al., 2008; Madau & Fragos, 2017; Santoliquido et al., 2020). GALAXYRATE couples the catalogues of merging compact objects with the properties of the formation and host galaxies. In other words, to reproduce the population of galaxies in which compact objects form and merge, it adopts the main observational scaling relations, such as the galaxy-stellar mass function (Chruslinska et al., 2019), the main sequence of star-forming galaxies (Popesso et al., 2022) and the fundamental metallicity relation (Curti et al., 2020).

In Chapter 2, I investigate the cosmic merger rate density evolution of compact objects merging in young star clusters. These are the most common birthplace of massive stars across cosmic history. Hence, a large fraction of BBHs, BHNSs and BNSs might have formed in young star clusters and might retain the signature of dynamical processes (such as exchanges or stellar collisions) occurring in star clusters. For instance, the merger efficiency of dynamical BBHs at solar metallicity is two orders of magnitude higher than the merger efficiency of isolated BBHs (Figure 2.1). The reason is that dynamical exchanges enhance the merger of BBHs formed from metal-rich stars. As a consequence, the dynamical BBH merger rate is higher than the isolated BBH merger rate between  $z = 0$  and  $z \sim 4$  (Figure 2.2). On the other hand, the merger rate density of dynamical BNSs is a factor of  $\sim 2$  lower than that of isolated BNSs. In this case, dynamical processes suppress the formation of relatively low-mass binaries.

I find a local merger rate density of  $\mathcal{R}_{\text{BBH}}^0 = 64_{-20}^{+34} \text{ Gpc}^{-3} \text{ yr}^{-1}$ ,  $\mathcal{R}_{\text{BHNS}}^0 = 41_{-23}^{+33} \text{ Gpc}^{-3} \text{ yr}^{-1}$  and  $\mathcal{R}_{\text{BNS}}^0 = 151_{-38}^{+59} \text{ Gpc}^{-3} \text{ yr}^{-1}$  for dynamical BBHs, BHNSs and BNSs, respectively. These rates are consistent with the values inferred from the third observing run of LIGO and Virgo (O3, Abbott et al., 2021b), within the estimated uncertainties. This is also true for the local merger rate density of isolated BBHs, BHNSs and BNSs ( $\mathcal{R}_{\text{BBH}}^0 = 50_{-37}^{+71} \text{ Gpc}^{-3} \text{ yr}^{-1}$ ,  $\mathcal{R}_{\text{BHNS}}^0 = 49_{-34}^{+48} \text{ Gpc}^{-3} \text{ yr}^{-1}$  and  $\mathcal{R}_{\text{BNS}}^0 = 283_{-75}^{+97} \text{ Gpc}^{-3} \text{ yr}^{-1}$ ).

The main difference between isolated and dynamical BBHs is BH mass: dynamical systems harbour BHs with mass up to  $m_{\text{BH,max}} \sim 90 \text{ M}_\odot$ , significantly higher than isolated binaries,  $m_{\text{BH,max}} \sim 45 \text{ M}_\odot$ . The mass distribution of both isolated and dynamical compact objects do not significantly change with redshift. These results provide a clue to differentiate the dynamical and isolated formation scenario of binary compact objects across cosmic time, in preparation for next-generation ground-based detectors.

In Chapter 3, I explore the main sources of uncertainty that affect the cosmic merger rate density evolution of isolated compact objects. I take into account uncertainties on the most relevant binary evolution processes, namely common envelope, supernova kicks, core-collapse supernova models and mass accretion by Roche-lobe overflow. These represent the main bulk of uncertainty on the merger rate density of isolated binaries. In addition, I vary the slope of the IMF. My results confirm that the core-collapse supernova model and the IMF produce negligible variations of the merger rate density.

The parameter  $\alpha$ , quantifying the efficiency of common-envelope ejection, is one of the main sources of uncertainty. The merger rate density of BNSs spans up to 2 orders of magnitude if  $\alpha$  varies from 0.5 to 10. For the same range of  $\alpha$ ,  $\mathcal{R}_{\text{BHNS}}(z)$  and  $\mathcal{R}_{\text{BBH}}(z)$  vary up to a factor of 2 and 3, respectively. Values of  $\alpha \geq 0.5$  give local BNS merger rate densities within the 90% credible interval inferred from GWTC-3 (Abbott et al., 2021b), when I adopt

our fiducial kick model. Large natal kicks instead ( $\sigma = 265 \text{ km s}^{-1}$ ) yield BNSs merger rate densities below the 90% credible interval from GWTC-3. Therefore, only models with moderately low kicks predict values of the BNS merger rate within the 90% LVC credible interval inferred from GWTC-3.

I also investigate the effect of observational uncertainties on the cosmic SFR and on metallicity evolution.  $\mathcal{R}_{\text{BNS}}(z)$  is not significantly affected by metallicity evolution (Figure 3.8). In contrast, the metallicity evolution has a huge impact on the merger rate density of BBHs (Figure 3.8).  $\mathcal{R}_{\text{BBH}}(z)$  is inside the 90% credible interval inferred from GWTC-3 only if the metallicity spread is  $\sigma_Z < 0.35$ .

In Chapter 4, I present **GALAXYRATE**, which estimates the merger rate density of binary compact objects and the properties of their host galaxies, based on observational scaling relations. **GALAXYRATE** first generates the formation galaxy of each merging compact object, i.e. the galaxy in which the progenitor stars of the binary compact object form. Each formation galaxy is described by its stellar mass, SFR and metallicity. With **GALAXYRATE**, I can perform many realisations of the merger rate density and host galaxy properties across the cosmic time, in order to bracket the main uncertainties springing from both binary compact object formation and galaxy evolution. For instance, I consider two galaxy main sequence definitions (S14 and B18), and two metallicity evolutions (MZR and FMR). Furthermore, I adopt three catalogues of merging binary compact objects. In each catalogue, I vary the common-envelope efficiency parameter  $\alpha = 1, 3$  and  $5$ . This parameter has a great impact on the delay time distribution of binary compact objects (See Figure 4.19).

I find that the merger rate density evolution with redshift changes dramatically depending on the choice of the star-forming galaxy main sequence (S18 or B18), especially in the case of BBHs and BHNSs. The choice of the metallicity evolution has also an important effect on the slope of the merger rate density of BBHs and BHNSs. The slope of the merger rate density evolution with redshift of BBHs and BHNSs is steeper if I assume the MZR with respect to the FMR, because the latter predicts a shallower decrease of metallicity with redshift (Figure 4.6). In contrast, BNSs are not affected by the choice of the metallicity relation. Indeed, the merger rate density of BNSs and BHNSs is within the 90% credible interval estimated by GWTC-3 (Abbott et al., 2021b) for all considered assumptions, while the merger rate density of BBHs predicted by our models is higher than the observed range.

I compare the merger rate density obtained with **GALAXYRATE** (Section 4.2.3) with that obtained with **COSMORATE**. I find that the merger rate density evolution of BNSs obtained with **COSMORATE** and **GALAXYRATE** are in good agreement, while the BBH and BHNS merger rate densities evaluated with **GALAXYRATE** are higher than those obtained with **COSMORATE**, if I assume the fitting formulas from Madau & Fragos (2017) and a metallicity spread  $\sigma_Z = 0.3$  (Figure 4.6). The main reason is that the SFRD( $z, Z$ ) I obtain from the observational scaling relations supports a larger population of metal-poor stars with respect to the Madau & Fragos (2017) fitting formulas with  $\sigma_Z = 0.3$ . The differences between the BBH merger rate density obtained with **GALAXYRATE** and **COSMORATE** can be reconciled by assuming a larger metallicity spread  $\sigma_Z > 0.4$  in **COSMORATE**.

Overall, the host galaxies of BBHs and BHNSs are more massive than their formation galaxies (both assuming the MZR and the FMR), because both BBHs and BHNSs tend to

form in smaller metal-poor galaxies and to merge in larger metal-rich galaxies. In contrast, the formation galaxies and host galaxies of BNSs are very similar to each other (Figures 4.7 and 4.8). The mass distribution of host galaxies is affected by the delay time distribution. In our models, different values of the common-envelope efficiency  $\alpha$  result in different distributions of the delay time (Appendix 4.6.1), with larger values of  $\alpha$  being associated with longer delay times. Figures 4.7 and 4.8 show that the contribution of high-mass galaxies increases with  $\alpha$ . In fact, with  $\alpha = 5$  (longer delay times), the formation galaxy has more time to merge with other galaxies and form a more massive host galaxy. On the other hand, for  $\alpha = 1$  (shorter delay times), a large fraction of BBHs are hosted in low-mass galaxies.

Passive galaxies can host compact objects mergers (Figure 4.14). Their contribution increases as approaching the local Universe, regardless of the adopted passive galaxy definition. However, the percentage of mergers hosted in passive galaxies crucially depends on this definition. If all the galaxies with  $sSFR < 10^{-10} \text{ yr}^{-1}$  are considered passive galaxies, I find that  $\sim 50 - 60\%$ ,  $\sim 45 - 70\%$  and  $\sim 40 - 75\%$  of all BNS, BHNS and BBH mergers in the local Universe are associated with a passive galaxy, respectively. In contrast, if I define passive galaxies as those galaxies with SFR at least 1 dex below the star-forming main sequence, only  $\sim 5 - 10\%$ ,  $\sim 15 - 25\%$  and  $\sim 15 - 35\%$  of all BNS, BHNS and BBH mergers in the local Universe are associated with a passive galaxy, respectively. Overall, binary compact objects have more chances to be hosted in passive galaxies if their delay time distribution is longer.

In Chapter 5, I use COSMORATE to estimate the merger rate density evolution of BBHs born from Pop. III stars (Figure 5.3). To account for the main uncertainties affecting the merger rate density, I explore a large parameter space consisting of four different models for the formation history of Pop. III stars (from Jaacks et al. 2019, J19, Liu & Bromm 2020b, LB20, Skinner & Wise 2020, SW20, and Hartwig et al. 2022, H22), and eleven different configurations of the initial orbital properties of Pop. III binary stars. This includes probing different IMFs, mass ratios, orbital period distributions, and eccentricity distributions. I generate the catalogues of Pop. III BBHs with our binary population-synthesis simulation code SEVN (Iorio et al., 2022), based on a new set of Pop. III stellar tracks with metallicity  $Z = 10^{-11}$  and ZAMS mass  $m_{\text{ZAMS}} \in [2.2, 600] M_\odot$  (Costa & et al., 2023).

The assumed star formation rate history of Pop. III stars affects both the normalisation and the shape of the BBH merger rate density evolution with redshift (Fig. 5.3):  $\mathcal{R}(z)$  peaks at  $z_p \approx 8 - 10$  for the models by J19 and LB20, and at  $z_p \approx 12 - 16$  for H22 and SW20. At redshift  $z = 0$ , all the considered SFRD models yield  $\mathcal{R}_{\text{BBH}}^0 \leq 2 \times 10^{-1} \text{ Gpc}^{-3} \text{ yr}^{-1}$  in our fiducial model LOG1, about two orders of magnitude lower than the local BBH merger rate density inferred from LVK data (Abbott et al., 2021b).

We estimate the mass distribution of Pop. III BBHs for all of the models and as a function of redshift. Both the primary and secondary BH born from a Pop. III binary star tend to be substantially more massive than the primary and secondary BH born from a metal-rich binary star (Figs. 5.7, 5.8). This happens mainly because stellar winds are suppressed at low  $Z$ . The median mass of the primary BHs born from Pop. III stars is  $m_1 \approx 30 - 40 M_\odot$  across the entire redshift range, while the median mass of primary BHs born from metal-rich stars is  $m_1 \approx 8 M_\odot$  (Fig. 5.4).

The mass ratio  $q$  between the secondary and primary BH is another feature that distinguishes BBHs born from Pop. III and metal-rich binary stars (Fig. 5.6). At low redshift ( $z \leq 4$ ), BBH mergers from Pop. III stars have low mass ratios (median values  $q \approx 0.5 - 0.7$ ) with respect to BBH mergers from metal-rich stars (median values  $q \approx 0.9$ ). In contrast, at high redshift even BBH mergers from Pop. III stars have a typical  $q \sim 0.9$ . This happens because the median secondary BH mass of Pop. III BBH mergers decreases with redshift. This feature is a consequence of the delay time distribution: Pop. III BBHs with relatively small secondary BH mass are associated with longer delay times than Pop. III BBHs with equal mass BHs (Fig. 5.10).

The results indicate that the overall uncertainty in the evolution of the merger rate density of Pop. III BBH mergers spans at least two orders of magnitude and depends on various factors, such as the SFRD model, initial orbital properties of Pop. III binary stars, and stellar/binary evolution physics.

## 6.1 Future developments

My research takes advantage of the relation between gravitational-wave detections and observational astronomy, to further expand the exploration of our Universe. In other words, my final goal is to study the evolution of compact object mergers and their host galaxies across cosmic time. Identifying the host galaxy properties of merging compact objects can help to disentangle which are the most likely formation channels of gravitational-wave sources. In addition, it might help to address different aspects of binary stellar evolution still under debate. For instance, various setup of the common envelope and mass transfer efficiency shape the delay time distribution, which in turn affects the properties of the host galaxies (Santoliquido et al., 2022). Moreover, compact objects mergers can act also as standard sirens, which together with the redshift information of the host galaxy can be used as an alternative to constraining the value of the Hubble constant. The importance of these objectives will further grow in light of the expected capabilities of the next-generation detectors.

With GALAXYRATE, I showed, for instance, that BBHs form at high redshift in low-mass metal-poor galaxies and merge in the local Universe in high-mass metal-rich galaxies (see Figure 4.7 and 4.8). In the next future, I will further explore the relation between gravitational wave sources and their host galaxies, using GALAXYRATE as a basis.

We now know that the mergers of two neutron stars ignite a short gamma-ray burst. This was for the first time observed  $\sim 1.7$  s after the gravitational-wave event GW170817 (Abbott et al., 2017c). Therefore, as a first step, I will compare the population of host galaxies of binary neutron stars with the most recent catalogues of observed host galaxies of short gamma-ray burst. Nugent et al. (2022) provide the largest sample to date of short gamma-ray burst host galaxies, comprising 69 galaxies with median measured redshift  $z = 0.64^{+0.83}_{-0.32}$ , thus within the current horizon of gravitational-wave detectors. This comparison is extremely important, since it can provide us with essential constraints both on the adopted observational scaling relations and on the physical details governing the evolution of binary neutron stars. For instance, GALAXYRATE evaluates the fraction of BNSs that merge in quiescent galaxies (see Figure 4.14), under many different parameter configurations. This

number can be compared to the fraction of short gamma-ray burst observed in quiescent galaxies ( $\sim 10\%$ , Nugent et al., 2022).

The properties of host galaxies are determined by calculating a conditional probability that links the properties of the formation galaxy with those of the host galaxy (see Section 4.2.4 and Figure 4.5). This evaluation procedure is the most computationally intensive task within GALAXYRATE. To overcome this issue, I will apply Machine Learning to evaluate the host galaxy properties in a faster and more refined way. Among many several algorithms, normalising flows (Kobyzev et al., 2021) is the ideal type of neural network for my purpose. Some implementation of normalising flows have been already made available in PYTORCH<sup>1</sup>. By implementing a faster evaluation of the conditional probability, I can compare the results coming from different cosmological simulations (e.g., HORIZON-AGN (Dubois et al., 2016), ILLUSTRIS-TNG (Pillepich et al., 2017), FIRE (Hopkins et al., 2014)). This operation is fundamental to understand the impact of the choice of the adopted cosmological simulation on my results. Moreover, the interpretation of cosmological simulation outcomes through machine learning has already begun (e.g., Jespersen et al. (2022)). Further exploration of this component of GALAXYRATE might lead to new interesting results.

These improvements will lead to a better understanding of the relation between the host galaxies and the properties of compact object mergers. These results can be directly applied to foster the efforts of the GRANDMA collaboration<sup>2</sup>, which is one of the worldwide program for the follow-up of the electromagnetic counterparts of gravitational-wave detections. The LIGO-Virgo-KAGRA collaboration infers a wide sky localisation area for each detected compact object merger, which must be searched for the identification of multimessenger events. To aid in the detection of electromagnetic counterparts, a galaxy ranking within the sky localisation can greatly facilitate the process. This galaxy ranking nowadays is mainly done by considering the galaxy stellar mass (e.g. Ducoin et al. (2022)). I will take advantage of the unprecedented speed of GALAXYRATE to provide a galaxy ranking that is a consequence of a wide parameter exploration, that takes in account both the various evolution pathways of compact objects and cosmological scenarios.

---

<sup>1</sup><https://github.com/VincentStimper/normalizing-flows>

<sup>2</sup><https://grandma.ijclab.in2p3.fr/>



# List of Figures

1.1	Diagram of a basic interferometer design . . . . .	3
1.2	Sensitivity of past, current, and future detectors . . . . .	4
1.3	Sensitivity evolution and observing runs . . . . .	5
1.4	Horizon distance of third-generation detectors . . . . .	6
1.5	Parameter estimation in GWTC-3 . . . . .	7
1.6	Inferred evolution of merger rate density with redshift . . . . .	11
1.7	Impact of stellar winds on BH mass . . . . .	13
1.8	Compact object mass spectrum . . . . .	15
1.9	Metallicity evolution with redshift of neutral gas . . . . .	21
1.10	COSMORATE schematic chart . . . . .	23
1.11	GALAXYRATE schematic chart . . . . .	25
2.1	Merger efficiency of compact objects formed in $N$ -body simulations	35
2.2	Merger rate density of BBHs formed in $N$ -body simulations . . . . .	36
2.3	Merger rate density of BHNSs formed in $N$ -body simulations . . . . .	38
2.4	Merger rate density of BNSs formed in $N$ -body simulations . . . . .	39
2.5	Mass distributions of compact objects formed in $N$ -body simulations	41
3.1	Merger efficiency at varying $\alpha$ . . . . .	52
3.2	Merger rate density at varying $\alpha$ . . . . .	53
3.3	Merger rate density at varying SN kick models . . . . .	55
3.4	Merger rate density with rapid and delayed SN models . . . . .	56
3.5	Merger rate density at varying mass transfer efficiency . . . . .	57
3.6	Merger rate density with different IMF . . . . .	59
3.7	Merger rate density as function of metallicity and SFR parameters	60
3.8	Uncertainties on the merger rate density due to metallicity and SFR	61
3.9	Progenitor metallicities on the merger rate density . . . . .	63
3.10	Slope of the merger rate density for various models . . . . .	64
3.11	Merger rate density with mock simulations . . . . .	66
3.12	Comparison of the merger rate density obtained with cosmological simulations . . . . .	69
4.1	Galaxy stellar mass functions . . . . .	77
4.2	Different evolutions of the star formation rate density . . . . .	79
4.3	Comparison of metallicity models of galaxies . . . . .	80

---

4.4	Metallicity-specific star formation rate density . . . . .	82
4.5	Examples of conditional probabilities . . . . .	84
4.6	Merger rate density evaluated with <code>GALAXYRATE</code> . . . . .	87
4.7	Mass distribution of host galaxies - MZR . . . . .	89
4.8	Mass distribution of host galaxies - FMR . . . . .	90
4.9	SFR distribution of host galaxies - MZR . . . . .	91
4.10	SFR distribution of host galaxies - FMR . . . . .	92
4.11	Metallicity distribution of host galaxies - MZR . . . . .	93
4.12	Metallicity distribution of host galaxies - FMR . . . . .	93
4.13	Merger rate per galaxy . . . . .	94
4.14	Percentage of mergers in passive galaxies . . . . .	95
4.15	Impact of varying GSMF on the merger rate density . . . . .	97
4.16	Impact of SFR distribution uncertainties on the merger rate density	98
4.17	Merger rate density with different metallicity calibrations . . . . .	100
4.18	Merger efficiency adopted with <code>GALAXYRATE</code> . . . . .	103
4.19	Delay time distributions at varying $\alpha$ . . . . .	104
4.20	Comoving volume in <code>GALAXYRATE</code> . . . . .	105
4.21	Impact of the choice of the minimum galaxy stellar mass on the merger rate density . . . . .	107
4.22	Impact of solar metallicity on the merger rate density . . . . .	108
5.1	Pop. III star-formation rate density . . . . .	117
5.2	Evolution of the merger rate density for Pop. III BBH with H22 .	119
5.3	Evolution of the merger rate density for Pop. III BBH . . . . .	120
5.4	Median primary BH mass $m_1$ as a function of redshift . . . . .	122
5.5	Median secondary BH mass $m_2$ as a function of redshift . . . . .	123
5.6	Median BH mass ratio $q$ as a function of redshift . . . . .	124
5.7	Primary Pop. III BH mass distribution $m_1$ . . . . .	125
5.8	Secondary Pop. III BH mass distribution $m_2$ . . . . .	126
5.9	Distribution of formation channels . . . . .	128
5.10	Distribution of delay times of Pop. III BBHs . . . . .	130
5.11	Secondary BH mass distribution $m_2$ - formation channels . . . . .	131
5.12	Evolution of median $m_2$ for different natal kicks . . . . .	132
5.13	Evolution of the merger rate density for different natal kicks . . . . .	132
5.14	Properties of BBHs in LOG3 . . . . .	134
5.15	Merger rate density of Pop. II BBHs . . . . .	135

# List of Tables

1.1	Astrophysical rates in the local Universe inferred from GW detections	10
2.1	Merger rate density at various redshift bins	40
3.1	Summary of the models	49
3.2	Fits of the merger rate density	65
4.1	Adopted parameters in <i>GALAXYRATE</i>	86
4.2	Fits of the merger rate per galaxy	94
4.3	Solar metallicity measures	106
5.1	Initial conditions for Pop. III stars	115

# Bibliography

- Aasi J., et al., 2013, *Nature Photonics*, **7**, 613
- Aasi J., et al., 2015a, *Classical and Quantum Gravity*, **32**, 074001
- Aasi J., et al., 2015b, *Classical and Quantum Gravity*, **32**, 115012
- Abadie J., et al., 2010, *Classical and Quantum Gravity*, **27**, 173001
- Abbott B. P., et al., 2016a, *Physical Review X*, **6**, 041015
- Abbott B. P., et al., 2016b, *Phys. Rev. Lett.*, **116**, 061102
- Abbott B. P., Abbott R., Abbott T. D., Abernathy M. R., Acernese F., LIGO Scientific Collaboration Virgo Collaboration 2016c, *Phys. Rev. Lett.*, **116**, 241102
- Abbott B. P., et al., 2016d, *Physical Review Letters*, **116**, 241103
- Abbott B. P., et al., 2016e, *ApJ*, **818**, L22
- Abbott B. P., et al., 2017a, *Physical Review Letters*, **118**, 221101
- Abbott B. P., et al., 2017b, *Physical Review Letters*, **119**, 141101
- Abbott B. P., et al., 2017c, *Physical Review Letters*, **119**, 161101
- Abbott R., et al., 2017d, *Nature*, **551**, 85
- Abbott B. P., et al., 2017e, *ApJ*, **848**, L12
- Abbott B. P., Abbott R., Abbott T. D., Acernese F., Ackley K., Adams C., Adams T., 2017f, *ApJ*, **848**, L13
- Abbott B. P., et al., 2017g, *ApJ*, **851**, L35
- Abbott R., et al., 2018, *Living Reviews in Relativity*, **21**, 3
- Abbott B. P., et al., 2019a, *Physical Review X*, **9**, 031040
- Abbott B. P., et al., 2019b, *ApJ*, **882**, L24
- Abbott B. P., et al., 2020a, arXiv e-prints, p. arXiv:2004.08342

- Abbott R., et al., 2020b, arXiv e-prints, p. arXiv:2010.14527
- Abbott R., et al., 2020c, arXiv e-prints, p. arXiv:2010.14533
- Abbott R., Abbott T. D., Abraham S., Acernese F., Ackley K., Adams C., LIGO Scientific Collaboration Virgo Collaboration 2020d, *Phys. Rev. Lett.*, 125, 101102
- Abbott B. P., et al., 2020e, *ApJ*, 892, L3
- Abbott R., et al., 2020f, *ApJ*, 900, L13
- Abbott R., et al., 2021a, arXiv e-prints, p. arXiv:2111.03606
- Abbott R., et al., 2021b, arXiv e-prints, p. arXiv:2111.03634
- Abbott R., et al., 2021c, *ApJ*, 915, L5
- Abel T., Bryan G. L., Norman M. L., 2002, *Science*, 295, 93
- Acernese F., et al., 2015a, *Classical and Quantum Gravity*, 32, 024001
- Acernese F., et al., 2015b, in *Journal of Physics Conference Series*. p. 012014, doi:10.1088/1742-6596/610/1/012014
- Ade P. A. R., Aghanim N., Zonca A. e. a., 2016, *A&A*, 594, A13
- Adhikari S., Fishbach M., Holz D. E., Wechsler R. H., Fang Z., 2020, *ApJ*, 905, 21
- Alexander K. D., et al., 2017, *The Astrophysical Journal Letters*, 848, L21
- Alvarez M. A., Bromm V., Shapiro P. R., 2006, *ApJ*, 639, 621
- Anders E., Grevesse N., 1989, *Geo. et Cosmo. Acta*, 53, 197
- Antonini F., Gieles M., 2020, *MNRAS*, 492, 2936
- Antonini F., Rasio F. A., 2016, *ApJ*, 831, 187
- Antonini F., Toonen S., Hamers A. S., 2017, *ApJ*, 841, 77
- Arca Sedda M., 2020, *ApJ*, 891, 47
- Arca-Sedda M., Li G., Kocsis B., 2018, arXiv e-prints, p. arXiv:1805.06458
- Arca Sedda M., Mapelli M., Spera M., Benacquista M., Giacobbo N., 2020, *ApJ*, 894, 133
- Arca-Sedda M., Rizzuto F. P., Naab T., Ostriker J., Giersz M., Spurzem R., 2021, *ApJ*, 920, 128
- Arcavi I., et al., 2017, *ApJ*, 848, L33

- Artale M. C., Mapelli M., Giacobbo N., Sabha N. B., Spera M., Santoliquido F., Bressan A., 2019, *MNRAS*, **487**, 1675
- Artale M. C., Mapelli M., Bouffanais Y., Giacobbo N., Pasquato M., Spera M., 2020a, *MNRAS*, **491**, 3419
- Artale M. C., Bouffanais Y., Mapelli M., Giacobbo N., Sabha N. B., Santoliquido F., Pasquato M., Spera M., 2020b, *MNRAS*, **495**, 1841
- Arzoumanian Z., Chernoff D. F., Cordes J. M., 2002, *ApJ*, **568**, 289
- Ashkar H., et al., 2021a, arXiv e-prints, p. [arXiv:2108.04654](#)
- Ashkar H., et al., 2021b, *J. Cosmol. Astropart. Phys.*, **2021**, 045
- Askar A., Szkudlarek M., Gondek-Rosińska D., Giersz M., Bulik T., 2017, *MNRAS*, **464**, L36
- Asplund M., Grevesse N., Sauval A. J., Scott P., 2009, *ARA&A*, **47**, 481
- Atri P., et al., 2019, *MNRAS*, **489**, 3116
- Baibhav V., Berti E., Gerosa D., Mapelli M., Giacobbo N., Bouffanais Y., Di Carlo U. N., 2019, *Phys. Rev. D*, **100**, 064060
- Banerjee S., 2017, *MNRAS*, **467**, 524
- Banerjee S., 2020, arXiv e-prints, p. [arXiv:2004.07382](#)
- Banerjee S., Baumgardt H., Kroupa P., 2010, *MNRAS*, **402**, 371
- Bartos I., Kocsis B., Haiman Z., Márka S., 2017, *ApJ*, **835**, 165
- Belczynski K., Kalogera V., Bulik T., 2002, *ApJ*, **572**, 407
- Belczynski K., Perna R., Bulik T., Kalogera V., Ivanova N., Lamb D. Q., 2006, *ApJ*, **648**, 1110
- Belczynski K., Kalogera V., Rasio F. A., Taam R. E., Zezas A., Bulik T., Maccarone T. J., Ivanova N., 2008, *ApJS*, **174**, 223
- Belczynski K., Bulik T., Fryer C. L., Ruiter A., Valsecchi F., Vink J. S., Hurley J. R., 2010, *ApJ*, **714**, 1217
- Belczynski K., Holz D. E., Bulik T., O'Shaughnessy R., 2016, *Nature*, **534**, 512
- Belczynski K., et al., 2017a, preprint, ([arXiv:1712.00632](#))
- Belczynski K., Ryu T., Perna R., Berti E., Tanaka T. L., Bulik T., 2017b, *MNRAS*, **471**, 4702
- Belczynski K., et al., 2020, *A&A*, **636**, A104

- Belczynski K., et al., 2022, *ApJ*, **925**, 69
- Berger E., et al., 2007, *ApJ*, **664**, 1000
- Bethe H. A., Brown G. E., 1998, *ApJ*, **506**, 780
- Béthermin M., et al., 2012, *ApJ*, **757**, L23
- Bisigello L., Caputi K. I., Grogin N., Koekemoer A., 2018, *A&A*, **609**, A82
- Bisnovatyi-Kogan G. S., 1993, *Astronomical and Astrophysical Transactions*, **3**, 287
- Blaauw A., 1961, *Bull. Astron. Inst.*, **15**, 265
- Boco L., Lapi A., Goswami S., Perrotta F., Baccigalupi C., Danese L., 2019, *ApJ*, **881**, 157
- Boco L., Lapi A., Chruslinska M., Donevski D., Sicilia A., Danese L., 2021, *ApJ*, **907**, 110
- Bondi H., Hoyle F., 1944, *MNRAS*, **104**, 273
- Boogaard L. A., et al., 2018, *A&A*, **619**, A27
- Bouffanais Y., Mapelli M., Gerosa D., Di Carlo U. N., Giacobbo N., Berti E., Baibhav V., 2019, *ApJ*, **886**, 25
- Bouffanais Y., Mapelli M., Santoliquido F., Giacobbo N., Di Carlo U. N., Rastello S., Artale M. C., Iorio G., 2021, *MNRAS*, **507**, 5224
- Bowler R. A. A., et al., 2015, *MNRAS*, **452**, 1817
- Bray J. C., Eldridge J. J., 2016, *MNRAS*, **461**, 3747
- Bray J. C., Eldridge J. J., 2018, *MNRAS*, **480**, 5657
- Bressan A., Marigo P., Girardi L., Salasnich B., Dal Cero C., Rubele S., Nanni A., 2012, *MNRAS*, **427**, 127
- Brinchmann J., Charlot S., White S. D. M., Tremonti C., Kauffmann G., Heckman T., Brinkmann J., 2004, *MNRAS*, **351**, 1151
- Broekgaarden F. S., et al., 2021, *MNRAS*, **508**, 5028
- Bromm V., 2013, *Reports on Progress in Physics*, **76**, 112901
- Bromm V., Larson R. B., 2004, *ARA&A*, **42**, 79
- Bromm V., Loeb A., 2003, *Nature*, **425**, 812
- Bromm V., Yoshida N., Hernquist L., McKee C. F., 2009, *Nature*, **459**, 49
- Bryan G. L., et al., 2014, *ApJS*, **211**, 19

- Burrows A., Hayes J., 1996, *Phys. Rev. Lett.*, **76**, 352
- Caffau E., Ludwig H. G., Steffen M., Freytag B., Bonifacio P., 2011, *Solar Phys.*, **268**, 255
- Callister T. A., Farr W. M., 2023, arXiv e-prints, p. arXiv:2302.07289
- Callister T., Fishbach M., Holz D. E., Farr W. M., 2020, *ApJ*, **896**, L32
- Caputi K. I., et al., 2017, *ApJ*, **849**, 45
- Carr B. J., Hawking S. W., 1974, *MNRAS*, **168**, 399
- Carr B., Kühnel F., Sandstad M., 2016, *Phys. Rev. D*, **94**, 083504
- Carroll S., 2003, Spacetime and Geometry: An Introduction to General Relativity. Benjamin Cummings, <http://www.amazon.com/Spacetime-Geometry-Introduction-General-Relativity/dp/0805387323>
- Casey C. M., et al., 2018, *ApJ*, **862**, 77
- Chabrier G., 2003, *PASP*, **115**, 763
- Chakrabarti S., Chang P., O'Shaughnessy R., Brooks A. M., Shen S., Bellovary J., Gladysz W., Belczynski C., 2017, *ApJ*, **850**, L4
- Chen Y., Bressan A., Girardi L., Marigo P., Kong X., Lanza A., 2015, *MNRAS*, **452**, 1068
- Chen X., Wang J., Kong X., 2022, *ApJ*, **933**, 39
- Choksi N., Gnedin O. Y., Li H., 2018, *MNRAS*, **480**, 2343
- Choksi N., Volonteri M., Colpi M., Gnedin O. Y., Li H., 2019, *ApJ*, **873**, 100
- Chon S., Omukai K., Schneider R., 2021, *MNRAS*, **508**, 4175
- Chornock R., et al., 2017, *The Astrophysical Journal Letters*, **848**, L19
- Chruślińska M., 2022, arXiv e-prints, p. arXiv:2206.10622
- Chruslinska M., Belczynski K., Klencki J., Benacquista M., 2018, *MNRAS*, **474**, 2937
- Chruslinska M., Nelemans G., Belczynski K., 2019, *MNRAS*, **482**, 5012
- Chruślińska M., Jeřábková T., Nelemans G., Yan Z., 2020, *A&A*, **636**, A10
- Chruślińska M., Nelemans G., Boco L., Lapi A., 2021, *MNRAS*, **508**, 4994
- Chu Q., Yu S., Lu Y., 2021, *MNRAS*,
- Cigarrán Díaz C., Mukherjee S., 2022, *MNRAS*, **511**, 2782
- Claeys J. S. W., Pols O. R., Izzard R. G., Vink J., Verbunt F. W. M., 2014, *A&A*, **563**, A83

- Conselice C. J., Wilkinson A., Duncan K., Mortlock A., 2016, *ApJ*, **830**, 83
- Costa G., et al. 2023, MNRAS
- Costa G., Bressan A., Mapelli M., Marigo P., Iorio G., Spera M., 2021, *MNRAS*, **501**, 4514
- Coulter D. A., et al., 2017, *Science*, **358**, 1556
- Cowperthwaite P. S., et al., 2017, *The Astrophysical Journal Letters*, **848**, L17
- Cresci G., Mannucci F., Curti M., 2019, *A&A*, **627**, A42
- Crosby B. D., O'Shea B. W., Smith B. D., Turk M. J., Hahn O., 2013, *ApJ*, **773**, 108
- Curti M., Mannucci F., Cresci G., Maiolino R., 2020, *MNRAS*, **491**, 944
- Curti M., et al., 2022, arXiv e-prints, p. [arXiv:2207.12375](#)
- Daddi E., et al., 2007, *ApJ*, **670**, 156
- Dall'Amico M., Mapelli M., Di Carlo U. N., Bouffanais Y., Rastello S., Santoliquido F., Ballone A., Arca Sedda M., 2021, *MNRAS*, **508**, 3045
- De Cia A., Ledoux C., Petitjean P., Savaglio S., 2018, *A&A*, **611**, A76
- Dessart L., Burrows A., Livne E., Ott C. D., 2006, *ApJ*, **645**, 534
- Di Carlo U. N., Mapelli M., Bouffanais Y., Giacobbo N., Bressan S., Spera M., Haardt F., 2019a, arXiv e-prints, p. [arXiv:1911.01434](#)
- Di Carlo U. N., Giacobbo N., Mapelli M., Pasquato M., Spera M., Wang L., Haardt F., 2019b, *MNRAS*, **487**, 2947
- Di Carlo U. N., et al., 2020, arXiv e-prints, p. [arXiv:2004.09525](#)
- Di Carlo U. N., et al., 2021, *MNRAS*, **507**, 5132
- Dominik M., Belczynski K., Fryer C., Holz D. E., Berti E., Bulik T., Mandel I., O'Shaughnessy R., 2012, *ApJ*, **759**, 52
- Dominik M., Belczynski K., Fryer C., Holz D. E., Berti E., Bulik T., Mandel I., O'Shaughnessy R., 2013, *ApJ*, **779**, 72
- Dominik M., et al., 2015, *ApJ*, **806**, 263
- Donnari M., et al., 2019, *MNRAS*, **485**, 4817
- Donnari M., Pillepich A., Nelson D., Marinacci F., Vogelsberger M., Hernquist L., 2021, *MNRAS*, **506**, 4760
- Downing J. M. B., Benacquista M. J., Giersz M., Spurzem R., 2010, *MNRAS*, **407**, 1946

- Driggers J. C., Harms J., Adhikari R. X., 2012, *Phys. Rev. D*, **86**, 102001
- Dubois Y., Peirani S., Pichon C., Devriendt J., Gavazzi R., Welker C., Volonteri M., 2016, *MNRAS*, **463**, 3948
- Ducouin J. G., Corre D., Leroy N., Le Floch E., 2020, *MNRAS*, **492**, 4768
- Ducouin J. G., Desoubrie B., Daigne F., Leroy N., 2022, arXiv e-prints, p. [arXiv:2210.12120](https://arxiv.org/abs/2210.12120)
- Ebrová I., Bílek M., Yıldız M. K., Eliášek J., 2020, *A&A*, **634**, A73
- Efstathiou G., 2000, *MNRAS*, **317**, 697
- Eggleton P. P., 1983, *ApJ*, **268**, 368
- Eggleton P., 2006, Evolutionary Processes in Binary and Multiple Stars
- Einstein A., 1915, Sitzungsberichte der Königlich Preussischen Akademie der Wissenschaften, pp 778–786
- Einstein A., 1916, *Annalen der Physik*, **354**, 769
- Elbert O. D., Bullock J. S., Kaplinghat M., 2018, *MNRAS*, **473**, 1186
- Eldridge J. J., Stanway E. R., 2016, *MNRAS*, **462**, 3302
- Eldridge J. J., Stanway E. R., Tang P. N., 2019, *MNRAS*, **482**, 870
- Ellison S. L., Patton D. R., Simard L., McConnachie A. W., 2008, *ApJ*, **672**, L107
- Ertl T., Janka H. T., Woosley S. E., Sukhbold T., Ugliano M., 2016, *ApJ*, **818**, 124
- Farag E., Renzo M., Farmer R., Chidester M. T., Timmes F. X., 2022, *ApJ*, **937**, 112
- Farah A., Fishbach M., Essick R., Holz D. E., Galauadage S., 2022, *ApJ*, **931**, 108
- Farah A. M., Edelman B., Zevin M., Fishbach M., María Ezquiaga J., Farr B., Holz D. E., 2023, arXiv e-prints, p. [arXiv:2301.00834](https://arxiv.org/abs/2301.00834)
- Farmer R., Renzo M., de Mink S. E., Marchant P., Justham S., 2019, *ApJ*, **887**, 53
- Farmer R., Renzo M., de Mink S. E., Fishbach M., Justham S., 2020, *ApJ*, **902**, L36
- Farrell E., Groh J. H., Hirschi R., Murphy L., Kaiser E., Ekström S., Georgy C., Meynet G., 2021, *MNRAS*, **502**, L40
- Faucher-Giguère C.-A., Kaspi V. M., 2006, *ApJ*, **643**, 332
- Finkelstein S. L., et al., 2015, *ApJ*, **810**, 71
- Fishbach M., Holz D. E., 2020, *ApJ*, **904**, L26

- Fishbach M., Holz D. E., Farr W. M., 2018, *ApJ*, **863**, L41
- Fishbach M., et al., 2019, *ApJ*, **871**, L13
- Fishbach M., Essick R., Holz D. E., 2020, *ApJ*, **899**, L8
- Fishbach M., et al., 2021, *ApJ*, **912**, 98
- Fragione G., Kocsis B., 2018, *Phys. Rev. Lett.*, **121**, 161103
- Fragione G., Loeb A., 2019, *MNRAS*, **486**, 4443
- Fragione G., Loeb A., 2022, arXiv e-prints, p. arXiv:2212.04056
- Fragione G., Silk J., 2020, arXiv e-prints, p. arXiv:2006.01867
- Fragione G., Loeb A., Rasio F. A., 2020, *ApJ*, **902**, L26
- Fragos T., Willems B., Kalogera V., Ivanova N., Rockefeller G., Fryer C. L., Young P. A., 2009, *ApJ*, **697**, 1057
- Fragos T., Andrews J. J., Ramirez-Ruiz E., Meynet G., Kalogera V., Taam R. E., Zezas A., 2019, *ApJ*, **883**, L45
- Fryer C. L., 1999, *ApJ*, **522**, 413
- Fryer C. L., Kalogera V., 2001, *ApJ*, **554**, 548
- Fryer C. L., Kusenko A., 2006, *ApJS*, **163**, 335
- Fryer C., Burrows A., Benz W., 1998, *ApJ*, **496**, 333
- Fryer C. L., Belczynski K., Wiktorowicz G., Dominik M., Kalogera V., Holz D. E., 2012, *ApJ*, **749**, 91
- Furlong M., et al., 2015, *MNRAS*, **450**, 4486
- Gallazzi A., Brinchmann J., Charlot S., White S. D. M., 2008, *MNRAS*, **383**, 1439
- Gallegos-Garcia M., Berry C. P. L., Marchant P., Kalogera V., 2021, *ApJ*, **922**, 110
- Genzel R., et al., 2015, *ApJ*, **800**, 20
- Gessner A., Janka H.-T., 2018, *ApJ*, **865**, 61
- Giacobbo N., Mapelli M., 2018, *MNRAS*, **480**, 2011
- Giacobbo N., Mapelli M., 2019, *MNRAS*, **482**, 2234
- Giacobbo N., Mapelli M., 2020, *ApJ*, **891**, 141
- Giacobbo N., Mapelli M., Spera M., 2018, *MNRAS*, **474**, 2959

- Giersz M., Leigh N., Hypki A., Lützgendorf N., Askar A., 2015, *MNRAS*, **454**, 3150
- Glover S., 2013, in Wiklind T., Mobasher B., Bromm V., eds, Astrophysics and Space Science Library Vol. 396, The First Galaxies. p. 103 ([arXiv:1209.2509](https://arxiv.org/abs/1209.2509)), doi:10.1007/978-3-642-32362-1\_3
- Goldstein A., et al., 2017, *ApJ*, **848**, L14
- Goodwin S. P., Whitworth A. P., 2004, *A&A*, **413**, 929
- Gräfener G., Hamann W.-R., 2008, *A&A*, **482**, 945
- Gratton R., Bragaglia A., Carretta E., D’Orazi V., Lucatello S., Sollima A., 2019, *A&A Rev.*, **27**, 8
- Gray R., et al., 2020, *Phys. Rev. D*, **101**, 122001
- Graziani L., Schneider R., Marassi S., Del Pozzo W., Mapelli M., Giacobbo N., 2020, *MNRAS*, **495**, L81
- Grevesse N., Sauval A. J., 1998, *Space Sci. Rev.*, **85**, 161
- Gruppioni C., et al., 2020, *A&A*, **643**, A8
- Gualandris A., Colpi M., Portegies Zwart S., Possenti A., 2005, *ApJ*, **618**, 845
- Haiman Z., Thoul A. A., Loeb A., 1996, *ApJ*, **464**, 523
- Hansen B. M. S., Phinney E. S., 1997, *MNRAS*, **291**, 569
- Harry G. M., et al., 2002, *Classical and Quantum Gravity*, **19**, 897
- Hartwig T., Volonteri M., Bromm V., Klessen R. S., Barausse E., Magg M., Stacy A., 2016, *MNRAS*, **460**, L74
- Hartwig T., et al., 2022, *ApJ*, **936**, 45
- Heger A., Woosley S., Baraffe I., Abel T., 2002, in Gilfanov M., Sunyeav R., Churazov E., eds, Lighthouses of the Universe: The Most Luminous Celestial Objects and Their Use for Cosmology. p. 369 ([arXiv:astro-ph/0112059](https://arxiv.org/abs/astro-ph/0112059)), doi:10.1007/10856495\_57
- Heger A., Fryer C. L., Woosley S. E., Langer N., Hartmann D. H., 2003, *ApJ*, **591**, 288
- Hills J. G., Fullerton L. W., 1980, *AJ*, **85**, 1281
- Hirano S., Hosokawa T., Yoshida N., Umeda H., Omukai K., Chiaki G., Yorke H. W., 2014, *ApJ*, **781**, 60
- Hirano S., Hosokawa T., Yoshida N., Omukai K., Yorke H. W., 2015, *MNRAS*, **448**, 568
- Hobbs G., Lorimer D. R., Lyne A. G., Kramer M., 2005, *MNRAS*, **360**, 974

- Hong J., Vesperini E., Askar A., Giersz M., Szkudlarek M., Bulik T., 2018, *MNRAS*, **480**, 5645
- Hopkins P. F., 2015, *MNRAS*, **450**, 53
- Hopkins P. F., Quataert E., Murray N., 2012, *MNRAS*, **421**, 3522
- Hopkins P. F., Kereš D., Oñorbe J., Faucher-Giguère C.-A., Quataert E., Murray N., Bullock J. S., 2014, *MNRAS*, **445**, 581
- Hunt L., et al., 2012, *MNRAS*, **427**, 906
- Hunt L., Dayal P., Magrini L., Ferrara A., 2016, *MNRAS*, **463**, 2020
- Hurley J. R., Pols O. R., Tout C. A., 2000, *MNRAS*, **315**, 543
- Hurley J. R., Tout C. A., Pols O. R., 2002, *MNRAS*, **329**, 897
- Ilbert O., et al., 2013, *A&A*, **556**, A55
- Ilbert O., et al., 2015, *A&A*, **579**, A2
- Im M., et al., 2017, *ApJ*, **849**, L16
- Inayoshi K., Hirai R., Kinugawa T., Hotokezaka K., 2017, *MNRAS*, **468**, 5020
- Iorio G., et al., 2022, arXiv e-prints, p. [arXiv:2211.11774](https://arxiv.org/abs/2211.11774)
- Ishigaki M., Kawamata R., Ouchi M., Oguri M., Shimasaku K., Ono Y., 2015, *ApJ*, **799**, 12
- Ishiyama T., Sudo K., Yokoi S., Hasegawa K., Tominaga N., Susa H., 2016, *ApJ*, **826**, 9
- Ivanova N., et al., 2013, *A&A Rev.*, **21**, 59
- Jaacks J., Finkelstein S. L., Bromm V., 2019, *MNRAS*, **488**, 2202
- Janka H. T., Mueller E., 1994, *A&A*, **290**, 496
- Jaura O., Glover S. C. O., Wollenberg K. M. J., Klessen R. S., Geen S., Haemmerlé L., 2022, *MNRAS*, **512**, 116
- Jespersen C. K., Cranmer M., Melchior P., Ho S., Somerville R. S., Gabrielpillai A., 2022, *ApJ*, **941**, 7
- Jin S.-J., Wang L.-F., Wu P.-J., Zhang J.-F., Zhang X., 2021, *Phys. Rev. D*, **104**, 103507
- Johnson J. L., Greif T. H., Bromm V., 2007, *ApJ*, **665**, 85
- Kalogera V., et al., 2019, *Bull. Am. Astron. Soc.*, **51**, 242
- Kalogera V., et al., 2021, arXiv e-prints, p. [arXiv:2111.06990](https://arxiv.org/abs/2111.06990)

- Karlsson T., Johnson J. L., Bromm V., 2008, *ApJ*, **679**, 6
- Karlsson T., Bromm V., Bland-Hawthorn J., 2013, *Reviews of Modern Physics*, **85**, 809
- Kasen D., Metzger B., Barnes J., Quataert E., Ramirez-Ruiz E., 2017, *Nature*, **551**, 80
- Katsianis A., et al., 2017, *MNRAS*, **472**, 919
- Kewley L. J., Ellison S. L., 2008, *ApJ*, **681**, 1183
- Kilpatrick C. D., et al., 2022, *ApJ*, **926**, 49
- Kinugawa T., Inayoshi K., Hotokezaka K., Nakauchi D., Nakamura T., 2014, *MNRAS*, **442**, 2963
- Kinugawa T., Miyamoto A., Kanda N., Nakamura T., 2016, *MNRAS*, **456**, 1093
- Kinugawa T., Nakamura T., Nakano H., 2020, *MNRAS*, **498**, 3946
- Kinugawa T., Nakamura T., Nakano H., 2021, *MNRAS*, **501**, L49
- Kitayama T., Yoshida N., Susa H., Umemura M., 2004, *ApJ*, **613**, 631
- Klencki J., Moe M., Gladysz W., Chruslinska M., Holz D. E., Belczynski K., 2018, *A&A*, **619**, A77
- Klencki J., Nelemans G., Istrate A. G., Chruslinska M., 2021, *A&A*, **645**, A54
- Knebe A., et al., 2011, *MNRAS*, **415**, 2293
- Kobyzev I., Prince S. J., Brubaker M. A., 2021, *IEEE Transactions on Pattern Analysis and Machine Intelligence*, **43**, 3964
- Kopparapu R. K., Hanna C., Kalogera V., O'Shaughnessy R., González G., Brady P. R., Fairhurst S., 2008, *ApJ*, **675**, 1459
- Kovlakas K., et al., 2021, *MNRAS*, **506**, 1896
- Kroupa P., 2001, *MNRAS*, **322**, 231
- Kruckow M. U., Tauris T. M., Langer N., Kramer M., Izzard R. G., 2018, preprint, ([arXiv:1801.05433](https://arxiv.org/abs/1801.05433))
- Kumamoto J., Fujii M. S., Tanikawa A., 2019, *MNRAS*, **486**, 3942
- Kumamoto J., Fujii M. S., Tanikawa A., 2020, arXiv e-prints, p. [arXiv:2001.10690](https://arxiv.org/abs/2001.10690)
- Küpper A. H. W., Maschberger T., Kroupa P., Baumgardt H., 2011, *MNRAS*, **417**, 2300
- Kusenko A., Mandal B. P., Mukherjee A., 2008, *Phys. Rev. D*, **77**, 123009

- Lada C. J., Lada E. A., 2003, *ARA&A*, **41**, 57
- Lamberts A., Garrison-Kimmel S., Clausen D. R., Hopkins P. F., 2016, *MNRAS*, **463**, L31
- Lamberts A., et al., 2018, *MNRAS*, **480**, 2704
- Lapi A., Pantoni L., Boco L., Danese L., 2020, *ApJ*, **897**, 81
- Lara-López M. A., et al., 2010, *A&A*, **521**, L53
- Larson R. B., 1998, *MNRAS*, **301**, 569
- Leandro H., Marra V., Sturani R., 2022, *Phys. Rev. D*, **105**, 023523
- Leja J., et al., 2021, arXiv e-prints, p. [arXiv:2110.04314](https://arxiv.org/abs/2110.04314)
- Levan A. J., et al., 2017, *ApJ*, **848**, L28
- Libanore S., et al., 2021, *J. Cosmol. Astropart. Phys.*, **2021**, 035
- Libanore S., Artale M. C., Karagiannis D., Liguori M., Bartolo N., Bouffanais Y., Mapelli M., Matarrese S., 2022, *J. Cosmol. Astropart. Phys.*, **2022**, 003
- Liu B., Bromm V., 2020a, *MNRAS*, **495**, 2475
- Liu B., Bromm V., 2020b, *MNRAS*, **497**, 2839
- Liu B., Bromm V., 2020c, *ApJ*, **903**, L40
- Liu B., Bromm V., 2021, *MNRAS*, **506**, 5451
- Loredo T. J., 2004, in Fischer R., Preuss R., Toussaint U. V., eds, American Institute of Physics Conference Series Vol. 735, Bayesian Inference and Maximum Entropy Methods in Science and Engineering: 24th International Workshop on Bayesian Inference and Maximum Entropy Methods in Science and Engineering. pp 195–206 ([arXiv:astro-ph/0409387](https://arxiv.org/abs/astro-ph/0409387)), doi:10.1063/1.1835214
- Lyne A. G., Lorimer D. R., 1994, *Nature*, **369**, 127
- Mac Low M.-M., Ferrara A., 1999, *ApJ*, **513**, 142
- MacLeod M., Trenti M., Ramirez-Ruiz E., 2015, preprint, ([arXiv:1508.07000](https://arxiv.org/abs/1508.07000))
- Madau P., Dickinson M., 2014, *ARA&A*, **52**, 415
- Madau P., Fragos T., 2017, *ApJ*, **840**, 39
- Madau P., Rees M. J., 2001, *ApJ*, **551**, L27
- Maggiore M., et al., 2020, *J. Cosmol. Astropart. Phys.*, **2020**, 050

- Magnelli B., et al., 2012, *A&A*, **539**, A155
- Maiolino R., Mannucci F., 2018, arXiv e-prints,
- Maiolino R., Mannucci F., 2019, *A&A Rev.*, **27**, 3
- Maiolino R., et al., 2008, *A&A*, **488**, 463
- Mandel I., Broekgaarden F. S., 2022, *Living Reviews in Relativity*, **25**, 1
- Mandel I., Farmer A., 2018, arXiv e-prints, p. arXiv:1806.05820
- Mandel I., Müller B., 2020, *MNRAS*, **499**, 3214
- Mandel I., de Mink S. E., 2016, *MNRAS*, **458**, 2634
- Mandel I., Farr W. M., Colonna A., Stevenson S., Tišo P., Veitch J., 2017, *MNRAS*, **465**, 3254
- Mandel I., Farr W. M., Gair J. R., 2019, *MNRAS*, **486**, 1086
- Mandhai S., Lamb G. P., Tanvir N. R., Bray J., Nixon C. J., Eyles-Ferris R. A. J., Levan A. J., Gompertz B. P., 2022, *MNRAS*, **514**, 2716
- Mannucci F., et al., 2009, *MNRAS*, **398**, 1915
- Mannucci F., Cresci G., Maiolino R., Marconi A., Gnerucci A., 2010, *MNRAS*, **408**, 2115
- Mannucci F., Salvaterra R., Campisi M. A., 2011, *MNRAS*, **414**, 1263
- Mapelli M., 2016, *MNRAS*, **459**, 3432
- Mapelli M., 2018, arXiv e-prints, p. arXiv:1809.09130
- Mapelli M., 2020, *Frontiers in Astronomy and Space Sciences*, **7**, 38
- Mapelli M., Giacobbo N., 2018, *MNRAS*, **479**, 4391
- Mapelli M., Colpi M., Zampieri L., 2009, *MNRAS*, **395**, L71
- Mapelli M., Ripamonti E., Zampieri L., Colpi M., Bressan A., 2010, *MNRAS*, **408**, 234
- Mapelli M., Giacobbo N., Ripamonti E., Spera M., 2017, *MNRAS*, **472**, 2422
- Mapelli M., Giacobbo N., Toffano M., Ripamonti E., Bressan A., Spera M., Branchesi M., 2018, *MNRAS*, **481**, 5324
- Mapelli M., Giacobbo N., Santoliquido F., Artale M. C., 2019, *MNRAS*, **487**, 2
- Mapelli M., Santoliquido F., Bouffanais Y., Arca Sedda M., Giacobbo N., Artale M. C., Ballone A., 2020a, arXiv e-prints, p. arXiv:2007.15022

- Mapelli M., Spera M., Montanari E., Limongi M., Chieffi A., Giacobbo N., Bressan A., Bouffanais Y., 2020b, *ApJ*, **888**, 76
- Mapelli M., Bouffanais Y., Santoliquido F., Arca Sedda M., Artale M. C., 2022, *MNRAS*, **511**, 5797
- Marchant P., Langer N., Podsiadlowski P., Tauris T. M., Moriya T. J., 2016, *A&A*, **588**, A50
- Marchant P., Pappas K. M. W., Gallegos-Garcia M., Berry C. P. L., Taam R. E., Kalogera V., Podsiadlowski P., 2021, *A&A*, **650**, A107
- Margutti R., et al., 2017, *The Astrophysical Journal Letters*, **848**, L20
- Marigo P., Girardi L., Chiosi C., Wood P. R., 2001, *A&A*, **371**, 152
- Marks M., Kroupa P., Dabringhausen J., Pawlowski M. S., 2012, *MNRAS*, **422**, 2246
- Martinez M. A. S., et al., 2020, *ApJ*, **903**, 67
- Matichard F., et al., 2015, *Classical and Quantum Gravity*, **32**, 185003
- McAlpine S., et al., 2016, *Astronomy and Computing*, **15**, 72
- McCarthy K. S., Zheng Z., Ramirez-Ruiz E., 2020, *MNRAS*, **499**, 5220
- McKernan B., Ford K. E. S., Lyra W., Perets H. B., 2012, *MNRAS*, **425**, 460
- McKernan B., et al., 2018, *ApJ*, **866**, 66
- McLeod D. J., McLure R. J., Dunlop J. S., 2016, *MNRAS*, **459**, 3812
- McLeod D. J., McLure R. J., Dunlop J. S., Cullen F., Carnall A. C., Duncan K., 2021, *MNRAS*, **503**, 4413
- Miller M. C., Lauburg V. M., 2009, *ApJ*, **692**, 917
- Mirabel I. F., Rodrigues I., 2003, *Science*, **300**, 1119
- Mirabel I. F., Dhawan V., Mignani R. P., Rodrigues I., Guglielmetti F., 2001, *Nature*, **413**, 139
- Moffett A. J., et al., 2016, *MNRAS*, **457**, 1308
- Mukherjee S., Moradinezhad Dizgah A., 2021, arXiv e-prints, p. arXiv:2111.13166
- Mukherjee S., Wandelt B. D., Nissanke S. M., Silvestri A., 2021, *Phys. Rev. D*, **103**, 043520
- Muldrew S. I., Pearce F. R., Power C., 2011, *MNRAS*, **410**, 2617
- Nagakura H., Sumiyoshi K., Yamada S., 2019, *ApJ*, **878**, 160

- Nakar E., Gal-Yam A., Fox D. B., 2006, *ApJ*, **650**, 281
- Neijssel C. J., et al., 2019, *MNRAS*, **490**, 3740
- Nelemans G., Tauris T. M., van den Heuvel E. P. J., 1999, *A&A*, **352**, L87
- Nelson D., et al., 2015, *Astronomy and Computing*, **13**, 12
- Neumayer N., Seth A., Böker T., 2020, *A&A Rev.*, **28**, 4
- Ng K. K. Y., Vitale S., Farr W. M., Rodriguez C. L., 2021, *ApJ*, **913**, L5
- Ng K. K. Y., et al., 2022a, *ApJ*, **931**, L12
- Ng K. K. Y., Franciolini G., Berti E., Pani P., Riotto A., Vitale S., 2022b, *ApJ*, **933**, L41
- Nguyen C. T., et al., 2022, *A&A*, **665**, A126
- Nicholl M., et al., 2017, *The Astrophysical Journal Letters*, **848**, L18
- Nomoto K., Kobayashi C., Tominaga N., 2013, *ARA&A*, **51**, 457
- Nugent A. E., et al., 2022, *ApJ*, **940**, 57
- O'Connor E., Ott C. D., 2011, *ApJ*, **730**, 70
- O'Leary R. M., Kocsis B., Loeb A., 2009, *MNRAS*, **395**, 2127
- O'Shaughnessy R., Kalogera V., Belczynski K., 2010, *ApJ*, **716**, 615
- O'Shaughnessy R., Gerosa D., Wysocki D., 2017, *Physical Review Letters*, **119**, 011101
- Oesch P. A., et al., 2015, *ApJ*, **804**, L30
- Pantoni L., Lapi A., Massardi M., Goswami S., Danese L., 2019, *ApJ*, **880**, 129
- Pavlovskii K., Ivanova N., Belczynski K., Van K. X., 2017, *MNRAS*, **465**, 2092
- Peeples M. S., Werk J. K., Tumlinson J., Oppenheimer B. D., Prochaska J. X., Katz N., Weinberg D. H., 2014, *ApJ*, **786**, 54
- Perna R., Belczynski K., 2002, *ApJ*, **570**, 252
- Perna R., Artale M. C., Wang Y.-H., Mapelli M., Lazzati D., Sgalletta C., Santoliquido F., 2022, *MNRAS*, **512**, 2654
- Peters P. C., 1964, *Physical Review*, **136**, 1224
- Petrovich C., Antonini F., 2017, *ApJ*, **846**, 146
- Pian E., et al., 2017, *Nature*, **551**, 67

- Pillepich A., et al., 2017, preprint, ([arXiv:1703.02970](https://arxiv.org/abs/1703.02970))
- Planck Collaboration et al., 2020, *A&A*, **641**, A6
- Podsiadlowski P., Langer N., Poelarends A. J. T., Rappaport S., Heger A., Pfahl E., 2004, *ApJ*, **612**, 1044
- Pol N., McLaughlin M., Lorimer D. R., 2019, *ApJ*, **870**, 71
- Popesso P., et al., 2019, *MNRAS*, **483**, 3213
- Popesso P., et al., 2022, arXiv e-prints, p. [arXiv:2203.10487](https://arxiv.org/abs/2203.10487)
- Portegies Zwart S. F., McMillan S. L. W., 2000, *ApJ*, **528**, L17
- Portegies Zwart S. F., Yungelson L. R., 1998, *A&A*, **332**, 173
- Portegies Zwart S. F., Baumgardt H., Hut P., Makino J., McMillan S. L. W., 2004, *Nature*, **428**, 724
- Portegies Zwart S. F., McMillan S. L. W., Gieles M., 2010, *ARA&A*, **48**, 431
- Pozzetti L., et al., 2010, *A&A*, **523**, A13
- Prole L. R., Clark P. C., Klessen R. S., Glover S. C. O., 2022, *MNRAS*, **510**, 4019
- Punturo M., et al., 2010, *Classical and Quantum Gravity*, **27**, 194002
- Qu Y., et al., 2017, *MNRAS*, **464**, 1659
- Rafelski M., Wolfe A. M., Prochaska J. X., Neeleman M., Mendez A. J., 2012, *ApJ*, **755**, 89
- Rafelski M., Neeleman M., Fumagalli M., Wolfe A. M., Prochaska J. X., 2014, *ApJ*, **782**, L29
- Rasskazov A., Kocsis B., 2019, *ApJ*, **881**, 20
- Rastello S., Mapelli M., Di Carlo U. N., Giacobbo N., Santoliquido F., Spera M., Ballone A., 2020, arXiv e-prints, p. [arXiv:2003.02277](https://arxiv.org/abs/2003.02277)
- Reitze D., et al., 2019, in Bull. Am. Astron. Soc.. p. 35 ([arXiv:1907.04833](https://arxiv.org/abs/1907.04833))
- Renzini A., Peng Y.-j., 2015, *ApJ*, **801**, L29
- Repetto S., Davies M. B., Sigurdsson S., 2012, *MNRAS*, **425**, 2799
- Repetto S., Igoshev A. P., Nelemans G., 2017, *MNRAS*, **467**, 298
- Rodighiero G., et al., 2011, *ApJ*, **739**, L40
- Rodighiero G., et al., 2015, *ApJ*, **800**, L10
- Rodriguez C. L., Loeb A., 2018, *ApJ*, **866**, L5

- Rodriguez C. L., Morscher M., Pattabiraman B., Chatterjee S., Haster C.-J., Rasio F. A., 2015, *Physical Review Letters*, **115**, 051101
- Rodriguez C. L., Chatterjee S., Rasio F. A., 2016, *Phys. Rev. D*, **93**, 084029
- Rodriguez C. L., Amaro-Seoane P., Chatterjee S., Kremer K., Rasio F. A., Samsing J., Ye C. S., Zevin M., 2018, *Phys. Rev. D*, **98**, 123005
- Rodriguez C. L., Zevin M., Amaro-Seoane P., Chatterjee S., Kremer K., Rasio F. A., Ye C. S., 2019, *Phys. Rev. D*, **100**, 043027
- Rose J. C., Torrey P., Lee K. H., Bartos I., 2021, *ApJ*, **909**, 207
- Safarzadeh M., Berger E., 2019, *ApJ*, **878**, L12
- Sagert I., Schaffner-Bielich J., 2008, *A&A*, **489**, 281
- Salpeter E. E., 1955, *ApJ*, **121**, 161
- Samsing J., 2018, *Phys. Rev. D*, **97**, 103014
- Samsing J., MacLeod M., Ramirez-Ruiz E., 2014, *ApJ*, **784**, 71
- Sana H., et al., 2012, *Science*, **337**, 444
- Sánchez-Menguiano L., et al., 2016, *A&A*, **587**, A70
- Sánchez S. F., et al., 2014, *A&A*, **563**, A49
- Sanders R. L., et al., 2020, *MNRAS*, **491**, 1427
- Santini P., et al., 2021, *A&A*, **652**, A30
- Santoliquido F., Mapelli M., Bouffanais Y., Giacobbo N., Di Carlo U. N., Rastello S., Artale M. C., Ballone A., 2020, arXiv e-prints, p. arXiv:2004.09533
- Santoliquido F., Mapelli M., Giacobbo N., Bouffanais Y., Artale M. C., 2021, *MNRAS*, **502**, 4877
- Santoliquido F., Mapelli M., Artale M. C., Boco L., 2022, *MNRAS*, **516**, 3297
- Sargent M. T., Béthermin M., Daddi E., Elbaz D., 2012, *ApJ*, **747**, L31
- Savchenko V., et al., 2017, *The Astrophysical Journal Letters*, **848**, L15
- Schaye J., et al., 2015, *MNRAS*, **446**, 521
- Schechter P., 1976, *ApJ*, **203**, 297
- Schneider R., Ferrara A., Natarajan P., Omukai K., 2002, *ApJ*, **571**, 30

- Schneider R., Omukai K., Inoue A. K., Ferrara A., 2006, *MNRAS*, **369**, 1437
- Schneider R., Graziani L., Marassi S., Spera M., Mapelli M., Alparone M., Bennassuti M. d., 2017, *MNRAS*, **471**, L105
- Schreiber C., et al., 2015, *A&A*, **575**, A74
- Schwab J., Quataert E., Bildsten L., 2015, in American Astronomical Society Meeting Abstracts #225. p. 343.11
- Sedda M. A., 2020, *ApJ*, **891**, 47
- Singh N., Bulik T., Belczynski K., Askar A., 2022, *A&A*, **667**, A2
- Skinner D., Wise J. H., 2020, *MNRAS*, **492**, 4386
- Soares-Santos M., et al., 2017, *The Astrophysical Journal Letters*, **848**, L16
- Speagle J. S., Steinhardt C. L., Capak P. L., Silverman J. D., 2014, *ApJS*, **214**, 15
- Spera M., Mapelli M., 2017, *MNRAS*, **470**, 4739
- Spera M., Mapelli M., Giacobbo N., Trani A. A., Bressan A., Costa G., 2019, *MNRAS*, **485**, 889
- Stachie C., Coughlin M. W., Christensen N., Muthukrishna D., 2020, *MNRAS*, **497**, 1320
- Stacy A., Bromm V., 2013, *MNRAS*, **433**, 1094
- Stacy A., Bromm V., Lee A. T., 2016, *MNRAS*, **462**, 1307
- Stevenson S., Berry C. P. L., Mandel I., 2017, preprint, ([arXiv:1703.06873](https://arxiv.org/abs/1703.06873))
- Stone N. C., Metzger B. D., Haiman Z., 2017, *MNRAS*, **464**, 946
- Susa H., Hasegawa K., Tominaga N., 2014, *ApJ*, **792**, 32
- Tagawa H., Haiman Z., Kocsis B., 2019, arXiv e-prints, p. [arXiv:1912.08218](https://arxiv.org/abs/1912.08218)
- Talbot C., Thrane E., 2018, *ApJ*, **856**, 173
- Tang P. N., Eldridge J. J., Stanway E. R., Bray J. C., 2020, *MNRAS*, **493**, L6
- Tanikawa A., 2013, *MNRAS*, **435**, 1358
- Tanikawa A., Susa H., Yoshida T., Trani A. A., Kinugawa T., 2020, arXiv e-prints, p. [arXiv:2008.01890](https://arxiv.org/abs/2008.01890)
- Tanikawa A., Kinugawa T., Yoshida T., Hijikawa K., Umeda H., 2021a, *MNRAS*, **505**, 2170
- Tanikawa A., Susa H., Yoshida T., Trani A. A., Kinugawa T., 2021b, *ApJ*, **910**, 30

- Tanikawa A., Chiaki G., Kinugawa T., Suwa Y., Tominaga N., 2022a, *Pub. Astro. Soc. of Japan*, **74**, 521
- Tanikawa A., Yoshida T., Kinugawa T., Trani A. A., Hosokawa T., Susa H., Omukai K., 2022b, *ApJ*, **926**, 83
- Tauris T. M., van den Heuvel E. P. J., 2006, in , Vol. 39, Compact stellar X-ray sources. pp 623–665
- Tauris T. M., et al., 2017, *ApJ*, **846**, 170
- Tegmark M., Silk J., Rees M. J., Blanchard A., Abel T., Palla F., 1997, *ApJ*, **474**, 1
- Telford O. G., Dalcanton J. J., Skillman E. D., Conroy C., 2016, *ApJ*, **827**, 35
- Thrane E., Talbot C., 2020, *Publ. Astron. Soc. Aust.*, **37**, e036
- Timmes F. X., Woosley S. E., Weaver T. A., 1996, *ApJ*, **457**, 834
- Tiwari V., 2018, *Classical and Quantum Gravity*, **35**, 145009
- Toffano M., Mapelli M., Giacobbo N., Artale M. C., Ghirlanda G., 2019, *MNRAS*, **489**, 4622
- Tomczak A. R., et al., 2016, *ApJ*, **817**, 118
- Tornatore L., Ferrara A., Schneider R., 2007, *MNRAS*, **382**, 945
- Tremonti C. A., et al., 2004, *ApJ*, **613**, 898
- Tutukov A., Yungelson L., 1973, *Nauchnye Informatsii*, **27**, 70
- Uysal B., Hartwig T., 2023, *MNRAS*, **520**, 3229
- Valiante R., Schneider R., Volonteri M., Omukai K., 2016, in Active Galactic Nuclei 12: A Multi-Messenger Perspective (AGN12). p. 4, doi:10.5281/zenodo.163515
- Venumadhav T., Zackay B., Roulet J., Dai L., Zaldarriaga M., 2019, *Phys. Rev. D*, **100**, 023011
- Venumadhav T., Zackay B., Roulet J., Dai L., Zaldarriaga M., 2020, *Phys. Rev. D*, **101**, 083030
- Verbunt F., Igoshev A., Cator E., 2017, *A&A*, **608**, A57
- Vigna-Gómez A., et al., 2018, *MNRAS*, **481**, 4009
- Vijaykumar A., Saketh M. V. S., Kumar S., Ajith P., Choudhury T. R., 2020, arXiv e-prints, p. arXiv:2005.01111
- Villante F. L., Serenelli A. M., Delahaye F., Pinsonneault M. H., 2014, *ApJ*, **787**, 13

- Vink J. S., de Koter A., Lamers H. J. G. L. M., 2001, *A&A*, **369**, 574
- Vink J. S., Higgins E. R., Sander A. A. C., Sabhahit G. N., 2021, *MNRAS*, **504**, 146
- Vitale S., Farr W. M., Ng K. K. Y., Rodriguez C. L., 2019, *ApJ*, **886**, L1
- Vogelsberger M., et al., 2014a, *MNRAS*, **444**, 1518
- Vogelsberger M., et al., 2014b, *Nature*, **509**, 177
- Volpato G., Marigo P., Costa G., Bressan A., Trabucchi M., Girardi L., 2022, arXiv e-prints, p. arXiv:2212.09629
- Voss R., Tauris T. M., 2003, *MNRAS*, **342**, 1169
- Wang L., Spurzem R., Aarseth S., Nitadori K., Berczik P., Kouwenhoven M. B. N., Naab T., 2015, *MNRAS*, **450**, 4070
- Wang L., et al., 2016, *MNRAS*, **458**, 1450
- Wang L., Tanikawa A., Fujii M., 2022, *MNRAS*, **515**, 5106
- Webbink R. F., 1984, *ApJ*, **277**, 355
- Wheeler J. C., Sneden C., Truran James W. J., 1989, *ARA&A*, **27**, 279
- Wollenberg K. M. J., Glover S. C. O., Clark P. C., Klessen R. S., 2020, *MNRAS*, **494**, 1871
- Wong K. W. K., Gerosa D., 2019, *Phys. Rev. D*, **100**, 083015
- Wong T.-W., Valsecchi F., Ansari A., Fragos T., Glebbeek E., Kalogera V., McClintock J., 2014, *ApJ*, **790**, 119
- Woosley S. E., 2017, *ApJ*, **836**, 244
- Woosley S. E., Heger A., 2021, *ApJ*, **912**, L31
- Woosley S. E., Pinto P. A., Martin P. G., Weaver T. A., 1987, *ApJ*, **318**, 664
- Woosley S. E., Heger A., Weaver T. A., 2002, *Reviews of Modern Physics*, **74**, 1015
- Xu X.-J., Li X.-D., 2010, *ApJ*, **716**, 114
- Yang Y., Bartos I., Haiman Z., Kocsis B., Márka Z., Stone N. C., Márka S., 2019, *ApJ*, **876**, 122
- Ye C. S., Fong W.-f., Kremer K., Rodriguez C. L., Chatterjee S., Fragione G., Rasio F. A., 2020, *ApJ*, **888**, L10
- Yoshida N., Abel T., Hernquist L., Sugiyama N., 2003, *ApJ*, **592**, 645

- Yoshida N., Omukai K., Hernquist L., Abel T., 2006, *ApJ*, **652**, 6
- Yoshida T., Umeda H., Maeda K., Ishii T., 2016, *MNRAS*, **457**, 351
- Zackay B., Dai L., Venumadhav T., Roulet J., Zaldarriaga M., 2019a, arXiv e-prints, p. [arXiv:1910.09528](#)
- Zackay B., Venumadhav T., Dai L., Roulet J., Zaldarriaga M., 2019b, *Phys. Rev. D*, **100**, 023007
- Zahid H. J., Dima G. I., Kudritzki R.-P., Kewley L. J., Geller M. J., Hwang H. S., Silverman J. D., Kashino D., 2014, *ApJ*, **791**, 130
- Zevin M., Pankow C., Rodriguez C. L., Sampson L., Chase E., Kalogera V., Rasio F. A., 2017, *ApJ*, **846**, 82
- Zevin M., Samsing J., Rodriguez C., Haster C.-J., Ramirez-Ruiz E., 2019, *ApJ*, **871**, 91
- Zevin M., Spera M., Berry C. P. L., Kalogera V., 2020, arXiv e-prints, p. [arXiv:2006.14573](#)
- Zheng Z., Ramirez-Ruiz E., 2007, *ApJ*, **665**, 1220
- Ziosi B. M., Mapelli M., Branchesi M., Tormen G., 2014, *MNRAS*, **441**, 3703
- de Mink S. E., Mandel I., 2016, *MNRAS*, **460**, 3545
- du Buisson L., et al., 2020, arXiv e-prints, p. [arXiv:2002.11630](#)
- van Son L. A. C., de Mink S. E., Chruslinska M., Conroy C., Pakmor R., Hernquist L., 2022a, arXiv e-prints, p. [arXiv:2209.03385](#)
- van Son L. A. C., et al., 2022b, *ApJ*, **931**, 17
- van den Heuvel E. P. J., Portegies Zwart S. F., de Mink S. E., 2017, *MNRAS*, **471**, 4256